University of California
Berkeley
Seismological Laboratory

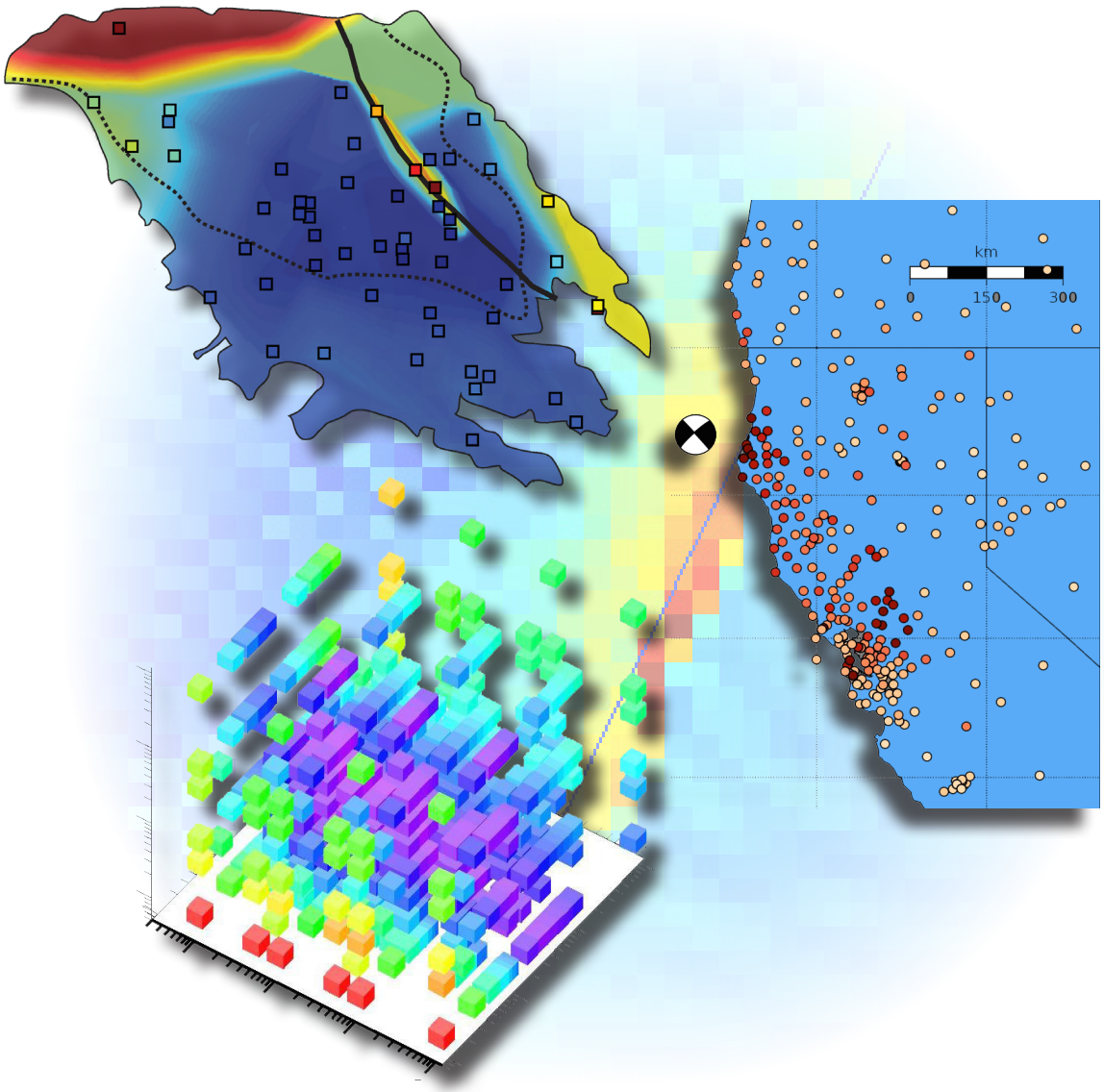

Annual Report

July 2013–June 2014

Berkeley Seismological Laboratory

Annual Report
July 2013—June 2014

Contents

Director's Report 1

Highlights 1
BSL Personnel News 2
Facilities Review 3
Acknowledgements 4

Research Studies 6

Mineral Physics

1 ***In Situ*** Deformation of MgO and $MgSiO_3$ Perovskite: Lower Mantle Implications 9
2 The Single Free Energy Surface of Amorphous $CaSiO_3$ from 0 to 44 GPa of Pressure 11
3 A Laboratory Rock-physics Study on How P-wave Properties Change with Respect to Ice Content in Saturated, Unconsolidated Saline Permafrost 13
4 High Temperature Miscibility of Terrestrial Materials: First Principles Calculations for the Early Earth 15

Earth Structure

5 Whole-mantle Spectral-Element Waveform Tomography: SEMUCB-WM1 19
6 Body Wave Tomography of the Juan de Fuca plate 21
7 Further Constraints on Lateral Variations of Structure at the Base of the Pacific LLSVP Using Shear Diffracted Waves 23
8 Full Waveform Seismic Tomography Using Stochastic Methods 25
9 3D Kirchoff Prestack Depth Migration of Receiver Function 27
10 Joint Inversion of Receiver Functions and SKS Data: An Application to the Canadian Craton 29
11 High Resolution Upper Mantle Discontinuity Images Across the Pacific Ocean from ***SS*** Precursors Using the Local Slant Stack Filters 31
12 Separating Intrinsic and Extrinsic Anisotropy 33

Rheology and Fault Mechanics

13 Probing the Lithospheric Rheology Across the Eastern Margin of the Tibetan Plateau 37
14 Post 1989 M_w 6.9 Loma Prieta Earthquake Viscous Relaxation Revealed from GPS and InSAR Data 39
15 Upper Mantle Rheology Illuminated from the 2011 Tohoku-Oki Earthquake 41
16 Geodetic Tracking and Characterization of Precipitation-Triggered Slow Moving Landslide Displacements in the Eastern San Francisco Bay Hills, California, USA 43
17 Temporal Changes in Seismic Velocity with Fluid Injection at The Geysers Geothermal Field, California 45
18 Hydrologic Modulation of Seismicity in Western China 1991–2013 47
19 Comparison of Hydrological Responses to the Wenchuan and Lushan Earthquake 49
20 Establishing the Magnitude Threshold of Dynamically Triggered Earthquakes 51
21 Evidence For a Triggered Foreshock Sequence Prior to the 2012 M7.0 Baja, CA Earthquake 53
22 Repeating Earthquakes and Inferred Deep Slip on the Calaveras Fault 55
23 High-Resolution Imaging of Hayward Fault Microearthquakes 57

Seismic Sources

24 Temporal Variations of Intraslab Earthquake Activity Following the 2011 Tohoku-Oki Earthquake 61
25 Moment Tensor Inversion of Seismic Events and Tremor-Tilt Observations Associated with the Sinkhole at Napoleonville Salt Dome, Louisiana 63
26 Preliminary Results of Moment Tensor Analysis at The Geysers Geothermal Field, CA 65

27 Moment Tensor Analysis of Shallow Sources 67
28 Lessons Learned from Broadband Waveform Modeling Across the Mendocino Triple Junction 69

Enhancements to Observational Systems

29 ElarmS-2: Rapid Accurate Alerts across California 73
30 Operational Real-Time GPS-enhanced Earthquake Early Warning 75
31 Evaluation of Smartphones as Seismometers 77
32 High-rate GPS Records Reveal Basin Amplification in the San Joaquin Delta 79
33 Predictability of Hydraulic Head Changes and Characterization of Aquifer System Properties from InSAR-Derived Ground Deformation 81
34 TremorScope: Imaging the Deep Workings of the San Andreas Fault 83
35 Normal Modes: Investigating Signal and Noise Phenomena Across Instrument Types and Deployment 85

Broadening Engagement **88**

1 Earthquake Research Affiliates Program 89
2 Engaging the Public 91
3 Science and Society 95

Operations **98**

1 Berkeley Digital Seismic Network (BDSN) 100
2 California Integrated Seismic Network (CISN) 109
3 Northern Hayward Fault Network 114
4 Parkfield Borehole Network (HRSN) 123
5 Data Acquisition and Quality Control 133
6 Bay Area Regional Deformation Network (BARD) 137
7 Northern California Earthquake Monitoring 143
8 Northern California Earthquake Data Center 151

Glossary of Common Acronyms **162**

Appendix I: Publications, Presentations, Awards and Panels **164**

Appendix II: Seminar Speakers **176**

BSL Organizational Chart **178**

Chapter 1

Director's Report

Highlights

It is a great pleasure to present this year's Berkeley Seismological Laboratory (BSL) Annual Report—my third report as Director. Each year it is exhilarating to be reminded of the wide range of BSL activities, as captured in these pages. This year we are also delighted to be **ranked number 1 in Geophysics and Seismology** for the first time by US News and World Reports. This is a ranking based on surveys sent to academics in the field. I see this as an acknowledgement of the dynamic and wide-ranging research program fostered by BSL faculty, researchers and students. The BSL is also unique for our cutting-edge geophysical observing facility that includes broadband and strong-motion seismometers, high-rate real-time GPS, and borehole instrumentation along active faults. Spanning both the research and network-facility realms, BSL provides an environment in which the extramural research program is strengthened and broadened by the facility, and the facility continues to push the boundaries of terrestrial observations in response to research needs. In addition, the BSL continues to reach out and connect with the consumers of our data and our science. These include researchers around the world, students, the public, and private or public sector institutions with a need and desire for an improved understanding of solid Earth processes.

In my report this year I highlight three of BSL's ongoing activities. The first is the wide reach of the BSL datasets as I review who is downloading data from our data center. Secondly, I want to highlight the progress that we have made toward building a public earthquake warning system for the United States. I will then provide a quick overview of the range of two-page research contributions in this year's report. Personnel news, a review of our facilities, and acknowledgements follow.

Firstly, the reach of BSL data resources. The BSL geophysical networks—which I highlighted in my report last year—include our broadband and strong motion seismic network (the Berkeley Digital Seismic Network, BDSN), the real-time GPS network (the Bay Area Regional Deformation Network, BARD), and our borehole seismic networks along active faults focused in the Parkfield area of central California and the Bay Area. When possible and appropriate, these different instrument types are co-located. In sum, our geophysical instrumentation occupies about 70 locations across Northern California (See Figure 1.1). Data from all these sites stream into our real-time processing center here at UC Berkeley and are used to provide rapid earthquake information. In addition, all the data are archived at the Northern California Earthquake Data Center (http://ncedc.org/) here at UC Berkeley, and delivered openly and immediately to the scientific community around the world. The study of solid Earth deformation requires long-term data collection for periods of decades, while also providing high sample rates—up to hundreds of samples per second—in order to capture the details of sudden, rapid events such as earthquakes. The NCEDC provides this service for the research community.

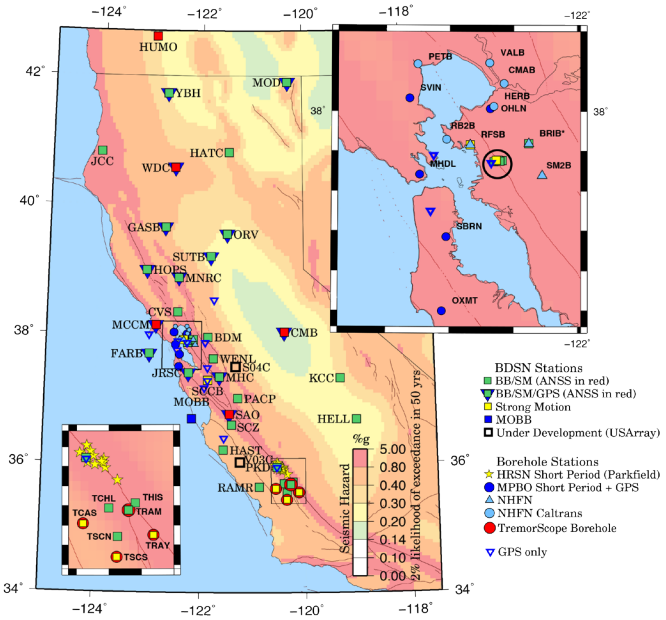

Figure 1.1: The BSL geophysical network. The color scale shows seismic hazard. The colors represent a percent of the acceleration due to gravity that has greater than a 2% probability of exceedance in the next 50 yers.

With the BSL networks we strive for extremely high-quality datasets. This means that the instruments are installed in high-quality, low-noise vaults. Extensive quality control is applied to our data to identify any deterioration of the instrumentation and remedy it immediately. The BDSN network boasts 99.23% data completeness for the 2013–2014 fiscal year. Also, 67% of the stations have a single data segment for the year, meaning that not a single data sample was lost. This level of completeness is unrivaled by any other seismic network and allows researchers to study very long-term deformation processes that have very small detectable signals.

In addition to archiving data from the BSL networks, the NCEDC archives data from all the major geophysical networks in Northern California, including networks operated by the US Geological Survey, the California Department of Water Resources, PG&E, and Calpine. The total size of the NCEDC digital archive today is 80 Tb, and data extend back to 1984, however, records extend all the way back to 1887, when UC Berkeley installed the first seismometers in the western hemisphere, and paper records—which are still periodically used by visiting scientists—go back to 1910. In the past year we added 10 Tb to the archive. The data are freely available via a range of tools, including a new suite of tools, "web services", developed over the last few years, that make use of the http-type requests to access

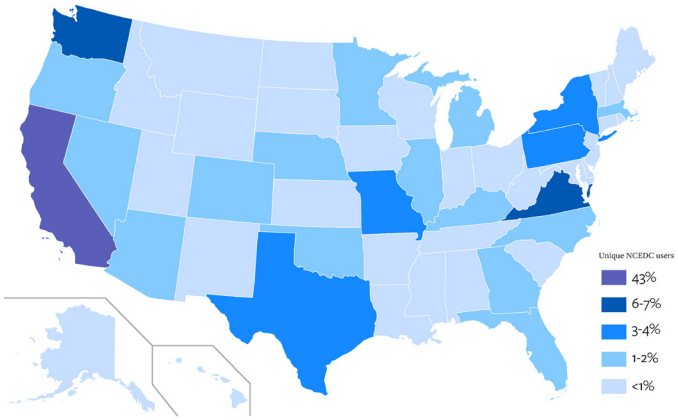

Figure 1.2: The distribution of NCEDC users as a percentage of the total US users for 2013–2014.

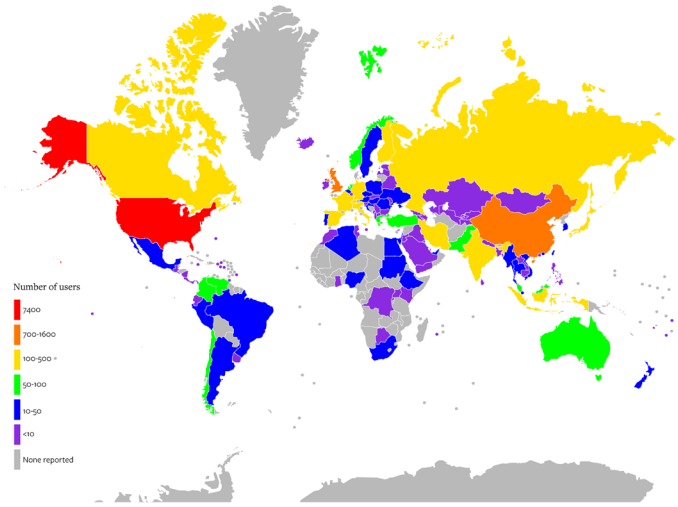

Figure 1.3: The distribution of NCEDC users worldwide colored according to total number of users on a per country basis for 2013–2014.

timeseries data and all associated metadata. For the past year we have compiled a list of people downloading data from the NCEDC. As some of the older data access tools do not allows us to track users, the list is incomplete. Still, we identified over 14,000 users. Figures 1.2 and 1.3 show the distribution of these users. Not surprisingly, the greatest number of users is here in the US, and specifically in California. However, the global reach of the data is remarkable. There are many users in Russia, China, Germany, the UK, India, Canada, Iran, Japan, France, Italy, Spain, Australia and Indonesia. There are also smaller numbers of users in dozens of other countries on every continent except Antarctica. While the funding for our geophysical network facility is primarily driven by the need for real-time earthquake hazard information in Northern California, the high-quality data we produce and archive are then used for a plethora of research activities that are truly global.

The second topic I would like to highlight is progress towards a public earthquake early warning (EEW) system. This past year has seen rapid progress towards a system for the west coast of the Unites States. The BSL has been involved in developing the capabilities for early warnings since 2005 both with active research programs and though leadership in the collaborative effort. At the beginning of this past year, Governor Jerry Brown signed into law the EEW legislation introduced by Senator Alex Padilla. The legislation calls for a statewide EEW system but does not allocate funding, instead calling on the Governor's Office of Emergency Services to identify sources of funding. At the end of this review year, the House Appropriations Committee in Washington DC included partial EEW funding in their FY2015 appropriation. The cost of building and operating a west coast system for the first 5 years is $120M, and while there is still much work to be done to obtain full funding, these were both significant steps forward.

This year has also seen significant technical progress with EEW. In March and April a series of earthquakes were felt across the Los Angeles region, the largest being the March 28, 2014, M5.1 La Habra earthquake. Recent improvements to the seismology-based ElarmS EEW methodology—developed here at BSL and now operating along the entire U.S. west coast—provided the first alerts for all of the earthquakes associated with this sequence. While the time needed to process the data still means that it was not possible to generate an alert for the epicentral region, the vast majority of Angelenos shaken by these quakes could have received a warning (Figure 1.4, see http://youtu.be/Lt7aBD4CUIQ). Also, our real-time GPS-based EEW methodology, named G-larmS, is now operational and is undergoing testing on the real-time system in Northern California. It uses the BSL's BARD network along with other GPS stations across the region to detect permanent displacements generated by earthquakes. A rapid inversion solves for the distribution of slip on the identified fault plane and provides a magnitude estimate that is more robust than seismology-based estimates for big (M>7) earthquakes.

The EEW project is an example of the synergies produced when active research programs are brought together with cutting-edge observational facilities, and where there are also direct interactions with consumers of hazard information. The arc of the project started with a few researchers and computers, asking the question of how quickly the magnitude of an earthquake can be determined. It progressed through initial, pseudo-real-time testing to full implementation on the real-time system in California. Now, while the research and development continues, BSL staff are talking to public and private sector entities about how best to use earthquake alerts. Legislators have taken note of the important implications of this new hazard-reduction capability, and are enacting legislation to support it at state and federal levels. BSL researchers and staff are, of course, supporting these efforts. Finally, all of this is only possible thanks to the close collaboration between BSL, Caltech, University of Washington, ETH Zürich, SCEC, the Gordon and Betty Moore Foundation and the U.S. Geological Survey.

Having highlighted the NCEDC and the EEW project, I want to provide a summary of the wide-ranging research conducted at the BSL. The active research efforts of the students, postdocs, researchers, faculty and visitors are at the heart of BSL activities. Section 2 of our report contains 36 research summaries describing ongoing projects. The research groups headed by nine of our faculty members have contributed to this year's report. The topics covered fall into five broad categories:

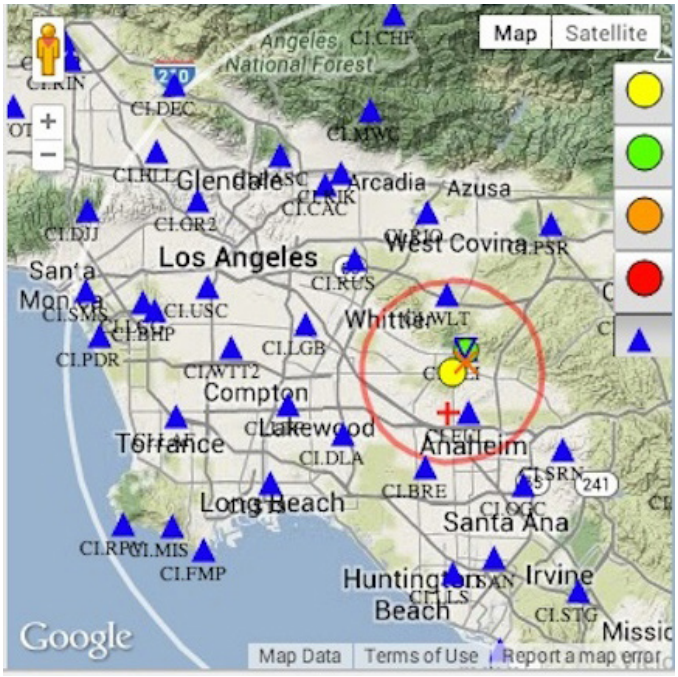

Figure 1.4: The red circle on this map of Southern California shows the area that would not have received alerts for the *M*5.1 La Habra earthquake. This is the so called blind zone caused by computational time and station density limitations.

1. The Mineral Physics section includes experimental and numerical experiments on the properties of minerals found in the Earth's crust and mantle, and on the miscibility of terrestrial materials in the early Earth. The effects of permafrost on seismic velocity are also described in this section.

2. The Earth Structure section includes new regional and global studies of structure and processes. Our focus on North America continues with studies of the Juan de Fuca plate and the Canadian Craton, while global imaging provides ever-improved constraints on upwelling and downwelling features in the mantle. New receiver function methods to constrain discontinuity structure are being developed, to improve imaging in complex regions, and across entire oceans.

3. The Rheology and Fault Mechanics section includes studies of deformation across Tibet, Japan and California as well as the more local process of land sliding. The links between hydrologic processes, seismicity and landslides are also explored in China and California. Fault processes are also investigated through triggering, repeating earthquakes and micro-seismicity on faults.

4. The Seismic Source section begins with a study of intraslab seismicity following the Tohoku-Oki earthquake. Seismic source characterization continues with studies of a sinkhole, the Geysers geothermal region and shallow seismicity. The final study in the section describes an effort to improve our ability to characterize offshore-seismicity on the Juan de Fuca plate.

5. Various research efforts contribute to improving observational capabilities. This year's Enhancements to Observational Systems research papers include a summary of both the seismic (ElarmS) and geodetic (GlarmS) earthquake early warning algorithms we are developing. A description of how we are using smartphone accelerometers to detect earthquakes, and observations of shaking amplification effects in data from high-rate GPS. Also, the application of InSAR to assessing aquifer changes, using data from borehole instrumentation to detect tremor on the San Andreas Fault, and assessing instrument quality using normal modes.

Many of these research efforts are stimulated and inspired by our facilities. These include our geophysical networks that continuously collect a variety of data from across Northern California, and the NCEDC that delivers the data to researchers around the world and within the BSL. More information about these networks and their development can be found in the Facilities Review below.

BSL Personnel News

One new PhD graduate student, William Hawley, and two Postdoctoral Fellows, Marco Calo and Estelle Chaussard joined the lab during the 2013-14 academic year. Three PhD students graduated, their names and thesis titles were: Mong-Han Huang, "Crustal Deformation During Co- and Postseismic Periods"; Zhao Zheng (Allen), "Refining Constraints on Seismic Discontinuities and Elastic Structure in the Earth's Upper Mantle"; and Scott French, "Global Full-Waveform Tomography using the Spectral Element Method: New Constraints on the Structure of Earth's Interior". Graduate student Ryan Turner completed his MS thesis entitled "Exploration of Slip Rate Variation on the Central San Andreas Fault Using Repeating Earthquakes and Geodesy". Three of our Postdoctoral Fellows moved on to new positions elsewhere. Serdar Kuyuk took up a faculty position at Sakarya University, Turkey. Lingsen Meng is now an assistant professor at UCLA, and Ronni Grapenthin will be starting as an assistant professor at New Mexico Tech in the Fall 2014 semester.

The BSL also continued to provide a range of research projects for undergraduate students, two of whom have contributed research reports. This year's cohort consisted of Rohan Agarwal, Amanda Atkinson, Joel Bai, Michael Faggetter, James Hoenig, Voon Hui Lai, Frances (Julie) Leiva, Brenda Luna, and Michael Tran.

As usual, a stream of visitors spent varying amounts of time at the lab. These included Pierre Clouzet from IPG Paris, and Yuzhu Liu from Tongji University visiting Barbara Romanowicz's group; Seung-Hoon Yoo visiting Doug Dreger's group, and Men-Andrin Meier and Yannick Behr from ETH Zürich visiting my group.

During the year one staff member retired, Gretchen vonDuering, who has been providing HR support to the BSL for the past few years. We had one new arrival, that of Steve Allen who joined the IT group. During the year, the BSL also transitioned into the new Campus Shared Services (CSS) model for administrative support. As a result several staff moved into CSS including Matt Carli (purchasing) and Marion Banks (travel). Our research administration staff, Clarissa Foreman and Raluca Iordache, also became part of CSS but remain located in McCone Hall. Judith Coyote (department manager) and Dawn Geddes (financial analyst) remain part of the BSL.

Facilities Review

The Berkeley Seismological Laboratory (BSL) is an Organized Research Unit (ORU) on the UC Berkeley campus. Its mission is unique in that, in addition to research and education in seismology, geophysics, and earthquake-related science, it is responsible for providing real-time earthquake information. This information is required by the UC Berkeley constituency, various local and state governments and private organizations including emergency response, and is consumed by the general public. The BSL is therefore both a research center and a facility/data resource, which sets it apart from most other ORUs. A major component of our activities is focused on developing and maintaining several regional observational networks, and participating, along with other agencies, in various aspects of the collection, analysis, archival, and distribution of data pertaining to earthquakes, while maintaining a vigorous research program on earthquake processes and Earth structure. In addition, the BSL staff spend considerable time on public relations activities, including tours, talks to public groups, response to public inquiries about earthquakes, and an informational web presence (http://earthquakes.berkeley.edu/).

UC Berkeley installed the first seismograph in the Western Hemisphere at Mount Hamilton (MHC) in 1887. Since then, it has played a leading role in the operation of state-of-the-art seismic instruments and in the development of advanced methods for seismic data analysis and interpretation. Notably, the installation, starting in 1927, of Wood-Anderson seismographs at four locations in Northern California (BKS, ARC, MIN, and MHC) allowed the accurate determination of local earthquake magnitude from which a unique historical catalog of regional earthquakes has been maintained to this day, providing crucial input to earthquake probability studies.

Over the years, the Berkeley Seismographic Stations (BSS), as the BSL was then called, continued to drive technological improvements. The first centrally telemetered network using phone lines in an active seismic region was installed by BSS in 1960. The BSS was the first institution in California to operate a three-component "broadband" system (1963). It played a major role in the early characterization of earthquake sources using "moment tensors" and source-time functions. The BSS also made important contributions to the early definitions of detection/discrimination of underground nuclear tests and, jointly with UCB Engineering, to earthquake hazards work.

Starting in 1986, the BSS acquired four state-of-the-art broadband instruments (STS-1), while simultaneously developing PC-based digital telemetry. These two developments laid the groundwork for the modern networks we operate today. As telecommunication and computer technologies made rapid progress, in parallel with broadband instrument development, paper record reading was abandoned in favor of automated analysis of digital data. One paper-based helicorder does remain operational, primarily for the press and visitors to view.

Today, the BSL's networks can be divided into three groups of instrumentation that are deployed at a total of ~70 sites across Central and Northern California. The instrumentation types predominantly consist of broadband plus strong motion seismic, borehole seismic, and GPS equipment, and are often co-located when appropriate. Data from all instrumentation stream continuously into the BSL's real-time monitoring system which provides earthquake warnings, notification and characterization. It is also delivered to the archive where it can be accessed immediately by researchers from around the world for scientific study.

The Berkeley Digital Seismic Network (BDSN) is our regional seismic network of about 40 sites where both broadband and strong motion seismic instrumentation is installed. This network is the backbone of the BSL's operations, feeding the necessary data for real-time estimation of location, size and rupture parameters for earthquakes in Central and Northern California. This network has been steadily growing since the 1990's and consists of very high quality, low-noise sites, making the data ideal for a range of research efforts. The array can be used to study local or global earthquake sources, and provides data for investigation of 3D crustal structure in California and its effects on regional waveform propagation, which in turn affect the intensity of ground shaking in larger earthquakes. Recent additions to the network include an ocean bottom seismometer in the Monterey Bay (MOBB) providing real-time data via an undersea cable (operated in collaboration with MBARI), and also the Tremorscope stations along the Cholame section of the San Andreas Fault just south of Parkfield.

The real-time data are also Berkeley's contribution to the California Integrated Seismic Network (CISN), which is a federation of networks that jointly provide all real time earthquake information in the state. Since 1996, the BSL and the USGS in Menlo Park have closely cooperated to provide the joint earthquake notification program for Northern California. This program capitalizes on the complementary capabilities of the networks operated by each institution to provide rapid and reliable information on the location, size and other relevant source parameters of regional earthquakes. The real-time earthquake information is made available through the BSL's website (http://earthquakes.berkeley.edu).

The BSL's borehole networks represent the second grouping of instrumentation. The High Resolution Seismic Network (HRSN) was installed in 1987 and now consists of 12 operating sites. Additional borehole sites will soon be added as part of the Tremorscope project (see Research Section 2.34). These instruments have led to wide-ranging research into earthquake processes due to their high sensitivity, low noise, and proximity to micro-earthquakes, earthquake clusters and tremor sources along the highly studied Parkfield section of the San Andreas Fault (see Research Section 2.23). In the Bay Area, the Hayward Fault Network also includes 15 borehole instruments that have been installed progressively since the 1990s. The goal of this network is again to collect high signal-to-noise data for micro-earthquakes along the Hayward Fault to gain insight into the physics that govern fault rupture and its nucleation.

The third instrumentation type is GPS. The BSL operates the Bay Area Regional Deformation (BARD) Network consisting of 32 primary sites, 18 collocated with BDSN seismometers. All sites record with a 1 Hz sample rate and telemeter the data to the BSL in real time. Continuous GPS data track the motion of the

tectonic plates and allow us to assess the strain buildup along faults as well as its release either through creeping episodes or through earthquakes. The application of GPS data feeds to real-time earthquake information is also a relatively new development. Very rapid processing now generates displacement waveforms that in turn support the development of improved real-time earthquake analysis methods for significant earthquakes.

The BSL's IT group is active in the development of new software for the collection, archival and real-time analysis of the various geophysical data streams that we collect. In 2009, the new AQMS seismic network software package was rolled out following a multi-year development effort by the BSL in collaboration with other CISN partners. This software provides all the real-time processing components needed by regional seismic networks and is now being rolled-out across the US. The development of real-time GPS processing software is a current area of focus for the lab along with development, testing and implementation of earthquake early warning algorithms that can process data quickly enough to provide alerts to people a few seconds to tens of seconds before shaking is felt.

Archival and distribution of data from the BSL and other regional geophysical networks is performed at the Northern California Earthquake Data Center (NCEDC), operated at the BSL in collaboration with USGS Menlo Park. The data reside on a mass-storage device (current holdings ~80 Tb), and are accessible online (http://www.ncedc.org). In addition to BSL network data, data from the USGS Northern California Seismic Network (NCSN), and other northern California networks, are archived and distributed through the NCEDC. The NCEDC also maintains, archives and distributes various earthquake catalogs.

Finally, the field engineering team is responsible for maintaining our existing ~70 geophysical observatories across Northern California, and designing and installing new sites. Of particular note is the completion in 2011 of the ARRA-funded upgrades. These urgently needed equipment upgrades replaced aging dataloggers at almost all BSL observatories, providing more robust and more rapid transmission of data from the sites to the BSL real-time system. The group is now focused on the design and installation of the new Tremorscope borehole and surface stations just south of Parkfield along the Cholame section of the San Andreas Fault, and on upgrading the HRSN.

All of these operations are supported by an operations and research staff of nine, an IT staff of eight, and an engineering staff of three. Our administrative support group is largely shared with the Department of Earth and Planetary Science and consists of six, with additional support provided by Campus Shared Services. In addition, there are currently three Postdoctoral Scholars and fifteen PhD graduate students associated with the lab, along with eighteen affiliated faculty.

The BSL budget is made up of approximately 50% extramural research support and 50% facility/operations support. The operations/facility support comes from the university, the USGS, the state and several other external sources. Core University funding to our ORU currently provides salary support for one staff scientist (shared by three researchers), one IT staff member, one engineer, 50% of our operations manager, and one administrative assistant. University support represents about one fifth of the total infrastructure support budget. The remaining support comes from extramural grants and contracts, primarily from the USGS, DOE, NSF, and the State of California, through its Office of Emergency Services (CalOES). Currently, grants from the Gordon and Betty Moore Foundation contribute significantly to our operations as do the contributions from the members of our Earthquake Research Affiliates Program.

Acknowledgements

I would like to thank our technical and administrative staff, scientists and students for their efforts throughout the year and their contributions to this annual report. In particular I would like to thank our affiliated faculty, whose research groups are contributing to this report: Professors Roland Bürgmann, Doug Dreger, Raymond Jeanloz, Michael Manga, Burkhard Militzer, Barbara Romanowicz, Chi-Yuen Wang and Rudy Wenk. Individual contributions to activities and report preparation are mentioned in the corresponding sections, except for the appendix sections, which were prepared by Clay Miller.

The BSL Advisory Committee plays an important role providing feedback and guidance on BSL activities and priorities. The committee members are Prof. Steven Glaser (Chair – Civil and Environmental Engineering, UC Berkeley), Prof. Josh Bloom (Astronomy, UC Berkeley), Dr. Thomas Brocher (US Geological Survey), Prof. Michael Manga (Earth and Planetary Science, UC Berkeley), Prof. John Vidale (University of Washington).

I also wish to especially thank the individuals who have regularly contributed to the smooth operation of the BSL facilities: Steve Allen, Mario Aranha, Doug Dreger, John Friday, Peggy Hellweg, Ivan Henson, Ingrid Johanson, Clay Miller, Josh Miller, Pete Lombard, Bob Nadeau, Doug Neuhauser, Charley Paffenbarger, Jenn Strauss, Sarah Snyder, Jennifer Taggart, Taka'aki Taira, Stephen Thompson, Bob Uhrhammer, and Stephane Zuzlewski, and, in the administrative office, Crysthel Catambay, Judith Coyote, Clarissa Foreman, Dawn Geddes, Raluca Iordache and Hanna Knight.

I am particularly grateful to Clay Miller, Jennifer Taggart, Jenn Strauss and Peggy Hellweg for their help in putting together this annual report and bringing it to completion.

The Annual Reports of the Berkeley Seismological Laboratory are available on the web at http://earthquakes.berkeley.edu/annual_report.

Chapter 2

Research Studies

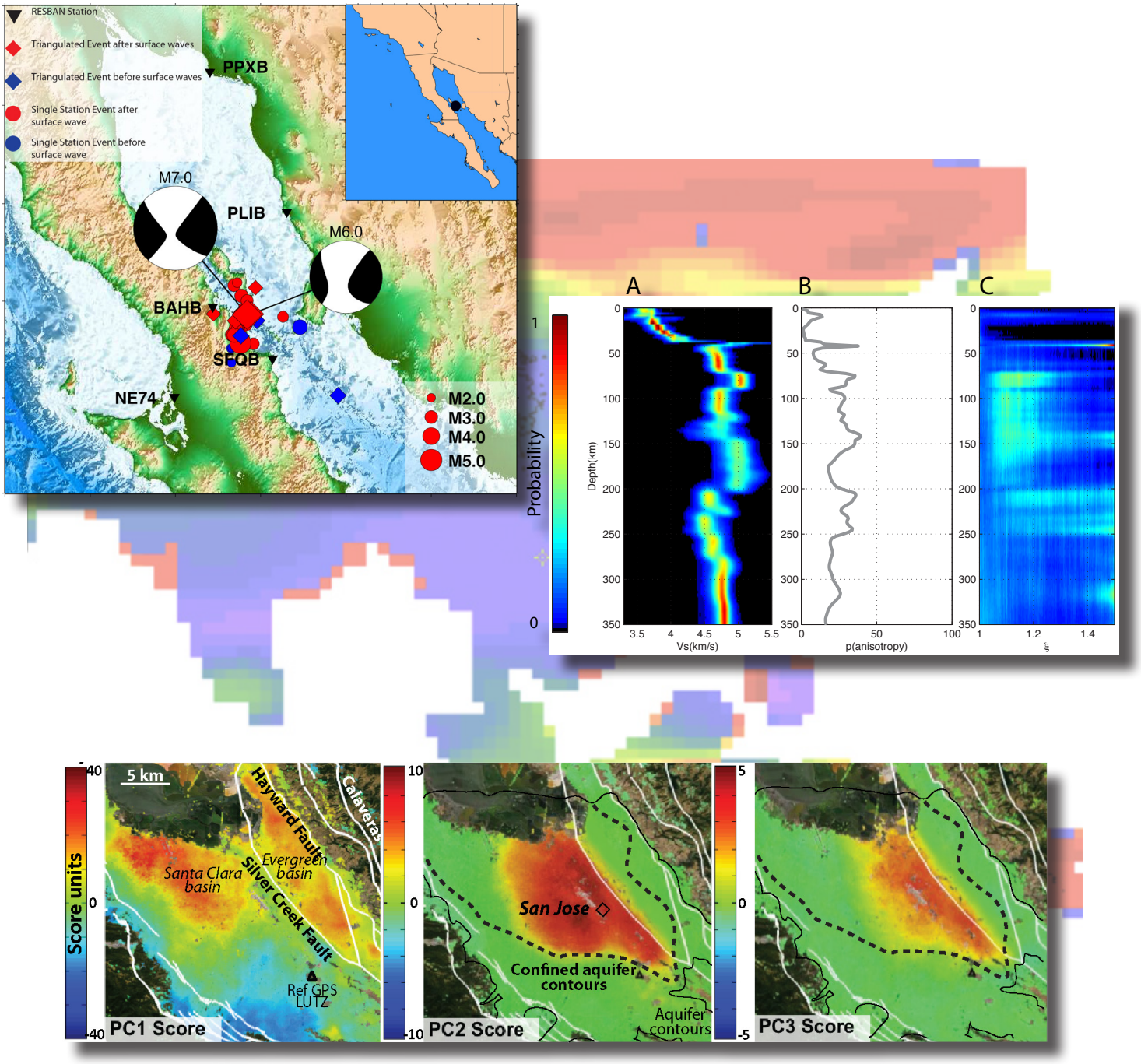

Research Studies:
Mineral Physics

1 *In Situ* Deformation of MgO and $MgSiO_3$ Perovskite: Lower Mantle Implications

Eloisa Zepeda-Alarcon, Pamela M. Kaercher, Hans-Rudolf Wenk

Introduction

Knowledge of deformation of mantle minerals is important for understanding geodynamic implications of seismic data and constraining geophysical modeling. The pursuit to characterize and understand the Earth's interior has been a long standing topic in Earth science. Particularly, there is seismic evidence that there are regions of elastic anisotropy in the mantle (*Panning & Romanowicz*, 2006), and there has been great discussion as to what physical mechanisms are responsible for it (*Mainprice*, 2007). In the upper mantle, seismic anisotropy has been correlated to subduction zones and attributed to the crystallographic preferred orientation (CPO) of olivine as a consequence of the high strains imprinted by subduction (*Long*, 2013). Mineral physics has confirmed the development of CPO in olivine using, for example, a radial diamond anvil cell (rDAC) up to pressures comparable to those of the mantle (*Wenk et al.*, 2004). In the mantle transition zone, seismic anisotropy has been attributed to CPO of wadsleyite (*Kawazoe et. al.*, 2013). The core mantle boundary is a region with strong elastic anisotropy. It has been shown that the observed texture of the mineral phase post-perovskite could explain the measured seismic anisotropy of the region (*Wenk et. al.*, 2011).

There is strong evidence that the bulk composition of the upper and lower mantle are similar, which leads us to believe that the velocity contrast between these two regions is mainly due to the phase transition of olivine $(Mg,Fe)_2SiO_4$ to perovskite $(Mg,Fe)SiO_3$ and ferropericlase (Mg,Fe)O (*McDonough & Sun*, 1995). Studies on $MgSiO_3$ perovskite show that dislocation creep is present at pressures and temperatures of the uppermost lower mantle, implying the possibility of the development of CPO in these conditions (*Cordier et. al.*, 2004). Also, polycrystalline MgO develops noticeable anisotropy at pressures found at the uppermost lower mantle (*Merkel et. al.*, 2002). However if two phases occur together, stronger perovskite and weaker ferropericlase, the deformation behavior is much more complex and this has not been previously investigated in detail.

Here we present two-phase deformation experiments of perovskite and MgO aggregates at pressures of the lower mantle (up to 54 GPa). In these experiments we quantify the amount of CPO developed by certain crystallographic planes. We can then do modeling with the visco plastic self-consistent (VPSC) code to predict what slip system activity could be responsible for the observed CPO. Knowledge of the slip system activity and resulting CPO of the aggregate can inform the interpretation of seismic models as to what flow patterns can be attributed to the measured seismic anisotropy, and also to make predictions of the expected CPO through geodynamic modeling.

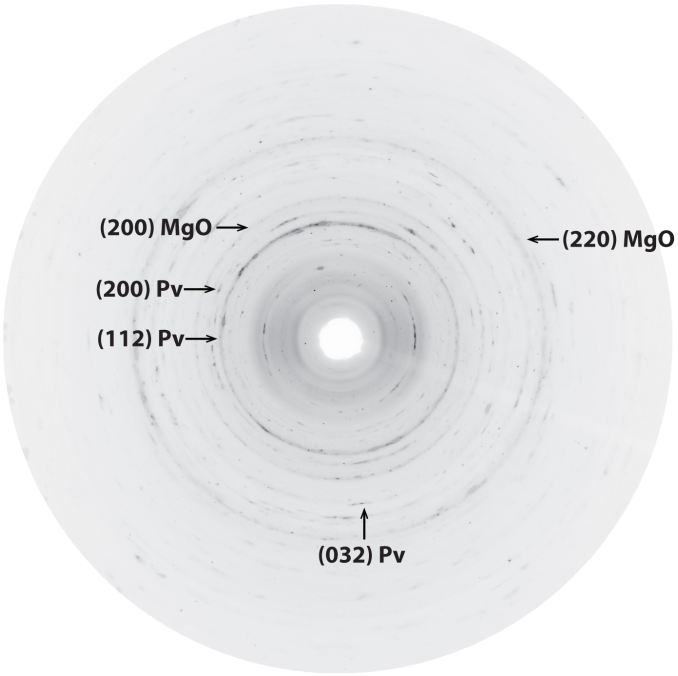

Figure 2.1.1: Raw diffraction image from MAR3450 detector at the Advanced Photon Source of Argonne National Lab. Diffraction of monochromatic X-rays off certain crystallographic plains, *e.g.* (200) of MgO and perovskite (Pv), generate Debye rings shown here.

Experiment and Analysis

To achieve pressures comparable to those of the lower mantle, these experiments were done in a diamond anvil cell in the radial geometry (rDAC) (*Wenk et. al.*, 2006). A mixture of enstatite and MgO was ground to a fine powder and loaded to a boron epoxy gasket on the rDAC. A gas membrane that inflates and pushes on the rDAC increases the pressure in the sample chamber. The enstatite and MgO mixture was brought up to about 30 GPa and then laser heated to induce a phase transformation to perovskite and MgO. This aggregate was then further deformed up to 54 GPa. The CPO developed by the aggregate due to the uniaxial stress imposed by the diamond anvils is assessed using synchrotron radiation to record the full Debye rings (Figure 2.1.1). The pressure is increased *in situ* and diffraction images are recorded at every pressure step. If CPO is present there will be a systematic intensity variation along a single Debye ring. The analysis of this intensity was done using the software MAUD (*Lutterotti & Bortolotti*, 2003), where an orientation distribution is calculated and an inverse pole figure of the compression direction can be plotted.

Results and Discussion

We have found that, in general, the two-phase system develops a weaker CPO than if the two phases are deformed separate-

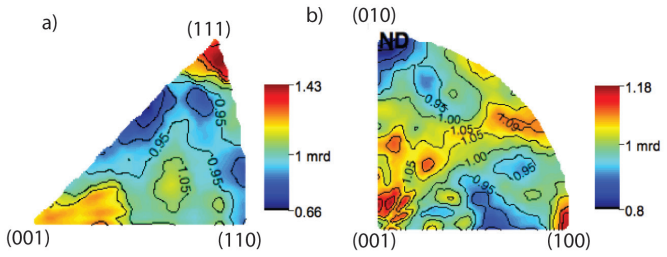

Figure 2.1.2: a) MgO inverse pole figure of the compression direction at 54 GPa. Shows how poles of the (111) crystallographic planes of MgO preferably align in the compression direction. b) Perovskite inverse pole figure of the compression direction at 54 GPa in the same sample chamber as MgO. The (001) and (100) align preferrably in the compression direction. Scale is shown in multiples of random distribution (mrd).

ly (*e.g. Merkel et. al.*, 2002; *Wenk et. al.*, 2004), this could explain why the bulk of the lower mantle is fairly isotropic. The MgO develops texture about 2 times stronger than the perovskite (Figure 2.1.2). Through a Rietveld analysis it was found that MgO preferably aligns poles of the (111) planes parallel to the compression direction and that the perovskite develops a weak (001) and (100) texture in the compression direction (Figure 2a and b). It is important to do these experiments with the two phases together since the hardness contrast between them can change the deformation of the aggregate. Particularly, it is expected that when a soft and a harder phase deform together, the soft phase will absorb deformation and the hard phase will deform very weakly and develop little crystallographic preferred orientation. This is consistent with our results since it is the MgO that has the stronger texture (Figure 2a). Previous rDAC deformation experiments on single-phase polycrystalline MgO found a strong (100) texture at 35.4 GPa (*Merkel et. al.*, 2002). Not only is the texture found in this study much weaker but it is of a different crystallographic plane, implying a different slip system activity. The perovskite texture in Figure 2.1.2b is comparable in orientation but weaker than the one found in a single-phase perovskite powder sample at 43 GPa in *Wenk et. al.*, 2004.

Further work is to model the two-phase system under compression with the VPSC code to see what possible combinations of slip systems and their activities might be responsible for the CPO observed in the experiments. It is also possible to model what the expected shear and compression wave velocities (V_s and V_p) are for the aggregate in different directions.

The study of the deformation of these lower mantle minerals is key in understanding seismic signatures from the mantle transition zone and the core mantle boundary (*e.g. Cottaar et. al.*, 2014), both very important and controversial regions of the mantle.

Acknowledgements

Use of the Advanced Photon Source, an Office of Science User Facility operated for the U.S. DOE Office of Science by Argonne National Laboratory, was supported by the U.S. DOE under Contract No. DE-AC02-06CH11357. E. Z.-A. and P.M.K. were supported in part by the Carnegie/DOE Alliance Center (CDAC) which is part of the Stewardship Science Academic Program of DOE/NNSA, Cooperative Agreement DE-NA0002006. Authors acknowledge support from NSF EAR 1343908.

References

Cordier P., Ungar T., Zsoldos L. and Tichy G., Dislocation creep in $MgSiO_3$ perovskite at conditions of the uppermost mantle, *Letters to Nature*, v. 428, p. 837-840, 2004/

Cottaar S., Li M., McNamara A., Romanowicz B., Wenk H.-R., Synthetic seismic anisotropy models within a slab impinging on the core-mantle boundary,*Geophysical Journal International*, *submitted*, 2014.

Kawazoe T., Ouchi T., Nishihara Y., Nishiyama N. and Fujino K., Seismic anisotropy in the mantle transition zone induced by shear deformation of wadsleyite, *Geophysical Journal International*, v. 216, p. 91-98, 2013.

Long M.D., Constraints on subduction geodynamics from seismic anisotropy, *Reviews of Geophysics*, v. 51, p. 76-112, 2013.

Lutterotti L., Matthies S., Wenk H.-R., Schultz A.S. and Richardson J.W. Jr., Combined texture and structure analysis of deformed limestone from time-of-flight neutron diffraction spectra, *Journal of Applied Physics*, v. 81, no. 2, p. 594-600, 1997.

Mainprice D., Seismic Anisotropy of the Deep Earth from a Mineral and Rock Physics Perspective, *Treatise on Geophysics*, v. 2.16, p. 437-491,2007.

McDonough W.F. and Sun S.-s., The composition of the Earth, *Chemical Geology*, v. 120, p. 223-253, 1995.

Merkel S., Wenk H.-R., Shu J., Shen G., Gillet P., Mao, H-k. and Hemley, R., Deformation of polycrystalline MgO at pressures of the lower mantle, *Journal of Geophysical Research*, v. 107, p. 2271, 2002.

Panning M. and Romanowicz B., A three-dimensional radially anisotropic model of shear velocity in the whole mantle, *Geophysical Journal International*, v. 167, p.361-379, 2006.

Wenk H.-R., Cottaar S., Tomé C.N., McNamara A. and Romanowicz B., Deformation in the lowermost mantle: From polycrystal plasticity to seismic anisotropy, *Earth and Planetary Science Letters*, v. 306, p.33-45, 2011.

Wenk H.-R., Lonardelli I, Merkel S, Miyagi L, Pehl J, Speziale S and Tommaseo CE, Deformation textures produced in diamond anvil experiments, analyzed in radial diffraction geometry, *Journal of Physics: Condensed Matter*, v. 18, p. S933-S947, 2006.

Wenk H.-R., Lonardelli I., Pehl J., Devine J., Prakapenka V., Shen G. and Mao H.-K., In situ observation of texture development in olivine, ringwoodite, magnesiowüestite and silicate perovskite at high pressure, *Earth and Planetary Science Letters*, v. 226, p. 507-519, 2004.

2 The Single Free Energy Surface of Amorphous $CaSiO_3$ from 0 to 44 GPa of Pressure

Zack Geballe, Sarah Arveson, Sergio Speziale and Raymond Jeanloz

Introduction

The study of high-pressure silicate melts is important for Earth Science because their material properties control the thermal, chemical and dynamic history of the earth's crust and mantle. The densities and compressibilities of high-pressure pyroxene-composition ($XY(Si,Al)_2Si_2O_6$) melts are basic properties, but even density is difficult to measure directly. Instead, experimental probes such as Raman and X-ray diffraction have been used to reveal structural changes in high-pressure melts, and molecular dynamics simulations are relied upon to estimate density *(e.g. Funamori et al.,* 2004).

To allow use of other probes of structure and elasticity, amorphous solids, which may be analogous to melts, can be studied. Once quenched to low temperature, they can be more easily probed than the refractory melts, which must be maintained at high temperatures. Yet amorphous materials do not necessarily reflect properties of the melt or even the properties of other amorphous forms of the material.

In the case of amorphous $CaSiO_3$, however, comparisons between various amorphous materials can be made. Similarity in nuclear magnetic resonance (NMR) and refractive index measurements on decompression-amorphized $CaSiO_3$ and the melt-quenched glass suggests their structures are similar: silica tetrahedra linked together in chains that are truncated by cations or linked together in clusters, evidenced by the ^{29}Si NMR spectra, as well as a complete lack of higher-coordinated silicon atoms. Yet no studies have compared compression-amorphized $CaSiO_3$ to other amorphous forms and few data sets address the reversibility of pressure or temperature cycling of amorphous $CaSiO_3$.

Method and Results

We studied amorphous $CaSiO_3$ between 0 to 44 GPa in diamond anvil cells using Brillouin spectroscopy with complementary X-ray diffraction. Two types of samples were studied: glassy $CaSiO_3$ that was quenched from its melt (*Vo-Thahn et al.*, 1996, *Kubicki et al.*, 1992) and a powder of natural wollastonite, the crystalline form of $CaSiO_3$ that is stable at ambient conditions. The density of the glass starting material was measured to be $2.92 \pm 0.02\ g/cm^3$ using a sink-float method. The powder sample was squeezed until it became transparent at ~35 GPa, at which point nearly all X-ray diffraction peaks disappeared from the image-plate detector, showing that most of the sample amorphized, consistent with *Serghiou et al.* (1993). The pressure-amorphized powder was first studied with no pressure medium (*i.e.* sample squeezed between diamonds), and then the sample was transferred to a second diamond cell and surrounded with a methanol-ethanol-water pressure medium. The glass starting material was surrounded in an argon pressure medium. Brillouin spectra were collected in 40° equal-angle

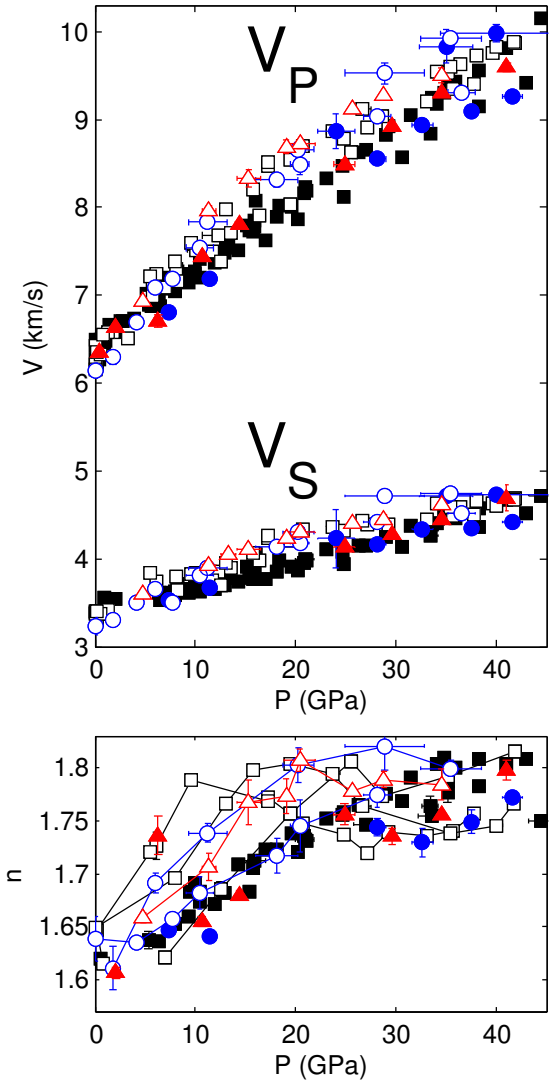

Figure 2.2.1: Longitudinal and shear wave speed (top) and index of refraction (bottom) of amorphous $CaSiO_3$ as a function of pressure during compression (solid symbols) and decompression (open symbols) between 0 and 44 GPa. Colors and shapes indicate starting material: melt-quenched $CaSiO_3$ glass (black squares), non-hydrostatically compressed powder (blue circles), and pressure-amorphized wollastonite in a pressure transmitting medium (red triangles). Error bars on individual data points are from scatter during rotations about the diamond cell axis, in the case that rotations were performed.

forward-scattering in order to measure both longitudinal and transverse sound speeds (V_P and V_S), and in 180° backscattering in order to measure the product of refractive index, n, with V_P. Pressure was measured from the fluorescence line shift of two to four rubies spheres placed near the edge of the gasket hole.

We find that the amorphous forms of $CaSiO_3$ studied here are highly reproducible under high stress conditions. Upon compression and re-compression, acoustic velocities and refractive

indices of all samples agree within the scatter of ~3% (Figure 2.2.1), suggesting that a single energy surface approximates the pressure dependence of all starting materials. Upon decompression, hysteresis is observed (up to 6% in V_P, 8% in V_S, and 5% in n), but it is small is comparison to the hysteresis of other silicate glasses. Moreover, similarly shaped hysteresis curves are observed for all pressure cycles with no systematic difference between the different samples. Finally, the velocities change nearly linearly with pressure, suggesting no kinks in the free energy surface (*i.e.* no first order phase transitions from 0 to 44 GPa). The differences that do exist between compression and decompression data suggest a structural phase transition, but it is likely to be a gradual evolution in order to explain the smoothly varying, reproducible velocity data.

Therefore, these data add evidence that amorphous $CaSiO_3$ is a highly meta-stable glass. Its reproducibility with pressure cycling and its independence of synthesis conditions are shown schematically in Figure 2.2.2. Both amorphous forms of $CaSiO_3$ studied here (melt-quenched and compression-amorphized; paths 1 and 3 in Figure 2.2.2) have indistinguishable refractive index, longitudinal wave speed and shear wave speed between 0 and 44 GPa. Melt-quenched and decompression-amorphized solids (paths 1 and 2 in Figure 2.2.2) also have the same refractive index and ^{29}Si NMR spectrum at ambient pressure and temperature (*Kanzaki et al.,* 1991*; Ringwood and Major,* 1971). Together, this implies that all three forms of amorphous $CaSiO_3$ created in a broad region of pressure-temperature space are structurally similar. And because pressure cycling causes smooth and relatively reversible changes in sound speeds, we connect the low and high pressure amorphous solids by a yellow shaded region to represent the single, smoothly varying free energy curve connecting low to high pressure amorphous $CaSiO_3$.

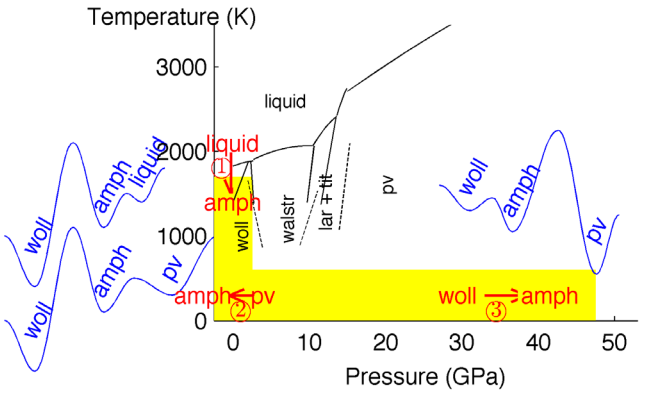

Figure 2.2.2: Pressure-temperature phase diagram of $CaSiO_3$ with schematic of potential wells to explain three observed glass transitions: (1) Melt-quenched glass formation (e.g. *Vo-Thanh et al., 1996; Kubicki et al., 1992; Ringwood and Major 1971*; and the glass used in this study), (2) amorphization by decompression of perovskite (e.g. *Ringwood and Major, 1971; Kanzaki et al., 1991)*, (3) amorphization by compression of wollastonite (*Serghiou and Hammack, 1993;* this study). Black lines mark equilibrium phase boundaries (dashed lines: *Akaogi et al., 2004*; solid curves: *Zerr et al., 1997*). Yellow marks the region in which we conclude a single type of glass is meta-stable. Red arrows mark observed locations of pressure-amorphizations.

Acknowledgements

We thank Pascal Richet, Rus Hemley and Bjorn Myssen for providing us samples of $CaSiO_3$ glass and Tim Teague for providing us with natural crystalline wollastonite.

References

Akaogi, M., et al., High-pressure transitions of diopside and wollastonite: phase equilibria and thermochemistry of $CaMgSi_2O_6$, $CaSiO_3$ and $CaSi_2O_5$-$CaTiSiO_5$ system: *Physics of the Earth and Planetary Interiors,* 143-144, p. 145-156, 2004.

Funamori, N., et al., Exploratory studies of silicate melt structure at high pressures and temperatures by in situ X-ray diffraction: *Journal of Geophysical Research*, 109, p. B03203, 2004.

Kanzaki, M., Stebbins, J. and Xue, X., Characterization of quenched high pressure phases in $CaSiO_3$ system by XRD and ^{29}Si NMR: *Geophysical Research Letters*, 18, p. 463-466, 1991,

Kubicki, J., Hemley, R. and Hofmeister, A., Raman and infrared study of pressure-induced structural changes in $MgSiO_3$, $CaMgSi_2O_6$, and $CaSiO_3$ glasses: *American Mineralogist*, 77, p. 258-269, 1992.

Ringwood, A., and Major., A., Synthesis of majorite and other high pressure garnets and perovskites: *Earth and Planetary Science Letters*, 12, p. 411-418, 1971.

Serghiou, G. and Hammack, W., Pressure-induced amorphization of wollastonite ($CaSiO_3$) at room temperature: *Journal of Chemical Physics*, 98, p. 9830-9834, 1993.

Vo-Thahn, D., Polian, A. and Richet, P., Elastic properties of silicate melts up to 2350 K from Brillouin scattering: *Geophysical Research Letters,* 23, p. 423-426, 1996.

Zerr, A., Serghiou, G. and Boehler, R., Melting of $CaSiO_3$ perovskite to 430 kbar and first in-situ measurements of lower mantle eutectic temperatures, 24, p. 909-912, 1997.

3 A Laboratory Rock-physics Study on How P-wave Properties Change with Respect to Ice Content in Saturated, Unconsolidated Saline Permafrost

Shan Dou, Seiji Nakagawa, Jonathan Ajo-Franklin, Douglas Dreger

Introduction

Saline permafrost is the subset of permafrost that contains dissolved salts in its pore-water. In contrast with its non-saline counterpart, saline permafrost freezes at lower sub-zero temperatures because of freezing-point depression of the dissolved salts. When temperatures drop below the freezing point, dissolved salts are not integrated into ice crystals and thus remain in residual pore-water, a process which prevents further freezing as increased salt concentrations lower the freezing point. Hence, saline permafrost remains only partially frozen unless the eutectic point (~−21°C for NaCl solution) is reached. Because the range of permafrost temperatures found in nature (~−15°C to 0°C) is usually higher than the eutectic point, natural saline permafrost is most likely to be unfrozen or partially frozen, which results in a wide range of possible ice content under various salinity and temperature conditions.

Dissolved salts in saline permafrost primarily originate from marine deposits and/or seawater transgressions, hence, saline permafrost is widespread in subsea and coastal areas of Arctic and Antarctica. Saline permafrost is highly sensitive to thermal disturbances and mechanically weaker than its non-saline counterpart. Hence, temperature increases under a warming climate—even for sub-zero increases—could easily cause saline permafrost to destabilize. The low bearing capacity of saline permafrost has long been the culprit for deforming and damaging a large number of cold-region infrastructure components (*Brouchkov, 2003*). Predictive models of surface deformation and structural stability in a warming climate thus require approaches for estimating and predicting the influence and distribution of saline permafrost.

Seismic methods—including surface seismic and acoustic well-log measurements—are among several available methods for detecting and delineating saline permafrost, owing to the sensitivity of seismic velocities to ground-ice content (the higher the ice content, the higher the velocities). However, even after seismic velocity profiles have been acquired, an interpretation step is necessary to infer ice content from seismic velocities. Because a broad range of ice content can be present in saline permafrost, seismic interpretations are susceptible to errors unless a robust rock-physics relationship is available. However, the mapping between velocities and ice content depends heavily on the assumptions made about ice geometry: for a given velocity value, the estimated ice content could be low when ice is assumed as a cement material to bond sediment grains together, but high when ice is assumed as a pore-filling material without contacting the sediment grains. Therefore, in order to establish an effective rock-physics relationship for saline permafrost, the validity of the plausible assumptions about ice must be examined with the aid of high-quality data that are associated with a broad range of ice content.

To cover a broad range of ground-ice content through field surveys would require unrealistically extensive sampling, further complicated by the complexity of natural permafrost systems. Thus, we prefer using laboratory data that are obtained from simpler sediments under controlled experimental conditions to gain a fundamental understanding of the rock-physics relationship. Although unconsolidated sediments constitute dominant portions of the near-surface saline permafrost, relevant laboratory studies are scarce.

In this study, we investigate how seismic properties change with respect to ice content in unconsolidated saline permafrost. We conducted laboratory ultrasonic P-wave measurements in a transmission geometry using samples consisting of water-saturated 20–30 Ottawa sand (quartz sand; grain size 600–850 μm, D_{50} ~ 720 μm) within a temperature range of 10°C to −30°C and a salinity range of 0.0–2.5 M (0–13 wt%). Due to the wide range of temperatures and salinities, the fine temporal sampling of the automated data acquisition system, as well as the dissolved salts' ability to fine-tune ice content, we obtained high-quality data that provide an unprecedented opportunity for observing how P-wave properties change with respect to ice content in saturated, unconsolidated saline permafrost.

Ultrasonic Pulse-transmission Setup and Data

A pulse-transmission configuration was set up for the ultrasonic measurements of water-saturated unconsolidated sediments upon freezing (Figure 2.3.1).

Based upon the phase diagram of aqueous NaCl solution, we convert the temperatures into the corresponding ice saturation (the volume fraction of ice in the pore space) for each set of the initial (*i.e.*, prior to freezing) pore-water salinity that was experimented with 20–30 sand. Then, we present the data and the

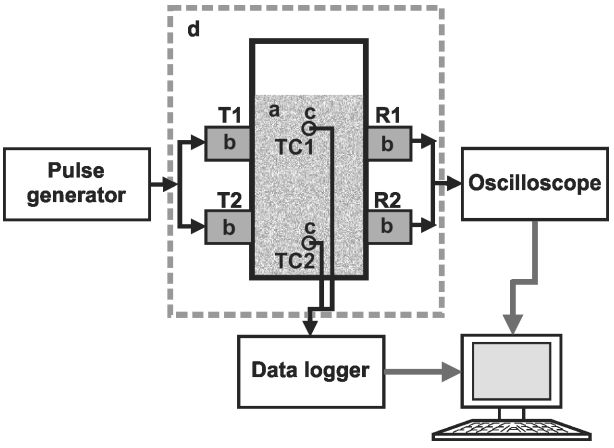

Figure 2.3.1: Column setup of pulse-transmission ultrasonic data acquisition. a) column with sand packs; b) immersion transducers; c) thermocouples (TC1 and TC2); d) bench-top freezer; T, Transmitters; R, Receivers.

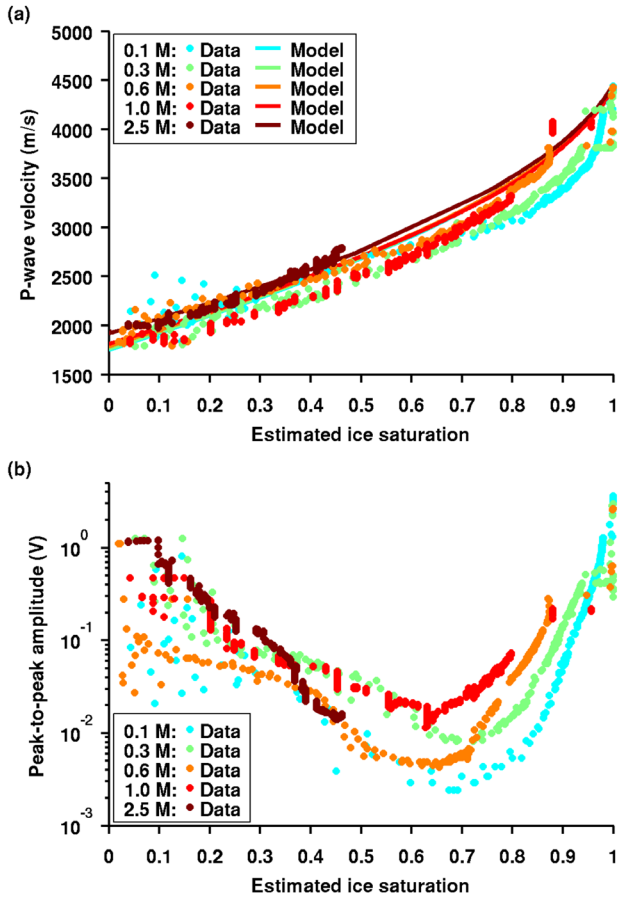

Figure 2.3.2: P-wave properties of saturated 20–30 Ottawa sand as functions of the estimated ice saturation. (a) Comparison of model-predicted and measured P-wave velocities, and (b) measured P-wave amplitudes as a function of ice saturation.

velocity modeling results as functions of ice saturation (Figure 2.3.2): Whereas P-wave velocities increase monotonically with increasing ice content, P-wave amplitudes exhibit skewed "V"-shape trends (decrease and then increase), indicating a positive correlation between attenuation and velocities at low to moderate ice saturations—an unexpected observation that sets partially frozen saline permafrost aside from most geological materials.

Effective-medium Velocity Modeling

Based upon our laboratory data, we have developed an effective-medium velocity model that assumes the coexistence of load-bearing/cement ice and non-load-bearing/non-cement ice before reaching 100% ice saturation (Figure 2.3.3). The good agreement between the model-predicted and the measured P-wave velocities suggests that ice is neither purely cementing nor purely pore-filling in saturated, unconsolidated saline permafrost.

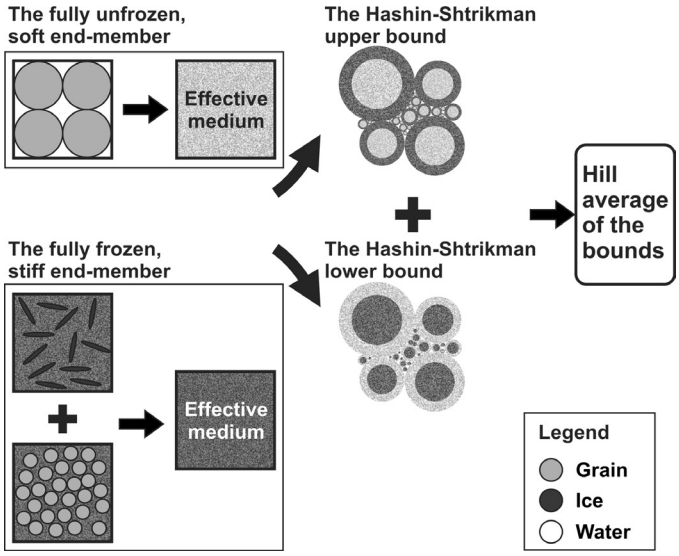

Figure 2.3.3: Intuitive interpretation of the two-end-member mixing effective-medium model.

Acknowledgements

As part of the Next-Generation Ecosystem Experiments (NGEE-Arctic) project sponsored by the Office of Biological and Environmental Research in the DOE Office of Science, this study is supported through contract DEAC0205CH11231 to Lawrence Berkeley National Laboratory and through contract DE-AC05-00OR22725 to Oak Ridge National Laboratory.

References

Brouchkov, A., Frozen saline soils of the Arctic coast: their distribution and engineering properties, *Proceedings of the 8th International Conference on Permafrost*, National Academy of Sciences, p.95-100, 2003.

4 High Temperature Miscibility of Terrestrial Materials: First Principles Calculations for the Early Earth

Sean M. Wahl, Burkhard Militzer

Introduction

Terrestrial planets are, to first order, made up of a metallic iron core and a mantle composed of silicate and oxide minerals. Chondritic meteorites show that these materials initially condensed together from the protoplanetary nebula. Numerous scenarios have been put forward to describe how these reservoirs interacted as they separated to form the core (*Rubie*, 2007). However, these typically assume the major components occur in two immiscible phases as they do at low temperatures. In the case of a hot early history of a growing planet, this assumption is not necessarily correct. At sufficiently high temperatures, entropic effects dominate and any mixture of materials will form a single, homogeneous phase. Late stage giant impacts, such as the hypothesized moon-forming impact, may have heated significant portions of the target to >10,000 K (*Canup*, 2004). It is therefore necessary to consider a high temperature mixture of the 'rocky' and metallic terrestrial components. The presence of such a mixed phase will affect the chemistry of iron-silicate differentiation on the early earth. Here we assess the stability of a mixed rock-metal phase as a mixture of Fe and 'rock' (MgO).

Simulation Methods

We performed density functional theory molecular dynamics (dft-md) simulations for phases in a model reaction between liquid iron, and solid (B1) or liquid magnesium oxide. MgO was selected for the representative rock phase because it has been experimentally determined to be the rocky component that is least soluble in iron (*Ozawa et. al*, 2008). The change in Gibbs free energy of this system per formula unit FeMgO for the model reaction was describe by

$$\Delta G_{mix} = \frac{1}{24} G_{(FeMgO)24} - \frac{1}{32}\left[G_{(MgO)32} + G_{Fe32}\right] \qquad (1.1)$$

We performed the dft simulations using the standard Vienna Ab-initio Simulation Package (VASP package) (*Kresse & Furthmüller*, 1996), but required the addition of the thermodynamic integration technique in order to determine the Gibbs free energy of the phases. This technique involves integration of the free energy over a series of systems with interactions controlled by a hybrid potential. The hybrid potential describes a mixture between the DFT potential and classical potential that has an analytic solution for the Gibbs free energy. This is currently the most accurate means for determining chemical potentials of a reaction using first principles simulations.

Shape of the Solvus

We characterized the shape of the Fe-MgO solvus by performing calculations at five additional intermediate compositions between the Fe and MgO end members. These were performed at 50 GPa for one temperature above the solvus and one below The Gibbs free energies of all simulations at intermediate conditions are consistent with a binary system with a miscibility gap. From these results we construct Fe-MgO phase diagram at 50 GPa, as shown in Figure 2.4.1. The miscibility gap is notably asymmetric, with temperatures decreasing faster towards the Fe-rich end member than the MgO-rich end. This shape is similar to the exsolution gap found experimentally determined for the Fe-FeO system at lower pressures.

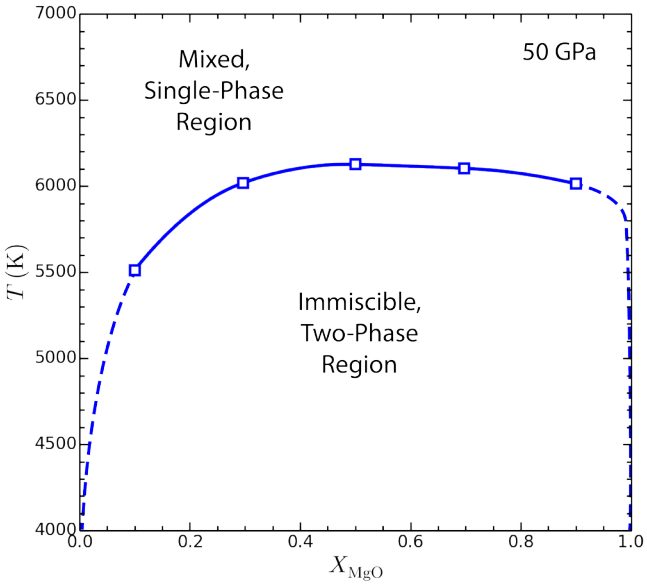

Figure 2.4.1: Solvus phase diagram of the Fe-MgO system at P = 50 GPa. The shape is consistent with X_{MgO} = 0.5 being representative composition for estimating the solvus. The asymmetry at low X_{MgO} has consequences for the solubility of Mg in the early core.

The Fe-rich side of our solvus is consistent with low solubilities found in experiments at 3000 K. From this we predict a >1% MgO saturation limit down to 4200 K, with concentrations steeply decreasing to be below consistent with low concentrations found in experiments at ~3000 K (*Ozawa et al.*, 2008). This suggests that delivery of excess, nominally insoluble, light components to the core would have been substantial for a hot early Earth. This would be followed by exsolution of a Mg-rich material at the top of the cooling core. This process has been suggested as a possible solution to the problem of the earth's core having insufficient energy to generate a magnetic field before nucleation of the inner core (*Stevenson*, 2012).

Solvus Closure Temperature

Figure 2.4.2 summarizes our results, showing all the conditions at which simulations were performed. We find the solvus closure at ambient pressure to be 4090 +/- 20 K. While there is little experimental work on this exact system, this is superficially consistent with the 'accidental' discovery of the Fe-silicate

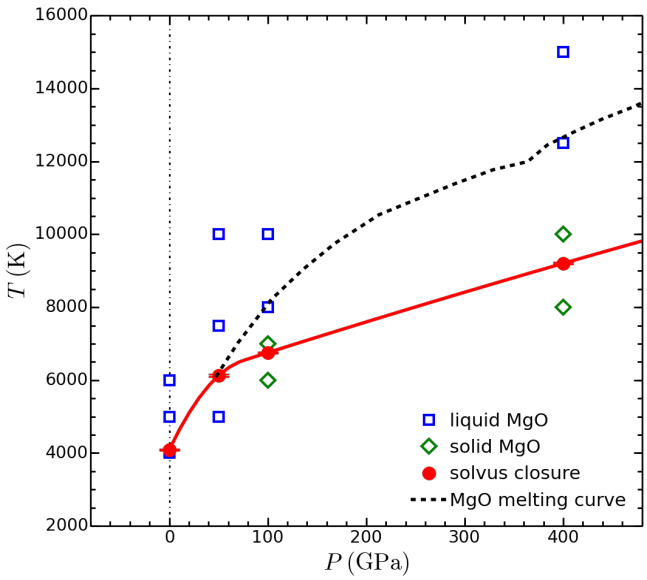

Figure 2.4.2: Pressure dependence of the solvus closure. The P-T condition of all thermodynamic integration calculations on the Fe-MgO system. Blue markers denote conditions where MgO was treated as a liquid. Green markers denote conditions where MgO was treated as a solid (B1). Red circles show the solvus closure temperature inferred from simulations as the point where a 1:1 mixture prefers a homogenous solution. The dashed, black line shows the MgO melting temperature from *Boates and Bonev,* 2013.

solvus by *Walker*, 1993. We find that the solvus temperature increases with pressure to 6020 +/-30 K at 50 GPa, but its slope decreases at lower mantle and core pressures. At core-mantle boundary pressures, the solvus closure temperature would be ~7000 K.

This pressure dependence of solvus closure determines the depth at which phases separate from the fully mixed state. Its slope with respect to pressure is less steep than the calculated isentropes of the mixed FeMgO phase. For a homogeneous, liquid layer of the planet, isentropes approximate adiabatic temperature profiles of the interior of the planet at different point in its evolution. As a result, separation begins in the exterior of the planet and proceeds inwards as the planet cools. Since iron separating in the outer portion of the planet is denser than the rocky phase, it would sink until it reached a depth where it dissolves into the mixed phase again. This may promote compositional stratification, and possibly multi-layer convection between an upper iron-poor and deeper iron-rich layer.

Acknowledgements

This work was supported by NASA and the NSF. Computational resources were provided in part by the NASA Advanced Supercomputing Division.

References

Boates, B. and Bonev, S. A., Demixing Instability in Dense Molten $MgSiO_3$ and the Phase Diagram of MgO, *Phys. Rev. Lett.* 110, 13, 135504, 2013.

Canup, R. M., 2004, Dynamics of Lunar Formation, *Annu. Rev. Astron. Astrophys.* 42, 1, 441-75, 2004.

Kresse, G. and J. Furthmuller, 1996, Efficient iterative schemes for ab initio total energy calculations using a plane-wave basis set,Phys. Rev. B-Cond. Mat.,54,16,11169-86, 1996.

Ozawa, H., Hirose, K. Mitome, M., Bando, Y., Sata, N. and Ohishi, Y., Chemical equilibrium between ferropericlase and molten iron to 134 GPa and implications for iron content at the bottom of the mantle, *Geophys. Res. Lett*., 35, 5, L05308, 2008.

Rubie, D. C., Nimmo, F., and Melosh, H. J., Formation of Earths core, *Treatise Geophys*. 9, 51-90, 2007.

Stevenson, D., How to keep a Dynamo Running in spite of High Thermal Conductivity, *AGU Fall Meet. Abstr., 2012.*

Walker, D., Norby, L. and Jones, J. H.,Superheating effects on metal-silicate partitioning of siderophile elements, *Science* 262, 5141, 1858-61, 1993.

Research Studies:
Earth Structure

5 Whole-mantle Spectral-Element Waveform Tomography: SEMUCB-WM1

Scott French and Barbara Romanowicz

Introduction

Over the past year, we have developed the first-ever model of whole-mantle radially anisotropic shear velocity obtained using the spectral element method (SEM: e.g. Capdeville et al., 2003) for waveform forward modeling. This work was motivated by the earlier success of the SEM-based "hybrid" waveform inversion approach in upper mantle and transition zone imaging (*Lekic and Romanowicz*, 2011; *French et al.*, 2013). Here, we briefly describe our efforts in achieving this result, while also presenting some details of the model, known as SEMUCB-WM1. A full discussion of model construction, as well as a detailed discussion of model structure and associated uncertainties appears in a manuscript recently submitted for publication (*French and Romanowicz*, 2014, *submitted to GJI*).

Dataset

Our inversion dataset contains fundamental and overtone mode surface-wave and body-wave waveforms. Surface-wave data are filtered at 400–60 s period, while body waves are filtered in two passbands: 300–36 s or 32 s. The 32 s filter is used after the model has converged at 36 s. In addition to modifying the passband of our body-wave dataset during the inversion, we also enlarge our datasets: initially using the same 203 events as in SEMum (*Lekic and Romanowicz*, 2011), and later adding 70 new events to improve coverage of the lower mantle. Data are processed using a waveform windowing scheme (*Li and Romanowicz*, 1996). Windows are selected based on similarity to SEM synthetics computed in the most recent model iteration. Data is reprocessed at each inversion iteration, thus allowing more data in as the model improves.

We supplement our waveform data with group-velocity dispersion maps at 25–150 s period (M. Ritzwoller, *pers. comm.* 2009). These data are used to calibrate our smooth crustal model and ensure its consistency with the underlying mantle structure (see *French et al.* 2013). Together with the mode-coupled SEM of *Capdeville et al.* (2003), the smooth crustal layer improves the time stability of the SEM. Better time stability allows larger time steps to be used, thereby reducing the overall cost of SEM simulations.

Inversion

Our inversion for whole-mantle structure proceeds in three iterations: each uses both the surface and body-wave datasets, while only the second and third iterations included the enlarged (273 event) set and only the third iteration uses the shorter 32 s body-wave filter passband. Our starting model combines SEMum2 (*French et al.*, 2013) down to 800 km with SAW24B16 (*Mégnin and Romanowicz*, 2000) below. We use the generalized least-squares formalism of *Tarantola and Valette* (1982), yielding a quickly converging Gauss-Newton scheme for optimizing the tomographic model (and thus reducing the number of SEM simulations required). We include *a priori* information in our inversion to constrain the permissible length scales of model structure (see *Lekic and Romanowicz*, 2011). By the end of the inversion, our dataset contains >447,000 waveform windows, fitting the surface-wave data nearly as well as in the earlier SEMum2 model, while showing body-wave variance reduction above 50%. The SEM simulations for our inversion, excluding sensitivity kernel and parallel linear algebra calculations, represent nearly 3M CPU hours of computation.

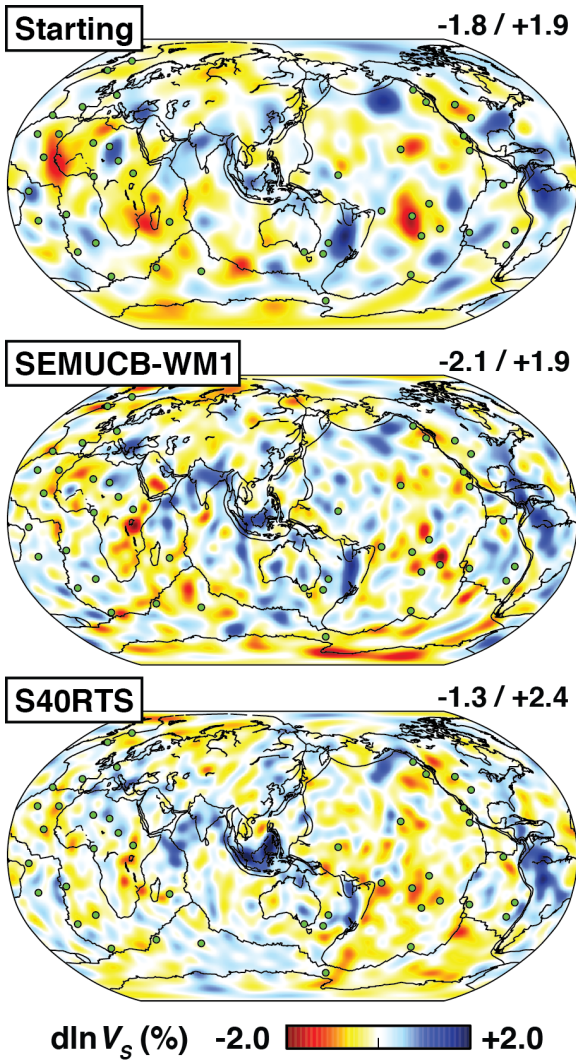

Figure 2.5.1: Comparison between starting and final-iteration models (top and middle panels, respectively) at 1000 km, as well as model S40RTS of *Ritsema et al.* (2011) (bottom panel). At this depth, the starting model is SAW24B16 of *Mégnin and Romanowicz* (2000). Inset values: maximum peak-to-peak variation in each model.

Model Structure and Discussion

As upper-mantle structure remains very close to SEMum2, we here focus on the lower mantle. In Figure 1, we show iso-

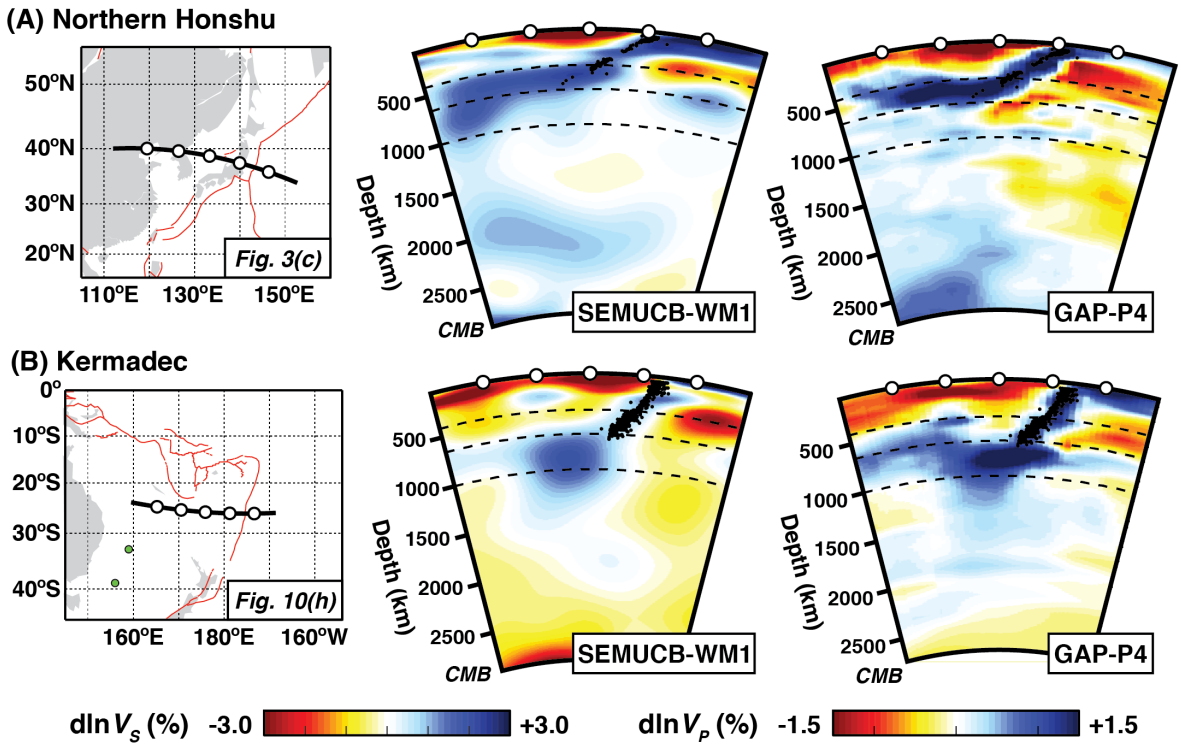

Figure 2.5.2: Whole-mantle cross-sections through subduction zones, comparing SEMUCB-WM1 V_S and V_P from GAP-P4 (*Obayashi et al.*, 2013). Map panels indicate lines of section (inset figure numbers reference the same lines of section in *Fukao and Obayashi* (2013)). Black circles on sections: deep earthquakes. Dashed lines: 410, 650, and 1000 km depth (top to bottom). Note the different V_S and V_P saturation levels.

tropic V_S variations at 1000 km depth in three models: our staring and final-iteration models, as well as S40RTS (*Ritsema et al.*, 2011). We find that structure has sharpened significantly from our starting model, including more concentrated fast anomalies, interpreted as subducted slabs, and distinct narrow slow anomalies near many major hotspots (e.g. South Pacific Superswell, Iceland). While SEMUCB-WM1 and S40RTS are broadly consistent at this depth, they clearly differ in detail; particularly in these features associated with hotspots. We will return to lower-mantle low-velocity structure in greater detail in a future publication. In Figure 2, we compare subduction-zone cross-sections through SEMUCB-WM1 V_S structure and the V_P model GAP-P4, used by *Fukao and Obayashi* (2013) to survey global slab behavior. We find excellent agreement in both the lateral distribution of high-velocity anomalies (and correlation with deep seismicity), as well as apparent slab-stagnation depth. We also see fairly good agreement in upper-mantle/transition-zone slow anomalies. These independent observations give us further confidence that the newly developed lower-mantle structure of our model is robust.

Acknowledgements

We acknowledge support from the National Science Foundation (grant EAR-0738284). SWF acknowledges support from an NSF Graduate Research Fellowship. Computations were performed at the National Energy Research Scientific Computing Center, supported by the Department of Energy Office of Science (Contract No. DE-AC02-05CH11231).

References

Capdeville, Y., Chaljub, E., Vilotte, J.-P., Montagner, J.-P., Coupling the spectral element method with a modal solution for elastic wave propagation in global earth models, *Geophys. J. Int.*, 152, 34–67, 2003.

French, S., Lekic, V., Romanowicz, B., Waveform Tomography Reveals Channeled Flow at the Base of the Oceanic Asthenosphere, *Science*, 342, 227–230, 2013.

Fukao, Y., Obayashi, M., Subducted slabs stagnant above, penetrating through, and trapped below the 660 km discontinuity, *J. Geophys. Res.*, 118(11), 5920–5938, 2013.

Lekic, V., Romanowicz, B., Inferring upper-mantle structure by full waveform tomography with the spectral element method, *Geophys. J. Int.*, 185, 799–831, 2011.

Li, X., Romanowicz, B., Global mantle shear velocity model developed using nonlinear asymptotic coupling theory, *J. Geophys. Res.*, 101, 245–22, 1996.

Mégnin, C., Romanowicz, B., The three-dimensional shear velocity structure of the mantle from the inversion of body, surface and higher-mode waveforms, *Geophys. J. Int.*, 143, 709–728, 2000.

Obayashi, M., Yoshimitsu, J., Nolet, G., Fukao, Y., Shiobara, H., Sugioka, H., Miyamachi, H., Gao, Y., Finite frequency whole mantle p wave tomography: Improvement of subducted slab images, *Geophys. Res. Lett.*, 40(21), 5652–5657, 2013.

Ritsema, J., Deuss, A., van Heijst, H., Woodhouse, J., S40RTS: a degree-40 shear-velocity model for the mantle from new Rayleigh wave dispersion, teleseismic traveltime and normal-mode splitting function measurements, *Geophys. J. Int.*, 184, 1223–1236, 2011.

Tarantola, A., Valette, B., Generalized Nonlinear Inverse Problems Solved Using the Least Squares Criterion, *Rev. Geophys.*, 20, 219–232, 1982.

6 Body Wave Tomography of the Juan de Fuca plate

William B. Hawley and Richard Allen

Introduction

The Juan de Fuca plate is a small oceanic plate that is being subducted underneath the northwestern corner of the contiguous United States. This is the only part of the country other than Alaska that contains an active subduction zone. The Cascadia Initiative (CI) is a four-year-long deployment of 70 ocean bottom seismometer (OBS) stations that covers the Juan de Fuca plate from the western side of the mid-ocean ridge that creates the plate to the Cascadia trench. This is an ideal location for a regional-scale OBS array because the plate is small enough to be covered by an array of seismometers, yet large enough to help understand large-scale oceanic plates and their relationship to the mantle below. In this contribution, we present a preliminary teleseismic P-wave velocity model of the region using the CI stations, as well as stations on shore, including those from the Transportable Array, the Berkeley Digital Seismic Network, the Cascade Chain Volcano Monitoring (run by Cascades Volcano Observatory and USGS), and the University of Washington, among others.

Noise Analysis

Seismic stations on the ocean floor provide a new and valuable scientific resource, even when used to augment the data that we have from land-based stations. The noise characteristics of the two types of stations, however, can be very different. For OBS stations, the noise is generally derived from wind and waves, both by direct forcing at longer periods and by coupling to elastic waves in the earth at shorter periods (*Webb*, 1998).

In order to filter out this noise, we analyzed the P-wave arrival signal in a number of bands, including bands that are often used in purely land based studies, and bands that have been published as being suitable for observing teleseismic body waves (*e.g., Lewis and Dorman*, 1998). Much of the intermediate frequency range—about 0.5 to 2 Hz, those frequencies that produce the best teleseismic arrivals on land-based stations—is dominated by noise in the ocean stations. In order to cross correlate the arrivals, we needed to be able to pick the arrival at each station in the same frequency band. In looking for the best band, therefore, we placed priority on obtaining data from the OBS stations, while still ensuring we obtained reliable data from the land-based stations.

With this in mind, we determined that using the relatively low-frequency and narrow passband from 0.08 to 0.11 Hz (about 9 to 12.5 s period) resulted in the clearest body wave arrivals for the OBS stations.

Methods

For this analysis, we use stations from the 7D network (the CI OBS stations), as well as some from UC Berkeley, the Transportable Array of USArray, the University of Washington, and the Cascade Chain Volcano Monitoring by USGS and CVO. We used 36 teleseismic ($30^o<\Delta<110^o$) earthquakes with magnitudes ranging from 6.8 to 7.5 for arrivals that were well above the noise, but still relatively simple. We filtered the data from 0.08 to 0.11 Hz, and picked P arrivals out of the filtered data. Arrivals that were not sufficiently above the noise were thrown out.

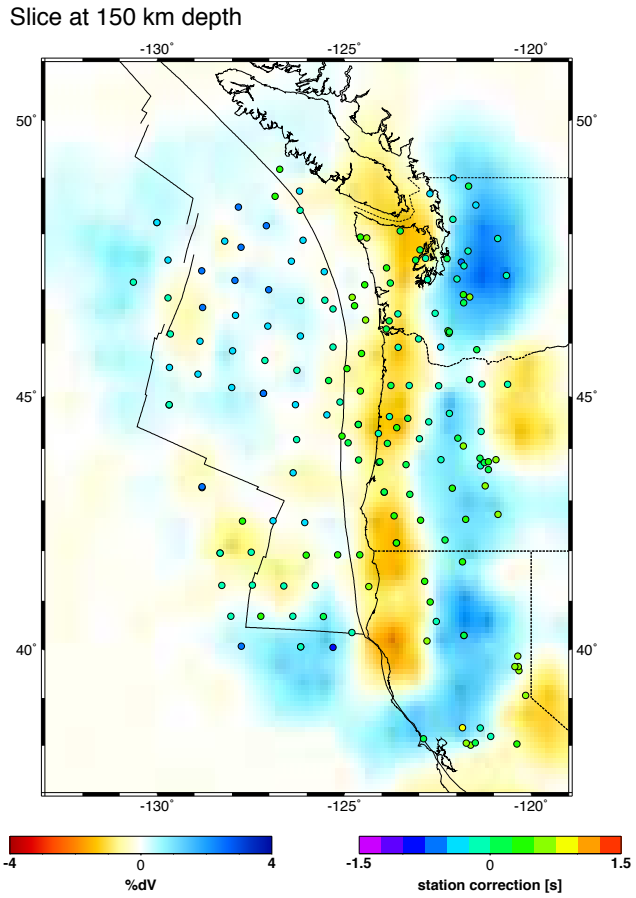

Figure 2.6.1: A horizontal slice at 150 km depth from our model. The three tectonic plates are labeled, deliniated by the thin black lines. The background color shows the relative P-wave velocity as a percent deviation from the average of the model, as shown by the left color bar. The colored dots are stations; the color represents the station correction applied to each station, as shown by the right color bar.

After applying the filter, we use the multi-channel cross correlation method (*VanDecar and Crosson*, 1990) to measure the arrival times for each of the 10,340 station-event pairs. Because the period of the waves is about 10 seconds, visually picking an arrival a fraction of a wavelength early or late would incur an error of multiple seconds. Cross correlation minimizes this error. Station-event pairs with cross-correlations coefficients that were not sufficiently high were discarded. The minimum acceptable coefficient varied for each event, but it was generally around 0.9.

We use this data to perform an inversion. For each station-event pair, we use finite-frequency kernels to determine the sensitivity matrix, and we then solve for the compressional

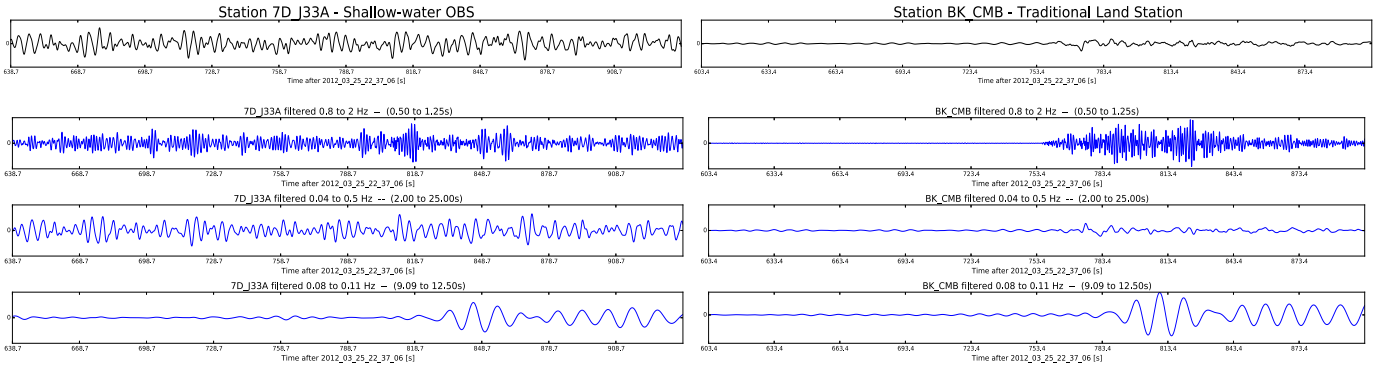

Figure 2.6.2: Seismograms from two different environments showing a recording of the same earthquake, a M7.1 in the Chilean trench. Each seismogram is centered on the IASP91-predicted P arrival. The left column is a noisy OBS station in shallow water; the right column is a traditional land-based station in the Berkeley network. The top row shows a raw seismogram, the second row shows the result of applying a bandpass filter of 0.8 to 2 Hz, the third shows the result of a 0.04 to 0.5 Hz filter, and the bottom row shows the 0.08 to 0.11 Hz filter we used in this study. Note that for the OBS, the P arrival is only visible in the final filter.

wave velocity using an iterative least-squares algorithm (*Dahlen et al.*, 2000; *Hung et al.*, 2000). Included in the process of the least-squares inversion is allowance for a station correction at each station. This is meant to account for under-sampled regions in the upper lithosphere and crust that could contribute to delays in the inversion.

Discussion

Figure 1 shows two important features: first, a high velocity region that runs from the northern to southern boundaries of our model through west-central Oregon and Washington and into California; and second, a strong low-velocity region just to the west of the high-velocity region.

The high-velocity region that spans the north-south extent of our model and appears between about 120°W and 122°W is the subducting Juan de Fuca plate. Within this slab, we see two regions of weaker high-velocity, one between 45°N and 46°N, the other between 41°N and 42°N. There is additionally a fairly strong low velocity region to the east of the more northerly of these 'gaps.'

We also see variations in strength in the low-velocity region directly to the west of the slab; note that south of about 44°N the strong regions in the slab correspond to *weak* regions in the low-velocity region and vice versa, while north of 44°N the strong regions in the slab correspond to *strong* regions in the low-velocity region and vice versa. While it is not evident in Figure 2.6.1, the low-velocity region to the west of the slab is not local to a specific depth; the region remains directly beneath the slab down to the bottom of our model. Because it is not localized, and because it is underneath as opposed to above the slab, we do not interpret this as melting oceanic lithosphere, but a process that is dynamic and particular to the area. We are investigating this feature further.

Acknowledgements

We would like to thank the Ocean Bottom Seismograph Instrument Pool (OBSIP) Management Office (OMO) staff for help in managing and understanding the OBS data. IRIS and the Cascadia Initiative Expedition Team provided the data for this work.

References

Dahlen, F.A., S.-H. Hung, and G. Nolet, Fréchet kernels for finite-frequency traveltimes–I. Theory, *Geophysical Journal International*, 141: 157-174, 2000.

Hung, S.-H., F.A. Dahlen, and G. Nolet, Fréchet kernels for finite-frequency traveltimes–II. Examples, *Geophysical Journal International*, 141: 175-203, 2000

Lewis, B.T.R. and L.M.Dorman, Recording Teleseisms on the Seafloor; an example from the Juan de Fuca Plate, *Bulletin of the Seismological Society of America*, 88, 1, p.107-116, 1998.

VanDecar, J.C. and R.S. Crosson, Determination of teleseismic relative phase arrival times using multi-channel cross-correlation and least-squares, *Bulletin of the Seismological Society of America*, 80, 1, 150-169, 1990.

Webb, S.C., Broadband Seismology and Noise under the Ocean, *Reviews of Geophysics*, 36, 1, p.105-142, 1998.

7 Further Constraints on Lateral Variations of Structure at the Base of the Pacific LLSVP Using Shear Diffracted Waves

Meng Cai and Barbara Romanowicz

Introduction

Large Low Shear Velocity Provinces (LLSVPs) are regions of reduced shear wave velocity in the lowermost ~500-1000 km of the mantle, which are located antipodally beneath the central Pacific and Africa and rooted in D". Their lateral boundaries are sharp as evidenced by the observation of complex local waveforms in seismic phases, and their density may be larger than in the surrounding structures. Ultra Low Velocity Zones (ULVZs) appear to correlate with edges of the Pacific LLSVPs as well as the locations of hotspots. The ULVZs are constrained by modeling to be several hundred kilometers in diameter and tens of kilometers in thickness. *Cottaar and Romanowicz* (2012) identified an intriguingly large ULVZ structure (called the preferred model) at the core-mantle boundary, at the northern border of the Pacific LLSVP and in the vicinity of Hawaii. Since this work was published, several recent earthquakes in different locations have illuminated this unusually large ULVZ structure and revealed quite similar waveform complexities. Owing to the strong sensitivity of the seismic data to the structure, we can model a simplified 3D ULVZ, providing further constraints on the geometry and location. The results of this study are aimed at confirming and better characterizing this unusual structure, as a first step towards searching for other possible structures of this type in the vicinity of the Pacific LLSVP.

Method and Data

Most recent seismological investigations of the lowermost mantle have used global datasets to analyze the travel time shift and amplitude variation of different seismic phases. We are using numerical forward modeling of the shear diffracted (Sdiff) phase observed at broadband stations from the USArray and other permanent networks in North America for large deep earthquakes (depth>200 km and $6<M_w<7$) in the western Pacific region at distances of 80°-130°. In this study, we used the April 17th, 2014 event (depth 208.6 km, M_w 6.9) to illustrate the affect of the ULVZ in north-central Pacific on the Sdiff waveforms.

The modeling approach is to consider the variations with azimuth and epicentral distance of Sdiff travel time residuals computed with respect to the reference 1D Preliminary Reference Earth Model (PREM, *Dziewonski and Anderson,* 1981). We also compute corresponding waveforms for 3D synthetics using the Coupled Spectral Element Method (CSEM, *Capdeville et al.,* 2003) to further interpret the waveforms of the main phase and post-cursor. This method is computationally effective for the study of D" with full 3D spectral element solution in a layer of limited thickness above the core-mantle boundary, coupled with 1D normal mode solution in the rest of the mantle and in the core.

We find that the focal mechanism provided by Centroid Moment Tensor (CMT) catalog for this event may not be optimal in that it does not accurately predict the observed amplitude ratios between the main phase and the depth phase, so modifying the focal mechanism may be necessary before we attribute amplitude variations as a function of azimuth to the structure in the D" region. This requires analyzing records from different

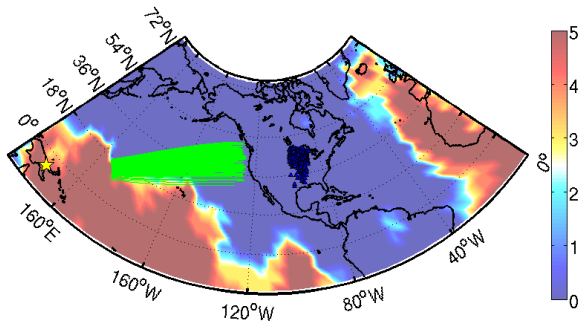

Figure 2.7.1: The location of the event is indicated by a yellow star and the stations are indicated by blue triangles, the great circle paths are indicated by green lines from entrance to exit points of a lowermost mantle layer about 300 km thick from core-mantle boundary. Background is cluster analysis result of five tomographic models (*Lekic et al.,* 2012*).* The numbers on the right indicate how many of the models agree that a particular location has shear velocity lower than average.

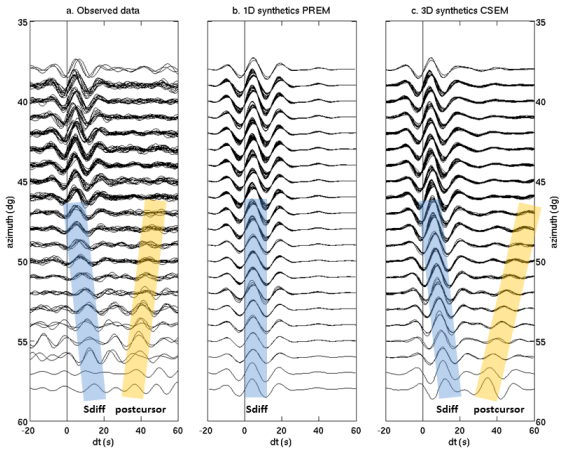

Figure 2.7.2: The comparison of tangential velocity waveforms from (a) observed data, (b) 1D PREM and (c) 3D CSEM at distances between 110° and 120°. The traces have been band-pass filtered between 10-20 s. The main Sdiff (blue) and post-cursor (yellow) are highlighted in (a) and (c) for the data and the waveforms calculated for the preferred model.

locations and azimuths using a grid search method to get the best solution.

Results

Figure 2.7.1 presents the Sdiff paths to 217 available stations from the US transportable array and permanent stations in North America that sample the border of the northern Pacific LLSVP. Based on the CMT data for this event, we computed the 1D synthetics for the PREM model in Figure 2.7.2b and 3D synthetics using CSEM for a model in which we have added a ULVZ as shown in Figure 2.7.2c. The model explains the time shift of the main Sdiff phase well (about 15 s at the most) and also the relative arrival time of the post-cursor with respect to Sdiff (about 40 s at the most), as a function of azimuth. However, the synthetics are not able to reproduce the strong amplitude reduction in the Sdiff phase at certain azimuths between 46° and 60° (Figure 2.7.3a), nor the amplitude reduction in the post-cursor phase (Figure 2.7.3b).

In Figure 2.7.3b, the post-cursor is too weak at azimuths smaller than 48°, so these measurements are only possible for larger azimuths. The synthetics reproduce the trend of increasing amplitude of the post-cursor at large azimuths, but the amplitude is slightly under-estimated compared to observed data. In Figure 2.7.3c, the travel time in 3D synthetics matches the general trend of both the Sdiff and the post-cursor phases with observed data. Some scatter in the travel time of post-cursors between 46°-48° azimuths may be due to the difficulty of measuring the peak of post-cursors, including possible cycle slips.

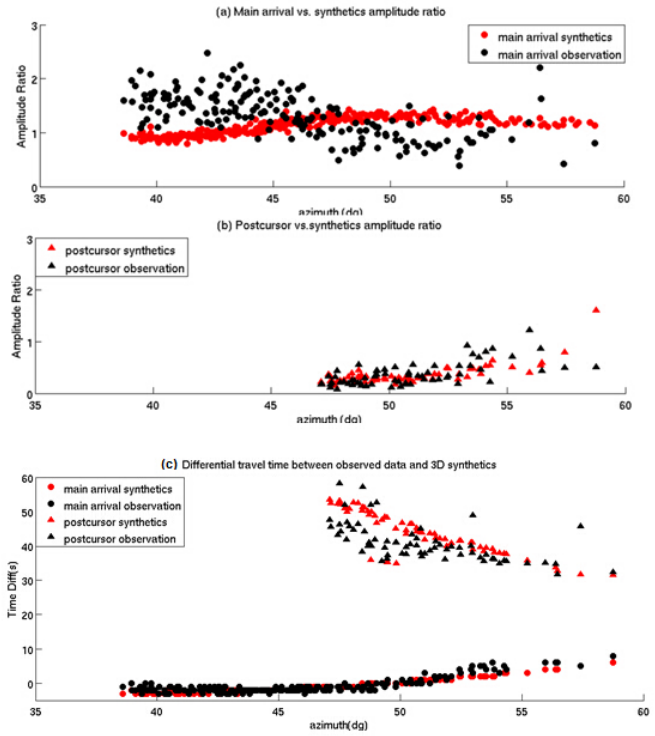

Figure 2.7.3: Amplitude ratio (a, b) and differential travel time (c) comparison between observed data (black) and 3D CSEM synthetics (red) for the main arrival Sdiff (circle) and post-cursor (triangle), measured by cross-correlation with 1D PREM synthetics filtered between 10-20 s.

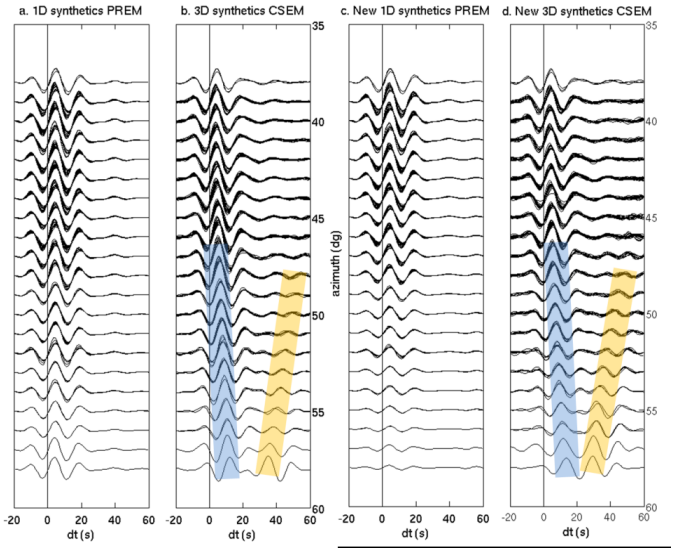

Figure 2.7.4: The comparison of tangential velocity waveforms from (a) original 1D PREM, (b) original 3D CSEM, (c) updated 1D PREM and (d) updated 3D CSEM at the distance between 110° and 120°.

On the other hand, Figure 2.7.4 indicates that after adjusting the focal mechanism, updated 3D synthetics have a clear Sdiff phase amplitude reduction as the azimuth increases, and a clear Sdiff phase amplitude reduction as the azimuth decreases, which can explain the trend in the observed data. This is also the case in 1D synthetics. However, the post-cursor synthetics at the large azimuth now have a slight time shift, which may be due to the uncertain geometry and location of the ULVZ.

Conclusions

The preferred model has been confirmed using the amplitude and travel time variations of the main Sdiff phase and time delayed post-cursor for an event not previously used in *Cottaar and Romanowicz* (2012), but there are still some features in the data that the preferred model cannot explain well. Adjusting the focal mechanism of the earthquake source can help improve the fits for the amplitude variation with azimuth, but may degrade the travel times of the post-cursors. There is potential for further constraining the shape and location of ULVZ by analyzing Sdiff phase data from new events in different locations, which can better cover the study area from all available directions.

References

Capdeville, Y., Romanowicz, B. and Toh, A., Coupling spectral elements and modes in a spectral earth: an extension to the "sandwich" case, *Geophys. J. Int.*, 154, 44-57, 2003.

Cottaar, S. and Romanowicz, B., An unusually large ULVZ at the base of the mantle near Hawaii, *Earth Planet. Sci. Lett.*, 355, 213-222, 2012.

Dziewonski, A.M. and Anderson, D.L., Preliminary reference Earth model, *Physics of the Earth and Planetary Interiors*, 25, 297-356, 1981.

Lekic, V., Cottaar, S., Dziewonski, A.M. and Romanowicz, B., Cluster analysis of global lower mantle tomography: a new class of structure and implications for chemical heterogeneity, *Earth Planet. Sci. Lett.*, 357-358, 68-77, 2012.

8 Full Waveform Seismic Tomography Using Stochastic Methods

Marco Calò, Thomas Bodin, Barbara Romanowicz

Introduction

Seismic tomography is currently evolving towards 3D earth models that satisfy full seismic waveforms at increasingly high frequencies thanks to the advent of powerful numerical methods such as the Spectral Element Method (SEM) and the drastic increase of computational resources. However, the production of such models requires handling complex misfit functions with more than one local minimum. Standard linearized inversion methods have two main drawbacks: 1) they produce models highly dependent on the starting model; 2) they do not provide a means of estimating true model uncertainties. Furthermore, current 3D SEM based models use as input either 1D, or smooth 3D models that include only the major known discontinuities (*e.g.* Moho, 400 km, 660 km) and do not consider the presence of other sharp variations of the velocities with depth such as the Mid-Lithospheric discontinuity (MLD) and the Lithosphere-Astenosphere boundary (LAB). However, these issues can be addressed with stochastic methods that can sample the space of possible solutions efficiently. Such methods are prohibitively challenging computationally in 3D, but increasingly accessible in 1D. In this project, we directly tackle the non-linearity of the inverse problem by using stochastic methods to construct a 3D starting model for SEM based tomography with a good estimate of the depths of the main layering interfaces. The procedure to carry out the starting 3D model is based on three main steps:

1. Regionalization of the study area to define provinces within which lateral variations are considered smooth;

2. Construction of 1D models of Vs and of radial anisotropy (Xi) in each province as well as the corresponding error distribution using a joint inversion approach where high frequency body waves are combined with long period Love and Rayleigh waves by updating a trans-dimensional stochastic inversion method (*Bodin et al.*, 2014).

3. Merging of the models using data-driven smoothing operators.

The patterns observed by applying the 1D stochastic inversion at several stations deployed in the North American continent represent important observations themselves for describing lithospheric structures of the region and are the subject of two papers in preparation.

Regionalization of the NA Continent

We applied k-means cluster analysis to the SEMum global tomography model (*Lekic and Romanowicz*, 2011) in the range depth 50–350 km to separate the North America region in three main provinces (Oceanic, Transition, and Cratonic zone). The mean standard deviation of the velocity profiles in each province is 0.05 km/s and the largest Euclidean norm between the average 1D profile of each region and the 1D models does not exceed 0.15 km/s. These values suggest that each macro region encloses 1D profiles that are very similar in the depth range considered and that a separation of North America in three areas is the minimum order of the cluster analysis that has to be applied to obtain a regional scale separation of the continent.

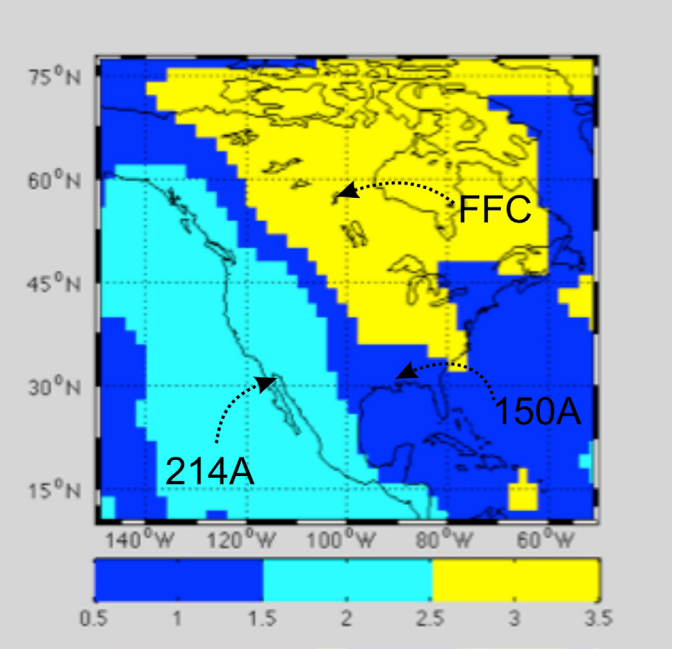

Figure 2.8.1: Separation of the North America continent in three macro-regions using the k-means cluster analysis technique. Each region is marked by a similar Vs profile in the range depth 50–350 km.

Construction of the 1D models

We calculated 1D Vs and radial anisotropy (Xi) profiles and posterior noise estimation at 24 stations deployed in the NA continent using an updated version of the trans-dimensional Markov-chain algorithm (*Bodin et al.*, 2014). In this version we jointly invert three datasets:

1. Rayleigh and Love phase velocity profiles from 25 s to 250 s, extracted from the global model of *Ekstrom et al.*, (2011).

2. Rayleigh and Love group velocity profiles from 16 s to 150 s, extracted from the global model of *Shapiro et al.*, (2002).

3. Averaged seismograms for calculating receiver functions using the cross-convolution method (*Bodin et al.*, 2014).

Synthetic tests reproducing the real data conditions show that both data and inversion methods are suitable to properly estimate posterior errors, absolute velocity values, and sharp discontinuities down to 300 km.

Figure 2.8.2 reports two examples of these tests, one us-

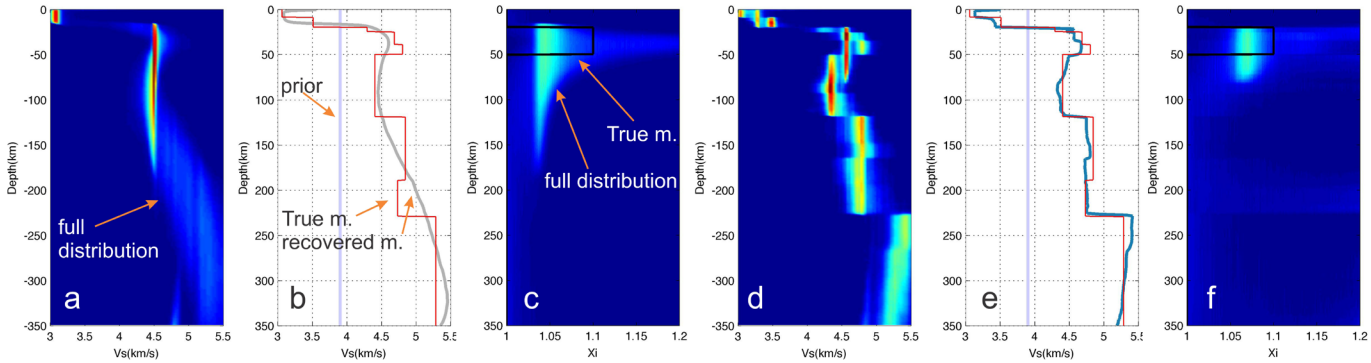

Figure 2.8.2: a,b,c) Test using group and phase velocities of Rayleigh and Love waves calculated in the period range of 16–250 s on a 1D Vs model with a radial anisotropic layer. a) posterior distribution of the Vs model, b) True Vs model, initial distribution of the prior, and recovered model, c) anisotropic layer (in black) and posterior distribution. d,e,f) Test using body wave, and group and phase velocities of Rayleigh and Love waves calculated on a 1D Vs model with a radial anisotropic layer. d) posterior distribution of the Vs model, e) True Vs model, initial distribution of the prior, and recovered model, f) anisotropic layer (in black) and posterior distribution.

ing only the surface wave data (Figure 2.8.2a,b,c) and another one using the complete dataset (Figure 2.8.2d,e,f). With these tests we show that the contribution of the surface waves allows us to constrain the absolute velocity values in depth even when we impose a width centered on a prior model far from the true model used to calculate the dispersion curves. However, a good reconstruction of the discontinuities is obtained only when adding information provided by the body waves (Figure 2.8.2d,e,f). These results show that both data and inversion methods are suitable to properly estimate posterior errors, absolute velocity values, and sharp discontinuities down to 300–350 km. Figure 2.8.3 reports an example of three 1D Vs distributions obtained for three stations (one in each macro-region). The 1D profiles show the presence of several discontinuities at different depths both in the crust and in the upper mantle.

Construction of the 3D Starting Model

The set of 1D radially anisotropic profiles allowed us to construct a 3D starting model for the North American lithosphere. The 1D models have been regrouped in families following the separations in macro-regions carried out with the cluster analysis. For each subregion, the 1D models have been averaged using a weighting function based on the posterior error distributions associated with each profile. Finally we connected the 1D profiles laterally using stochastic smoothing operators, to generate the 3D reference model. We are currently considering different strategies for adjusting the smoothing operators by simulating wave propagation through this model using a regional spectral element code (RegSEM, *Cupillard et al.*, 2012) and confronting the predictions to a set of observed waveforms, summed over a collection of events.

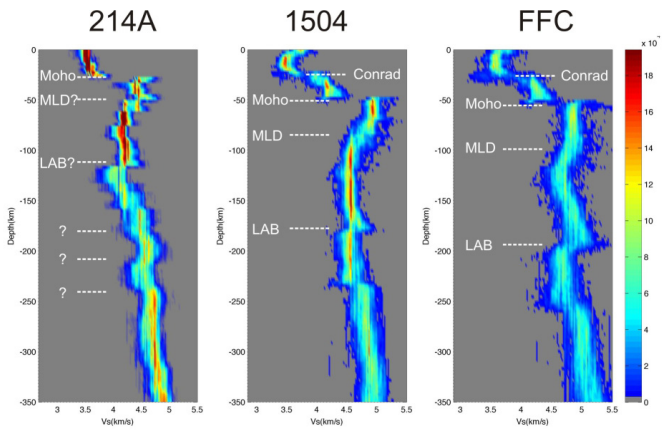

Figure 2.8.3: Examples of 1D Vs profiles calculated at three stations using the experimental data. Each station is located in a macro-region in which the NA continent has been divided (Figure 2.8.1).

Acknowledgements.

This project is funded by the "UC Lab-fee" collaboration program (UCOP grant 12-LR-236345) and is in collaboration with M. Maceira and C. Larmat at Los Alamos National Laboratory.

References

Bodin T., H Yuan, B Romanowicz, Inversion of receiver functions without deconvolution—application to the Indian craton, *Geophys. J. Int*. doi:10.1093/gji/ggt431, 2014.

Cupillard, P., Delavaud, E., Burgos, G., Festa, G., Vilotte, J.-P., Capdeville, Y. and Montagner, J.-P., RegSEM: a versatile code based on the spectral element method to compute seismic wave propagation at the regional scale, *Geophys. J. Int*, 188: 1203–1220. doi: 10.1111/j.1365-246X.2011.05311.x, 2012.

Ekström, G., A global model of Love and Rayleigh surface wave dispersion and anisotropy, 25–250 s, *Geophys. J. Int*, 187: 1668–1686. doi: 10.1111/j.1365-246X.2011.05225.x, 2011.

Lekic, V. and B. Romanowicz, Inferring upper-mantle structure by full waveform tomography with the spectral element method, *Geophys. J. Int*. v.185, no.2, p.799-831, 2011.

Shapiro, N.M. and M.H. Ritzwoller, Monte-Carlo inversion for a global shear velocity model of the crust and upper mantle, *Geophys. J. Int*, v.151, no. 1, p.88-105, 2002.

9 3D Kirchoff Prestack Depth Migration of Receiver Function

Cheng Cheng, Thomas Bodin, Richard Allen

Introduction

Time domain P receiver function, as a source removing and receiver side isolating technique, has been widely used to study the earth's interior structure in the past decade in global seismology imaging. After the deconvolution of large seismic array data, it characterizes the receiver side P-to-S conversions present within the coda of teleseismic P essentially. In order to extract the tectonic information out of this travel time ensemble, many methods have been introduced to post process the receiver function data. For example, the least-squares optimization and Mote Carlo inversion as in 1-D inversion, joint inversion with surface wave, common conversion point (CCP) stacking. Among all these methods, CCP and the later post-stack depth mapping is widely used for determining the geographic depth of the earth discontinuity. The basic idea for CCP depth mapping is that it implements the ray tracing and moveout correction for the incoming teleseismic plane wave based on a 1D earth reference model and it assumes a flat layer. This works well in mapping the reflectivity of relatively flat discontinuities, such as the Moho depth, the LAB depth etc., but it encounters difficulty when there are large heterogeneities and dipping layers, such as the subduction plate in the upper mantle. The uncertainty goes to both the CCP procedure and the later migration procedure, which can be as large as 20% in the 35 degree case (*Rondenay,* 2009). Here we introduce our solution in this complicated case: a 3D Kirchoff pre-stack depth migration method, with the application to the P receiver function. By implementing our method, both the real earth's 3D heterogeneity and the dipping interface can be accounted for. Also, this method is significant for its reduced computation time compared with the common pre-stack migration methods.

Method

Without doing the flat layer assumption and 1D moveout correction, we do the 3D ray tracing accounting for the 3D heterogeneity of the earth. It is done in the initial 3D model using the Fast Marching Method (FMM). FMM is a numerical method for solving boundary value problems for the travel time Eikonal equation. Typically, the ray tracing problems transfer to solve the evolution of a closed curve as a function of time T with speed F(x) in the normal direction at a point x on the curve using an up-wind finite difference solver. Compared with the traditional shooting method, this curve tracing tool is much faster and more stable, which is fundamental for our migration scheme. Also, our ray tracing is done for each of the three components of P receiver functions, which are P wave from the source to the model grid, P wave from the source to the receiver and converted S wave from the model grid to the receiver. Once the FMM ray tracing procedure is finished, travel times for all the source-grid-receiver pairs have been restored in the three matrices respectively using the Kirchoff migration in the next step.

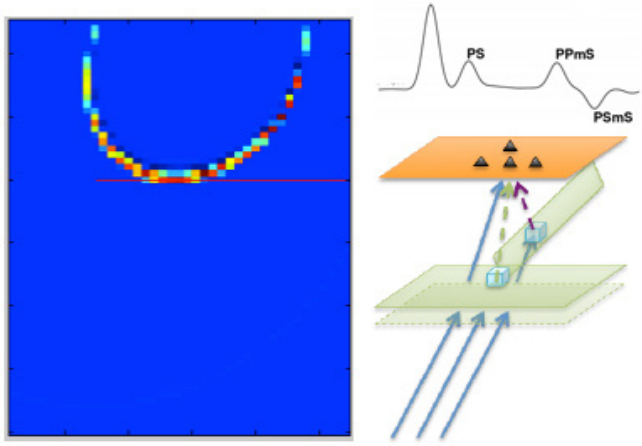

Figure 2.9.1: A diagram showing the principle of the receiver function Kirchoff migration method. The left panel is the result after one migration, the red line is the real position of the discontinuity, the semicircle is the waveform position of the PS receiver function spike after the migration procedure.

Figure 2.9.1 illustrates how Kirchoff migration works in our receiver function case. In the left image panel, the red line indicates the real position of the discontinuity. The semicircle is the migrated results in a 3D velocity model. This result is also called the impulse response of a process and is especially useful since a seismic section can be considered to consist of a series of spikes—the migrated reflectors will occur where the semicircles constructively interfere. Where the amplitude of the spikes on the input time section are distributed along a semicircle on the output migrated depth section is what is called the Kirchoff migration. Destructive interference will cancel out noise. Finally the discontinuity, which is real, comes out after the summation of the amplitudes along the semicircle and placing the summed amplitude at the apex. This form of migration formed the basis of the algorithms and is called diffraction summation, diffraction stack or more generally Kirchoff migration.

Another important process in our prestack migration scheme is the application of two weighting factors. One of which is for the factor of that we only use the radial component of P receiver function and another weighting factor serves for eliminating the off-great-circle energy.

Synthetic testing results

Figure 2.9.2 shows some preliminary synthetic results of our receiver function depth mapping using the prestack Kirchoff migration method, and is also compared with CCP depth mapping results. The first column shows the results of a flat layer. We can see that in this case both methods perform well in imaging the 0 degree discontinuity. Also we notice that even in the 0 degree case, the prestack Kirchoff migration doesn't have the multiples because the multiple energy stacked unconstruc-

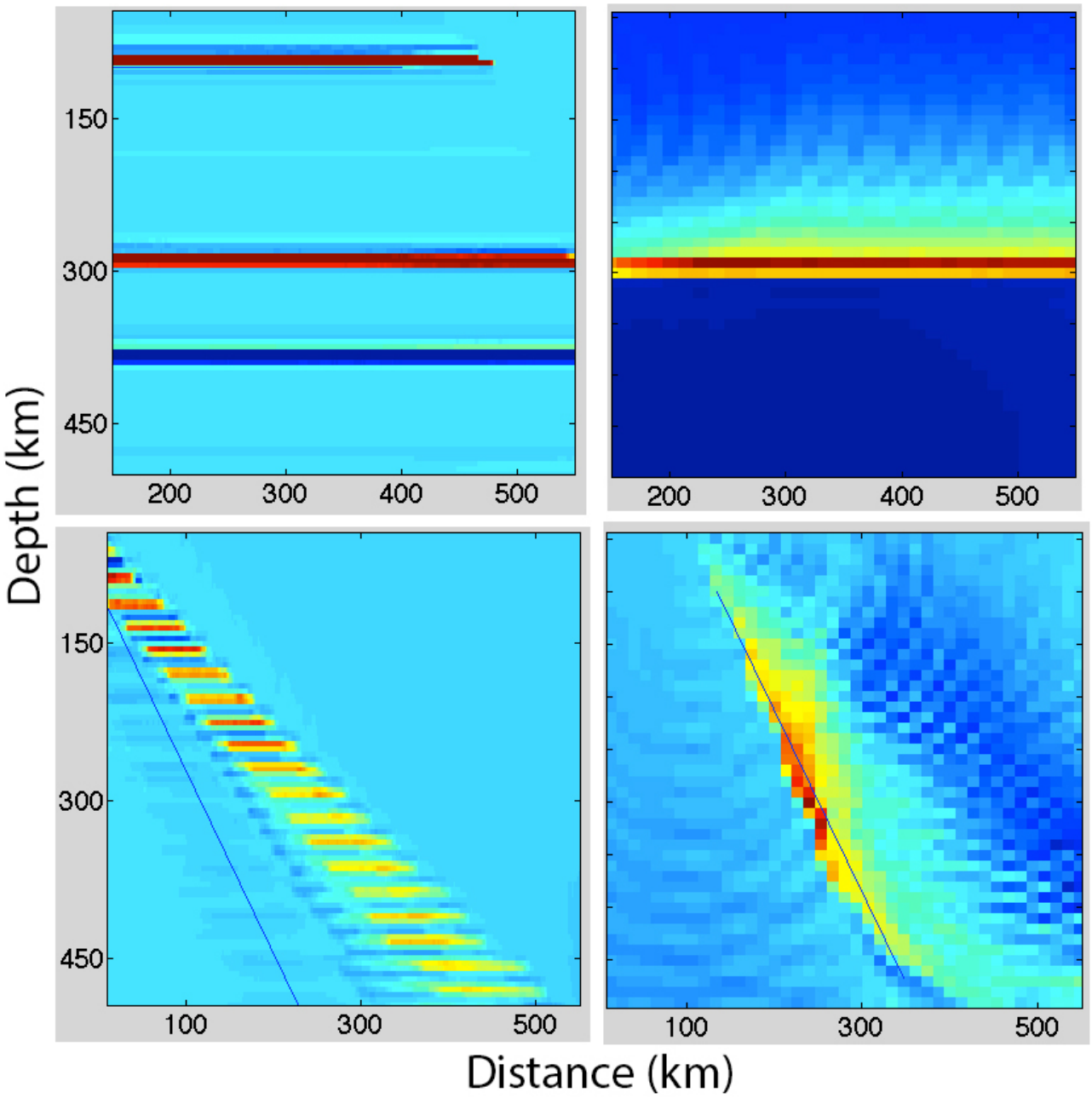

Figure 2.9.2: Comparison between the CCP depth mapping and 3D prestack Kirchoff migration of receiver function. Images in the left column are generated by CCP and the ones in the right are generated by prestack. The discontinuity in top two images are at 30 km with a 0 degree dipping layer and the one in the bottom two images has a 60 degree dipping layer.

tively and has been canceled out. The second column shows the 60 degree dipping layer case, the 3D Kirchoff migration performs much better in imaging the position and the dipping angle. The CCP depth mapping has underestimated the dipping angle, also the discontinuity is displayed as a wide band, which is not true. For comparison, the 3D FMM Kirchoff prestack migration has imaged the dipping layer at the right 60 degree angle and the right position.

In conclusion, from the preliminary testing results, our 3D prestack Kirchoff migration of receiver functions has accounted for the 3D heterogeneity of the earth model and doesn't make the 1D flat layer assumption. It has good performance in imaging big angle dipping layers and has potential applications for subduction zone imaging.

References

Rondenay, S., Upper mantle imaging with array recordings of converted and scattered teleseismic waves, *Surv. Geophys.*, 30, 377-405, 2009.

10 Joint Inversion of Receiver Functions and SKS Data: An Application to the Canadian Craton

Julie Leiva, Thomas Bodin, Barbara Romanowicz

Introduction

In order to improve layered structure models of the upper mantle beneath individual seismic stations, a new method involving a two step joint inversion of core refracted shear wave (SKS) splitting and receiver function (RF) data is currently being explored. This combination of seismic data results in a more robust structure model of the Canadian craton, and produces a probabilistic shear velocity (Vs) model acquired from RF data that incorporates azimuthal anisotropy from SKS splitting measurements. Our main focus involves resolving structure to a depth of up to 350 km beneath each seismic station, with an emphasis on layering around the lithosphere-asthenosphere boundary (LAB) and within the lithosphere itself. Knowledge of the structure around the LAB in cratonic regions will help improve the understanding of the formation of cratons and continents.

Methodology

Our inversion process utilizes a transdimensional Bayesian method that incorporates a Markov Chain Monte Carlo (MCMC) scheme to create probabilistic models, where the degree of layering, anisotropic strength and anisotropic direction are treated as unknowns.

Initially, our methodology involved a joint inversion of RF, surface wave dispersion (SWD) and SKS data that produced models of shear velocity and anisotropic parameters (strength and fast axis direction) in a single step. However, this proved to be a computationally expensive technique; the computation time was heavily improved by separating the process into two separate steps where the Vs model was first obtained by inverting RF and SWD data, and then performing a subsequent inversion for anisotropy. The latter step uses the acquired Vs model as a heavily constrained reference model, effectively limiting the second part of the inversion to solve for anisotropic parameters.

A joint inversion of RF, SWD and SKS data has proven to be advantageous; by combining different sets of data that are sensitive to sharp changes in shear velocity and anisotropy, we are able resolve finer structure with depth and distinguish both isotropic and anisotropic boundaries. Receiver functions are used to detect interfaces where seismic conversions occur (Ps and Sp), and thus expose sharp velocity changes which are necessary in constructing Vs models. SKS splitting data account for azimuthal anisotropic effects integrated over the mantle on the receiver side. Seismic anisotropy in the upper mantle is a product of past and present tectonic and mantle processes and their resultant deformation, and thus provides additional structural information. However, since SKS data relies on integration over the entire upper mantle, depth resolution for SKS data is poor. SWD data are included to improve resolution in the upper 250 km, where the LAB and the focus of our research are contained.

Results and Future Work

The full two step process has been applied to synthetic data, and the full joint inversion was able to be applied in a single step due to the relatively low computational cost. The final results of Vs, strength of anisotropy, and fast axis direction by layer are shown in Figure 2.10.1. This inversion combined three Ps RF traces and seven SKS traces, as well as SWD with periods of up to 250s. The true structural model contains five isotropic and two anisotropic layers, with anisotropic strength equal to 4% and 6%, and the fast axis direction 45° and 60°, respectively. Figure 2.10.1 shows well resolved layering, shear velocities, and anisotropic parameters.

The first step of the inversion process has been applied to the permanent seismic station YKW3 from the Canadian National Seismograph Network (CN). YKW3 is located in Yellowknife, Northwest Territories and at the northern edge of the craton and provides archived seismic data through Incorporated Research Institutions of Seismology (IRIS) from as early as 1994. Results from the first step of the inversion process are shown in Figure 2.10.2, where RF and SWD data were inverted to find the Vs model. In this case, one Ps RF trace and nine SKS traces were used, as well as SWD with periods of up to 150 s. The resultant Vs model is currently being modified to use as a reference model in the second step of the joint inversion for real data.

Future work involves finishing the second part of the inversion for data from YKW3. Steps will be taken to improve computation time for real data and to further enhance our methods prior to applying this technique to other CN stations within the Canadian craton. Subsequent work can then be done in other cratonic regions across the world in order to better understand craton and continent formation on a global scale.

Acknowledgements

This work is supported by the Lab fees Research Program, grant number 12-LR-236345.

References

Bodin, T., Sambridge, M., Tkalčić, H., Arroucau, P., Gallagher, K., and N. Rawlinson, Transdimensional inversion of receiver functions and surface wave dispersion, *J. Geophys. Res,* 117, B02301, 2012.

Bodin, T., Yuan, H., and B. Romanowicz, Inversion of Receiver Functions without Deconvolution, *Geophys. J. Int., 196,* 1025-1033, 2014.

Romanowicz, B., and H. Yuan, On the interpretation of SKS splitting measurements in the presence of several layers of anisotropy, *Geophys. J. Int., 188,* 3, 1129-1140, 2012.

Yuan, H. and B. Romanowicz, Lithospheric layering in the North American Craton, *Nature, 466,* 7310, 1063-1068, 2010.

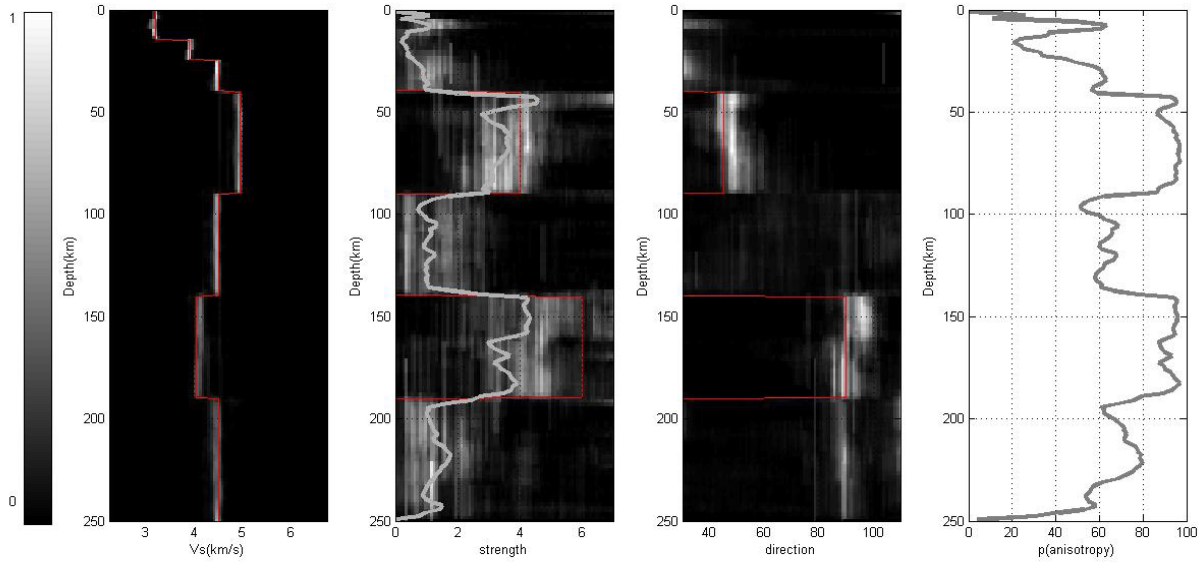

Figure 2.10.1: Results of synthetic data for the full joint inversion, where red lines indicate the true models. From left to right: a) a probabilistic solution for a shear velocity structure model down to 250 km; b) strength of anistropy with depth, where the white line indicates the mean of the data; c) fast axis direction with depth; d) the probability of anisotropy within each layer. Note that the Vs model was allowed to be inverted for in this step, due to the relatively low computational cost.

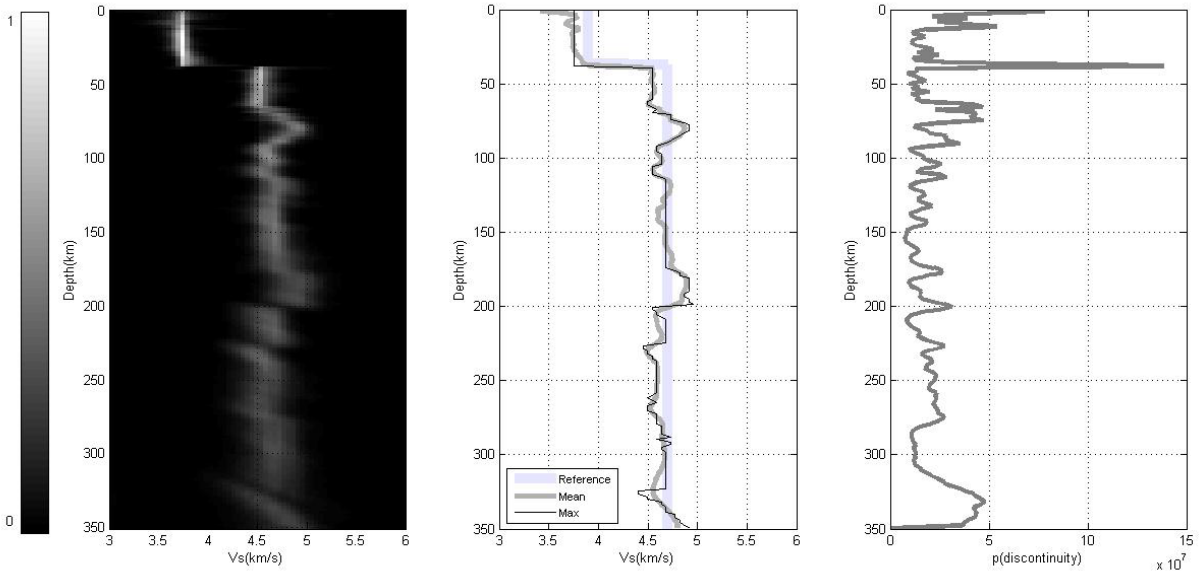

Figure 2.10.2: Results from the first step of the two step process for real data from station YKW3. From left to right: a) a probabilistic solution of the shear velocity structure model down to 350 km beneath the station, where white coloration indicates higher probability; b) a comparison of the single layer reference model to the average and maximum models; and c) the probability of the existence of a discontinuity.

11 High Resolution Upper Mantle Discontinuity Images Across the Pacific Ocean from *SS* Precursors Using the Local Slant Stack Filters

Zhao Zheng, Sergi Ventosa, Barbara Romanowicz

Introduction

The upper mantle discontinuities (primarily the 410 and the 660) place important constraints on the temperature, composition and dynamics of the earth's mantle. To image these discontinuities, one effective data type is the *SS* precursors (*Shearer*, 1991), which are shear waves reflected off the bottom of the discontinuities (Figure 2.11.1). A major advantage of the *SS* precursors, compared to other data types such as receiver functions or triplications, is that they provide coverage for the vast oceanic areas where few seismic deployments are available.

In recent years, with the improvement in the resolution of global mantle tomography (e.g. *French et al.*, 2013), there has been an increasing demand for higher resolution images of mantle discontinuities as well, in order to examine possible correlations between the two. However, several challenges have limited the spatial resolution of the discontinuity images retrieved from the *SS* precursors. First of all, the precursors are weak in amplitude (typically 5-10% of the *SS* main phase), often at or below noise level. Stacking is therefore necessary. In the past, common-midpoint (CMP) stacking over large geographic bins (radius of 10° or 5°) has been common (for a review, see *Deuss*, 2009), which limits the resolution. Secondly, *SS* precursors suffer from interference from other phases, such as the postcursors to S_{diff} (or *S* at shorter distances) and the precursors to *ScSScS*. To circumvent this issue, several past studies have limited the epicentral distance of data selection to the "safe ranges", for example, 95-115° and 140-145°, although theoretically *SS* precursors exist over the entire range of 80-160°. This has reduced the amount of available data by a significant fraction and may have led to loss of resolution.

Recent deployment of the dense US Transportable Array (TA) has provided unprecedented opportunities to achieve higher resolution for *SS* precursor studies. To overcome the above-mentioned limitations, here we employ a new tool called the Local Slant-Stack Filters (LSSF), which seeks to maximize

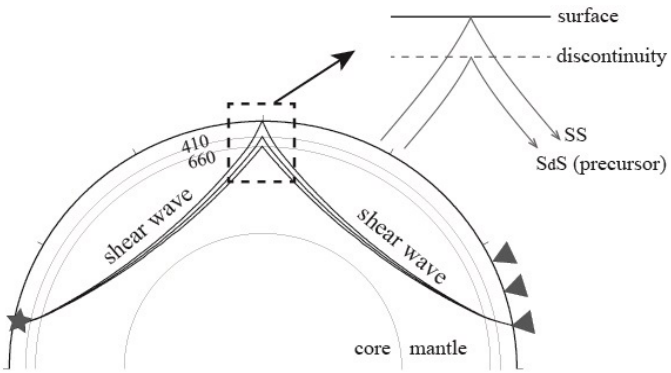

Figure 2.11.1: The ray paths of SS and its precursors. The SS precursors are reflected shear waves off the bottom side of the discontinuities (e.g. the 410 and the 660) in the Earth's upper mantle.

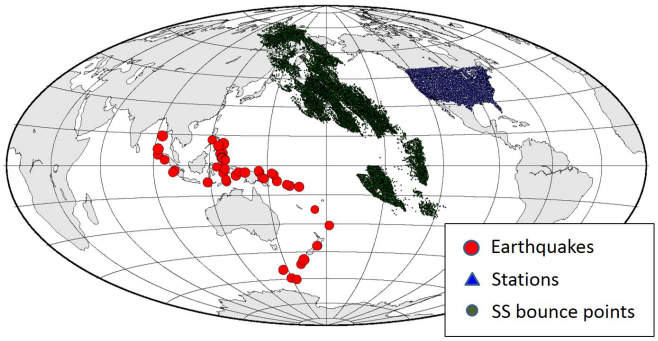

Figure 2.11.2: A map showing the *SS* precursor dataset used in this study.

spatial resolution by exploiting the advantage of a dense array. We present images of the 410 and 660 topography for a vast area across the Pacific Ocean, and compare them to a recent high resolution global upper mantle shear wave tomography model, *SEMum2* (*French et al.*, 2013).

Data and Method

We collect a dataset of *SS* precursors from 47 high quality events in the southwestern rim of the Pacific Ocean recorded by the TA between 01/2004 and 12/2013, with the following criteria: $6.0 \le M_w \le 7.8$, depth ≤ 75 km, $80° \le \Delta \le 160°$, which are consistent with previous *SS* precursor studies. The *SS* bounce points sampling area is shown in Figure 2.11.2. We look at the transverse component displacement seismograms filtered in 15–75 s, and apply various quality control procedures.

We then apply the LSSF filters to clean up these *SS* precursor record sections. Briefly, the LSSF sweeps across time and space in a record section, and conducts a slowness decomposition (slant stacking) in the vicinity of each point; then in the slowness domain, filters are designed to extract signals with a target slowness (or slowness range) and remove other signals with undesired slownesses as well as random noise. Readers are referred to *Ventosa et al.* (2012), *Zheng et al.* (2013) and *Zheng* (2014) for details. After the record sections are cleaned up, differential travel times between a precursor and the *SS* main phase are measured from each single trace, and then converted to the discontinuity depth at that bounce point. All the depth measurements are then combined to produce a map of discontinuity topography for the entire study region.

Results

Figure 2.11.3 shows a map of the 410 discontinuity depth. Overall the 410 does not show large topography. Several small-scale warm anomalies are seen in the central and south Pacific (labeled *A*, *B* and *C* in Figure 2.11.3a), with variable size and strength. Interestingly, the locations of these anomalies coin-

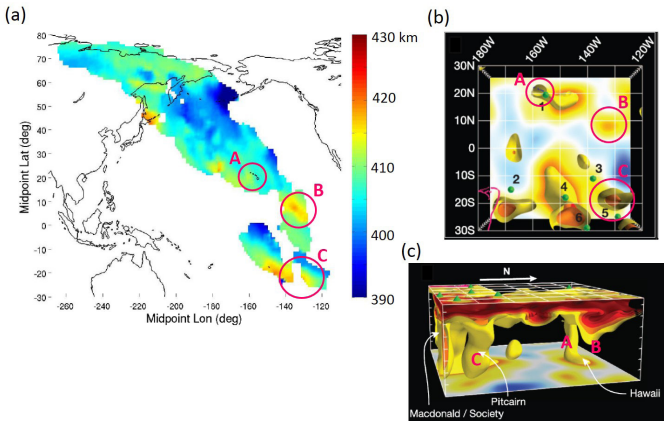

Figure 2.11.3: (a) A map of the 410 discontinuity topography for the study region. Warm colors represent longer *SS*-$S_{410}S$ differential travel time, or an apparently deeper 410, suggesting a warm anomaly if explained by temperature effect alone on olivine phase transformation. Cold colors respresent the contrary. (b) Top view and (c) side view of the tomography model *SEMum2* (*French et al.*, 2013). Low shear velocity anomalies (V_s reduction >2%) are shown in yellow.

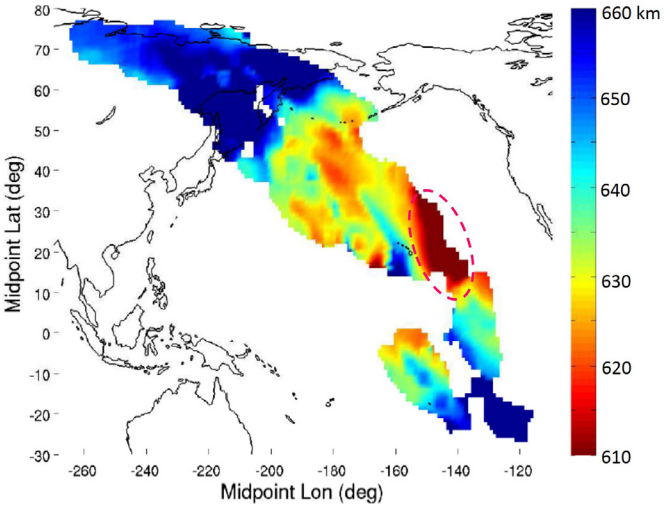

Figure 2.11.4: A map of the 660 discontinuity topography for the study region. The dashed oval outlines an anomalous area east of Hawaii, which shows significantly shorter *SS*-$S_{660}S$ differential travel times.

cide with a few low velocity columns penetrating the 410 discontinuity revealed by the tomography model *SEMum2* (Figure 2.11.3b and c). These low velocity columns can be explained as uprising hot mantle materials, which would have a "warm" signature on the 410 topography. It is remarkable that not only the locations, but also the horizontal extent and the magnitude of these three anomalies are in good agreement between the two maps.

Figure 2.11.4 shows the 660 discontinuity topography. Overall the 660 has larger topography than the 410. It is depressed in the subduction zones (colder) at the northwestern rim of the Pacific and uplifted in the oceanic regions (warmer), as previously observed. One striking feature is an area of extremely warm color to the east of Hawaii. This area is sampled by three events in the dataset, and they all give consistent results. Cross sections of the whole mantle tomography model *SEM_UCBwm* (*French* and *Romanowicz*, 2014) plotted along and perpendicular to the *SS* ray path (*Zheng*, 2014) indicate that ray path of the $S_{660}S$ precursor grazes the eastern boundary of a prominent quasi vertical low velocity anomaly for a fairly long distance, whereas the paths of the $S_{400}S$ precursor and the *SS* phase travel through a high velocity anomaly above the low velocity body. This would predict a significantly longer *SS*-$S_{660}S$ and a normal *SS*-$S_{410}S$ differential travel time, or when converted from time to depth, an apparently normal 410 and a significantly shallower 660, which agrees very well with the discontinuity images here.

Conclusions

We present high resolution topography images of the 410 and 660 discontinuities for a vast region across the Pacific Ocean measured from *SS* precursors. The high density US Transportable Array data combined with a new processing technique, namely the Local Slant Stack Filters (LSSF), have allowed for higher spatial resolution than previous studies. Sensible correlations are observed between several fine-scale heterogeneities in our discontinuity images and corresponding anomalies in the mantle tomography model *SEMum2*.

Acknowledgements

This study was supported by NSF EAR #0738284 and ERC Advanced Grant "WAVETOMO". Data are downloaded from IRIS.

References

Deuss, A., Global observations of mantle discontinuities using SS and PP precursors, *Surv. Geophys. 30*, 301-326, 2009.

French, S., V. Lekic, & B. Romanowicz, Waveform tomography reveals channeled flow at the base of the oceanic asthenosphere, *Science*, *342*(6155), 227-230, 2013.

French S. & B. Romanowicz, Whole-mantle radially anisotropic shear-velocity structure from spectral-element waveform tomography, *Geophys. J. Int.* (submitted), 2014.

Shearer, P.M., Constraints on upper mantle discontinuities from observations of long-period reflected and converted phases, *J. Geophys. Res., 96*, 18147-18182, 1991.

Zheng Z., S. Ventosa, & B. Romanowicz, The application of the Local Slant-Stack Filters (LSSF) for high resolution upper mantle discontinuity imaging, *BSL Annual Report*, 2013.

Zheng Z., Refining Constraints on Seismic Discontinuities and Elastic Structure in the Earth's Upper Mantle, *PhD thesis*, UC Berkeley, California, 2014.

12 Separating Intrinsic and Extrinsic Anisotropy

Thomas Bodin, Yann Capdeville, Barbara Romanowicz

Introduction

It can be proven that if one had an unlimited number of sources, receivers, and an unlimited frequency band, one would be able to entirely describe an elastic medium from the displacement of elastic waves propagating through it, and observed at its surface. However, in seismology there are a number of elements that limit the ability to image structure. Firstly, the seismic records are limited both in time and frequency, and the number of sources and receivers are limited. There are also a number of observational and theoretical errors that propagate into the recovered images.

In recent years, advances in numerical methods such as the spectral element method have allowed us to model more accurately the entire seismic wave-field. Numerically computed seismograms automatically contain the full seismic wavefield, including all body and surface wave phases as well as scattered waves generated by lateral variations of the model Earth properties. The accuracy of the numerical solutions and the exploitation of complete waveform information result in tomographic images that are both more realistic and better resolved (*French et al.*, 2013).

However, computational time increases proportionally to the fourth power of frequency, and limits the frequency range of waveforms to relatively long periods (typically longer than 40 or 50 s for global scale images). Hence the geological interpretation of global tomographic models is limited, mainly due to two reasons:

1. Because the frequency range of global inversions remains limited, and because features smaller than the shortest wavelength cannot be mapped, the constructed images are smooth and do not contain discontinuities that are crucial to understand the structure and evolution of the earth.

2. The relations that link the true earth to the effective (and unrealistic) earth that is seen by long period waves are strongly non-linear and their inverse is highly non-unique. For example, it is difficult to quantitatively interpret the level of imaged anisotropy in tomographic models, as it may be the effect of either real local anisotropy or unmapped velocity gradients such as layering.

Down-scaling Smooth Models

As we have seen, a tomographic inversion of long period waves can only retrieve at best a smooth effective model (and less in the case of an incomplete data coverage). This smooth equivalent earth fits the long period data. However, It is not a simple spatial average of the true earth, but the result of highly non-linear "up-scaling" relations (*Capdeville et al.,* 2010). We propose a novel approach to interpret tomographic images in terms of geological structures (discontinuities). We call this inverse problem the inverse homogenization: for a given smooth 1D profile extracted from a tomographic model, what are the possible fine scale (*i.e.,* layered) models that are equivalent to this smooth 1D profile, *i.e.,* that provide a similar data fit .

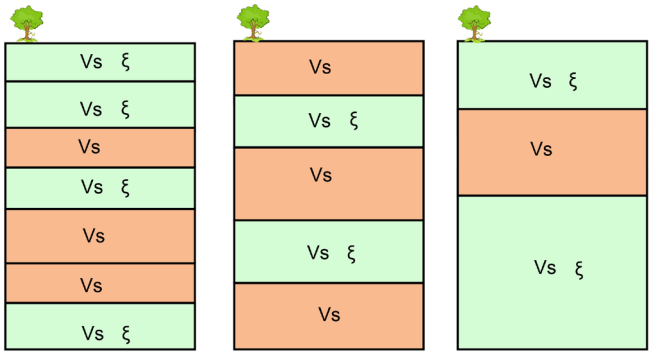

Figure 2.12.1: Adaptive parameterization used for the inverse homogenization. The number of layers as well as the number of parameter in each layer (one for isotropic layers, and two for anisotropic layers) are unknown in the inversion. This is illustrated here with three different models with different parameterizations. The parameterization is itself an unknown to be inverted for during the inversion scheme. Of course, data can always be better fitted as one includes more parameters in the model, but within a Bayesian formulation, preference will be given to simple models that explain observations with the least number of model parameters.

Although there is an infinite number of layered models that are equivalent to a smooth tomographic profile, these models share common features, and Bayesian statistics can be used to appraise this ensemble. In particular, a probabilistic approach allows us to quantify the trade-off between anisotropy and heterogeneity. Indeed, a smooth anisotropic model can either be explained by a large number of isotropic layers or by a few anisotropic layers. To break this trade-off, and distinguish between real anisotropy and small-scale layering, higher frequency data sensitive to discontinuities, such as receiver functions, can be used to constrain the location of horizontal discontinuities.

As shown in Figure 2.12.1, we describe our layered models with a transdimensional parameterization (*Bodin et al.,* 2014), where the number of layers, as well as the number of parameters per layer are free variables, *i.e.,* unknown parameters In this way, the number of layers will be variable in the ensemble solution, as well as the number of parameters in each layer: 1 for isotropic layers (V_S) and 2 for anisotropic layers (V_S and ξ).

A Probabilistic Seismic Model Under the North-American Craton

We construct a 1D probabilistic seismic profile under North-West Canada, by combining in a joint Bayesian inversion a full-waveform radially anisotropic tomographic profile (SEMum2, *French et al.*, 2013) with receiver functions.

The goal here is to investigate the structure and history of the North American craton. At the same time, we explore whether lithospheric layering as seen by scattered body waves (receiver functions) is compatible with the radial anisotropy imaged

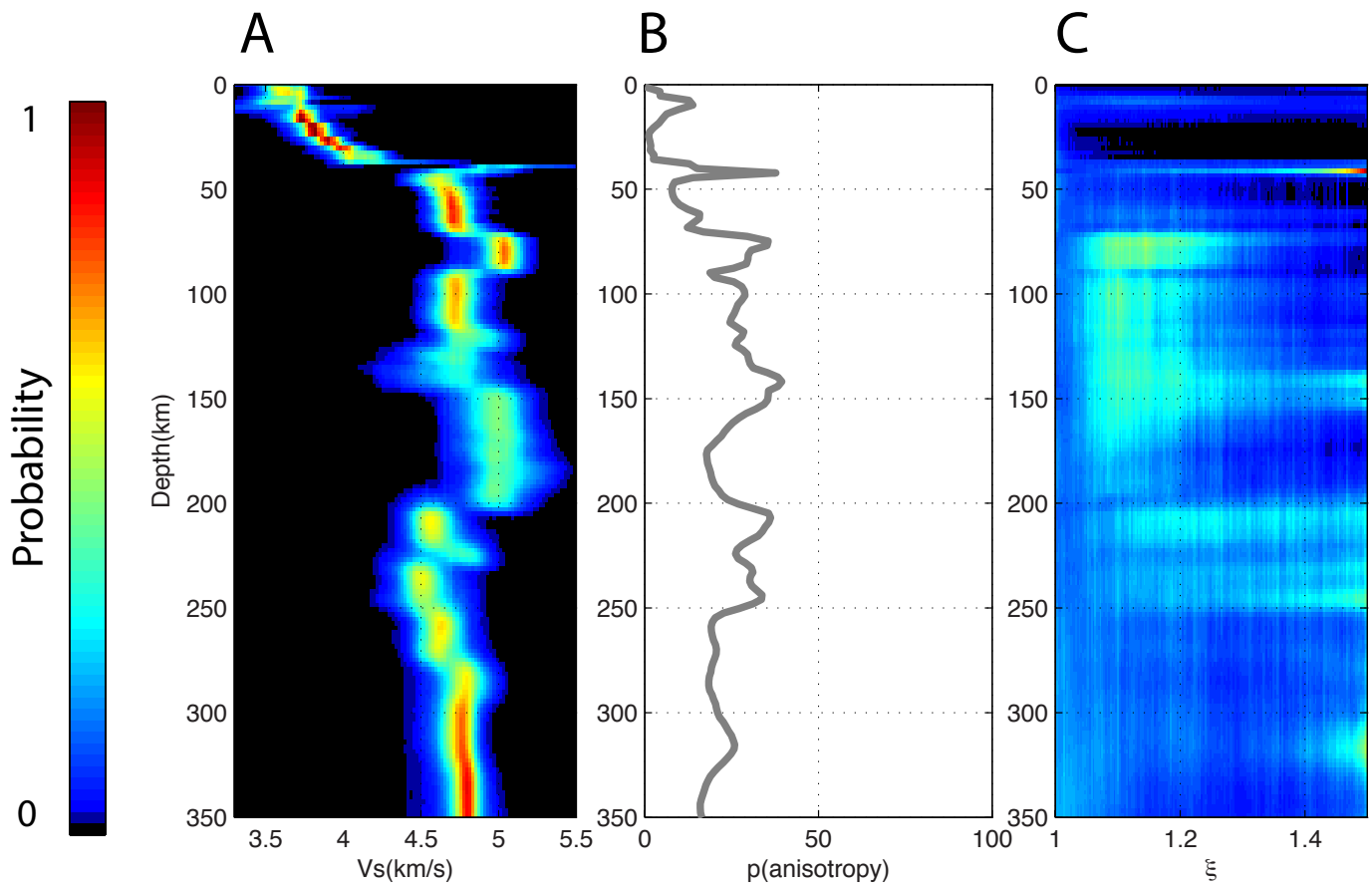

Figure 2.12.2: Left Probability distribution for Vs. Middle: probability of having an anisotropic layer. Right: probability for ξ .

from global tomography.

The solution is given by an ensemble of 1D models with variable number of layers, thicknesses, and elastic parameters. Figure 2.12.2A shows the marginal distribution for S-wave velocities as a function of depth, simply constructed from the density plot of the ensemble of models in the solution. Here a number of expected lithospheric discontinuities have been imaged, such as the mid-lithospheric discontinuity at 90 km and a sharp lithosphere-asthenosphere boundary at 200 km.

Since here we are interested in the relative contribution of layering to the observed anisotropy in SEMum2, we can look at the probability at each depth to have intrinsic anisotropy. For each model, each layer is either isotropic or anisotropic. Therefore, at each depth, one can count the ratio of isotropic to anisotropic layers in the ensemble of models. When no information is brought by the data (prior distribution), the probability to have anisotropy is 50%. However here, the probability is lower and around 20% across much of the depth profile. This implies that intrinsic anisotropy is not required to fit the smooth tomographic profile. In other words, the discontinuities required to fit the converted body waves may be enough to explain the anisotropy in the tomographic model. We view this as an important result, indicating that radial anisotropy (at least under cratons) should not be directly interpreted in tomographic models.

The third panel in Figure 2.12.2C shows the probability distribution for ξ at each depth. Note that, for a given depth, around 80% of models are isotropic with $\xi = 1$, and this distribution only represents the level of anisotropy in the 20% remaining models.

Acknowledgements

This project was supported by the French-Berkeley Fund (FBF). Thomas Bodin wishes to acknowledge support from the Miller Institute. Computational resources were also provided by the Institutional Computing program of LANL.

References

Bodin T., H Yuan, B Romanowicz, Inversion of receiver functions without deconvolution—application to the Indian craton- Geophys. J. Int. doi:10.1093/gji/ggt431, 2014.

Capdeville Y., Guillot, L., and Marigo, J., 1-d non periodic homogenization for the seismic wave equation. Geophys. J. Int. 181 (2), 897-910, 2010.

French, S., Lekic, V., & Romanowicz, B., Waveform tomography reveals channeled ow at the base of the oceanic asthenosphere, Science, 342(6155), 227-230, 2013.

Research Studies:
Rheology and Fault Mechanics

13 Probing the Lithospheric Rheology Across the Eastern Margin of the Tibetan Plateau

Mong-Han Huang, Roland Bürgmann, Andrew M. Freed (Dept. of Earth, Atmospheric, and Planetary Sciences, Purdue University, IN)

Introduction

The fundamental geological structure, geodynamics, and rheology of the Tibetan Plateau have been debated for decades. Two end-member models have been proposed: (1) the deformation of Tibet is broadly distributed and associated with ductile flow in the mantle and middle or lower crust, (2) the Tibetan Plateau formed during interactions between rigid lithospheric blocks with localized deformation along major faults. The nature and distribution of continental deformation is governed by the varying rheology of rocks and faults in the lithosphere. Insights into lithospheric rheology can be gained from observations of postseismic deformation, which represent the response of the Earth's interior to coseismic stress changes. Here we use up to 2 years of interferometric synthetic aperture radar (InSAR) and GPS measurements to investigate postseismic displacements following the 2008 M_w7.9 Wenchuan earthquake in eastern Tibet and probe the differences in rheological properties across the edge of the Plateau. We find that near-field displacements can be explained by shallow afterslip on the Beichuan Fault (BCF), which is anti-correlated with the coseismic slip distribution. Far-field displacements cannot be explained with a homogeneous rheology, but instead require a viscoelastic lower crust (from 45–60 km depth) beneath Tibet and a relatively strong Sichuan block. The inferred strong contrast in lithospheric rheologies between the Tibetan Plateau and the Sichuan Basin is consistent with models of ductile lower crustal flow that predict maximum topographic gradients across the Plateau margins where viscosity differences are greatest.

Postseismic Deformation

A number of processes contribute to postseismic deformation. Afterslip is the continuous slip of the fault after the mainshock and is often found to occur downdip of the fault rupture zone. We use a dislocation model in a layered Earth structure to investigate the afterslip distribution by inverting the geodetic data. We modify the fault geometry proposed by *Shen et al.* (2009) and extend the fault depth to 65 km depth for afterslip at the downdip extension (Figure 2.13.1a). The afterslip occurs on both shallow and deep parts of the BCF that represent the fit to the near- and far-field displacements.

We use a 3D finite element model (*Huang et al.*, 2014) to construct a regional rheologic model composed of an elastic Tibet upper crust and Sichuan crust, a viscoelastic Tibet lower crust, and a viscoelastic upper mantle. We use the bi-viscous Burger's rheology to represent the transient and steady state periods of the postseismic deformation. The Burger's rheology is composed of a Maxwell fluid connected in series with a Kelvin solid to represent the steady state and transient viscosities. The best-fitting model involves a low-viscosity lower crust in Tibet between 45 and 60 km in depth.

Constraining Tibet's Lithospheric Rheology

A Maxwell fluid with a constant viscosity fails to explain the postseismic displacement rate changes, and shows the need for a model in which the effective viscosity increases with time. The change of effective viscosity implies either transient rheology or stress-dependent power-law rheology or both. In this study, we try to distinguish the main mechanism that contributes to the postseismic displacements and the contrasting rheology between Tibet and Sichuan, and thus adopt a simple bi-viscous Burgers rheology. As the viscoelastic relaxation model can explain most of the early postseismic transients in the middle field, we can rule out afterslip as being the major cause of the initial rapid displacements. The best-fitting model predicts a transient viscosity (ηK) of 1017.9 Pa s and a steady-state viscosity (ηM) of 1018 Pa s, whereas the Sichuan Basin block has a high-viscosity upper mantle (> 1020 Pa s) underlying an elastic 35 km-thick crust

Models of Tibetan lower crustal channel flow predict that the Plateau margins are steepest where the viscosity of the surrounding blocks are highest, and thus impede and divert the flow (*Clark et al.*, 2005). These models predict the strongest viscosity contrasts with the Sichuan and Tarim Basin blocks (η = 1016–18 Pa s in a 15–20 km thick lower crustal layer versus ~1020–21 Pa s in adjacent crust), where topographic gradients are greatest. Our preferred viscosity structure deduced from the postseismic deformation transients across the Longmen Shan is consistent with such contrasting lithospheric rheology and deformation between eastern Tibet and the Sichuan Basin.

Acknowledgements

We thank D. Dreger, Z. Shen, I. Ryder, and F. Pollitz for discussions and constructive suggestions. This work is support by the National Science Foundation grant (EAR-1014880).

References

Clark, K. M., Bush, J. W. M., and Royden, L. H. Dynamic topography produced by lower crustal flow against rheological strength heterogeneities bordering the Tibetan Plateau. *Geophys. J. Int.*, 162, 575-590, 2005.

Huang, M.-H, Bürgmann, R., and Freed, A. M. Probing the lithospheric rheology across the eastern margin of the Tibetan Plateau. *Earth Planet Sci. Lett.*, 396, 88-96, 2014.

Shen, Z.K., J. Sun, P. Zhang, Y. Wan, M. Wang, R. Bürgmann, Y. Zeng, W. Gan, H. Hiao, and Q. Wang, Slip maxima at fault junctions and rupturing of bariers during the 2008 Wenchuan earthquake, *Nat. Geosci.*, 2, 718-724, 2009.

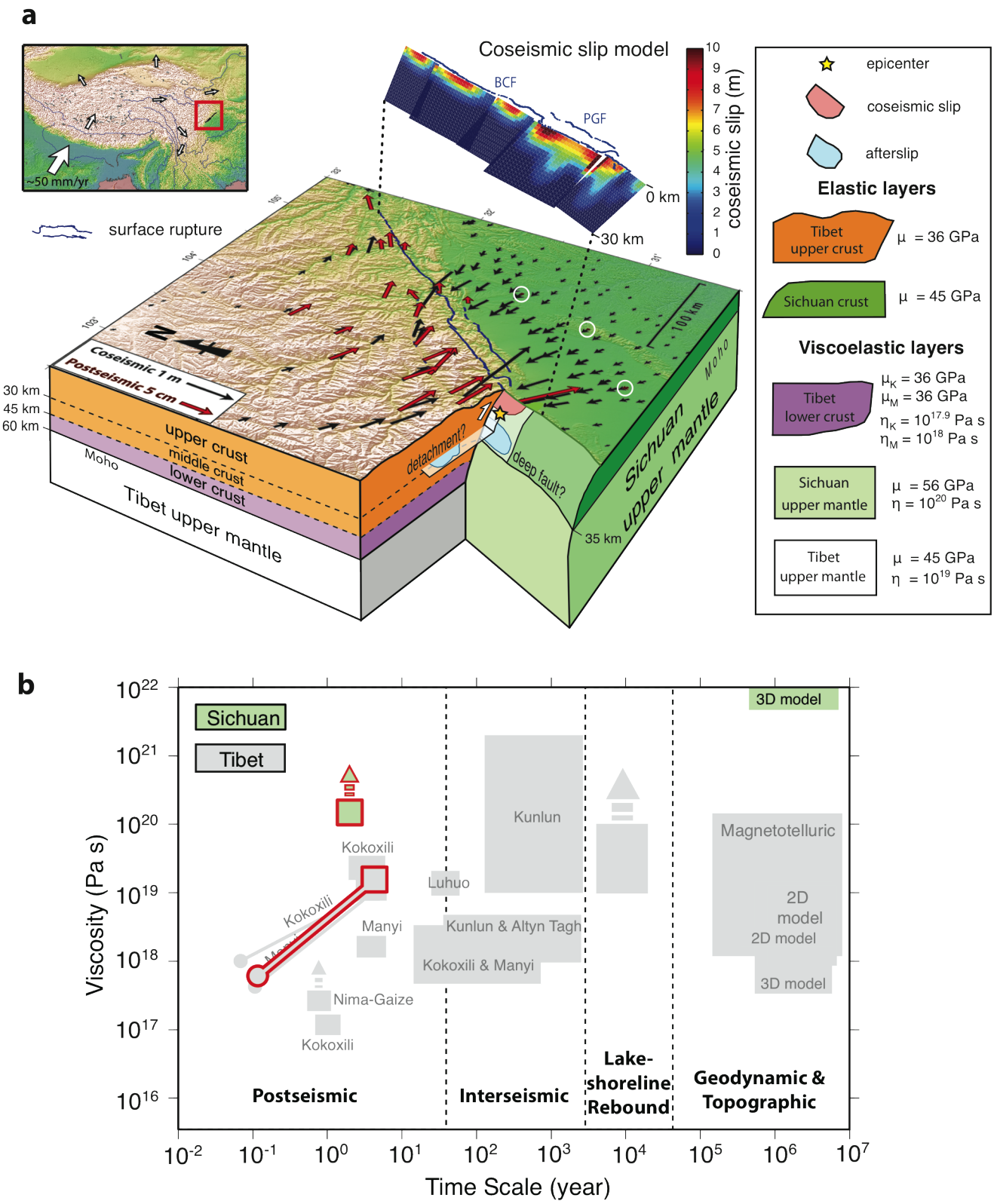

Figure 2.13.1: (a) Three-dimensional representation of eastern Tibet. The upper left map shows the Tibetan Plateau. The black and red arrows in the 3D block diagram are the co- and estimated first year postseismic GPS measurements. The detachment and deep faults are based on *Shen et al.* (2009). The coseismic slip is based on *Huang et al.* (2014). (b) Viscosity estimates of Tibet's lower crust for different time scales. The rectangles represent the range of viscosity of the lower crust estimated using constraints for different time scales. The circles represent the initial effective viscosity of a Burgers-type rheology. The arrows above the rectangles indicate that the estimated viscosity represents a lower bound. The estimated value for the Sichuan block (green square) is for the mantle below 35 km depth.

14 Post 1989 M_w 6.9 Loma Prieta Earthquake Viscous Relaxation Revealed from GPS and InSAR Data

Mong-Han Huang, Roland Bürgmann, Ingrid Johanson, Fred Pollitz (U.S. Geological Survey)

Introduction

The 1989 M_w 6.9 Loma Prieta earthquake provided the first opportunity to probe the crustal and upper mantle rheology in the San Francisco Bay Area since the 1906 M_w 7.9 San Francisco earthquake. Here we use geodetic observations including GPS and InSAR to characterize the 1989 M_w 6.9 Loma Prieta earthquake postseismic displacement from 1989.8 to 2013. Pre-earthquake deformation rates are constrained by nearly 20 years of USGS trilateration measurements and removed from the postseismic measurements prior to the analysis. We observe 1–4 mm/yr GPS horizontal displacement toward the Loma Prieta epicenter, and ~2 mm/yr land subsidence in Almaden, Ca between 1992 and 2002 followed by ~1 mm/yr uplift until 2013. Insights into lithospheric rheology can be gained from observations of postseismic deformation, which represent the response of the earth's interior to coseismic stress changes. We model the viscoelastic relaxation by assuming a viscoelastic 11 km-thick lower crust below a 19 km-thick elastic upper crust, underlain by a viscoelastic upper mantle. The best fitting model is composed of an elastic upper crust, a viscous lower crust ($\eta = 10^{19}$ Pa s), and a bi-viscous upper mantle ($\eta_M = 10^{18}$ Pa s; $\eta_K = 10^{17}$ Pa s), which is consistent with rheologic studies in southern California and models of the post-1906 relaxation. Repeating earthquake activities following the Loma Prieta event seem to correlate with surface displacement, both driven by the viscoelastic relaxation from the upper mantle

The Postseismic Deformation

We mainly use GPS data collected by *Segall et al.* (2000) for the early period (1989.8–1998), and later period (1994–2013) data are obtained from USGS measurements (http://earthquake.usgs.gov/monitoring/gps) (*Savage and Svarc*, 2010). Figure 2.14.1a shows the GPS observed first 5 years, 5–10 years, and 10–15 years postseismic deformation, after removing secular interseismic motion. For the first 5 years, the postseismic displacement (red arrows in Figure 2.14.1a) is generally less than 5 cm near the Loma Prieta earthquake area. The postseismic displacement after the first 5 years is significantly smaller (orange and blue arrows in Figure 2.14.1a). In addition, there is a change of direction in postseismic deformation after the first 5 years. *Segall et al.* (2000) estimated time-dependent afterslip on the fault plane using GPS data collected between 1989.8 and 1998.3. They found that the afterslip dominated the postseismic deformation until 1994, which may explain the change of the direction in postseismic deformation 5 years after the main shock.

Viscoelastic Relaxation

We consider simple elastic coseismic dislocations to calculate the coseismic stress changes and the postseismic relaxation in a layered viscoelastic representation of the earth's lithosphere to evaluate the inferred surface deformation. We assume Earth's upper crust (0–19 km in depth) as elastic, and the lower crust (19–30 km) and upper mantle (below 30 km) are both viscoelastic. We vary the viscosities of the lower crust and upper mantle between 10^{17} and 10^{20} Pa s. The bi-viscous upper mantle with transient (η_K) and steady-state (η_M) viscosities can allow for transient deformation following the Loma Prieta main shock. We calculate the misfit between the GPS time series and the predicted viscoelastic relaxation models to investigate the crustal and upper mantle rheology. Figure 2.14.1b and c show the fitting of predicted viscoelastic relaxation to early and late postseismic periods. We only calculate the misfit between 1994 and 2007 in order to avoid the afterslip driven postseismic deformation between 1989.8 and 1994. The best fitting model (Figure 2.14.1c) predicts a viscosity of the upper mantle that is about 10 times lower than the lower crust.

Our results show evidence that afterslip in the shallower portion of the coseismic fault plane dominates the early (1989.8-1994) Loma Prieta postseismic deformation. The postseismic deformation after 1994 resulted from the viscoelastic relaxation of the upper mantle and lower crust. The predicted upper mantle viscosity is ~10^{18} Pa s (Figure 2.14.1d), which is in good agreement with upper mantle rheology in southern California based on a similar approach.

Acknowledgements

The authors would like to thank D. Dreger, E. Chaussard, R. Turner, and J. Suppe for discussions and constructive suggestions. All of the USGS GPS campaign data are downloaded from the USGS website. This project is supported by the National Science Foundation grant (EAR-0951430) and NASA (NXX-08AG50G).

References

Pollitz, F., Bürgmann, R., and Segall P. Joint estimation of afterslip rate and postseismic relaxation following the 1989 Loma Prieta earthquake. *J. Geophys. Res.*, *103*, 26975-26992, 1998.

Segall, P, Bürgmann, R., and Matthews, M. Time-dependent triggered afterslip following the 1989 Loma Prieta earthquake. *J. Geophys. Res.*, *105*, 5615-5634, 2000.

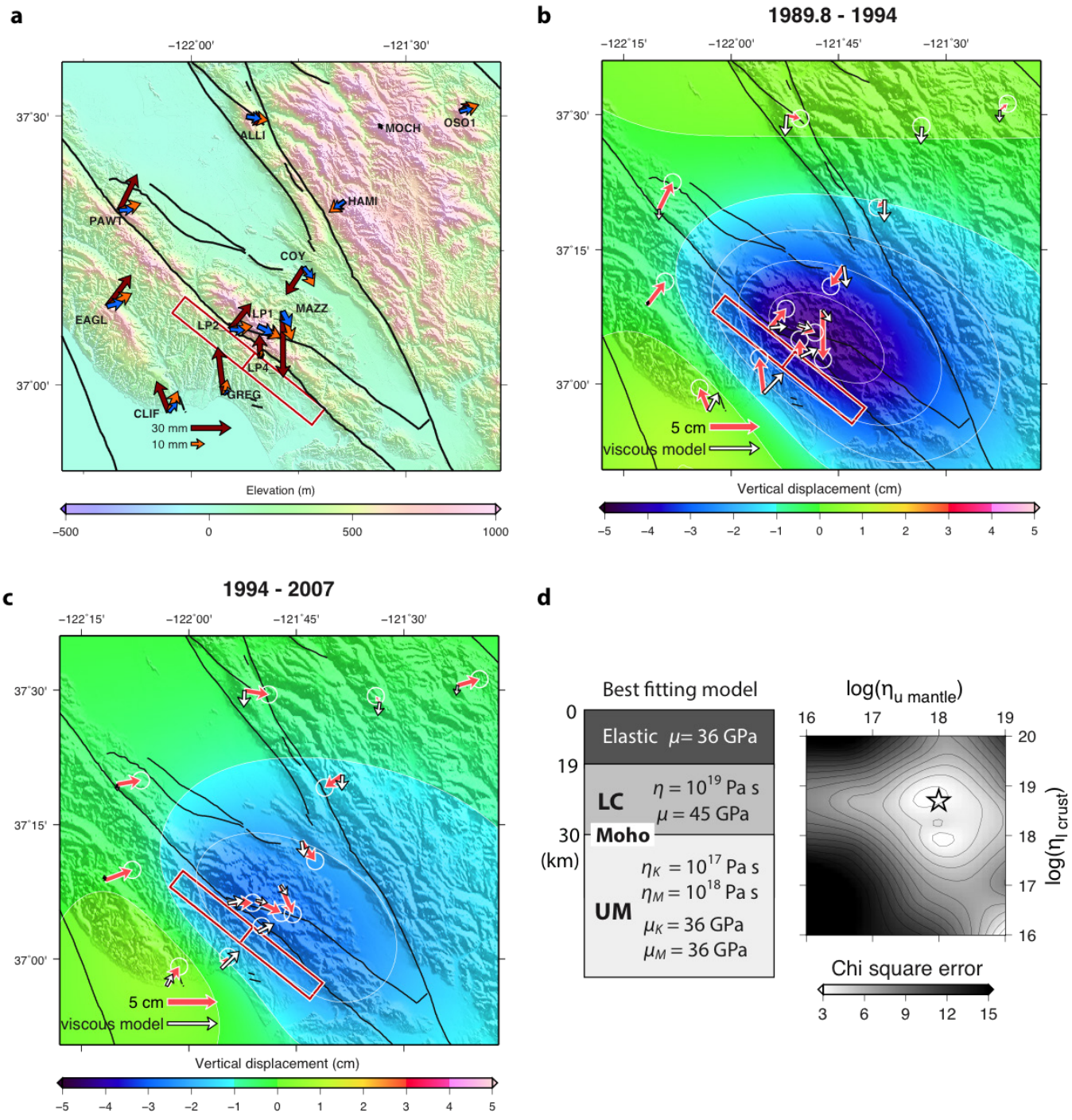

Figure 2.14.1: (a) The arrows show the postseismc deformation of the Loma Prieta earthquake in different periods (red: 1989.8–1994; orange: 1994–1999; blue: 1999–2004), and all of the measurements are relative to the average displacement of stations HAMI, MOCH, and OSO1. The red rectangles are the coseismic fault planes (*Pollitz et al.*, 1998), and the black lines are the fault lines in the Bay Area. Note the change of amplitude and direction of the postseismic displacement in different periods. (b) Predicted viscoelastic relaxation in the first four years (1989.8–1994). The pink arrows are GPS displacement estimated based on the time series downloaded from the USGS website (http://earthquake.usgs.gov/monitoring/gps) and *Segall et al.* (2000), and the white arrows are the viscoelastic model predictions. The background color represents the vertical displacement due to the viscoelastic relaxation. (c) Predicted viscoelastic relaxation between 1994 and 2007. Note the viscoelastic fitting to the later period is better than the early period, hence implying the early period may be dominated by afterslip, which agrees with *Segall et al.* (2000). (d) Left: The model fitting and the rheologic structure based on the best-fitting viscoelastic relaxation model. Right: The chi-square error distribution with different combinations of lower crust and upper mantle viscosities.

15 Upper Mantle Rheology Illuminated from the 2011 Tohoku-Oki Earthquake

Yan Hu, Roland Bürgmann

Introduction

Viscoelastic postseismic deformation of the devastating M_w9.0 Tohoku earthquake has been recorded at more than 1200 continuous Global Positioning System (GPS) and six GPS/Acoustic (GPS/A) stations offshore (Figure 2.15.1). The high quality data in NE Japan provide a unique opportunity for us to better understand the three dimensional (3D) upper mantle rheology and distribution and evolution of the afterslip of the megathrust event.

In this work, we integrate the wealth of geodetic data from NE Japan and modeling experiences developed at other margins to investigate the effects of mantle rheology on postseismic deformation following the 2011 earthquake (*Hu et al.*, 2014).

Finite Element Model

We use a 3D finite element model (FEM) that is able to incorporate the complex slab geometry and tectonic structure in the real Earth. The model shown in Figure 2.15.1 consists of an elastic upper plate, an elastic subducting plate, a viscoelastic continental mantle wedge, and a viscoelastic oceanic upper mantle. Time-dependent, stress-driven afterslip of the fault is simulated by a 2 km-thick weak shear zone attached to the fault. Locked portions of the shear zone are outlined from historic asperities in NE Japan and 5 m coseismic slip contours of the 2011 Earthquake (*Hu et al.*, 2014). Reference rock properties of each tectonic unit are labeled in Figure 2.15.1.

Bi-viscous Burger's rheology (*Bürgmann and Dresen*, 2010) is assumed to represent the viscoelastic behavior of the rheological units. In this work, we assume that the transient Kelvin viscosity is one order of magnitude lower than the steady-state Maxwell viscosity. At shallow depths of the shear zone (≤50 km), the stead-state viscosity is constrained from repeating earthquakes (*Uchida et al.*, 2013) and is 10^{17} Pa s. We vary the viscosity in the deep shear zone (10^{16}–10^{20} Pa s), mantle wedge (10^{18}–10^{21} Pa s) and oceanic mantle (10^{19}–10^{22} Pa s) and construct hundreds of test models. We then calculate the total misfit for each test model for time windows of 6 months, 1 year, 1.5 years and 2 years. The minimal misfit is thus the preferred finite element model of NE Japan.

Model Results

Out test models indicate that the viscosity of the deep shear zone may be traded-off by the mantle wedge viscosity (Figure 2.15.2c). The range in the viscosities of the deep shear zone, mantle wedge and oceanic mantle are 10^{17}–5×10^{18} Pa s, 7×10^{18}–5×10^{19} Pa s, and 5×10^{19}–5×10^{20} Pa s (Figure 2.15.2). In the best-fit model, that is, the model of minimal misfit shown in Figure 2, viscosities of the deep shear zone, mantle wedge and oceanic mantle are 10^{18} Pa s, 10^{19} Pa s, and 10^{20} Pa s, respectively. The best-fit model successfully reproduces the first-order pattern of the GPS observations both on land and offshore (Figure 2.15.3). Cumulative afterslip simulated in the weak shear zone is up to ~3.5 meters two years after the earthquake (Figure 2.15.3a). The equivalent moment magnitude of the afterslip is 8.39.

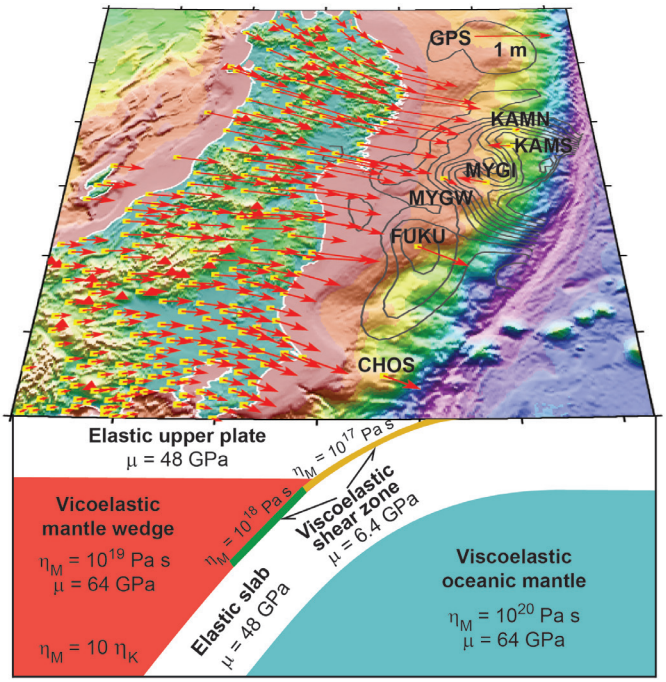

Figure 2.15.1: GPS observations (red arrows) in NE Japan and conceptual representation of the finite element model. μ, η_M, and η_K are shear modulus, steady-state and transient viscosities, respectively. Poisson's ratio is assumed to be 0.25 for the entire domain. Grey contours are coseismic slip distribution (*Iinuma et al.*, 2012).

We also study effects of the following second-order processes on the surface deformation. (1) We study poroelastic rebound in the top 6 km continental and top 16 km oceanic lithosphere (Figure 2.15.4a). (2) The lower crust beneath the arc may be weakened by fluids dehydrated from the subducting slab, and its viscosity is believed to be several orders of magnitude lower than that of the surrounding material (Figure 2.15.4b). (3) We include the elastic Philippine Sea (PHS) slab and a weak shear zone attached to the subducting PHS slab (Figure 2.15.4c). (4) We consider a 200 km-thick weak asthenosphere beneath the oceanic lithosphere (Figure 2.15.4d). Figure 2.15.4 illustrates contributions to the viscoelastic postseismic deformation only due to these second-order processes above.

Acknowledgements

We are thankful for the computing facility provided by Bruce Buffett, and thankful for the publicly available GPS time series of GEONET by GSI. This work was funded by NSF award EAR-1246850 and benefited from support by the Miller Institute for Basic Research in Science.

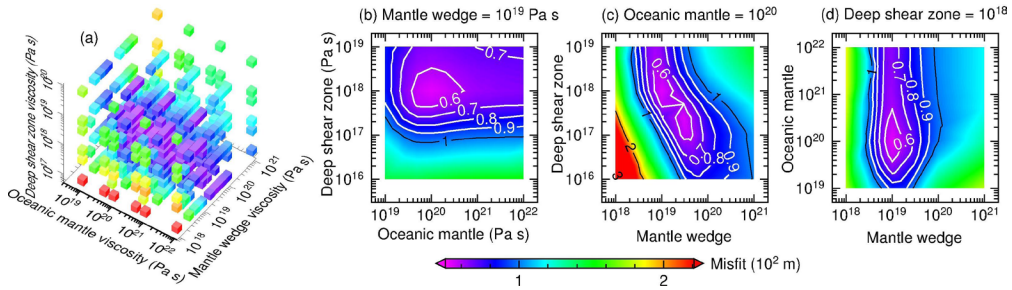

Figure 2.15.2: Systematic tests on the rheology of the deep shear zone, mantle wedge and oceanic mantle. (a) Misfit of the test models in terms of the steady-state viscosity in the rheological units. Each cube represent one test model. (b-d) Trade-off between the viscosities in two rheological units while the viscosity of the third unit is fixed. Color contours are total misfit and are the same as the line contours.

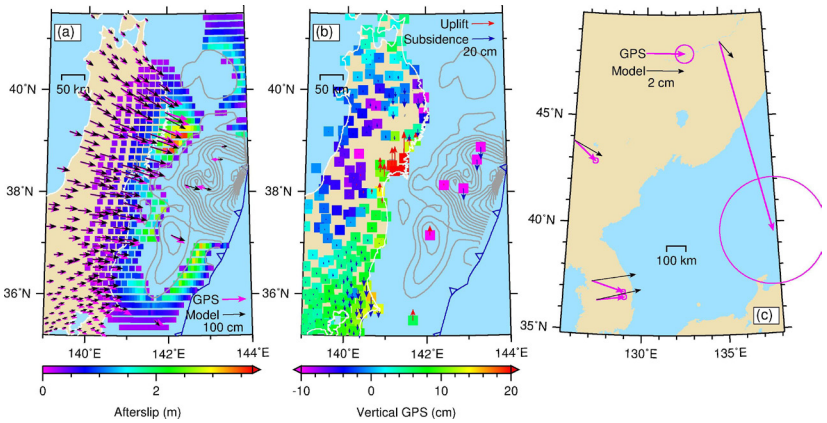

Figure 2.15.3: Comparison of GPS observations with the best-fit model two years after the earthquake. (a) Magenta and black arrows are GPS and model-predicted displacements, respectively. Color contours are afterslip in meters simulated by the weak shear zone. (b) Red and blue arrows are modeled uplift and subsidence, respectively. Color contours are the observed vertical displacements. (c) Similar to (a), very-far-field displacements.

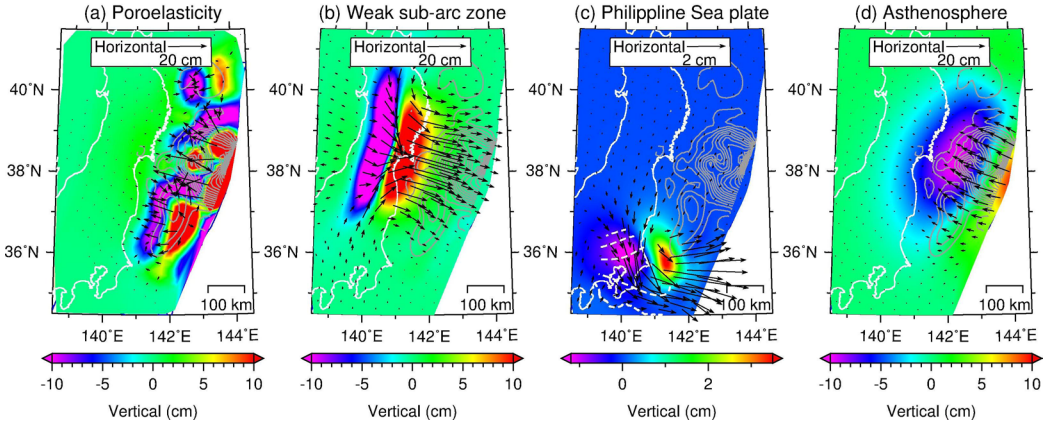

Figure 2.15.4: Surface deformation due to second-order processes, such as poroelastic resbound in the top layer of the lithosphere (a), fluids-weakened zone beneath the arc (b), afterslip in the subducting Philippine Sea slab (c), and weak asthenosphere beneath the oceanic lithosphere (d). Black arrows and color contours are horizontal and vertical displacements two years after the earthquake except in (a), respectively.

References

Bürgmann, R., and G. Dresen, Rheology of the lower crust and upper mantle: Evidence from rock mechanics, geodesy, and field observations, *Annu. Rev. Earth Planet. Sci.*, *36*, 531–567, doi:10.1146/annurev.earth.36.031207.124326, 2008.

Hu, Y., et al., Contributions of poroelastic rebound and a weak volcanic arc to the postseismic deformation of the 2011 Tohoku earthquake, *Earth Planet Science*, under review, 2014.

Iinuma, T., et al., Coseismic slip distribution of the 2011 off the Pacific Coast of Tohoku Earthquake (M9.0) refined by means of seafloor geodetic data, *J. Geophys. Res.*, *117*, B07409, doi:10.1029/2012JB009186, 2012.

Uchida, N., and T. Matsuzawa, Pre- and postseismic slow slip surrounding the 2011 Tohoku-oki earthquake rupture, *Earth Planet. Sci. Lett.*, doi:10.1016/j.epsl.2013.05.021i, 2013.

16 Geodetic Tracking and Characterization of Precipitation-Triggered Slow Moving Landslide Displacements in the Eastern San Francisco Bay Hills, California, USA

Julien Cohen-Waeber, Roland Bürgmann, Nicholas Sitar, Alessandro Ferretti, Chiara Giannico, Marco Bianchi

Introduction

Contemporary geodetic technologies, such as continuous Global Positioning Systems (GPS) and Interferometric Synthetic Aperture Radar (InSAR), allow for remote detection and characterization of ground surface displacements with sub-centimeter precision and accuracy. These technologies are complementary with one another in that GPS allows real time tracking of a finite point while InSAR time series analyses allow widespread surface deformation tracking, though still far from real time.

This project combines GPS and InSAR for the temporal and spatial characterization of landslide deformation. Both methods have shown accelerated surface deformation as an effect of precipitation, though not in relation to recent seismic activity. These observations also suggest intra-slide deformation patterns not previously measurable. Ultimately, both InSAR and GPS studies not only confirm strong correlation and sensitivity to periods of precipitation, but similar kinematic behavior and downslope sliding velocities of around 30 mm/year.

InSAR Time Series Analyses

A review of three independent InSAR time series analyses of landslides in the Berkeley Hills, from separate satellite acquisitions and over different time intervals from 1992–2011 shows remarkable consistency (*Hilley et al.,* 2004*, Quigley et al.,* 2010*, Giannico et al.,* 2011). In each case, surface deformation showed a clear correlation to precipitation, with similar mean downslope velocities (approx. 30 mm/year) and periods of acceleration during each wet season. These studies also suggest observable internal deformation when each slide is divided into groups of coherently moving masses and different sections mobilize separately (*Quigley et al.,* 2010*, Cohen-Waeber et al.,* 2013).

In Figure 2.16.1 (Top), the study of TerraSAR-X data acquisitions from 2009–2011, (*Giannico et al.,* 2011) utilizing the SqueeSARTM algorithm by Tele-Rilevamento Europa (*Ferreti et al.*, 2011), confirms these displacement trends in different parts of the same landslide. In this case, a significantly higher spatial resolution revealed that these slides are in fact moving as bodies of smaller coherent masses. By differencing the average displacements of the top, middle and bottom of the landslides, a pattern of apparent extension then shortening with the progression of precipitation is visible, in what could be called an "accordion effect" (*Cohen-Waeber et al.,* 2013). Figure 2.16.1 (Bottom) illustrates early seasonal acceleration and deceleration of the lower landslide portions in contrast to the upper landslide portions.

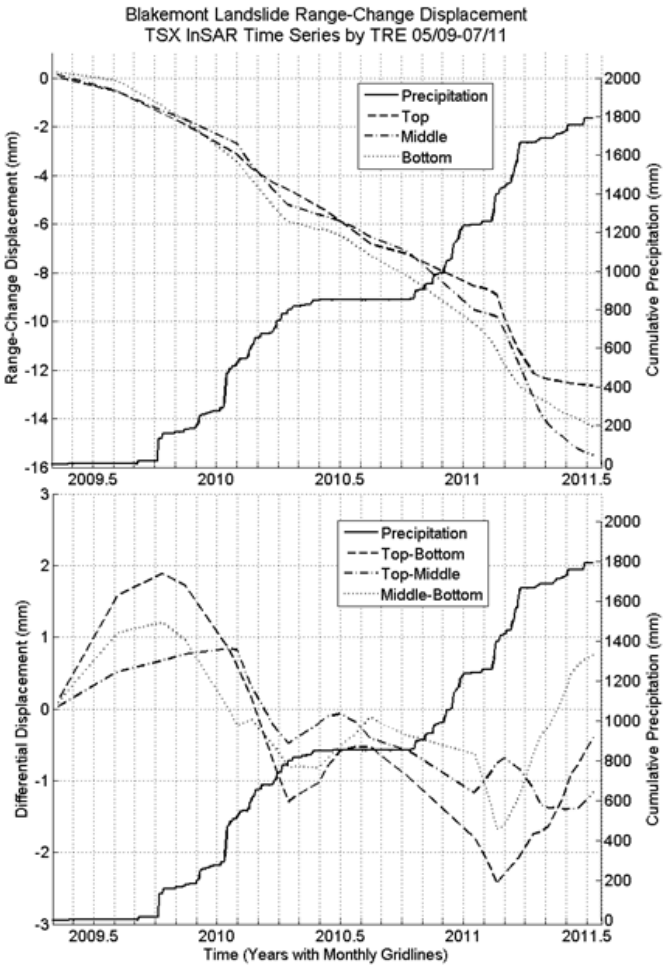

Figure 2.16.1: (TOP) Average downslope range-change displacement and (BOTTOM) differential of average downslope displacements from TRE SqueeSARTM analysis of TerraSAR-X data acquisitions (2009–2011) in areas of Blakemont Landslide, versus cumulative precipitation (right axes).

Continuous GPS Tracking

To fully capture temporal landslide surface displacements, seven continuous GPS stations were installed on Lawrence Berkeley Laboratory (LBL) and Berkeley hills landslides, with data collection rates of 1 Hz for average daily solutions and 20 Hz in case of seismic activity. Each station is anchored on deep seated, reinforced concrete foundations and its measurements differenced from a near-by stable monument to limit non-landslide displacements as tectonic activity, clay activity or atmospheric error.

Through three mild wet seasons (since January 2012), well-defined precipitation-triggered slope movement has been

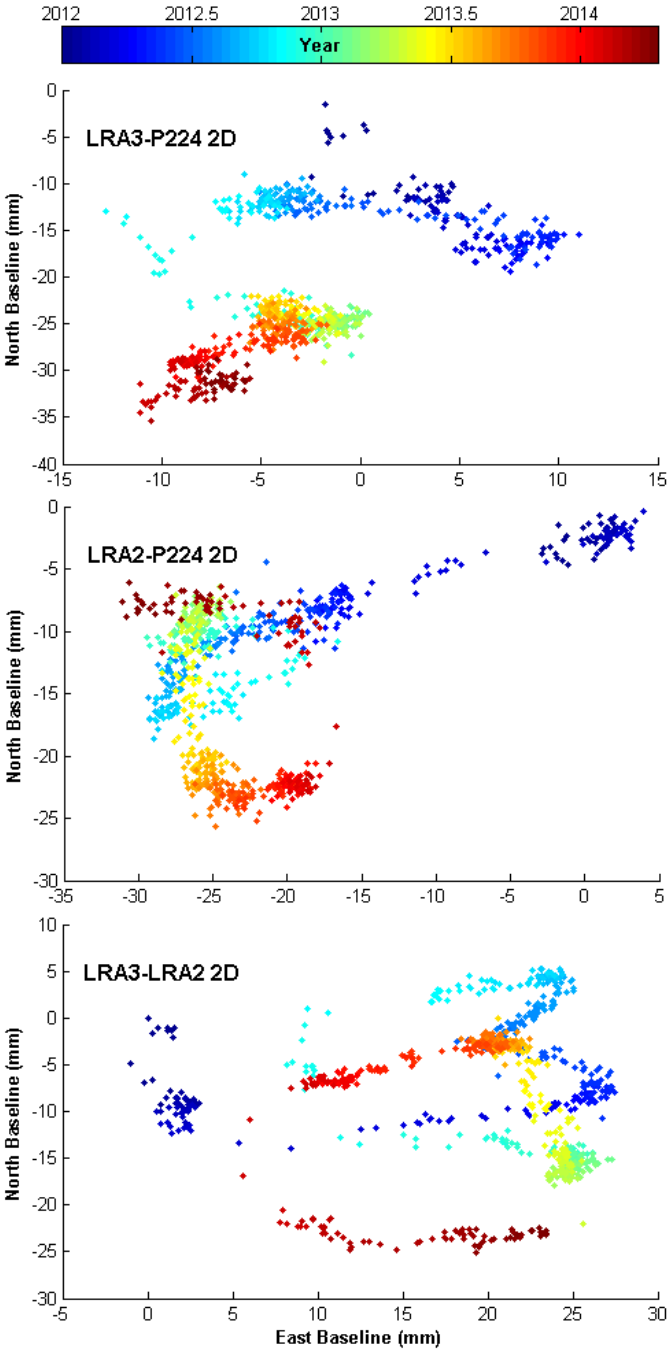

Figure 2.16.2: GPS displacement time series of stations LRA3 (TOP) and LRA2 (MIDDLE) with respect to reference station P224 approximately 5 km to the southeast. Both stations are located on the same landslide and suggest internal differential movement when differenced (BOTTOM).

recorded from daily solutions, as shown through the displacement time series of stations LRA1 and LRA2 (Figure 2.16.2, Top, Middle). While an apparent antenna oscillation can be attributed to seasonal disturbance from surficial clay activity, the stations exhibit overall downslope displacements with similar average velocities as shown through the InSAR analyses. Furthermore, differencing these two stations located on the same landslide captures a sense of internal deformation and suggests the same "accordion effect" (Figure 2.16.2, Bottom).

Preliminary Conclusions

InSAR and GPS have demonstrated here their capability to record and characterize landslide motions that otherwise would not have been observed with such level of detail. While both methods of observation have not yet been compared on one landslide over the same period, they are complementary. Overall, our observations from several studies have yielded similar precipitation triggered down-slope velocities, and comparable internal mechanisms, exhibiting progressive accordion-like downslope failure typical to slow moving flow slides. Ultimately, tracking over longer periods will provide important insight on the triggering mechanisms and internal landslide behaviors described, including yet to be recorded seismically induced landslide motions.

Acknowledgements

We gratefully acknowledge our financial support from the Lawrence Berkeley National Laboratory, Earth Science Division Director's fund.

References

Cohen-Waeber J. et al., GPS Instrumentation and Remote Sensing Study of Slow Moving Landslides in the E. San Francisco Bay Hills, CA, *Proceedings of the 18th Int. Conf. on Soil Mech. and Geotech. Eng.*, Paris, France, 2013.

Ferretti A. et al., A New Algorithm for Processing Interferometric Data-Stacks: SqueeSAR, *IEEE Geoscience and Remote Sensing 49(9)*, 3460-3470, 2011.

Giannico C. and Ferretti A., SqueeSARTM Analysis Area: Berkeley, *Processing Report*, Tele-Rilevamento Europa, Milano, IT, 2011.

Hilley G.E. et al., Dynamics of Slow Moving Landslides From Permanent Scatterer Analysis, *Science 304*, 1952-1955, 2004.

Quigley K. C. et al., Seasonal Acceleration and Structure of Slow Moving Landslides in the Berkeley Hills.,*Proc. of the 3rd Conf. on Earthquake Hazards in the E. San Francisco Bay Area*; edited by Keith Knudsen, CA Geol. Surv. Special Report 219, 169-178, 2010.

17 Temporal Changes in Seismic Velocity with Fluid Injection at The Geysers Geothermal Field, California

Voon Hui Lai, Taka'aki Taira, Douglas Dreger, Mong-Han Huang

Introduction

The effort to increase the production of geothermal power by injection of fluid is often hampered by the concern over the induced seismicity which accompanies the geothermal operations. Changes in seismic wave velocities can act as a proxy to stress changes at a reservoir, providing information about the structural change due to fluid movement or natural tectonic events. Traditional observations from measuring repeating natural and active seismic sources are limited because the seismic sources are episodic. By apply the method of cross-correlating seismic noise between two receivers (*Shapiro and Campillo,* 2004), we are able to retrieve Green's functions which are highly sensitive to velocity changes as the waves are scattered back and forth throughout the medium enhancing the signal of time delays due to a velocity change along their path.

This ambient noise correlation technique has been applied to study temporal variations in crustal properties at several geological settings including the San Andreas Fault at Parkfield, CA and volcanoes (*Brenguier et al.,* 2008a; *Brenguier et al.,* 2008b). In this paper, we use a similar approach to study the temporal seismic variations at the Geysers Geothermal Field, CA, towards understanding the controlling factors of the seismic velocity variations and the mechanics of how stress changes at a geothermal environment.

Location

The Geysers in Northern California is one of the world's largest geothermal fields, with over 350 operating production and injection wells, and is also a very seismically active region.

In early 2012, the Northern California Earthquake Data Center (NCEDC), in collaboration with the Lawrence Berkeley National Laboratory (LBNL), the Berkeley Seismological Laboratory (BSL), and the U.S. Geological Survey (USGS), began to collect continuous data at the Geysers using its BG network consisting of 30 short-period (4.5 Hz) geophones, translating into 435 possible combinations of station pairs with average distance between stations within 5 km (Figure 2.17.1). The dense seismic network at the Geysers provides a unique opportunity to conduct studies on ambient seismic noise monitoring.

Methodology

For the analysis, we use the Rayleigh-dominant time series obtained from the vertical component of the continuous seismic record from March 16, 2012 to December 31, 2013 (656 days). To prepare the data, we remove the instrument response and mean, and apply a whitening procedure to broaden the frequency band of the ambient seismic data in cross-correlation and remove effects from noise sources with specific frequencies. The

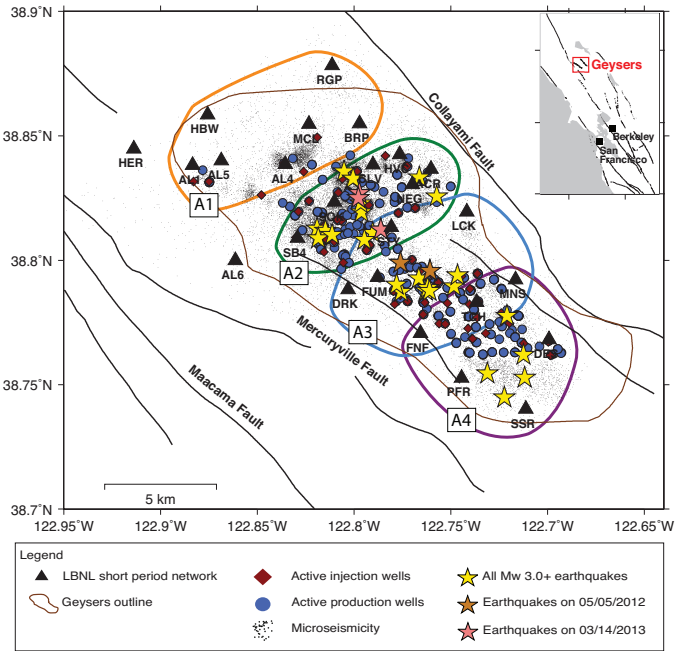

Figure 2.17.1: Map of the Geysers showing locations of the geophones (triangles), active production (diamonds) and injection wells (circles), and *M*3.0+ earthquakes (stars) during the study region. Orange and pink stars mark the location of *M*4.0+ earthquakes and its aftershocks on May 5, 2012 and March 14, 2013. For subsequent analysis, the study region is divided into four smaller areas, each consisting of 6–7 geophones.

frequency range we use for the noise correlation is 0.5–0.9 Hz, which is sensitive to the reservoir depth (less than 3 km).

Before cross-correlation, we divide the records into shorter, overlapping time windows as described in *Seats, Lawrence, and Prieto* (2012). After obtaining the hourly noise correlation functions, we further stack the time series using a time window of 1 day and subsequently 30-days, to be consistent with the temporal resolution of the geothermal operations data, which come in a monthly basis. Lastly, we apply the stretching method described in *Wegler et al.* (2009) to measure the relative seismic velocity shift (dv/v) between each daily Green's function and the reference Green's function.

The expected dv/v value is very small (< 1%) hence stringent data quality control is necessary. First in the preparation stage, data with time gaps due to occasional telemetry dropouts are removed from the analysis. We review the power density spectral plot for each station and reject stations with an unstable noise spectrum around 0.1–0.9 Hz. In the measurement phase, we only accept the dv/v measurement when the daily Green's function and reference Green's function show similarity with a coherence value above 0.8. Finally, we remove Green's functions for pairs of stations in which one of them consistently produces a poor coherence value below 0.5.

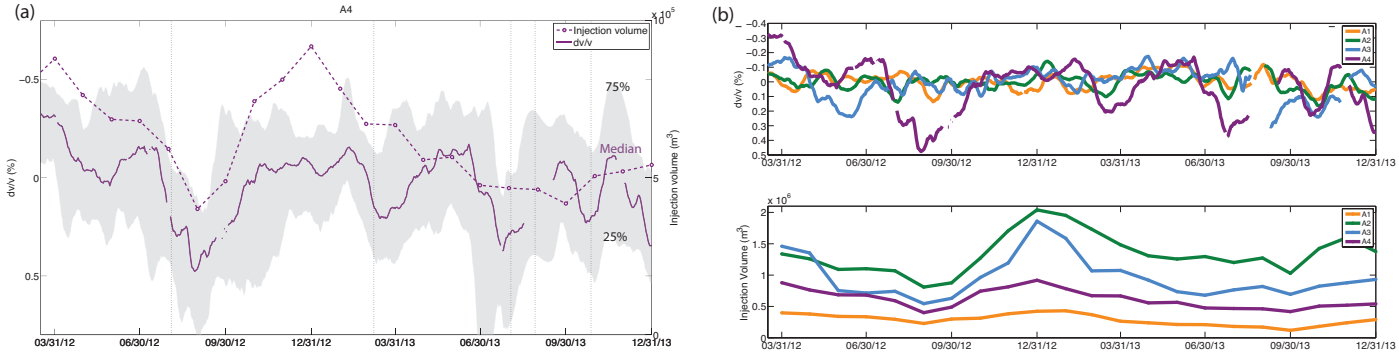

Figure 2.17.2: (a) Graph shows the strong correlation between median dv/v and injection volume over ~21 months at Area 4 (A4). Gray shade shows the interquartile range of the daily dv/v measurement. Dashed lines indicates the onset times of the *M* 3+ eartquakes that occurred at Area 4. Note that the y-axis for dv/v is reversed. (b) This graph shows (top) the dv/v measurement for all areas compared to (bottom) their respective monthly injection volume. The gaps seen in lines are due to data unavailability.

Results

The dv/v value for each area, namely A1, A2, A3 and A4 (see Figure 2.17.1), is estimated by taking the median of all the dv/v values obtained from each station pair within the marked area. Taking the median enhances the signal from a few common sources, which have effects that have spatial extent such as large earthquakes and fluid diffusion. This approach also minimizes the effect from outlier measurements and possible effects from non-homogenous noise sources as the station pairs used span a wide range of azimuths.

Our result shows there is a strong anti-correlation (R = -0.61) between dv/v and fluid injection volume at Area A4 (Figure 2.17.2). The correlation value with injection volume diminishes in order of A4, A3, A2 and A1, from south to north across the reservoir (see Table 2.17.1).

Area	Correlation with Injection Volume	Total Injection volume (m3)	# of M3.0+ Earthquakes
A1	0.1356	6.8E+06	0
A2	-0.1147	3.1E+07	16
A3	-0.3500	2.2E+07	10
A4	-0.6109	1.4E+07	5

Table 1. Table shows overall correlation value of the dv/v measurement with injection volume and the number of M3.0+ earthquakes during the study period for each enclosed area.

Discussion

The strong negative correlation between dv/v and fluid injection volume at Area 4 may be showing the effect of fluid where an increase in injection volume introduces more fluid diffusing throughout the area, which reduces the shear modulus and in turn, the shear velocity.

The varying correlation values across different areas may result from earthquakes, which damage the structure and affect the dv/v measurement. This effect is most pronounced at Area 2 and Area 3 where there were few *M*4.0+ earthquakes during the study period (see Figure 2.17.1).

In addition, Area A4 has a lower injection volume (1.4 x 10^7 m^3) compared to A2 and A3, yet shows the highest correlation between dv/v and injection volume. It seems counterintuitive, as higher injection volume would reduce the shear modulus further. This observation may reflect the heterogeneity of structure across the Geysers, where there are different fluid saturation and permeability for each region, affecting how the injected fluid diffuses throughout the region and changes the shear modulus.

Our result indicates the potential of using ambient noise as independent observational data to retrieve information on temporal seismic velocity changes at geothermal areas. This information can be used to understand the change in the stress field and ultimately, the geomechanical status of the reservoir due to geothermal operations.

Acknowledgements

This work is funded by the National Science Foundation under the award number NSF, EAR-1053211. We also thank Roland Gritto and Avinash Nayak for their insightful discussion. Waveform data, metadata, or data products for this study were accessed through the Northern California Earthquake Data Center (NCEDC), doi:10.7932/NCEDC.

References

Brenguier, F., Campillo, M., Hadziioannou, C., Shapiro, N. M., Nadeau, R. M., & Larose, E., Postseismic relaxation along the San Andreas fault at Parkfield from continuous seismological observations, *Science*, 321(5895), 1478-1481, 2008.

Brenguier, F., Shapiro, N. M., Campillo, M., Ferrazzini, V., Duputel, Z., Coutant, O., & Nercessian, A., Towards forecasting volcanic eruptions using seismic noise, *Nature Geoscience*, 1(2), 126-130, 2008.

Seats, K. J., Lawrence, J. F., & Prieto, G. A., Improved ambient noise correlation functions using Welch's method, *Geophysical Journal International*, 188(2), 513-523, 2012.

Shapiro, N. M., Campillo, M., Stehly, L., & Ritzwoller, M. H., High-resolution surface-wave tomography from ambient seismic noise,*Science*, 307(5715), 1615-1618, 2005.

Wegler, U., Nakahara, H., Sens-Schönfelder, C., Korn, M., & Shiomi, K., Sudden drop of seismic velocity after the 2004 Mw 6.6 mid-Niigata earthquake, Japan, observed with Passive Image Interferometry, *Journal of Geophysical Research: Solid Earth* (1978–2012), 114(B6), 2009.

18 Hydrologic Modulation of Seismicity in Western China 1991–2013

Noah Randolph-Flagg, Jesse Day, Roland Bürgmann, Michael Manga

Introduction

Deep drilling projects and induced seismicity suggest that much of the earth's crust—even deep in continental interiors—is near critically stressed and prone to fail after small (<1 MPa) stress changes (*e.g., Zoback and Harjes,* 1997). It has been suggested that stresses due to hydrologic loading from rain and snow (*e.g., Heki*, 2003), changes in pore fluid pressure (*e.g., Hainzl et al., 2006)*, solid earth tides (*e.g., Knott, 1897)*, and thermally induced stresses due to thermal expansion (*e.g., Hainzl et al., 2013)* may produce stresses sufficient to generate earthquakes. Because many of these stresses are periodic or quasi-periodic, periodicity in seismicity may be widespread and provide insight into how earthquakes nucleate.

Periodic modulation of earthquakes has been observed in the High Himalaya in Nepal (*Bollinger et al*., 2007; *Bettinelli et al*., 2008; *Ader and Avouac*, 2013), the San Andreas fault near Parkfield, CA (*Christiansen et al.*, 2007; *Ben-Zion and Allam*, 2013; *Amos et al.,* 2014), Mt. Hochstaufen in Germany (*Hainzl, 2006; 2013*), mountains in Japan (*Heki*, 2003), and some hydrothermal systems (*Saar and Manga*, 2003; *Christiansen et al.*, 2005; *Braunmiller et al.*, 2013, *Rydelek et al.*, 1988; *Gao et al.*, 2000; *Wilcock*, 2001.) Unlike past studies which focused on seismicity over small areas, we examine apparently similar modulation in seismicity from 1991–2013 throughout an ~100,000 km^2 area including the Tibetan Plateau, Altyn Tagh, Tarim Basin, and Tien Shan. This diversity of tectonic and climatic setting allows us to assess different mechanisms and statistical tests.

Data

We analyze earthquakes between 20° and 60° N and between 105° and 70° E from two catalogs: the Annual Bulletin of Chinese Earthquakes (ABCE) 1991 to 2005 (n=22,513) and the China Earthquake Networks Center Catalog (CENC) 2006 to 2013 (n=5,162.) We also compare background seismicity in the ABCE catalog to repeating earthquakes in the ABCE catalog (n=2,379) as identified by *Schaff and Richards* (2011). Using the Gutenberg-Richter relationship between earthquake occurrence and magnitude we assess catalog completeness for 1991-2005 and 2009–2013 after the 2008 M_w 7.9 Wenchuan earthquake and aftershock sequence. Although both seismic catalogs are incomplete for $M_w < 5$ the catalog completeness does not change seasonally, meaning that the seasonal modulation we observe is not simply due changes in station coverage and, therefore, both catalogs are used in whole.

We use three methods to see if the seasonal modulation is observable in background seismicity or only in foreshocks and aftershocks. First, we compare seismicity to a global catalog of $M_w > 8$ and a local catalog of $M_w > 7$. We also test two declustering methods. The Reasenberg (1985) method identifies the likelihood that earthquakes are related in a spatial-temporal window based on Omori's Law. In contrast the stochastic epidemic-type aftershock sequence (ETAS) declustering method of *Zhuang et al.* (2002) calculates the likelihood that each earthquake is a background event.

Results and Discussion

Seismicity in the Tibetan Plateau and surrounding areas suggests seasonal modulation (Figure 2.18.1). This seasonality is only visible in the shallowest earthquakes (< 5 km) making hydrologic loading, pore fluid pressure changes, and thermal elastic expansion all plausible causes (Figure 2.18.2).

We use three tests to quantify the statistical significance of the seasonal modulation. The most common test, the Schuster test (*Schuster*, 1897), calculates a p-value for one frequency at a time comparing the observed correlation with the likelihood of the correlation appearing wholly by chance. We also use a novel multi-frequential approach (*Dutilleul*, 2001), which finds the frequencies that add together to best fit the time series. This approach could allow us to identify different mechanisms as different frequencies. Finally, we use a simple analysis of variance test (ANOVA), which calculates the statistical difference between the mean seismicity of different seasons. All of these approaches show statistically significant ~12 month periods for both declustered and complete catalogs. The phase of this period varies spatially (Figure 2.18.1b and c) and the amplitude changes significantly year to year.

We show that loading on either side of the Plateau is significant (Figure 2.18.1a) and that seismicity correlates with peak hydrological loading determined from GRACE gravity-change measurements (Figure 2.18.1b and c). If surface loading is the primary mechanism for modulating seismicity, it should suppress thrust and strike-slip faulting and therefore negatively correlate with nearby seismicity. In contrast, if normal faults dominate or if pore fluid pressures rather than loading modulate seismicity, nearby seismicity will positively correlate with GRACE data. In the future we hope to further explore the spatial variation in seasonality and fault type and compare the potential contributions of earth tides, pore fluid pressures, and thermoelastic expansion.

Acknowledgements

The first author has been supported in this research by a Fulbright Research Fellowship in China and an NSF Graduate Research Fellowship. We are grateful to Chris Johnson (BSL) and Prof. Pierre Dutilleul (McGill) for help with statistics.

References

Ader, T., Avouac, J., Detecting periodicities and declustering in earthquake catalogs using the Schuster spectrum, application to Himalayan seismicity, *Earth and Planetary Science Letters*, 908-34, 2013.

Amos, C. B., P. Audet, W. C. Hammond, R. Bürgmann, I. A. Johanson, and G. Blewitt, Contemporary uplift and seismicity in central California driven by groundwater depletion, *Nature*, v. 509, 2014.

Ben-Zion, Y, Allam, A.A. Seasonal Thermoelastic Strain and

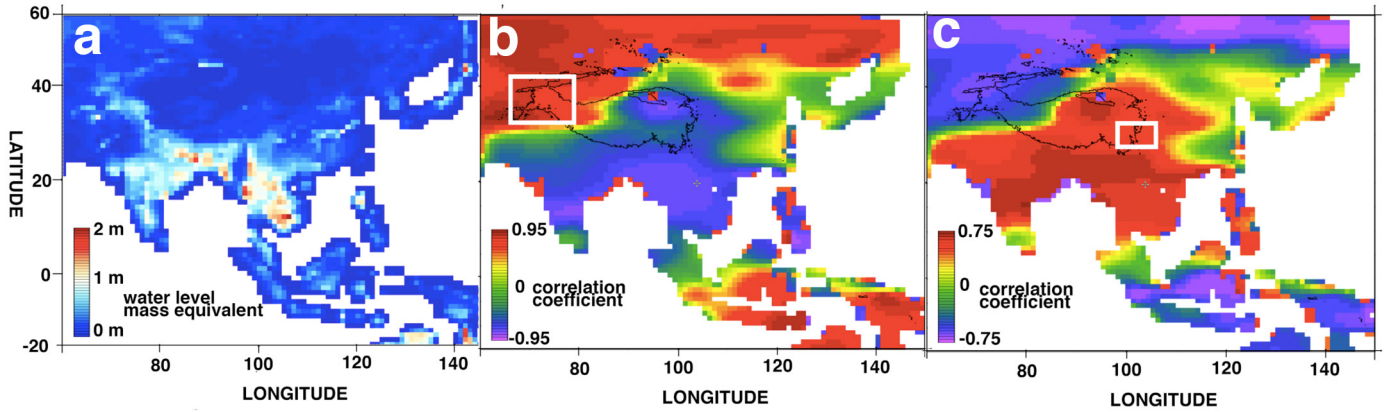

Figure 2.18.1a: Map of average annual change in mass storage in water equivalent thickness from GRACE satellites (http://grace.jpl.nasa.gov/data/). This shows over 1 m of annual loading along the foot of the Himalaya and almost 1 m along the western and northern edge of the Tibetan Plateau; b and c) Map of correlation coefficient comparing the monthly earthquake time series (1991–2005) in the white boxes to monthly GRACE loading data (2002–2013.) b shows the region where peak water storage in the fall corresponds with peak seismicity in the fall while c) shows where peak water storage in the spring corresponds with peak seismicity in the spring.

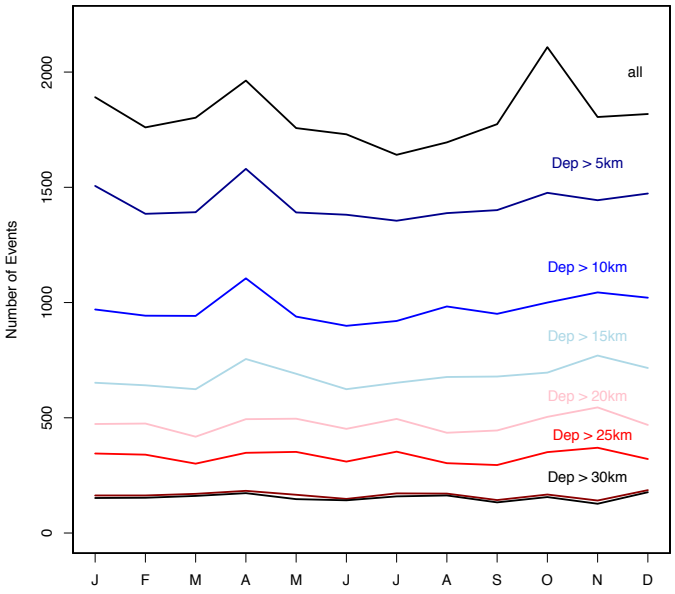

Figure 2.18.2: Cumulative monthly seismicity for different depths. Seaonal modulation is strongest at shallow depths.

Postseismic Effects in Parkfield Borehole Dilatometers, *Earth and Planetary Science Letters.*

Bettinelli, P., Avouac, J.-P., Flouzat, M., Bollinger, L., Ramillien, G., Rajaure, S., Sapkota, S., Seasonal variations of seismicity and geodetic strain in the Himalaya induced by surface hydrology. *Earth and Planetary Science Letters v.* 266, 332, 2008.

Bollinger, L., Perrier, F., Avouac, J.-P., Sapkota, S., Gautam, U., D.R., Tiwari, Seasonal modulation of seismicity in the Himalaya of Nepal. *Geophysical Research Letters v.* 34, 2007.

Braunmiller, J. , Nabelek, J, Trehu, A., A seasonally modulated earthquake swarm near Maupin, Oregon, *Geophys. J. Int., 2014.*

Christiansen, L, Hurwitz, S, Saar, M, Ingebritsen, S, Annual modulation of seismicity along the San Andreas Fault near Parkfield, CA, *Geophysical Research Letters, v.* 34, 2007.

Christiansen, L.B., S. Hurwitz, M.O. Saar, S.E. Ingebritsen, and P.A. Hsieh, Seasonal seismicity at western United States volcanic centers, *Earth Planetary Science Letters,* 240, 307-321, 2005.

Dutilleul, P., Multi-frequential periodogram analysis and the detection of periodic components in time series. *Communications in Statistics-Theory and Methods* v. 30, 2001.

Gao, S.S., Silver, PG, Linde, A.T. Sacks, I.S., Annual modulation of triggered seismicity following the 1992 Landers earthquake in California, *Nature*, 406, 2000.

Hainzl, S., T. Kraft, J. Wassermann, H. Igel, and E. Schmedes, Evidence for rainfall triggered earthquake activity, *GRL.* v 33, 2006.

Hainzl, S., Y. Ben-Zion, C. Cattania, and J. Wassermann, Testing atmospheric and tidal earthquake triggering at Mt. Hochstaufen, Germany, *Journal of Geophysical Res. v.* 118, 2013.

Heki, K., 2003, Snow load and seasonal variation of earthquake occurrence in Japan, *Earth Planet. Sci. Lett.*, 207, 159–164, 2003.

Knott, C., On Lunar Periodicities in Earthquake Frequency. *Proceedings of the Royal Society of London* 60, 457, 1897.

Reasenberg, P., Second-Order Moment of Central California Seismicity, 1969-1982. *Journal. Geophysical Research* v. 90, 1985.

Saar, M.O., and Manga, M., Seismicity induced by seasonal groundwater recharge at Mt. Hood, Oregon, *Earth Plan. Sci. L.,* v 214, 2003.

Schaff, D., and Richards, P., On finding and using repeating seismic events in and near China, *J of Geophysical Research*, v. 116, 2011.

Schuster, A., On Lunar and Solar Periodicities of Earthquakes. *Proceedings of the Royal Society of London* v. 61, 455, 1897.

Zoback, M., Harjes, HP, Injection-induced earthquakes and crustal stress at 9 km depth at the KTB deep drilling site, Germany, *Journal of Geophysical Research*, v. 102, 1997.

19 Comparison of Hydrological Responses to the Wenchuan and Lushan Earthquake

Zheming Shi, Michael Manga, Chi-Yuen Wang

Introduction

Earthquake-induced hydrological changes have been documented for thousands of years. These include: liquefaction, formation of new springs, disappearance of previous active springs, changes in stream and spring discharge, changes in the properties of groundwater such as geochemistry, temperature and changes in the activities of mud volcanoes and geysers (*Manga and Wang*, 2007). Understanding the origin of hydrological response may provide unique insight into the interaction between hydrogeologic and tectonic processes at scales in space and time that may help us understand the long term evolution of groundwater flows. However, instrumental records of these changes have become available only in the last several decades. And many of the previous studies use water level data from wells constructed in unconsolidated sediments (*Roeloffs*, 1998; *Wang*, 2001), only a few studies are based on measurements in hard rocks. Furthermore, identifying the dominant mechanism(s) for observed responses is often difficult because observations are limited to a single earthquake. Comparison of responses to multiple earthquakes with similar focal mechanisms occurring on the same fault zone may thus be useful for testing hypotheses. An ideal case is provided by the occurrence of the large (M_w6.6) Lushan earthquake on April 20, 2013, in Sichuan, China, nearly five years after the devastating M_w7.9 Wenchuan earthquake. The two earthquakes have the same thrust focal mechanism (Figure 2.19.1) and occurred on the same fault (the Longmenshan fault). Both earthquakes caused large hydrological changes. The similarity of focal mechanisms and the abundance of hydrological responses provide an excellent opportunity for testing the proposed mechanisms for hydrological responses. Here, we report the documented co-seismic hydrological changes following the two earthquakes. We then analyze and compare the co-seismic response, which allows us to assess mechanisms responsible for the hydrological changes.

Data and Analysis

Groundwater level and liquefaction data were collected after the two earthquakes in the near- to intermediate-field. In total, 12 groundwater wells were selected, with epicenter distances between 95 to 525 km to the Wenchuan epicenter and 29 to 442 km to the Lushan epicenter (Figure 2.19.1). Water level declined in wells on both sides of the Longmenshan fault (#1, #2, #4) and Huayingshan fault (#6, #7, #8, and #9), which is parallel to the Longmenshan fault. Water levels rose in wells along the strike of the Longmenshan fault, #3, #5, #11 and #12. For the Lushan earthquake, 9 of the 12 wells show co-seismic water level changes. Wells #1, #2 and #12 show no co-seismic changes in water level. Comparing the water level changes for the two earthquakes, only wells #3, #4,#5, #6, and #7 show the same sign of co-seismic changes, while wells #8, #9, and #11 have opposite sign of water level changes. Well #10, which did not respond to the Wenchuan earthquake, showed a rise in water level following the Lushan earthquake. There is no clear relationship with the epicenter distance or the response amplitude, both in the near-field and in the intermediate-field (*Shi et al.*, 2014).

Widespread liquefaction phenomena occurred in the Sichuan basin, covering an area 500 km in length and 200 km in width (Figure 2.19.1). For the Lushan earthquake, on the other hand, liquefaction only occurred near river terraces and alluvial flats along the Shuangshi-Dachuan fault, and the reported liquefaction phenomena occurred within 20 km of the epicenter (reported by Institute of Geology, CEA).The maximum distance from the epicenter of the major liquefaction features for the Wenchuan earthquake is about 210 km, about 10 times greater than the maximum distance of liquefaction for the Lushan earthquake. Using an empirical scaling relation from *Wang* (2007), we find that the minimum seismic energy density to trigger liquefaction in the Wenchuan earthquake is about 1.4 J/m^3, but is 20 times greater (~30 J/m^3) in the Lushan earthquake.

Mechanisms of the Hydrological Responses

Two mechanisms are usually used to explain water level changes in the consolidated rock: (1) Co-seismic static strain; (2) Permeability enhancement. We begin by evaluating the mechanism of co-seismic static strain by comparing the observed water level changes with those predicted by the dislocation model. Only the directions of changes in water level are consistent with the strain field in Wenchuan earthquake, and the predicted magnitudes of co-seismic water level changes are much smaller than was observed in both earthquakes. This indicates that the co-seismic strain model may not be the dominant mechanism causing water level changes both in near- and intermediate-field. However, the mechanism of permeability changes maybe responsible for the water level changes. The mechanism of permeability enhancement predicts a statistically random sign of the water level changes if a sufficiently large number of observations are available (*Wang and Chia*, 2008), consistent with our data. The analyses of tidal response to the Wenchuan earthquake in some near-field wells also show permeability enhancement following the Wenchuan earthquake (*Lai et al.*, 2013). Thus the hypothesis of permeability changes induced by dynamic stress produced by seismic waves may be valid not only in the intermediate-field, but also in the near-field. The maximum distance to liquefaction sites for the Wenchuan earthquake is about 10 times larger than Lushan earthquake, while the minimum seismic energy density required to trigger liquefaction is only 1/20 of that in the latter. This suggests either that the occurrence of liquefaction is more sensitive to low seismic frequencies or that the Wenchuan earthquake changed the sensitivity of unconsolidated materials, and properties had not completely recovered during the five year interval between the two earthquakes.

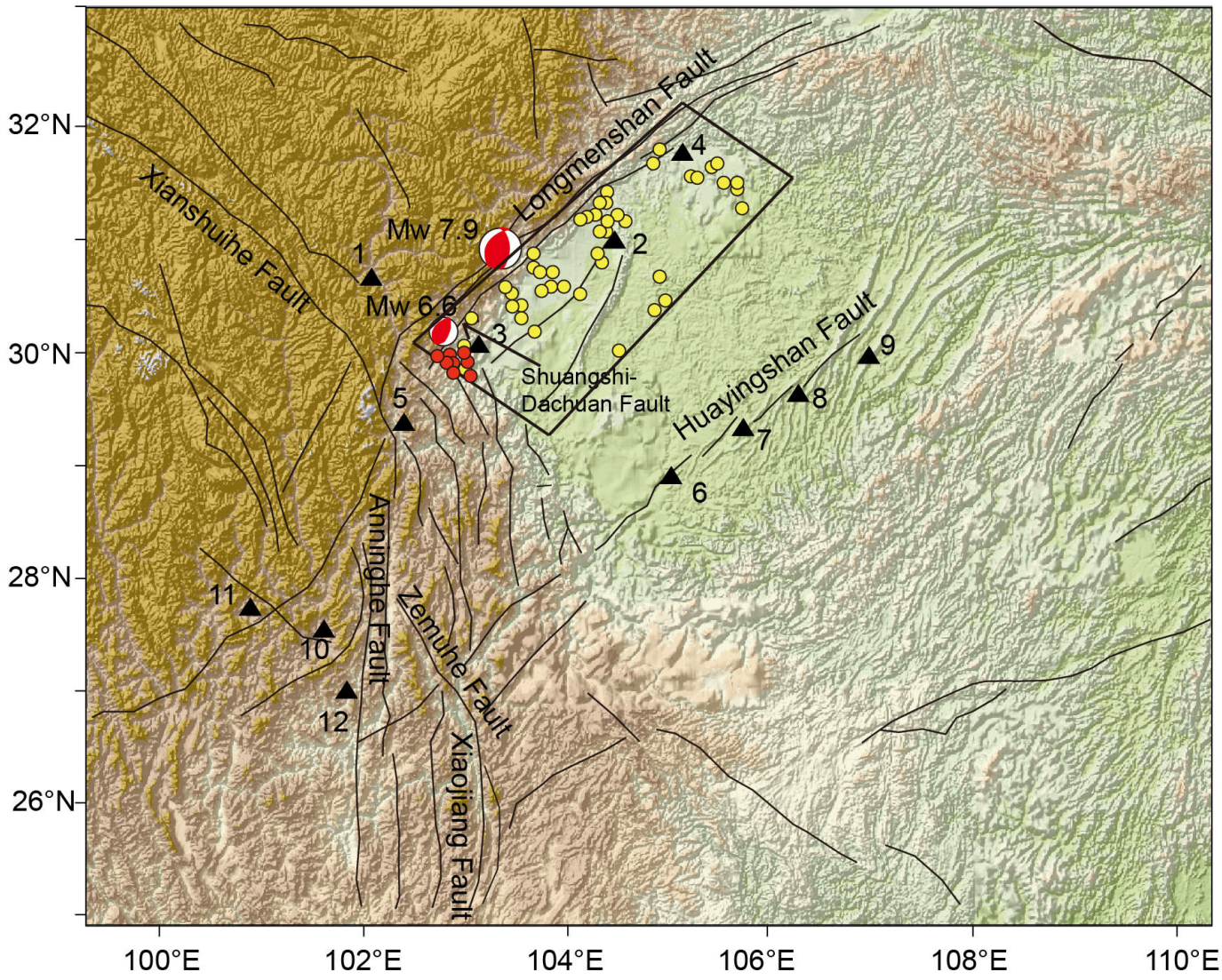

Figure 2.19.1: Geological setting, locations of groundwater monitoring wells (blue triangles) and epicenters of the Wenchuan (M_w 7.9) and the Lushan (M_w 6.6) earthquakes. Beach balls show the low hemisphere projection of the focal mechanism. The red lines represent faults. The yellow and red circles express the liquefaction phenomena that occurred following the Wenchuan and Lushan earthquake, respectively.

Acknowledgements

This research is supported by the US National Science Foundation. Zheming thanks the financial support from the China Scholarship Council.

References

Manga, M., Wang, C-Y., Earthquake hydrology In: Treatise on geophysics (ed. G S). Amsterdam, *Elsevier*, *4*, 293-320, 2007.

Lai, G. J., Ge, H. K., Xue, L., Brodsky, E. E., Huang, F. Q., Wang, W. L., Tidal response variation and recovery following the Wenchuan earthquake from water level data of multiple wells in the near field. *Tectonophysics*, *619-620*, 115-122, 2014.

Roeloffs, E. A., Persistent water level changes in a well near Parkfield, California, due to local and distant earthquake. *Journal of Geophysical Research*, *103*, 868-889, 1998.

Shi, Z. M., Wang, G. C., Wang, C-Y., Manga, M., Liu, C. L. Comparison of hydrological responses to the Wenchuan and Lushan earthquakes. *Earth and Planetary Science Letters*, *391*, 193-200, 2014.

Wang C-Y.,Coseismic hydrologic response of an alluvial fan to the 1999 Chi-Chi earthquake, Taiwan. *Geology*, *29*,831-834.2001.

Wang C-Y.,Liquefaction beyond the Near Field. *Seismological Research Letters*, *78*,512-517, 2007.

Wang C-Y & Chia Y., Mechanism of water level changes during earthquakes: Near field versus intermediate field. *Geophysical Research Letters*, *35*,L12402, 2008.

20 Establishing the Magnitude Threshold of Dynamically Triggered Earthquakes

Christopher W. Johnson and Roland Bürgmann

Introduction

The relationship between stress perturbations and the advancement or suppression of future earthquakes is an ongoing area of research in active tectonics. Studies of earthquake triggering provide insight into the state of stress on a fault and the conditions prior to and during an earthquake nucleation sequence. Static triggering results from the elastic deformation and stress changes due to slip on a fault during an earthquake. In the near-field, a static stress transfer of ~0.1 MPa has been shown to influence regional earthquake activity by promoting or suppressing earthquakes (*Stein*, 1999). In the far-field; *i.e.*, at distances where static stress changes are negligible, studies of dynamic triggering examine the effects of a stress pulse on critically stressed faults and the subsequent change in seismic activity (*Freed*, 2005). Dynamic triggering refers to changes in earthquake activity due to the transient stress perturbation during the passage of seismic waves. Separating the effects of static vs. dynamic stress changes is necessary to advance the understanding of global earthquake interaction (*Felzer and Brodsky*, 2005; *Richards-Dinger et al.*, 2010; *van der Elst and Brodsky*, 2010) and requires investigating seismicity more than 2–3 rupture lengths from the mainshock.

Beyond the traditional aftershock zone, the largest transient stress perturbation from a remote earthquake occurs during the passage of the surface waves. Surface waves are capable of instantly triggering low magnitude earthquakes (M<5), as well as non-volcanic tremor, and sometimes increasing activity in the subsequent days to weeks after the seismic waves have passed (*Hill et al.*, 1993; *Pankow et al.*, 2004). Rarely observed is the immediate triggering of M>5.0 earthquakes beyond the aftershock zone (*Parsons and Velasco*, 2011), which suggests that larger-magnitude events are not susceptible to transient stress changes (*Parsons et al.*, 2012). Recent observations of large magnitude earthquakes (M>8) promoting M>5.5 aftershocks in the far-field has prompted seismologists to continue the investigation into dynamic stresses and the relationship to earthquake nucleation (*Gomberg and Sherrod*, 2014; *Pollitz et al.*, 2012).

In this study we examine global seismicity of M≥5.5 events in the months following the passage of large-amplitude surface waves in regions beyond the aftershock zone. Our goal is to investigate the triggering potential of M≥7.5 and a possible threshold for triggering M>5.5 events. This study develops a systematic method that examines all M>7.5 events in 35 years using the Global Centroid Moment Tensor catalog (http://www.globalcmt.org/) establishing global earthquake rates following the largest events. The techniques of this study allow us to characterize enhanced or suppressed activity following a stress perturbation and to consider the activity related to different fault mechanisms of either mainshocks or trigger candidates.

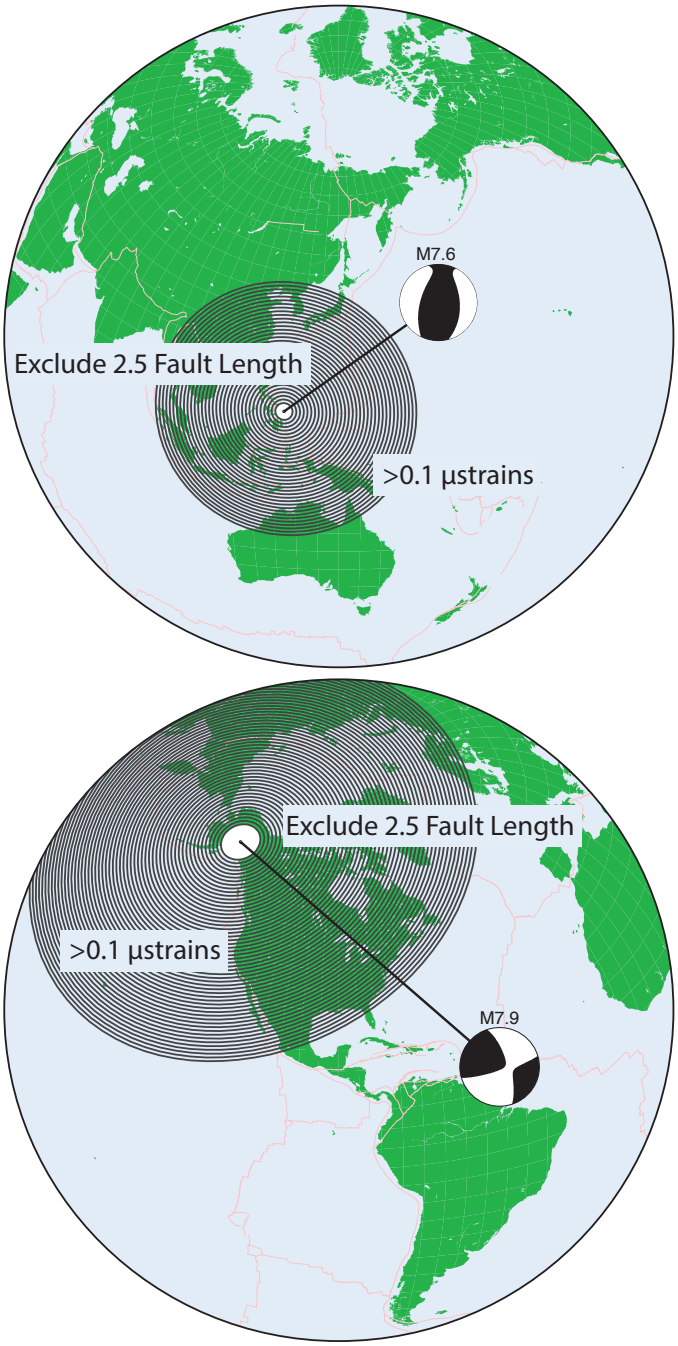

Figure 2.20.1: The region of elevated strain is indicated in the figure for two separate mainshocks. The importance of scaling the magnitudes is shown by the extent of large-amplitude surface waves for two events that cover very different regions of the globe. Shaded regions indicate the area for event selection before and after each mainshock. The exclusion zone is a radial region spanning 2.5 fault lengths from the mainshock and is shown in white. The distal limit is scaled to the magnitude using the estimated seismic wave amplitude relative to the maximum strain threshold. The top figure indicates the region for a M7.6, with an exclusion zone of 230 km and selecting events out to a radial distance of 3600 km. The bottom figure is showing a M7.9, with an exclusion zone of 500 km and selecting all events to a radial distance of 5900km.

Summary

This study incorporates only far-field seismic activity following $M \geq 7.5$ mainshocks using all $M \geq 5.5$ events in the catalog. Our method builds on the results by *Parsons and Velasco* (2011) that indicate no increase in $5 < M < 7$ events following $M \geq 7$ mainshocks beyond 1000 km. We study the triggering potential by separating $M \geq 7.5$ mainshocks by fault mechanism and develop a rate curve using a two-day moving average. The rate curve for each mainshock is then stacked and normalized by the total number of mainshocks. Our method is scaled spatially, using a region of elevated strain that is unique to each mainshock and determined using empirical wave amplitudes (Figure 2.20.1). This allows us to consider only far-field activity occurring in regions that are dynamically strained during the passage of seismic waves. We adopt a threshold of ≥0.1 μstrains that is previously shown to trigger activity in seismically active areas (*Peng et al.*, 2010; *Pollitz et al.*, 2012; *van der Elst and Brodsky*, 2010) to define the region of interest in this study.

The results shown in Figure 2.20.2 represent the stacked rate curves for four $M \geq 8.0$ strike-slip events. This curve excludes the 2012 $M8.6$ east-Indian Ocean event that produced a 10 day increase in global earthquake activity of $M \geq 5.5$ events (*Pollitz et al.*, 2012). We remove the event, which is also the largest strike-slip event on record, in order to establish the triggering potential of other large-magnitude strike-slip earthquakes. A rate increase above the 95% confidence interval is observed following time zero but additional pulses of activity are present at other points in time. Using this approach, we are continuing to examine far-field earthquake activity for different mechanisms and magnitude thresholds. The initial findings indicate that dynamic triggering of $M \geq 5.5$ events is only observed following the very largest; *i.e.*, $M \geq 8.5$, earthquakes on record.

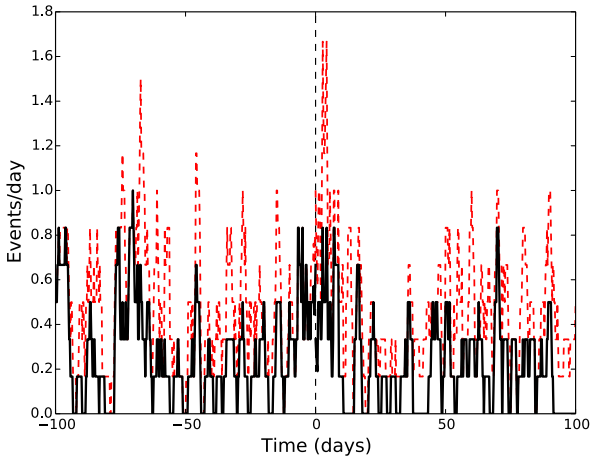

Figure 2.20.2: The rate curve shown is determined using four $M \geq 8.0$ strike-slip earthquakes between 1977–2012 for ±100 days. Time zero is relative to the mainshock origin time and the events per day is normalized by the total number of mainshocks. The red rate curve includes the $M8.6$ 2012 east-Indian Ocean that *Pollitz et al.* (2012) find to excite global activity in the 10 days following the event. The black curve omits the $M8.6$ events and does not indicate a strong pulse of activity after the mainshock. This initial result indicates that triggering of $M \geq 5.5$ events is only observed following the largest evetns on record.

Acknowledgements

This material is based upon work supported by the National Science Foundation Graduate Research Fellowship under Grant No DGE 1106400 for C.W. Johnson.

References

Felzer, K. R., and E. E. Brodsky, Testing the stress shadow hypothesis, *Journal of Geophysical Research*, *110*(B5), 2005.

Freed, A. M., Earthquake Triggering by Static, Dynamic, and Postseismic Stress Transfer, *Annual Review of Earth and Planetary Sciences*, *33*(1), 335-367, 2005.

Gomberg, J., and B. Sherrod, Crustal earthquake triggering by modern great earthquakes on subduction zone thrusts, *Journal of Geophysical Research: Solid Earth*, 2012JB009826, 2014.

Hill, D. P., et al., Seismicity Remotely Triggered by the Magnitude 7.3 Landers, California, Earthquake, *Science*, *260*(5114), 1617-1623, 1993.

Pankow, K. L., W. J. Arabasz, J. C. Pechmann, and S. J. Nava, Triggered Seismicity in Utah from the 3 November 2002 Denali Fault Earthquake, *Bulletin of the Seismological Society of America*, *94*(6B), S332–S347, 2004.

Parsons, T., and A. A. Velasco, Absence of remotely triggered large earthquakes beyond the mainshock region, *Nature Geoscience*, *4*(5), 312-316, 2011.

Parsons, T., J. O. Kaven, A. A. Velasco, and H. Gonzalez-Huizar, Unraveling the apparent magnitude threshold of remote earthquake triggering using full wavefield surface wave simulation, *Geochemistry, Geophysics, Geosystems*, *13*(6), 2012.

Peng, Z., D. P. Hill, D. R. Shelly, and C. Aiken, Remotely triggered microearthquakes and tremor in central California following the 2010Mw8.8 Chile earthquake, *Geophysical Research Letters*, *37*(24), 2010.

Pollitz, F. F., R. S. Stein, V. Sevilgen, and R. Burgmann, The 11 April 2012 east Indian Ocean earthquake triggered large aftershocks worldwide, *Nature*, *490*(7419), 250-253, 2012.

Richards-Dinger, K., R. S. Stein, and S. Toda, Decay of aftershock density with distance does not indicate triggering by dynamic stress, *Nature*, *467*(7315), 583-586, 2010.

Stein, R. S., The role of stress transfer in earthquake occurrence, *Nature*, *402*, 604-609, 1999.

van der Elst, N. J., and E. E. Brodsky, Connecting near-field and far-field earthquake triggering to dynamic strain, *Journal of Geophysical Research*, *115*(B7), 2010.

21 Evidence For a Triggered Foreshock Sequence Prior to the 2012 M7.0 Baja, CA Earthquake

Christopher W. Johnson and Roland Bürgmann

Introduction

The timing of earthquake nucleation processes and the initiation of slip on a fault is an ongoing area of research in active tectonics. Slip occurs on critically stressed faults when the accumulation of elastic stress exceeds the frictional strength. The effect of transient stress perturbations and their correlation with increased seismic activity can be studied through observations of dynamically triggered earthquakes induced by the passage of long-period surface waves (*Brodsky and van der Elst*, 2014). Previous studies conclude that surface waves are capable of instantly triggering low-magnitude earthquakes (M<5), as well as non-volcanic tremor, and sometimes results in increased activity in the subsequent days to weeks after the seismic waves have passed (*Gomberg et al.*, 2004; *Hill et al.*, 1993; *Peng et al.*, 2010). The absence of M>5.0 dynamically triggered earthquakes in these observations appears to suggest that these larger events are not susceptible to transient stress changes (*Parsons et al.*, 2012). This finding would negate a 'normal' Gutenberg-Richter scaling relationship for dynamically triggered earthquakes, if only low magnitude events are triggered by transient stresses.

On April 11, 2012 a complex intraplate seismic sequence occurred in the east Indian Ocean offshore from Sumatra resulting in a M8.6 event that ruptured 500 km on a series of conjugate faults and is the largest strike-slip event recorded with modern instrumentation (*Meng et al.*, 2012). No tsunami or massive destruction occurred but the global rate of large magnitude events (M>5.5) significantly increased for 10-days (*Pollitz et al.*, 2012). The triggered events were located in the regions of highest transient stains during the surface wave train (*Pollitz et al.*, 2012). This study is interested in the local activity preceding and following the M8.6 east-Indian Ocean earthquake near the nucleation site of some of the dynamically triggered M>5.5 earthquakes. This initial study focuses on the M7.0 event that occurred in the Gulf of California, Baja, California, Mexico (BC). The BC earthquake sequence consists of a M6.0 followed nine minutes later by a M7.0 and was preceded by the passage of surface waves from three remote large events. Our goal is to establish a record of activity around the time of the transient stress perturbation.

Data and Methods

The data used for this study are earthquake catalogs and seismic waveforms. The catalog data was obtained from the Servicio Sismológico Nacional de Mexico (SSN). As reported by *Pollitz et al.* (2012), no precursory increase in local activity is observed in the SSN catalog in the months prior to the M7.0 (Figure 2.21.1). To enhance the catalog record we utilize data recorded by a broadband network operated by Centro de Investigación Científica y de Educación Superior de Ensenada (CICESE). We obtained waveform records from April 5–15, 2012 for the analysis. The seismometers chosen are restricted to the stations nearest to the M7.0 event and we focus on the low magnitude events not contained in the catalog. The waveform data was analyzed for unreported earthquakes using a matched filter detection technique during the seven days before the M7.0 (*van der Elst et al.*, 2013). The templates were selected from the aftershocks and by visual inspection of the daily records preceding the M7.0 for unreported events. We observe 94 microseismic events in the period examined (Figure 2.21.2). Due to the limited observations of these small events, we estimate the location using the S-P arrival times and first motions. The magnitude is scale by amplitude and calibrated using aftershocks listed in the SSN catalog.

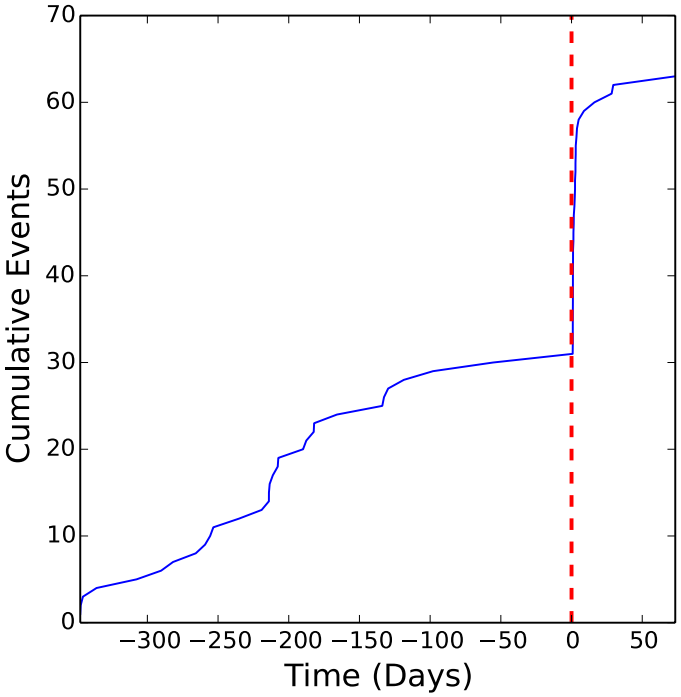

Figure 2.21.1: Gulf of California cumulative seismicity in the surrounding 300 km of the M7.0. Time zero is relative to the arrival of the M8.6 east Indian Ocean surface waves. The region is seismically quite prior to this event.

Summary

This effort did not produce evidence of immediate triggering during the passage of surface waves from the east-Indian Ocean earthquake. The BC analysis does reveal a cascade of microseismic events occurring six hours before the M7.0. The initiation of the foreshock sequence correlates in time with the passage of surface waves from a M6.7 earthquake located 1500 km SE in the Michoacán trench (Figure 2.21.3). The surface waves from the M8.6 east Indian Ocean and the M6.7 Michoácan earthquakes result in a dynamic stress perturbation of ~3 kPa and ~1 kPa, respectively. Stress changes of this order are shown

to excite tremor and microseismic events in geothermal regions and plate boundaries (*Peng et al.*, 2010).

The BC events are located on a transverse fault in a transtensional stress field along the North America—Pacific plate boundary. The initial interpretation is that the *M*6.0 and *M*7.0 earthquakes were dynamically triggered by teleseismic waves. The microseismic events are evident for six hours following the arrival of the Michoacán earthquake surface waves and cascade up to the cataloged foreshocks and the *M*7.0 event. The lack of microseismic activity initiating with the *M*8.6 east-Indian Ocean surface waves does not exclude the importance of this occurrence. The offshore location combined with the distance to the nearest station at ~45 km, with most observations only at the BAHB station, may not fully capture all the seismic activity on the fault. The amplitude and duration of the transient stress may have induced fluid migration or damaged frictional contacts along the fault which may promote eventual failure (*Brodsky*, 2003; *Parsons*, 2005). Additional observation of similar events using will be required to enhance the signal in future studies and resolve the changes in seismic activity prior to the nucleation of a potentially triggered large-magnitude event.

Acknowledgements

We thank R.C. Castro at CICESE for providing the RESBAN network seismic data. The catalog was obtained from SSN. This material is based upon work supported by the National Science Foundation Graduate Research Fellowship under Grant No DGE 1106400 for C.W. Johnson.

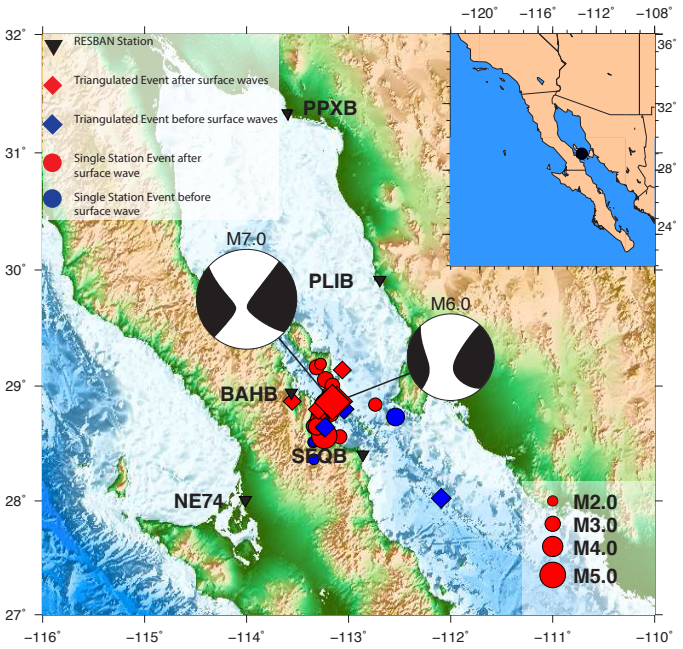

Figure 2.21.2: Map of Gulf of California indicating location of *M*6.0 and *M*7.0 events using http://www.globalcmt.org/ moment tensor solutions. Red and blue markers indicate the location of activity observed at the BAHB station. Additional stations are located >125 km from the area of activity with a low signal to noise ratio that limits observation of small events. Eight events were observed in the five days preceding the east Indian Ocean teleseismic surface waves (see Figure 2.21.3). No activity was observed during the first passage of the teleseismic surface waves.

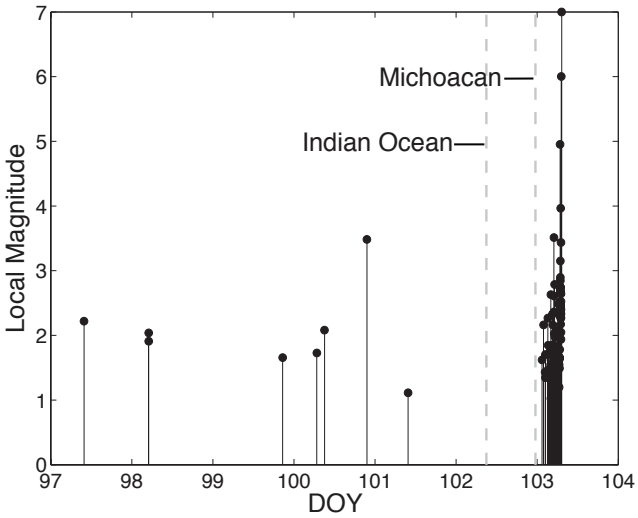

Figure 2.21.3: Local earthquakes with magnitude estimates observed before the *M*7.0 earthquake. The magnitude is calculated using a local magnitude method based on the maximum displacement for each event and calibrated with cataloged aftershocks. Gray lines indicate the surface waves arrival times of the east Indian Ocean (22 hours before *M*7.0) and Michoacán (6 hours before *M*7.0) earthquakes. No increase in activity is observed following the passage of the Indian Ocean surface waves. The increase is observed after the Michoacán, MX event located 1600 km to the southeast

References

Brodsky, E. E., A mechanism for sustained groundwater pressure changes induced by distant earthquakes, *Journal of Geophysical Research*, *108*(B8), 2003.

Brodsky, E. E., and N. J. van der Elst, The Uses of Dynamic Earthquake Triggering, *Annual Review of Earth and Planetary Sciences*, *42*(1), 317-339, 2014.

Gomberg, J., P. Bodin, K. Larson, and H. Dragert, Earthquake nucleation by transient deformations caused by the M=7.9 Denali, Alaska, earthquake, *Nature*, *427*(6975), 621-624, 2004.

Hill, D. P., et al., Seismicity Remotely Triggered by the Magnitude 7.3 Landers, California, Earthquake, *Science*, *260*(5114), 1617-1623, 1993.

Meng, L., J. P. Ampuero, J. Stock, Z. Duputel, Y. Luo, and V. C. Tsai, Earthquake in a maze: compressional rupture branching during the 2012 M(w) 8.6 Sumatra earthquake, *Science*, *337*(6095), 724-726, 2012.

Parsons, T., A hypothesis for delayed dynamic earthquake triggering, *Geophysical Research Letters*, *32*(4), 2005.

Parsons, T., J. O. Kaven, A. A. Velasco, and H. Gonzalez-Huizar, Unraveling the apparent magnitude threshold of remote earthquake triggering using full wavefield surface wave simulation, *Geochemistry, Geophysics, Geosystems*, *13*(6), 2012.

Peng, Z., D. P. Hill, D. R. Shelly, and C. Aiken, Remotely triggered microearthquakes and tremor in central California following the 2010 Mw 8.8 Chile earthquake, *Geophysical Research Letters*, *37*(24), 2010.

Pollitz, F. F., R. S. Stein, V. Sevilgen, and R. Burgmann, The 11 April 2012 east Indian Ocean earthquake triggered large aftershocks worldwide, *Nature*, *490*(7419), 250-253, 2012.

van der Elst, N. J., H. M. Savage, K. M. Keranen, and G. A. Abers, Enhanced remote earthquake triggering at fluid-injection sites in the midwestern United States, *Science*, *341*(6142), 164-167, 2013.

22 Repeating Earthquakes and Inferred Deep Slip on the Calaveras Fault

Robert M. Nadeau and Roland Bürgmann

Introduction

The Calaveras fault in the Eastern San Francisco Bay Area lies near major urban areas in the San Francisco Bay region, including San Jose, Fremont, and the cities of the San Ramon Valley corridor, and it has the potential to cause significant loss of life and property damage. Since 1850, there have been 13 earthquakes of M_L 5 or greater on or near the Calaveras fault. Monitoring of the fault with GPS, creepmeter, gravity, magnetic and seismic data suggests a connection to the Hayward fault with active creep along much of the fault trace. Investigation of the distribution of seismicity along the fault reveals that in regions where $M_L > 5$ earthquakes occur, little seismicity above M_L 1.4 is found and that pre-mainshock and aftershock microseismicity patterns are similar (*Oppenheimer et al.*, 1990). This spatial and temporal variability in creep and seismic behavior of the fault suggest that the situation at depth is significantly more complicated than a single locked/creeping region, leading to a time-dependent hazard for the Bay Area

Geodetic measurements of surface deformation provide information about the nature of elastic strain accumulation near seismogenic faults, their locking depth and slip rates, and variations of those parameters in space and time due to time-dependent processes. However, the inference of these properties on fault zones at depth requires various modeling assumptions that are sometimes not well constrained. A primary objective of this project is to help addresses the seismic potential and natural hazard presented by the Calaveras fault in the Eastern San Francisco Bay Area by providing additional constraints on the spatial and temporal distribution of inferred deep fault slip using repeating earthquakes.

Repeating Quakes on the Calaveras

Owing to their occurrence within the fault zone itself, repeating earthquakes provide more direct information on the geometry and time-variability of creep on faults at depth, and for the more complex situation expected within the deep Calaveras fault zone, the addition of repeating earthquake information should help constrain estimates of deep fault strain accumulation significantly. With this in mind, we compiled a catalog of characteristically repeating earthquakes (CREs) on the Calaveras fault over an ~ 29.5 year period along an ~85 km long fault section with spatio-temporal coverage that includes the hypocenters of the 1984 Morgan Hill M_w6.2 and 2007 Alum Rock M_w5.2 earthquakes (Figure 2.22.1).

Survey of Deep Slip Rate from Repeaters

One interesting feature of the spatial distribution of the repeating sequences is that a fairly large number occur on what *Manaker et al.* (2005) call the Alum Rock seismic trend just SW of the Alum Rock earthquake (ellipse in Figure 2.22.1). A survey view of the repeater inferred slip information for the entire study segment is shown in Figure 2.22.2. Between -10 to 15 km NW, an initially high and decreasing rate of accumulating slip beginning in 1984 corresponds to the post-seismic slip response of the Calaveras to the 1984 Morgan Hill *M*6.2 earthquake (hypocenter at 13 km NW). The Alum Rock trend of repeaters appears as the southwest splay between 20 to 30 km NW in map view. As this study progresses, it will be interesting to see what kind of slip behavior this and other secondary structures have. We will also look at a number of cross-sections of the relocated repeating and non-repeating seismicity stepping along the fault to further illuminate other structural discontinuities and how deep fault slip is partitioned on these structures.

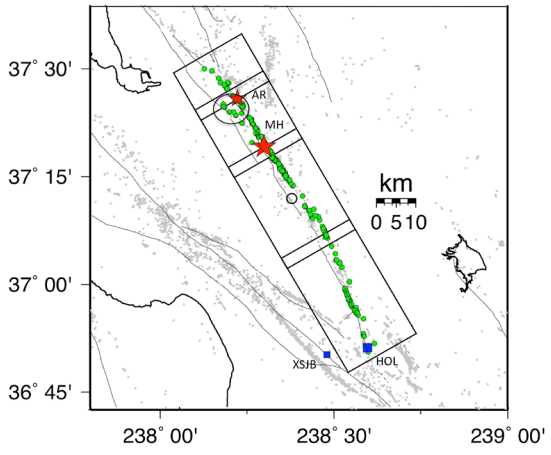

Figure 2.22.1. Locations of 236 repeating earthquake sequences (green/gray circles) identified in the Calaveras fault search area (boxes). 1024 repeated events belonging to these sequences were identifed between January 1, 1984 and May 31, 2013. Locations are based on the Double-Difference Real Time catalog (*Waldhauser and Schaff*, 2008; *Waldhauser*, 2009). Background seismicity > *M*2.0 are also shown (grey points). 2007 Alum Rock M_w5.2 and 1984 Morgan Hill M_w6.2 are stars labeled AR and MH, respectively. Hollister, CA and XSJB creep meter near San Juan Baustista, CA are squares labeled HOL and XSJB, respectively. Location of Alum Rock Seismic trend is indicated by ellipse containing AR location. The small open circle in center of search area corresponds to 0 km NW in Figure 2.22.2.

This information will also be combined with InSAR, GPS and other diverse geodetic datasets to provide improved constraints for a kinematic model of the variability of interseismic creep on the Calaveras fault. The goals of the modeling effort are to better delineate creeping zones on the Calaveras fault and their rates through time, to detect previously unknown transient slip events and to better characterize known events, such as postseismic slip following the 2007 Alum Rock earthquake.

Acknowledgements

Supported by the U.S. Geological Survey through award G13AP00035. Waveform data were provided by the Northern California Seismic System, USGS, Menlo Park by way of the

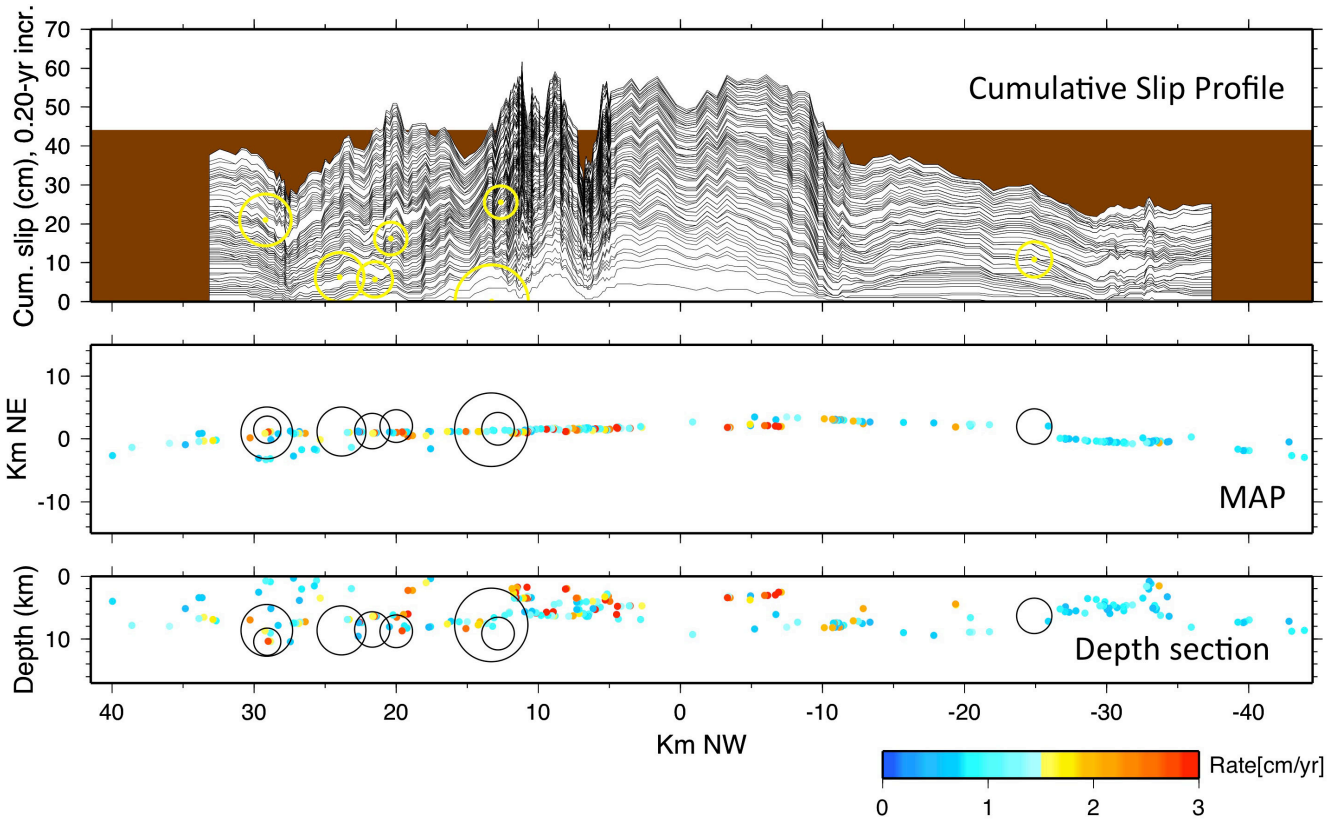

Figure 2.22.2: Top: Along fault, cumulative slip contours taken every 0.2 years since the beginning of 1984, smoothed over 15 sequences and stepped every 1 sequence along strike. The brown color shows the cumulative slip assuming a 1.5 cm/yr rate for the 29.414 year period. The yellow circles are M>4.5 earthquakes plotted at along fault locations and cumulative slip-time. Middle: Along fault locations of REQ sequences colored by average slip rate over the entire study period (scale at bottom). The Large black circles are M>4.5 events corresponding to the yellow circles at top. Bottom: Same as middle but in along fault depth section. The large circles located at 13 km NW in each panel corresponds to the 1984 Morgan Hill M6.2 earthquake hypocenter.

Northern California Earthquake Data Center (NCEDC) at the Berkeley Seismological Laboratory (BSL).

References

Waldhauser, F. and D.P. Schaff, Large-scale relocation of two decades of Northern California seismicity using cross-correlation and double-difference methods, *J. Geophys. Res., 113,* B08311, doi:10.1029/2007JB005479, 2008.

Manaker, D.M., Michael, A.J. and Burgmann, R., Subsurface structure and kinematics of the Calaveras-Hayward fault stepover from three-dimensional V-P and seismicity, San Francisco Bay region, California. *Bull. Seismol. Soc. Am., 95(2),* 446-470, 2005.

Oppenheimer, D.H., Bakun, W.H. and Lindh, A.G. (1990) Slip Partitioning of the Calaveras Fault, California, and Prospects for Future Earthquakes. *J. Geophys. Res, 95(B6),* 8483-8498, 1990.

Waldhauser, F., and D. P. Schaff, Large-scale relocation of two decades of Northern California seismicity using cross-correlation and double-difference methods, *J. Geophys. Res., 113,* B08311, doi:10.1029/2007JB005479, 2008.

Waldhauser, F., Near-real-time double-difference event location using long-term seismic archives, with application to Northern California, *Bull. Seism. Soc. Am., 99,* 2736-2848, doi:10.1785/0120080294, 2009.

23 High-Resolution Imaging of Hayward Fault Microearthquakes

Taka'aki Taira, Douglas S. Dreger, Robert M. Nadeau

Introduction

The connection between the strength of tectonic faults and earthquake rupture is central to studies of the physics of earthquakes. Earthquake stress drop is one of the source parameters for the earthquake rupture process that can be obtained from observed waveforms. The resultant stress drop could reflect the state of stress and the strength of the rocks in which the faulting occurs. To investigate spatial variations of fault strength along the Hayward fault (HF), California, we perform a finite-fault modeling for M 3+ HF earthquakes to obtain the spatial heterogeneity of stress drop within rupture area. We here summarize the slip distributions for the recent two M~3 Orinda earthquakes (Figure 2.23.1). The first Orinda earthquake (OR13-1) with a M_w of 3.0 occurred on October 7, 2013 at a depth of about 7 km. Subsequently, on October 15, the M_w 3.2 Orinda earthquake (OR13-2) occurred ~400 m southeast of the first M_w 3.0 Orinda earthquake. Our finite-fault source modeling reveals that the 2013 M_w 3.2 Orinda earthquake has a complex rupture process.

Hayward Fault Network

We make use of borehole seismograms from the Hayward Fault Network (HFN) to determine the slip models for M 3+ HF earthquakes. The HFN is an array of borehole instrumentation deployed along the HF, with the aim of improving monitoring of spatiotemporal evolution of microseismicity. The HFN was initially deployed with 10 borehole stations in 1995-1996 with a collaborative effort between the Berkeley Seismological Laboratory and U.S. Geological Survey. The 22 borehole stations are currently operational, which provide an unprecedented high-resolution coverage of the earthquake source study for HF earthquakes (Figure 2.23.1).

The stations are typically equipped with three-component

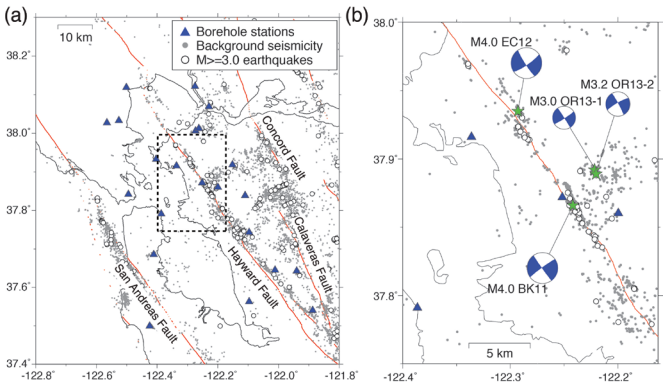

Figure 2.23.1: (a) Map view of HF seismicity in 1990–2013. Blue traiangles are the HFN borehole staions. Gray dots are the locations of background earthquakes from *Waldhaser and Schaff* (2008). Also shown are the locations of M 3+ earhquakes (open ciecles). (b) Enlarged veiw of HF seismicity near Berkeley defined by the dashed-black rectangle shown by Figure 2.23.1a.

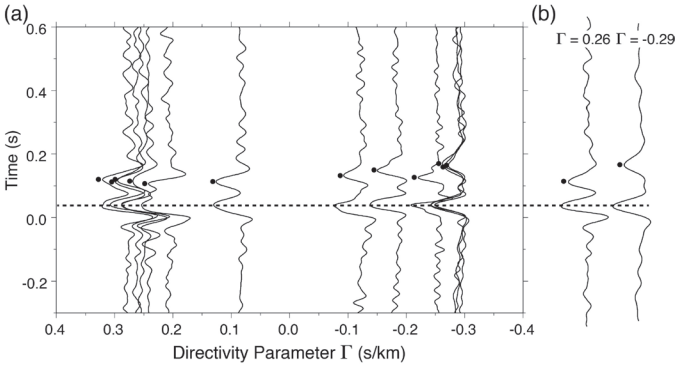

Figure 2.23.2: (a) MRFs for the 2013 M_w 3.2 Orinda earthquake plotted as a function of directivity parameter Γ, assuming rupture azimuth (f_r) at 331°N with phase velocity of 3.4 km/s. A positive value of Γ indicates station azimuth along the rupture direction. Black dots indicate the peaks of the second pulse on indivisual MRFs. (b) Two MRFs from stations at positive and negative Γ illustrate the increase of differential time between the two pulses with Γ.

short-period geophones (the natural frequency is either 2.0 Hz or 4.5 Hz) and accelerometers at a depth of 30–200 m. The seismic data are sampled at up to 500 Hz, although the majority of data used are sampled at 100 Hz. The seismic data has been archived at the Northern California Earthquake Data Center (NCEDC). All waveforms used in this study were extracted from the NCEDC.

Moment Rate Function

We employ an empirical Green's function (eGf) deconvolution approach to extract the moment rate function (MRF) for the two M~3 Orinda earthquakes (*Mori* and *Hartzell*, 1990). We find that the resulting MRFs of the 2013 M_w 3.2 Orinda earthquake display two clear peaks that suggest a radiation complexity in the rupture process. By using waveforms from different eGf events, we confirm that these two peaks on MRFs are not due to a choice of eGf events. To further explore the complexity of the 2013 M_w 3.2 Orinda earthquake, we plot the MRFs with the directivity parameter Γ (e.g., *Ammon et al.*, 2006) based on the equation, $G_i = \cos(f_i - f_r)/c$ where f_i and f_r are the azimuth of the i-th station from the epicenter and the rupture direction, respectively; c is the phase velocity. As shown in Figure 2.23.2, the second pulse appears to shift systematically to later times with an increase of the azimuth (*i.e.*, negative Γ) relative to the direction 331°N (parallel to the strike of HF) with a phase velocity of 3.40 km/s. The linear moveout of the second pulse suggests two distinct subevents involved in the rupture process and the two subevents are aligned along an azimuth of 331°N.

Finite-Fault Inversion

Following *Dreger* (1994), we invert the MRFs to obtain the spatial distribution of fault slip. In the inversion, we define the fault surface as a single 1 km x 1 km plane and divide it into 961

32 x 32 m subfaults. We employ a non-negative least-squares algorithm of *Lawson and Hanson* (1974) and apply a spatial smoothing with a constant smoothing factor.

The slip distribution of the 2013 M_w 3.2 Orinda earthquake shows two distinct subevents (Figure 2.23.3). The first subevent (subevent A) located near the hypocenter of this earthquake (depth of 6.6 km) and the other subevent (subevent B) located about 100 m northwest from the hypocenter at a depth of 6.2 km. The peak slips of the subevents A and B are 4 cm and 2 cm, respectively. With a grid-search approach, we find that a combination of rise time of 0.02 s and rupture velocity of 2.55 km/s provides the maximum variance reduction (96%) for the 2013 M_w 3.2 Orinda earthquake. The static stress drop is determined by using a method introduced by *Ripperger and Mai* (2004). The peak static stress drops for subevents A and B are determined to be 18 MPa and 10 MPa, respectively. Our finite-fault inversion suggests a strong spatial small-scale heterogeneity of the strength of fault within the 2013 M_w 3.2 Orinda earthquake rupture area.

In contrast, the slip distribution of the 2013 M_w 3.0 Orinda earthquake is characterized by failure of a single 0.05 km^2 asperity with a maximum slip of 4 cm (Figure 2.23.4). The high slip area is located immediately down-dip from the hypocenter. The maximum and median stress drops are estimated to be 22 MPa and 8 MPa, respectively. We identify an optimal combination of rise time = 0.015 and rupture velocity = 3.05 km/s for the 2013 M_w 3.0 Orinda earthquake.

Interestingly, our finite-fault inversion shows that the fault rupture also propagated up-dip slip toward the hypocenter of the 2013 M_w 3.2 Orinda earthquake. This result suggests a triggering of the 2013 M_w 3.2 Orinda earthquake by the static stress change imparted by the 2013 M_w 3.0 Orinda earthquake.

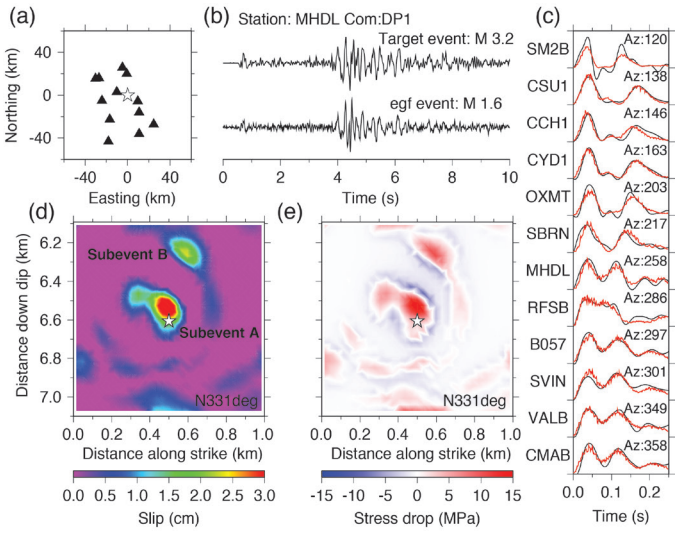

Figure 2.23.3: Finite-fault inversion result for the 2013 M_w 3.2 Orinda earthquake. (a) Map view of the target event (star) and the borehole stations (triangles). (b) Example waveforms for the target and eGf earthquakes. (c) Observed (black lines) and synthetic (red lines) MRFs. (d) Slip and (e) stress drop distributions. The variance reduction obtained for this inversion is 96%.

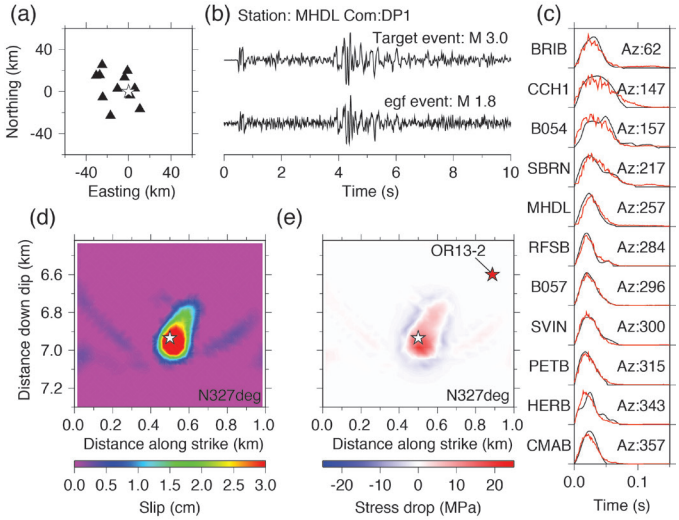

Figure 2.23.4: Same as Figure 2.23.3 except for the 2013 M_w 3.0 Orinda earthquake. Red star in Figure 2.23.4e is the hypocenter of the 2013 M_w 3.2 Orinda earthquake that occurred eight days after the 2013 M_w 3.0 Orinda earthquake. The variance reduction is 96% for this inversion.

Acknowledgements

Waveform data, metadata, and earthquake catalog for this study were accessed through the Northern California Earthquake Data Center. This work is partially supported by the U.S. Geological Survey through award G10AC00093.

References

Ammon, C.J. et al., Rupture process of the 2004 Sumatra-Andaman earthquake, *Science*, 308, doi:10.1126/science.1112260, 2005.

Dreger, D.S., Northridge, California earthquake, *Geophys. Res. Lett.*, 21(24), 2633–2636, doi:10.1029/94GL02661, 1994.

Lawson, C. L., and R. J. Hanson, Solving least squares problems, *Prentice Hall*, Englewood Cliffs, NJ, 1974.

Mori, J., and S. Hartzell, Source inversion of the 1988 Upland, California, earthquake: Determination of a fault plane for a small event, *Bull. Seismol. Soc. Am.*, 80(3), 507–518, 1990.

NCEDC, Northern California Earthquake Data Center, UC Berkeley. Dataset, doi:10.7932/NCEDC, 2014.

Ripperger, J., and P.M. Mai, Fast computation of static stress changes on 2D faults from final slip distributions, *Geophys. Res. Lett.*, 31, L18610, doi:10.1029/2004GL020594, 2004.

Waldhauser, F., and D.P. Schaff, Large-scale relocation of two decades of Northern California seismicity using cross-correlation and double-difference methods, *J. Geophys. Res.*, 113(B8), B08311, doi:10.1029/2007JB005479, 2008.

Research Studies:
Seismic Sources

24 Temporal Variations of Intraslab Earthquake Activity Following the 2011 Tohoku-Oki Earthquake

Brent Delbridge, Roland Bürgmann, Saeko Kita, and Toru Matsuzawa

Introduction

Understanding the mechanics of the subduction of cold oceanic lithosphere is crucial to the theory of plate tectonics and subduction zone seismogenesis. The locked zone between the subducting and overriding plates host the planet's largest earthquakes, including all of the recorded events of moment magnitude 9.0 or larger. These thrust events have been extensively studied, however a significant portion of subduction zone events are intraplate events, which occur within, rather than along the boundary of, the subducting slab. These intraplate earthquakes are frequent and often damaging events that pose a large seismic hazard to large populations along convergent boundaries across the globe. In general, we have a limited understanding of the processes producing these events due to the complexity and heterogeneity of their spatial and temporal distributions.

Most earthquakes deeper than 40 km are located within the subducting plate itself and form two inclined planes of seismicity separated by approximately 35 km, which delineate the plate curvature as it subducts into the surrounding mantle. The presence of these double seismic zones at intermediate depths complicate our understanding of subduction zone seismogenesis and requires an understanding of local sources of stresses. We expect that the large-scale tectonic processes such as slab-pull would create down-dip extensional stresses from the negative buoyancy from the sinking of the cold oceanic lithosphere, however *Hasagawa et al.* (1978) found that beneath Tohoku the earthquake focal mechanisms of the upper plane reflect down-dip compressional stresses, while the lower plane events are associated with down-dip extensional stresses.

In this study we examine the temporal changes of intraplate earthquake activity following the 2011 M_w 9.0 Tohoku-oki earthquake. Due to the large rupture area and displacement of the M_w 9.0 thrust event, we expect that the stress changes within the slab from the coseismic displacement and post-seismic changes in stressing rate due to mantle relaxation and afterslip could be comparable with those from slab pull and bending. Consequently, we examine if the intermediate-depth earthquakes down plate from the locked region reflect the stress change from the slab decoupling and corresponding postseismic processes. Specifically we expect that earthquake activity in the upper plane of the Tohoku region, which is largely down dip compressional, would be promoted, while the earthquake activity in the lower plane, which is largely down-dip extensional would be suppressed, relative to their pre-Tohoku-Oki earthquake levels. Capitalizing on insights into the large-scale and long-term behavior of deformation in subduction zones using models of thin sheets, we quantify the effect of slab bending on subduction zone seismogenesis. We combine laboratory-based rheological models, precise estimates of slab shape from relocated earthquake hypocenters, estimates of the state of stress in the plate from intraplate focal mechanisms, and response to the 2011 Tohoku-Oki earthquake to provide constraints and insights for intraplate subduction zone seismogenesis.

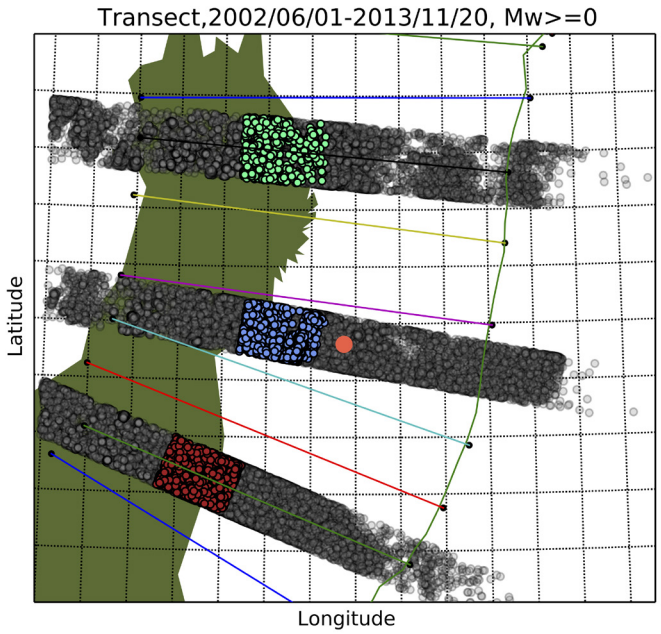

Figure 2.24.1: Map Overview of Study Area. The large orange circle shows the location of the 2011 M_w 9.0 Tohoku-Oki earthquake hypocenter. The green line shows the location of the Japan trench, and the colored circles show the location of events used in this analysis. The grey circles represent the transect hypocenters not included in the temporal analysis.

Tohoku State of Stress

The seminal work of *Isacks and Molnar* (1969) showed that intraplate earthquakes can by used to infer the large-scale stresses within the subducting slab and observed that below 300 km depth events are dominated by down-dip compression, whereas from 70–300 km depth the events are dominated by down-dip extension. These tensional events are thought to reflect the stresses associated with the negative buoyancy of the sinking plate, and the ability of the lithosphere to coherently transmit stresses.

However, the presence of double seismic zones and spatial heterogeneity complicate this simple picture, and require the regional stresses from slab bending and lateral variations to play a large role in the processes producing these events. In addition, observed temporal changes in intraplate earthquake activity associated with the coupling and uncoupling of the subducting lithosphere in the regions of large thrust events suggest that these stresses are comparable to the stresses associated with bending, unbending and slab-pull (*Ammon,* 2008). Further, the depth-dependent nature of the upper plane requires that the equilibrium thermal structure of the slab is also a controlling

factor in subduction zone seismogenesis (*Kita et al.,* 2010).

Previous studies have proposed models that suggest several mechanisms controlling the large-scale stress regimes generated during the subduction process (*Lay et al.,* 1989). The static stress field is associated with the large-scale stresses generated by bending, unbending, thermal equilibrium, and slab pull, with a superimposed dynamic stress field generated by the coupling and uncoupling of the subduction thrust separating the oceanic lithosphere and the overriding continental plate. This model was examined globally by *Lay et al.* (1989), but they were unable to determine with confidence the validity of this model due to insufficient data and the complexity of the intermediate-depth events. However, they were able to conclude qualitatively that intermediate depth events exhibit a strong temporal nature associated with large thrust events, in which the region may undergo a transition from down dip extensional to down-dip compressional stresses.

In order to resolve the contributions of the multiple mechanisms to the state of stress in the subducting slab we will examine the temporal variation of the intermediate earthquake activity in the Tohoku region following the 2011 Tohoku-Oki earthquake. Specifically, we hope to parse out the role of each of the following processes in the generation of the stress regimes inferred from the earthquake focal mechanisms: bending, slab-pull, dynamic coupling and postseismic processes. We utilize earthquake hypocenters from the JMA catalog, which utilizes a dense seismic network completed in 2002 that includes over 1200 stations and records approximately 105 events per year.

We test whether the Tohoku-Oki 9.0 thrust event promoted compressional events and suppressed extensional events at intermediate depths by examining how the relative number of events in the contractional upper plane and extensional lower plane of the Tohoku double seismic zone change before and after the thrust event. It is important to examine the ratio rather than the absolute number of extensional and compressional events due to the overall increase in seismicity following the M_w 9.0 event.

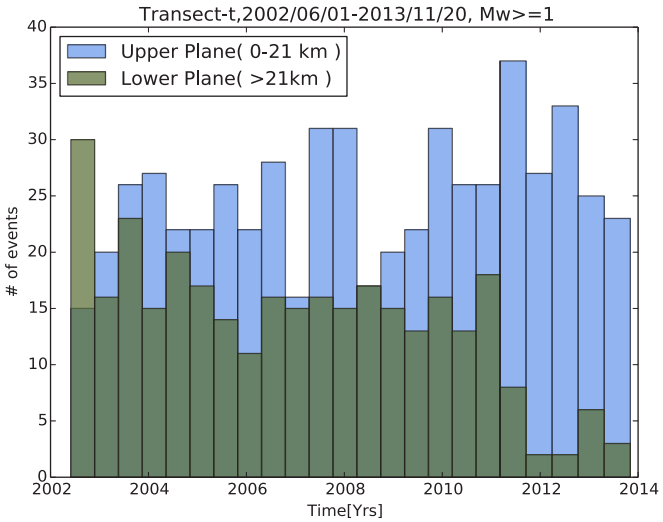

Figure 2.24.2: A histogram showing the earthquake rate in the upper plane (blue) and the lower plane (green) versus time for the Tohoku-Oki study area events show in blue in Figure 2.24.1.

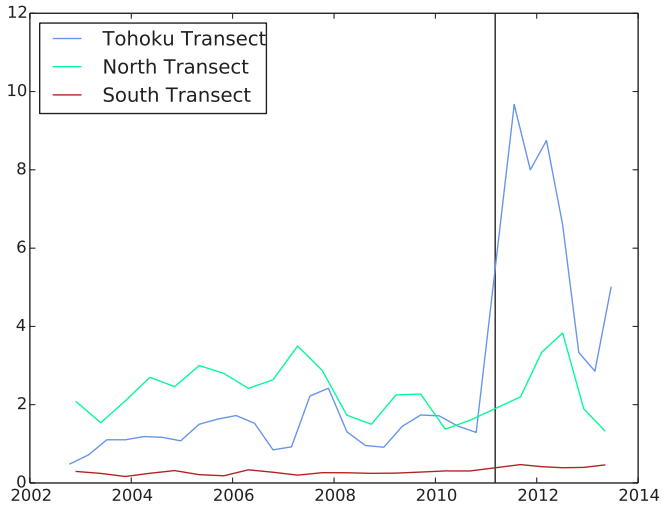

Figure 2.24.3: In order to test for a systematic bias following the Tohoku-Oki Earthquake we plot the activity ratio versus time plots for three regions. The color of the curves corespond to the events shown in Figure 2.24.1.

We find that following the Tohoku-Oki earthquake, the ratio of the number of events in the compressional upper plane to the extensional lower plane increased by a factor of three to five as shown in Figure 2.24.3. The spatial distribution of these events before and after the earthquake show that almost all activity in the extensional lower plane ceases close to the rupture zone, whereas the same region of the compressional upper plane remains seismically active. We conclude that the response of the seismicity at intermediate depths to the compressional stresses from the Tohoku-Oki earthquake are consistent with the conceptual model presented by *Lay et al.* (1989). In future work we hope to quantify and model the stress changes from the Tohoku earthquake and its postseismic relaxation, which will allow us to put absolute constraints on the pre-earthquake stress levels in the subducting slab.

Acknowledgements

This material is based upon work supported by the National Science Foundation Graduate Research Fellowship.

References

Ammon, C. J., Kanamori, H., & Lay, T., A great earthquake doublet and seismic stress transfer cycle in the central Kuril islands. *Nature*, 451(7178), 561-565, 2008.

Hasegawa, A., Umino, N., & Takagi, A., Double-planed structure of the deep seismic zone in the northeastern Japan arc. *Tectonophysics*, 47(1), 43-58, 1978.

Isacks, B., & Molnar, P., Mantle earthquake mechanisms and the sinking of the lithosphere. *Nature*, 223(5211), 1121-1124, 1969.

Kita, S., Okada, T., Hasegawa, A., Nakajima, J., & Matsuzawa, T., Existence of interplane earthquakes and neutral stress boundary between the upper and lower planes of the double seismic zone beneath Tohoku and Hokkaido, northeastern Japan. *Tectonophysics*, 496(1), 68-82, 2010.

Lay, T., Astiz, L., Kanamori, H., & Christensen, D. H., Temporal variation of large intraplate earthquakes in coupled subduction zones. *Physics of the earth and planetary interiors*, 54(3), 258-312, 1989.

25 Moment Tensor Inversion of Seismic Events and Tremor-Tilt Observations Associated with the Sinkhole at Napoleonville Salt Dome, Louisiana

Avinash Nayak and Douglas S. Dreger

Introduction

The formation of a large sinkhole at the Napoleonville salt dome (NSD), Assumption Parish, Louisiana (Figure 2.25.1) in August, 2012 was accompanied by a rich sequence of complex seismic events. Preliminary investigations suggest that the possible collapse of the sidewall of a plugged and abandoned brine cavern, Oxy Geismar 3, might be a potential cause of the sinkhole. It has been hypothesized that the collapse fractured to the surface, creating a disturbed rock zone, which provides a pathway for formation fluids, natural gas and crude oil from deeper strata that are now accumulating in the sinkhole and the surrounding aquifer.

Figure 2.25.1: Google Earth Image (dated March 12, 2013) shows the study region at the western edge of NSD, with 1000 ft and 10,000 ft contours indicated by white lines, locations of the five USGS broadband stations (white triangles), approximate location of the Oxy Geismar 3 cavern (white square), and an average point location of the sinkhole (white balloon).

Moment Tensor Inversion

We investigate source mechanisms of these seismic events, represented by a general point source centroid seismic moment tensor (MT). We use data recorded by a temporary network of broadband seismometers deployed by the U.S. Geological Survey (USGS). Because of uncertainties in hypocenters estimated from travel-times and large number of seismic events, we employ a grid-search approach, GRiD MT (*Kawakatsu*, 1998), which continuously scans the seismic wavefield and performs MT inversions of low frequency displacement waveforms (causal 0.1-0.2 Hz 4-pole Butterworth filter) assuming a discrete 3D grid of point sources. For a given time window of data, the source location and MT solution which give the best Variance Reduction (VR) is inferred to be the true seismic source. Green's functions are computed using frequency-wavenumber integration software FKRPROG using two separate 1D velocity models for the salt dome and the surrounding sediment sequence.

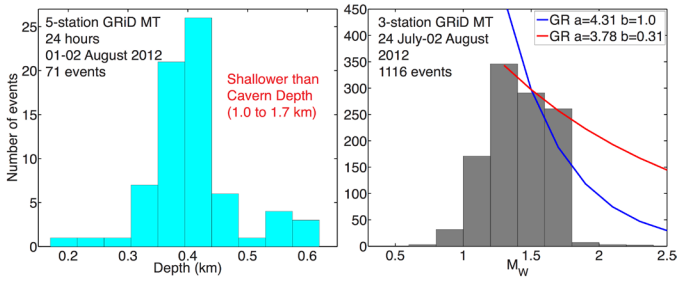

Figure 2.25.2: Source depth and M_W distribution. Red and blue lines are Gutenberg Richter relationships for various 'a' and 'b' values.

Application of GRiD MT to 24 hours of data during August 1–2, 2012 (just before the appearance of the sinkhole) with a 71% VR detection threshold reveals 71 events with magnitudes M_W 0.8 to 1.9. Their locations are well constrained to the western edge of the salt dome, close to the sinkhole, at an approximate depth of ~420 m, which is much shallower than the roof of the cavern at 1.0 km (Figure 2.25.2). The M_W distribution of ~1100 events detected during an extended period of time doesn't follow the Gutenberg Richter relationship and shows distinct absence of larger magnitude events indicating a structural limit on size of the source.

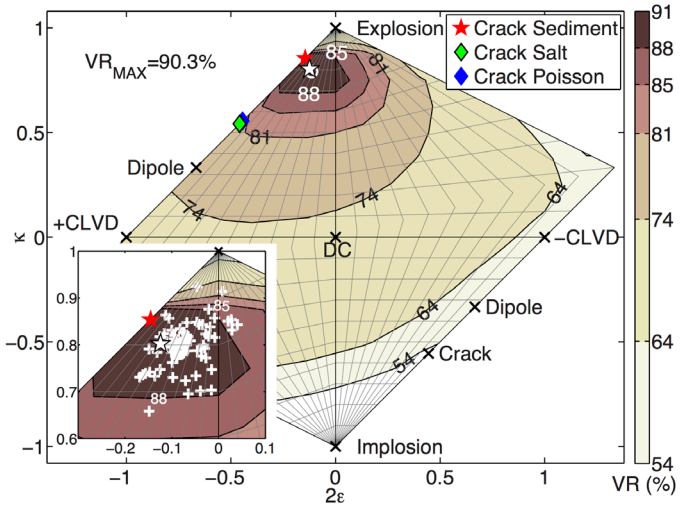

Figure 2.25.3: NSS of event TE1 on the Hudson source-type plot, major theoretical source-types (black crosses), tensile cracks in various media and full MT solution of event TE1 (white star). White circle is the source-type corresponding to the maximum VR recovered by NSS (VR_{MAX}). The inset shows distribution of 71 events of the seismic sequence (white '+' signs) in source-type space.

The MT solutions are comprised of large (66-92%) isotropic volume-increase components, and can be interpreted as a N-NE striking steeply dipping tensile crack in a high Poisson ratio (0.43) medium coupled with a normal-style double couple. For one representative event, TE1, the volume-increase component

is found to be statistically significant using an F-test and stable with respect to: (1) velocity models and stations used, (2) first motion polarities, and (3) uncertainties in GRiD MT location and MT elements. In the network sensitivity solution (NSS) of Figure 2.25.3, MT solutions that produce best fits (>80% VR) are tightly clustered in a region between theoretical explosions and tensile cracks, quite far away from theoretical deviatoric mechanisms and expected closing crack mechanisms, which produce fits only up to 50-75% VR. For further details on MT analysis of this sequence and a complete list of references, readers are referred to Nayak and Dreger (2014).

We believe that the events in this study are caused by high-pressure flow of natural gas or water-gas mixture through voids in the disturbed rock zone or pre-existing zones of weaknesses like fractures or faults at the edge of the salt dome by volumetric expansion or tensile failure mechanisms similar to those observed in geothermal and volcanic environments. This hypothesis is supported by the intense influx of natural gas (primarily methane) into the aquifer over an area of 5 km^2 around the sinkhole from the disturbed rock zone below. As of September 2013, ~16x10^3 Mcf natural gas has been vented or flared out as a remediation measure.

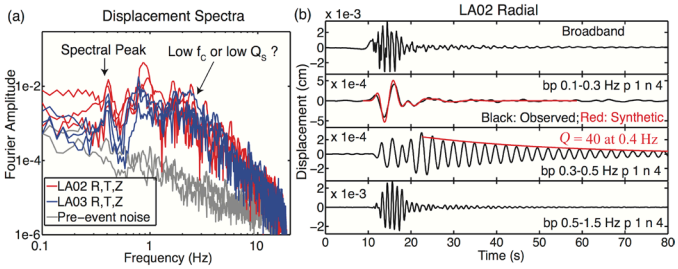

Figure 2.25.4: (a) Spectra at stations LA02 (over sediments) and LA03 (over salt dome); (b) Radial waveforms at LA02 in different frequency bands (see 0.4 Hz oscillatory waveform in third panel).

Tremor-Tilt Observations

We have also observed spectral peaks in data of discrete seismic events and Harmonic Tremor (HT) episodes prior to the appearance of the sinkhole. These seismic signals are usually observed only in volcanic environments and are attributed to oscillatory responses of fluid-filled cavities, gas bubbling and fluid flow through deformable channels. Figure 2.25.4 shows example of three-component spectra of a seismic event with a strong narrowband peak at 0.4 Hz observed at multiple stations. In time domain, it is equivalent to a ~60 s long exponentially decaying sinusoid with a standing wave attenuation factor, Q ~ 40, which is unlikely to be site response due to its long period and duration. The spectra also show a low corner frequency at ~2.0 Hz, which could be due to the slow nature of these events or strong anelastic attenuation in the young sediments.

One of the observed HT episodes is shown in Figure 2.25.5. The fundamental frequency of the HT first increases from ~1.6 Hz to ~2.5 Hz in ~40 s and thereafter stays constant for ~ 80 s. The first overtone frequency and the amplitude envelope follow a similar trend. Low frequency acceleration for the same time period shows a step, which is interpreted to be due to an

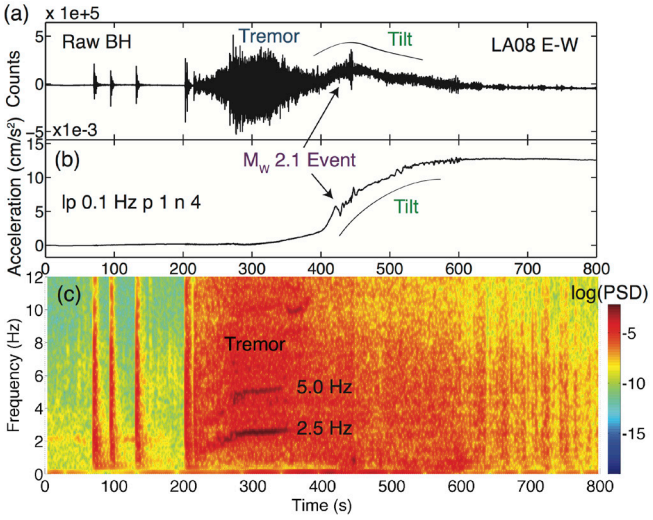

Figure 2.25.5: HT-Tilt episode on August 2, 2012: (a) raw broadband seismogram; (b) low frequency acceleration showing tilt; (c) spectrogram showing HT at 2.5 and 5.0 Hz.

apparent ground tilt of ~ 30.6 μrad. We have found these pseudo-tilt signals to be reliable by examining the horizontal and vertical amplitudes, low frequency SNR and colocated accelerometer waveforms. These observations indicate some common relationship between mechanisms of discrete volumetric events and harmonic tremor, possibly being driven by fluid flow, and surface deformation due to gas escape from the subsurface.

Acknowledgements

We thank William Ellsworth (USGS) for preliminary velocity models, data, mapping resources and helpful discussions. Stephen Horton (CERI, University Of Memphis) is thanked for providing the travel-time catalog of events in this study. We thank Julie Shemeta (MEQ Geo) and Mark Leidig (Weston Geophysical Corp.) for velocity models.

References

Kawakatsu, H., On the realtime monitoring of the long-period seismic wavefield: *Bull. Earthq. Res. Inst.*, 73, 267-274, 1998.

Nayak, A., and Dreger, D.S., Moment tensor inversion of seismic events associated with the sinkhole at Napoleonville Salt Dome, Louisiana: *Bull. Seismol. Soc. Am.*, 104, 4 (*in press*), doi: 10.1785/0120130260, 2014.

26 Preliminary Results of Moment Tensor Analysis at The Geysers Geothermal Field, CA

Sierra Boyd, Voon Hui Lai, and Douglas Dreger

Introduction

The Geysers geothermal field is one of the most seismically active regions in Northern California with shallow microseismicity correlated with geothermal energy operations. More recently there has been an increase in large magnitude, M > 4, events located within the microseismic cloud. Understanding induced seismicity and the physical mechanisms of large magnitude events associated with geothermal energy operations is needed to evaluate seismic hazard associated with reservoir production.

In our ongoing investigation, broadband seismic data from regional networks, inset map Figure 2.26.1, are used to study moment tensors of M > 3 earthquakes throughout the geothermal field. We apply techniques (*Ford et al.,* 2010), to develop a catalog of deviatoric and full moment tensor (FMT) solutions and an assessment of the uncertainty of non-double-couple components of 53 earthquakes at The Geysers from 1992–2014.

Results

Based on the F-test, most of the 53 events may be characterized as deviatoric. However there are 10 events with statistical significance above 80% and 4 above 90%. For these events we have investigated the stability and uncertainty in the long-period full moment tensor inversions using bootstrap, Jackknife and NSS techniques (*Ford et al*., 2010). In cases where events are found to have large positive isotropic components, we find from these sensitivity studies that the results are robust. We have also found cases in which small isotropic components are likely, although based on the waveform data alone and the F-test, they are not resolved. Through the combination of long-period waveforms and first-motions (FM), we are able to obtain stronger constraints on the moment tensor solutions. We are finding that those that best satisfy both data sets are comprised of a large strike-slip double-couple component with a relatively small 10% to 38% volume increase. The results of the constrained full moment tensor (CFMT) analysis of selected events are summarized in Table 2.26.1.

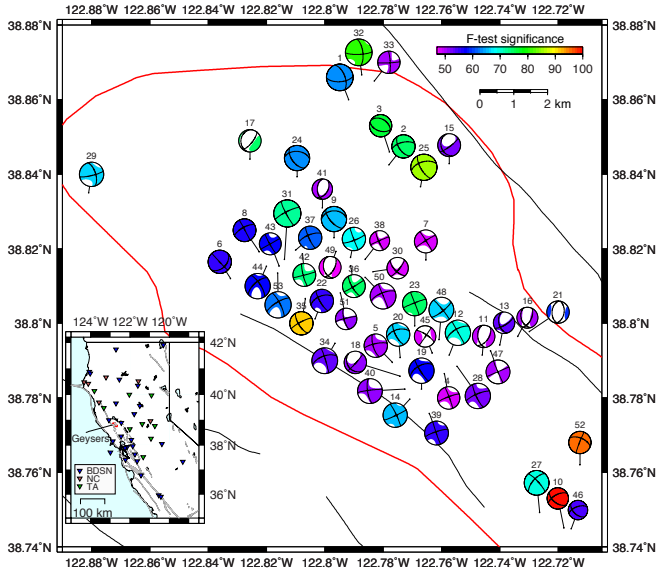

Figure 2.26.1: Full moment tensor solutions shaded by the statistical significance of the isotropic component as determined by the F-test

Acknowledgements

Data for this study come from the Berkeley Digital Seismic Network (BDSN), doi:10.7932/BDSN, operated by the UC Berkeley Seismological Laboratory, Northern California Seismic Network; and the Transportable Array. We thank Roland Gritto, P. Hellweg, T. Taira, P. Lombard, S.-H. Yoo, A. Guilhem, A. Chiang, H. Macbeth, David Oppenheimer, and C. Hartline for their help and support. This material is based upon work supported by the Department of Energy Geothermal Technologies Program under Award Number DE-EE0002756-002.Preliminary

References

Ford, S. R., D. S. Dreger, and W. R. Walter, Network sensitivity solutions for regional moment tensor inversions, *Bull. Seism. Soc. Am., 100,* 1962-1970, 2010.

Date	id #	M_w	FM fit deviatoric	FM fitFMT	FMT VR% DC/CLVD/ISO	FM fit CFMT	CFMT VR% DC/CLVD/ISO
Mar-1-2011	44	4.43	42	29	80.0 42/26/32	25	70.2 67/10/24
Feb-24-2008	37	3.99	48	23	78.7 33/19/48	21	69.5 43/19/38
May-12-2006	31	4.71	57	56	83.4 29/35/36	27	43.9 45/34/20
Jan-16-1995	9	4.14	38	40	68.9 27/8/65	23	57.4 86/4/10

Table 2.26.1: Summary of first-motion (FM) fits to deviatoric, full moment tensor (FMT), and constrained FMT (CFMT) solutions as measured by the number of discrepant first-motion observations. A high number of discrepant observations indicates a poor fit. The FMT and CFMT results are presented in columns 6 and 8, respectively, with the variance reduction (goodness of fit) and the percent components of double-couple (DC), compensated linear vector dipole (CLVD), and isotropic (ISO).

27 Moment Tensor Analysis of Shallow Sources

Andrea Chiang and Douglas S. Dreger

Introduction

For the nuclear explosion source-type identification problem, the uncertainty in a solution is as important as the best fitting parameters. A potential issue for shallow seismic sources that are effectively at the free-surface between the ground and air is that the vanishing traction at the free-surface can cause the associated vertical dip-slip (DS) Green's functions to have vanishing amplitudes (*Julian et al.*, 1998), which in turn can result in the indeterminacy of the M_{xz} and M_{yz} components of the moment tensor and bias in the moment tensor solution. The effects of the free-surface on the stability of the moment tensor method becomes important as we continue to investigate and improve the capabilities of regional full waveform moment tensor inversion for source-type identification and discrimination. It is important to understand its effects for discriminating shallow explosive sources in nuclear monitoring, but could also be important in natural systems that have shallow seismicity such as volcanic environments and geothermal systems. The HUMMING ALBATROSS quarry blast is an excellent dataset in terms of understanding the effects of free-surface vanishing traction using real data. These small chemical explosions are approximately 10 m deep and are recorded at up to several km distances. Therefore the data represent a rather severe source-station geometry in terms of vanishing traction issues. It is possible to obtain a robust full moment tensor solution that is comprised dominantly by an isotropic or explosive component, however the data provide the opportunity to evaluate capabilities of moment tensor inversion as a function of frequency and source depth.

Data and Methods

The HUMMING ALBATROSS data consist of both broadband and short-period seismic recordings (Figure 2.27.1). We applied the moment tensor based discrimination method to two ~M2-2.5 industrial explosions. Following the results of *Ford et al.* (2012) and *Chiang et al.* (2014) we incorporated full waveform data from five broadband stations and P-wave first motions from sixteen broadband and short-period stations into our moment tensor analysis. The broadband waveform data are filtered between 0.5 to 2 seconds depending on the signal-to-noise-ratios, and we examined the results in two frequency bands to understand the frequency dependence of free-surface vanishing traction. To further assess the uncertainties in the moment tensor inversion result, we looked at how the solution behaves in the *Hudson et al.* (1989) source-type space. Following the Network Sensitivity Solution (NSS) method proposed by *Ford et al.* (2010), we randomly generated 80 million moment tensor solutions that are uniformly distributed on the Hudson source-type plot, and for each random solution we compared the waveform fits and P-wave first motion picks between the data and synthetics. Here we compare two types of NSS result: waveform data only and waveform data with local P-wave polarity constraints.

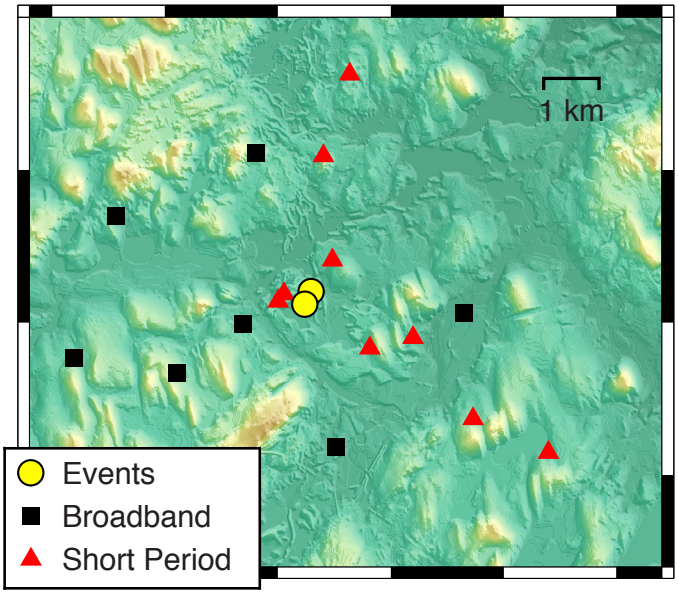

Figure 2.27.1: Event and station locations of the studied events. Circles are the two low magnitude industrial explosions, squares are the broadband stations, and triangles are the short-period stations. We used five broadband stations for the full waveform analysis and sixteen broadband and short-period stations for the P-wave first motion picks.

Source-Type Analysis

Given the frequency band and source-receiver distance, the moment tensor inversion is not sensitive to source depths shallower than ~150 m, but the solutions at these shallow depths remain stable and are dominated by a large isotropic component (Figure 2.27.2). Since we know the depth of the borehole where the explosions are detonated, we can constrain the source depth to be shallower than 15 m. The inversion result best fits the data at 11 m, so we fixed the source depth to 11 m for the subsequent NSS analysis.

In this report, we present findings for the first explosive shot since the moment tensor inversion and NSS results behave similarly for both explosions. The waveform NSS exhibits a trade off between volumetric sources and double-couple sources (Figure 2.27.3a-b). This trade off is likely caused by the combination of large Love waves on the tangential component and free-surface vanishing traction. The large Love wave causes the solution to deviate from a pure explosive mechanism. Vertical dip-slip and explosive mechanisms fitting equally well to the data (Figure 2.27.2) indicate free-surface effects also contribute to the observed trade off. The trade off becomes more pronounced at longer periods because free-surface effects are more severe at longer wavelengths. To eliminate the trade off we applied additional constraints from P-wave first motions, and the resulting NSS's show the best-fitting solutions to both waveform and P-wave first motion are constrained to mechanisms with a dom-

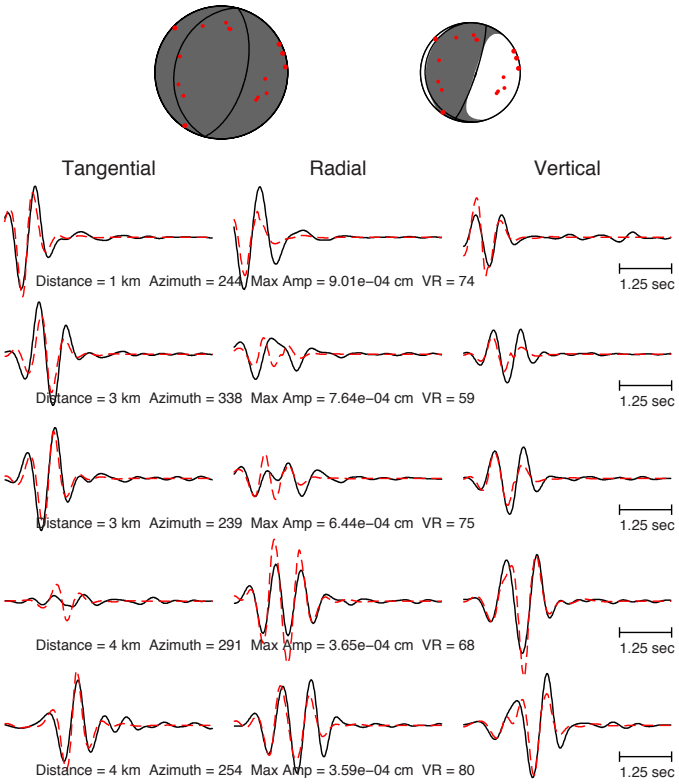

Figure 2.27.2: Full and deviatoric moment tensor solutions from waveform inversion. Displacement waveforms (black solid lines) and full moment tensor synthetics (red dashed lines) are filtered between 1.25 to 2 second period. P-wave up first motions (red dots) are plotted on top of the focal mechanisms.

inant isotropic or volumetric increase component, including the full moment tensor solution from waveform inversion (Figure 2.27.3c-d). The additional P-wave polarity information provides an important constraint because it eliminates mechanisms such as the vertical dip-slip (Figure 2.27.3), and discriminates the event as predominantly explosive.

Conclusions

Previous studies have shown that including P-wave first motions in addition to full waveform data can eliminate the common ISO-CLVD trade off (*Ford et al.*, 2012; *Chiang et al.*, 2014) and reduce the uncertainties of sparsely recorded underground explosions with strong Love waves (*Chiang et al.*, 2014). Here we demonstrated that although we cannot uniquely characterize the HUMMING ALBATROSS events as predominantly explosive using only waveform data, the combined waveform and first motion method enables the unique discrimination of these events. The combined method not only applies to larger man-made and natural seismic events, but also small magnitude, very shallow explosive sources that are effectively at the free surface. The combined method gives a well-constrained NSS even as we go towards longer periods, where the effects of free-surface vanishing traction are more pronounced. The combination of both low frequency full waveform data and high frequency P-wave polarities greatly enhances the capabilities of the moment tensor source-type discrimination method in cases

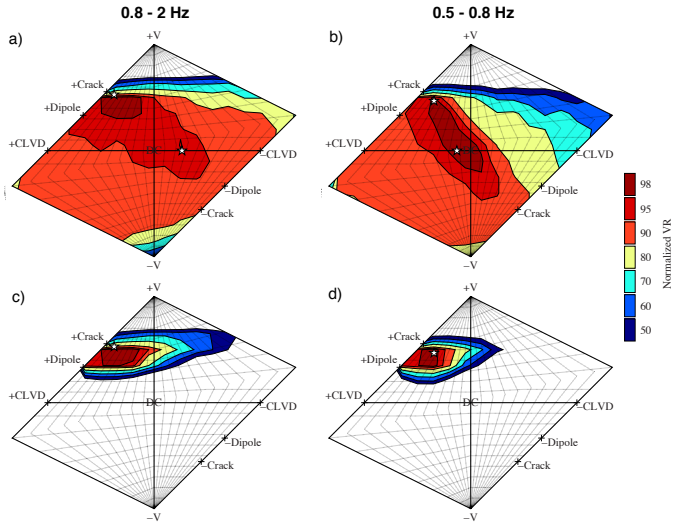

Figure 2.27.3: Network Sensitivity Solutions at two frequency bands. We plotted the full and deviatoric solutions (white stars) on top of the waveform NSS (a-b) and the combined waveform and first motion NSS (c-d).

of sparse station coverage, strong Love waves and free-surface effects due to very shallow source depths.

Acknowledgements

We acknowledge funding from the Air Force Research Laboratory, contract FA9453-10-C-0263 that is supporting this research.

References

Chiang, A., Dreger, D. S., Ford, S. R., Walter, W. R., Source characterization of underground explosions from combined regional moment tensor and first motion analysis, *Bull. Seismol. Soc. Am.*, *104*, doi:10.1785/0120130228, 2014 (*in press*).

Ford, S. R., Dreger, D. S., Walter, W. R., Network Sensitivity Solutions for regional moment-tensor inversions, *Bull. Seismol. Soc. Am., 100*, 1962-1970, doi:10.1785/0120090140, 2010.

Ford, S. R., Walter, W. R., Dreger, D. S., Event discrimination using regional moment tensors, *Bull. Seismol. Soc. Am., 102*, 867-872, doi:10.1785/0120110227, 2012.

Hudson, J. A., Pearce, R. G., Rogers, R. M., Source type plot for inversion of the moment tensor, *J. Geophys. Res., 94*, 765-774. 1989.

Julian, B. R., Miller, A. D., Foulger, G. R., Non-doublecouple earthquakes 1. Theory, *Rev. Geophys.*, *36*, 525-549, doi:10.1029/98rg00716, 1998.

28 Lessons Learned from Broadband Waveform Modeling Across the Mendocino Triple Junction

Michael Faggetter, Douglas Dreger

Introduction

The 1D calibrated Gil7 velocity model has been shown to generate realistic seismograms for Northern California *(Dreger and Romanowicz, 1994)* and is currently used for the automated calculation of moment tensors at long periods (greater than 10-20 s) at the Berkeley Seismological Laboratory (BSL). An improved model, Mend1 *(Tajima et al., 2000)*, is able to generate more realistic Green's Functions (GFs) for events in the Mendocino, CA region for the same period range. However, these 1D models are less suited to offshore, regional events near Mendocino since they cannot accurately reproduce the transitional oceanic-continental path, especially at higher frequencies. Broadband waveform modeling of offshore events is further complicated by factors such as the distance and azimuthal bias from stations. Also, the sparse distribution of earthquakes is likely to result in path-specific 1D velocity models that do not represent the full 3D structure.

In this study, a well-recorded M_w 4.47 aftershock from the recent M_w 6.8 event in the Mendocino region was used to develop an improved 1D model for offshore events. A standard forward modeling approach was adopted by comparing instrument-corrected, three-component broadband observations with synthetic data at multiple bandwidths. Station KMPB (Figure 2.28.1) was primarily used for this process due to its proximity to the hypocenter and location close to an SH-wave radiation maximum.

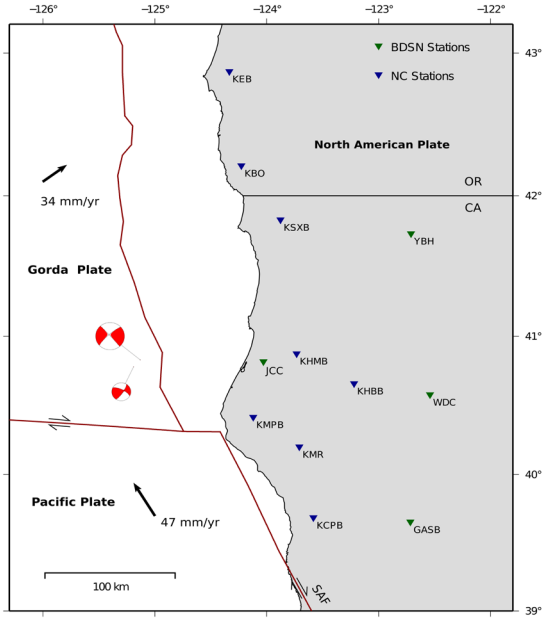

Figure 2.28.1: A map of the Mendocino region showing stations from the Berkeley Digital Seismic Network (BDSN) and Northern California Seismic Network (NCSN) that were investigated in this study. Focal mechanisms from the Berkeley Moment Tensor Catalog for the mainshock and largest aftershock are shown, scaled in size by magnitude, with lines pointing to their true epicentral locations. Single arrows depict plate motions relative to stable North America taken from the updated NUVEL-1A plate motion model of *DeMets et al.* (1994).

Synthetic Data

To generate synthetics, initial source parameters were taken from the BSL moment tensor catalog. *Chaytor et al.* (2004) hypothesized that many offshore strike-slip events in this region are the consequence of reactivating the normal, paleo-rift fabric in the central Gorda plate. Therefore, the preferred fault-plane solution was chosen based on the sub-parallel alignment to these fractures. The hypocentral depth was calibrated using the current velocity models.

1D GFs were calculated from an input velocity model using a frequency-wavenumber integration (FI) method *(Saikia, 1994)*. Fundamental-fault GFs were then summed to match the chosen mechanism and convolved with a calibrated ω^{-2} source-time function. The duration of this function was determined by comparing Gil7 synthetics with KMPB in the frequency domain. Changes to Q provided no significant improvement to the fit of the high frequency asymptote greater than the corner frequency, and initial values from Gil7 were retained for the new model.

Path Calibration

Multiple initial models were investigated based on seismic refraction studies from the Mendocino Triple Junction Seismic Experiment (MTJSE). Fits between the synthetics and observations were improved by iteratively perturbing parameters in the input velocity model.

Forward modeling by visual inspection between seismograms is reliable at long periods where fits to amplitude, and to some extent phase, can be determined. To more precisely match higher frequencies and obtain a reliable and quantitative measure of phase, a goodness-of-fit (GOF) measure was used. This measure was calculated from the weighted sum of five different metrics, each of which was converted to a normalized residual and summed following the method of *Olsen and Mayhew* (2010). The five metrics were measures of: 1) time-domain amplitudes between 0.1 and 1 Hz; 2) time-domain amplitudes for frequencies less than 0.1 Hz; 3) amplitude-independent phase for frequencies less than 0.1 Hz; 4) amplitude-independent phase at frequencies less than 0.5 Hz; 5) amplitudes of smoothed Fourier spectra less than 1 Hz.

By equally weighting each metric, this GOF measure was used as an objective function for a partially automated grid-search algorithm to improve upon the previous forward modeling.

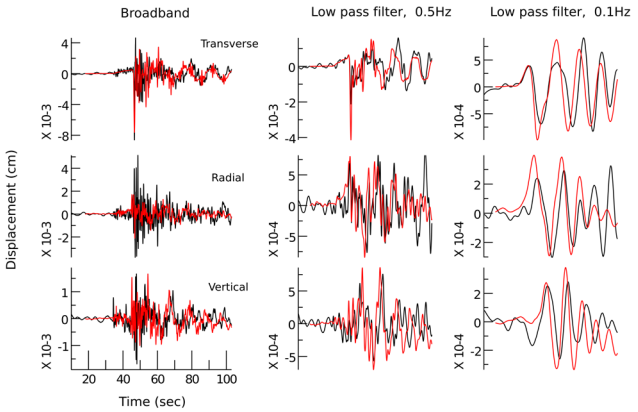

Figure 2.28.2: A comparison between MenPB synthetics (red) and instrument-corrected displacement time histories at KMPB (black). The first column shows unfiltered (broadband) data. The second and third columns show data filtered using a lowpass Butterworth filter with a corner frequency of 0.5 Hz and 0.1 Hz respectively.

Results

Table 2.28.1 lists the best 1D model for KMPB, named MenPB, obtained using this method. MenPB is derived from a complex hybrid of the current velocity models and was modified to include a double Moho. The latter feature is evidenced by *Beaudoin et al.* (1996) and others, and accurately reproduces several large amplitude reflections after the direct S wave, that are absent from structural models that simply increase with depth.

MenPB synthetics match observations well for all three components at KMPB up to 1 Hz. At least 60 seconds are well modeled on the tangential component, however the radial displacement record contains several late-arriving multi-path rays that are not reproduced with the 1D model (Figure 2.28.2). MenPB is able to fit observations particularly well for paths to stations of a similar azimuth to KMPB and to the northeast, including stations KMR and KSXB. Directly east of the event, surface wave amplitudes are significantly lower and are overestimated by the thick, low velocity surface layers in MenPB.

For a moment tensor inversion at long periods (0.02-0.05Hz), using GFs calculated using MenPB results in a mean increase in variance reduction of four compared to Gil7. For an inversion at 0.02–0.08 Hz, variance reduction increases by up to a factor of two for KMPB and KMR but with negligible change for stations to the northeast.

Conclusion

Ray paths that pervade the Gorda plate and the Franciscan accretionary complex are strongly influenced by thick, slow sediments in the shallow structure. For the northeast and southeast paths, waveforms contain large amplitude surface waves that persist for up to 50 seconds. For stations directly to the east, surface waves are damped by a predominantly continental path, and waveforms feature high frequency arrivals from reflections off the Moho and the mid-crustal high velocity layer. This wide azimuthal range of surface wave amplitudes, and the presence of multipath waves, emphasizes the difficulty of using simplified 1D models, even at long periods.

Layer Thickness (km)	Vp (km/s)	Vs (km/s)	Density (g/cc)
5	2.6	1.5	2.2
1	5.5	3.2	2.9
1	6.6	3.8	3.0
2	8.0	4.6	3.3
5	5.9	3.4	2.9
11	7.1	4.1	3.1
∞	8.0	4.6	3.3

Table 2.28.1: The Final calibrated 1D velocity model, MenPB.

A GOF measure was found to be an invaluable tool for forward modeling. Using multiple user-defined metrics provides flexibility that the routinely used 'variance reduction' does not. For example, metrics can be chosen to target specific criteria when modeling, resulting in more rapid convergence of models in a chosen passband. However, careful selection of the metrics and their weights prior to automated procedures is strongly advised.

Acknowledgements

Moment tensors were computed using the tdmt-invc_iso package developed by Douglas Dreger and Sean Ford of the Berkeley Seismological Laboratory, and Green's functions were computed using the FKRPROG software developed by Chandan Saikia. Data for this study come from the Berkeley Digital Seismic Network (BDSN), doi:10.7932/BDSN, and the Northern California Seismic Network (NCSN).

References

Beaudoin, B. C., Godfrey, N. J., et al., Transition from slab to slabless: Results from the 1993 Mendocino triple junction seismic experiment, *Geology, 24*, 195-199,1996.

Chaytor, J. D., Goldfinger, C., et al., Active deformation of the Gorda plate: Constraining deformation models with new geophysical data, *Geology, 32*, 353-356, 2004.

DeMets, C., Gordon, R. G., et al., Effect of recent revisions to the geomagnetic reversal time scale on estimates of current plate motions, *Geophysical Research Letters, 21*, 2191-2194, 1994.

Dreger, D. S. & Romanowicz, B., Source Characteristics of Events in the San Francisco Bay Area, *USGS Open-file report, 94-176*, 301-309, 1994.

Olsen, K. B. & Mayhew, J. E., Goodness-of-fit Criteria for Broadband Synthetic Seismograms, with Application to the 2008 M_w 5.4 Chino Hills, California, Earthquake, *Seismological Research Letters, 81*, 715-723, 2010.

Saikia, C. K., Modified frequency-wavenumber algorithm for regional seismograms using Filon's quadrature; modeling of Lg waves in eastern North America, *Geophysical Journal International, 118*, 142-158, 1994.

Tajima, F., Dreger, D. S., et al., Modeling of the transitional structure from ocean to continent in the Mendocino region using broadband waveform data, *EOS*, Transactions American Geophysical Union, 81, no. 48 (Fall Meet Suppl.), 2000.

Research Studies:
Enhancements to Observational Systems

29 ElarmS-2: Rapid Accurate Alerts across California

Jennifer Strauss, Richard Allen, Ronnie Grapenthin, Margaret Hellweg, Ivan Henson, Ingrid Johanson, H. Serdar Kuyuk, Doug Neuhauser

Introduction

The ElarmS methodology and algorithms are part of the ShakeAlert demonstration system in California, and are also being tested in the US Pacific Northwest and South Korea, and will be implemented for testing in Israel in the coming year. The methodology is a network-based approach to early warning in that it requires several seismic stations to detect P-waves before an alert is issued. The alerts are distributed to test users across California who receive an estimate of the shaking intensity at their location as well as the time until that shaking will start at their location.

The improved production grade E2 algorithm, released last year, improved both the early warning processing speed and the accuracy of the results. This was most apparent during the significant earthquakes (M>=4.5), which ruptured in California over the past year. The algorithm was further improved by investigating a global approach to providing magnitude estimates for early warning using only the P wave data.

Algorithm Performance

Over the last year in California, ElarmS successfully alerted on all significant earthquakes (*M*>=4.5, 10 earthquakes) and generated no false alarms. This includes events in Los Angeles, Santa Rosa, offshore Eureka, and the southern Sierra. The magnitude estimates were within 0.5 magnitude units in all cases.

The largest event was the *M*6.8 event offshore of Eureka. The initial ElarmS magnitude estimate was *M*6.3, with an estimated epicentral location only 7 km from the true location. Locations of small events are often difficult in this region stemming from the fact that the sensors are located onshore, and thus, only to the Eastern side of the rupture, and sparsely distributed. This larger event did not suffer from that effect; ElarmS also alerted on all of the larger (*M*>=4.5) aftershocks.

The speed of the alert depends on the quality of the seismic network around the epicenter. For the *M*5.1 Los Angeles Le Habra event (see Figure 2.29.2) the alert was 4.2 seconds after the origin time, which is typical for events in the Los Angeles region. For the Santa Rosa event, the alert was 6.8 seconds after the origin time, 10.8 s for the southern Sierra event, and 25.7 s for the (offshore) Eureka earthquake. Comparing the performance of ElarmS across the state for a wider range of magnitudes (*M*>=3) the effect of variable seismic network quality is very apparent. The performance is good to excellent in the San Francisco Bay and Los Angeles areas where station coverage is densest. In the greater San Francisco Bay Area, of the 38 *M*>=3.0 events reported by the ANSS, five were missed (all in the Geysers Geothermal Area) and there were no false events. In the Los Angeles region, of the 35 *M*>=3.0 events, four were missed and there were two false events.

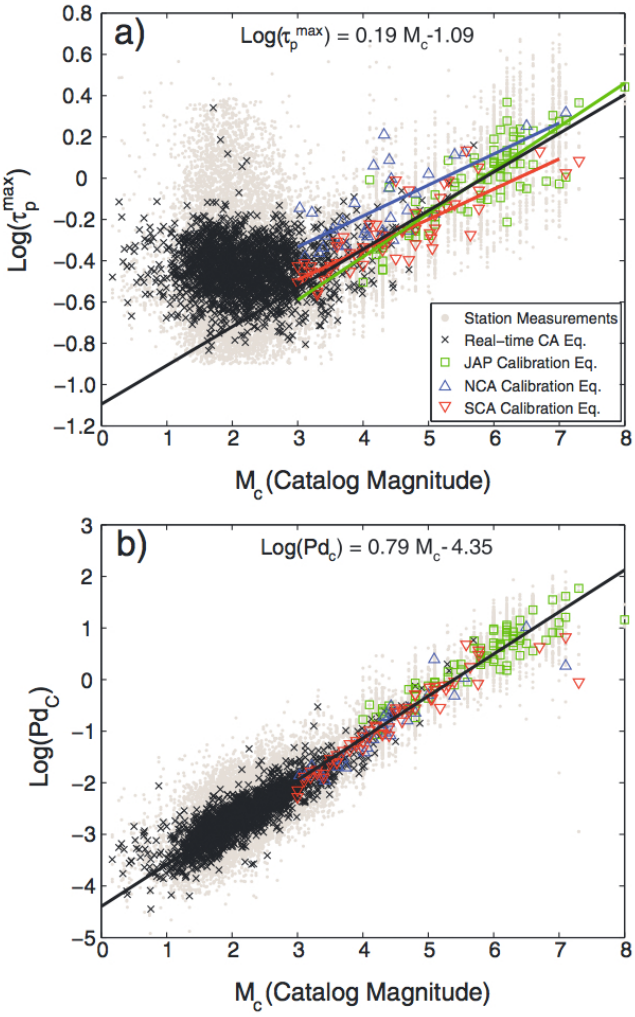

Figure 2.29.1: Scaling relationships between catalog magnitude and (a) τpmax and (b) Pdc. In (a) the best fit lines to the regional data sets are shown with colored lines, and the black line is the best linear fit to all the data excluding the real-time-detected earthquakes (equation shown). In (b) the black line (equation shown) is the least squares multiregression fit to the entire data set and represents our preferred global scaling relationship.

Global Magnitude Estimation

Rapid magnitude estimation is at the heart of Earthquake Early Warning Systems (EEWS). The challenge is to use only a few seconds of the P wave data from a limited number of stations to quickly determine a useful estimate of the earthquake magnitude. To respond to the emergency at hand, it is crucial that these magnitude estimates are as precise as possible (*Kuyuk and Allen*, 2013). For large earthquakes, substantial deviations between the estimated magnitude and the true earthquake's magnitude can lead to erroneous intensity predictions.

We have improved the precision of ElarmS by deriving a

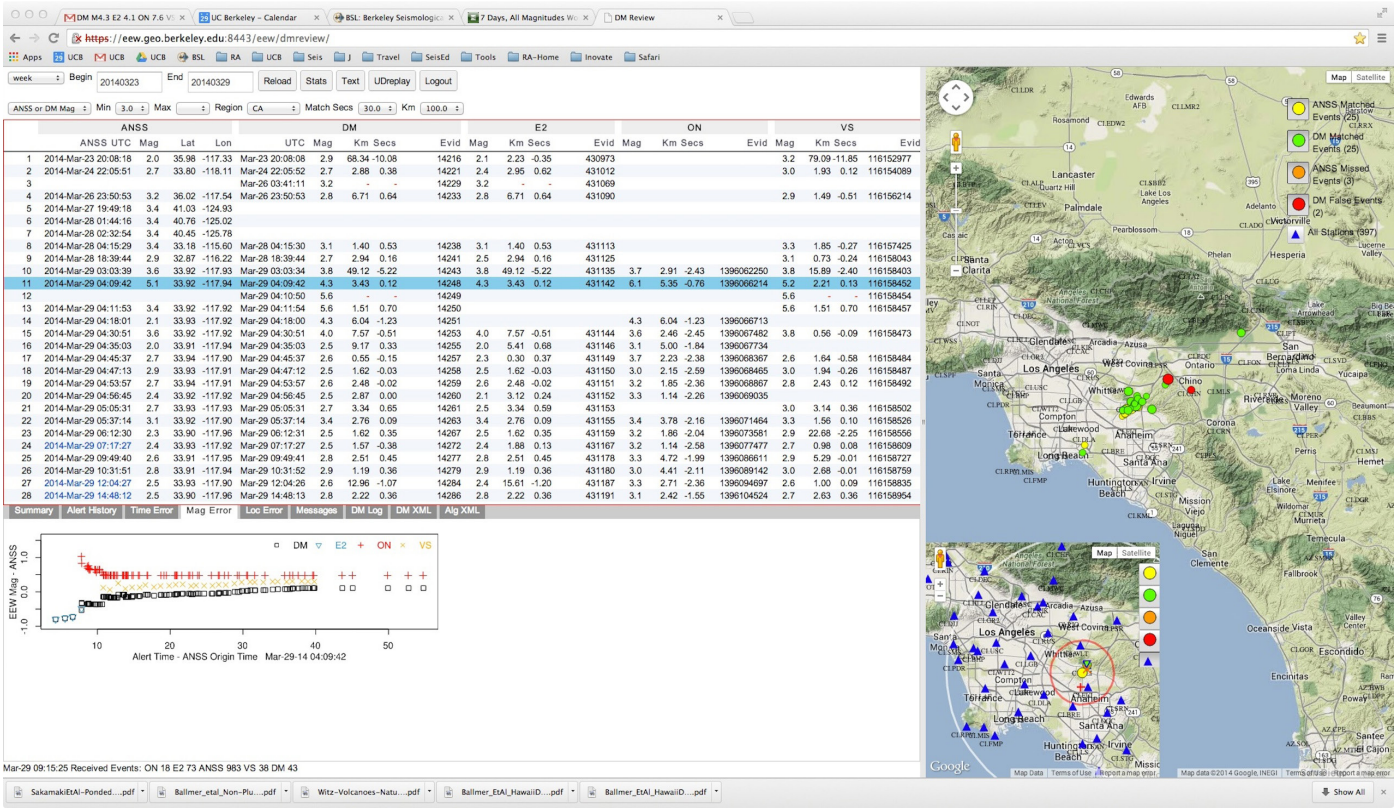

Figure 2.29.2: The Decision Module web-based performance evaluation tool was used to study the overall system response for the La Habra event. This tool aggregates information from all three algorithms individually with the overall ShakeAlert warning information. The E2 algorithm (blue triangle) can be seen in the inset plot bottom left, to have a quicker alert time for this rupture than the other algorithms. The map shows the location of the earthquake and the aftershocks in the region.

global scaling relationship to predict earthquake magnitude from P-wave data, which can be applied to data worldwide. To derive the scaling relationship we used waveform records from past/historic earthquakes and data from the current real-time ElarmS system running in California. Instead of using different scaling relationships for each individual region, we used a global data set and explored various approaches to estimate magnitude from the P-wave data.

Five different methods were investigated to estimate earthquake magnitude from P-wave data. The inclusion of real-time data provided an opportunity to test the methods on smaller earthquakes ($0.1 < M < 3.0$), which have been largely ignored in previous studies. Comparison of τ_p^{max} and Pd-based magnitude estimation methods indicate that Pd scaling is observed for all earthquakes, whereas the frequency filtering required for the τ_p^{max} observation results in sensitivity to only a limited frequency range (M>3.0 for the implementation tested here). We concluded that the best approach to derive EEW magnitude estimates is to use only the Pd parameter and the global scaling relationship

$$MGPd = 1.23\log(Pd) + 1.38\log(E) + 5.39$$

This new method provides smaller RMS errors than existing regional methods based only on Pd. Our results showed that this new technique using only Pd information is robust and delivers the most accurate global magnitude estimates for earthquakes up to $M \sim 7$. Above $M7$, a saturation effect is observed and the application of other finite source type methods is needed.

Acknowledgements

This project is possible thanks to the collaborative efforts of many people working at the CISN operating institutions: UC Berkeley, Caltech, USGS Menlo Park and USGS Pasadena. This work is funded by USGS/NEHERP awards G09AC00259 and G12AC20348, and by the Gordon and Betty Moore Foundation through Grant GBMF3024 to UC Berkeley.

References

Kuyuk, H. S. and Allen, R. M., A global approach to provide magnitude estimates for earthquake early warning alerts, *Geophysical Research Letters*, v. 40, p.6329-6333, 2013.

30 Operational Real-Time GPS-enhanced Earthquake Early Warning

Ronni Grapenthin, Ingrid A. Johanson, Richard M. Allen

Introduction

Moment magnitudes for large earthquakes (M_w>7.0) derived in real-time from near field seismic data can be underestimated due to instrument limitations, ground tilting, and saturation of frequency/amplitude-magnitude relationships. Real-time high-rate GPS resolves the build-up of static surface displacements with the S-wave arrival, thus enabling the estimation of slip on a finite fault and the event's geodetic moment. Here, we present the first operational system for real-time GPS-enhanced earthquake early warning as implemented at the BSL and currently running on data for Northern California. Using synthetic and real-data test cases, we explore its sensitivities to disturbances of *a priori* constraints (origin time, location, fault strike/dip). The work presented here is a continuation of *Grapenthin et al.* (2013a,b).

Data processing

The BSL generates real-time position estimates operationally using data from 62 GPS stations (BARD, PBO, USGS) in Northern California (Figure 2.30.1). A fully triangulated network defines 170+ station pairs for processing with the software trackRT (*Herring et al.*, 2010). The BSL uses G-larmS, the Geodetic Alarm System, to analyze the positioning time series, and determine static offsets and pre-event quality parameters. G-larmS derives and broadcasts finite fault and magnitude information through a least-squares inversion of the static offsets for slip based *a priori* fault orientation and location information. This Python implementation tightly integrates seismic alarm systems (CISN ShakeAlert, ElarmS-2) as it uses their P-wave detections to trigger its processing; quality control runs continuously.

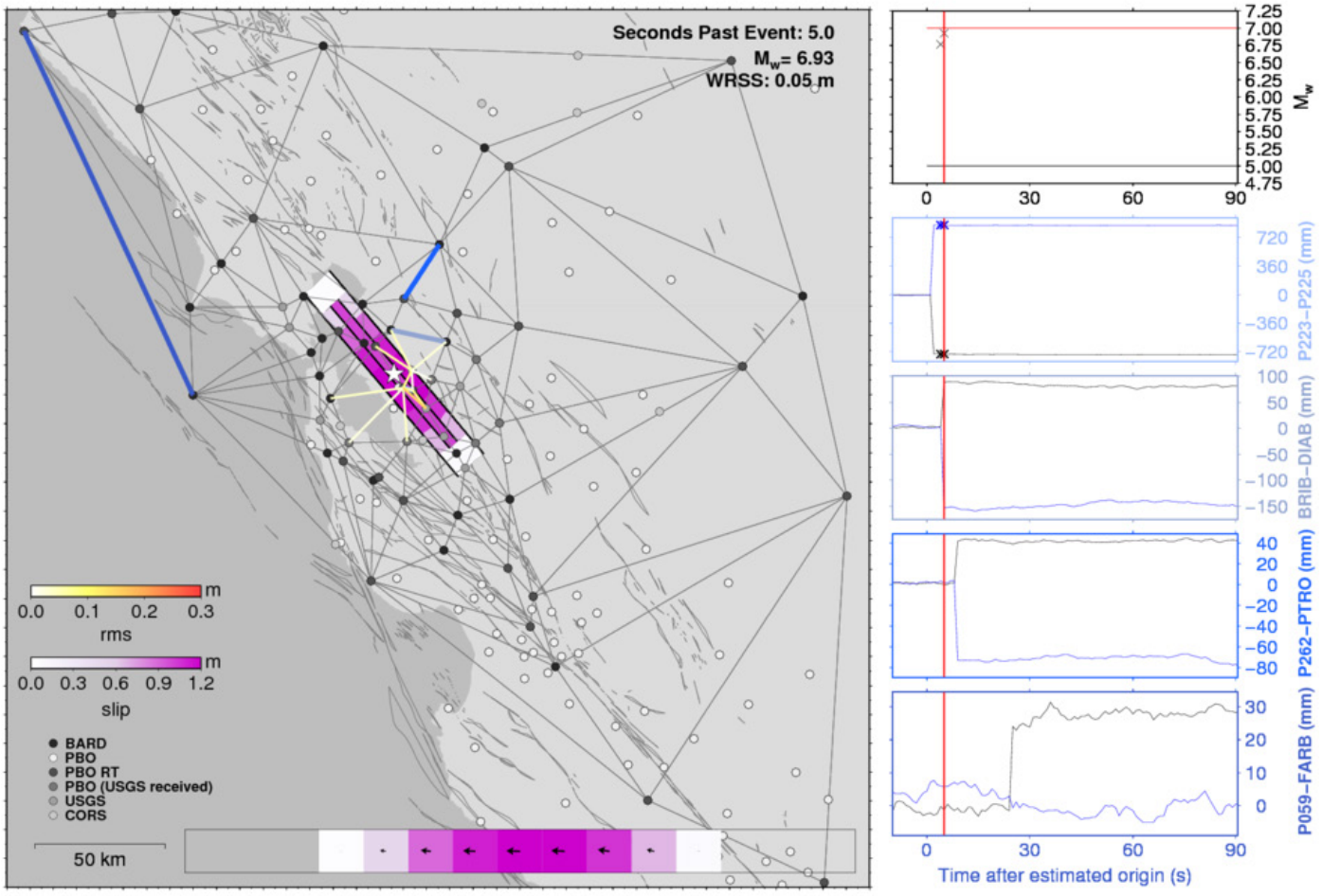

Figure 2.30.1: Snapshot during a real-time test of G-larmS (second solution, five seconds after event); the red line on the right side shows the timing of the snapshot. Top right figure shows the estimated earthquake magnitude for the slip model in purple on the left. Test is based on a simulated *M*7.0 earthquake. G-larmS begins estimating co-seismic offsets (blue and black symbols) after the S-wave arrival. Offsets are updated and input into an inversion for distributed fault slip every second. Testing was run in true real time; synthetic offsets were added to GPS position time series on-the-fly in order to capture true real-time noise and data availability.

Sensitivity Tests

To linearize the finite fault inversion step to increase processing speed we make assumptions about fault orientation and location. We test G-larmS' sensitivity to these assumptions using synthetic tests in which we add modeled offsets due to synthetic ruptures at the Hayward Fault to real-time data (Figure 2.30.1). In individual tests, we randomly perturb pre-defined fault strike and dip, and the event epicenter and origin time, which are derived from a seismic alarm message that triggers our processing.

Here, we show only the impact of misestimates in fault geometry is shown in Figure 2.30.2 (more details in *Grapenthin et al.*, 2014). We vary strike and dip of the model inversion fault by ±20 degrees and ±45 degrees, respectively. The upper row (Hayward 0 km) uses the same forward model as shown in the offset time series in Figure 2.30.1 (rupture from 0-12 km depth) and demonstrates that magnitude recovery (blue) and model fit (red) degrade quickly with small deviations from the nominal values.

The lower row in Figure 2.30.2 (Hayward 5 km) uses a forward model that slips only between 5 and 12 km depth. In the inversion, however, slip over the entire fault width along dip is assumed. While the model fits (red) are generally good for the full range of values, the magnitude recovery (blue) is poor. Asymmetries are due to asymmetries in the network (dip of 140 and 45 degrees are towards West and East, respectively which then constrained the inverse model to have lower overall magnitude.

Conclusions and Outlook

From the tests presented here, and others summarized by *Grapenthin et al.* (2014), we suggest, that slip for an earthquake occurring within small bounds of our assumptions, *i.e.* strike=320±5 degrees, dip=90±3 degrees, mislocation within 3 km orthogonal to surface trace, and surface rupture, will be well recovered for earthquakes within the network (depending on station distribution). Outside of these bounds, however, we may face unphysical slip models and poor magnitude recovery at relatively good fit of the model to the data.

While dense station coverage provides high resolution and, most importantly fast observations, it requires us to sample the parameter space for the non-linear finite slip inversion problem more thoroughly. The most problematic issue is choosing any parameter such that individual (near field) stations end up on the wrong side of the model fault. As the parameter space exploration in real-time cannot be exhaustive unless heavily parallelized, we have to exploit this property in the future. As real-time GPS is sought to contribute improved magnitude estimates within ±0.3 magnitude units and an approximate fault length for ground motion prediction to earthquake early warning, two simplifications are possible: (1) ignoring/down-weighting near-field data at single outlier stations in a dense network that produce significant misfits, (2) placing model faults between station pairs with highest strain. These can be combined and both reduce the complexity of the solution while providing approximate solutions. The trade off between speed and accuracy of the solutions is the subject of future investigation.

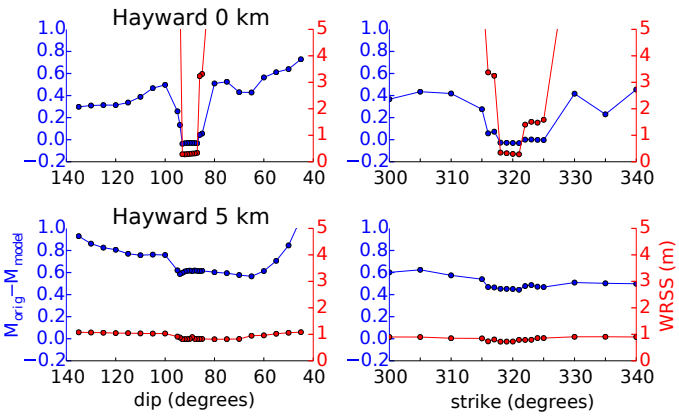

Figure 2.30.2: Sensitivities to wrong assumptions in strike and dip in the inversion. Two forward models (fault from 0-12 km and 5-12 km depth respectively) with 90° dip creating M_w7.0 equivalent slip were inverted for varying dip (left column) and strike (right column). Blue lines indicate magnitude recovery. The red line is the model misfit to the forward model.

Acknowledgements

This work is supported through the Gordon and Betty Moore Foundation, and CISN partners. We use data provided by the Plate Boundary Observatory operated by UNAVCO for EarthScope and supported by NSF (No. EAR-0350028 and EAR-0732947).

References

Grapenthin, R. et al., Operational Real-time GPS-enhanced Earthquake Early Warning, *J. Geoph. Res.*, submitted, 2014.

Grapenthin, R. et al., G-larmS - Integrating Real-Time GPS into Earthquake Early Warning I: Implementation, *BSL Annual Report 2012-2013*, 70-71, 2013a.

Grapenthin, R. et al., G-larmS - Integrating Real-Time GPS into Earthquake Early Warning II: Testing, *BSL Annual Report 2012-2013*, 72-73, 2013b.

Herring, R. T. A. et al., GAMIT/GLOBK Reference Manuals, Release 10.4, *MIT Technical Reports*, 2010.

31 Evaluation of Smartphones as Seismometers

Qingkai Kong, Richard Allen

Introduction

We are building a new seismic network using smartphones. The accelerometers in smartphones can be used to detect ground motion caused by earthquakes. Before we set up the network, we need to understand the capabilities of the smartphones as a seismic recording system. We conducted a series of tests to understand them, including a noise floor test, and shake table tests. The noise floor test shows us that the current smartphones can detect earthquakes larger than magnitude 4 within 10 km of the epicenter, and the shake table tests show us that the smartphones can reproduce the shaking quite well, even without being firmly attached to the shake table.

Noise Floor Test

A noise floor test is performed to understand smartphones' abilities to detect earthquakes. The phones are placed in a very quiet basement of a building on UC Berkeley's campus, ensuring that the signal the phones record are from internal noise of the phone and the environmental noise of the surrounding area. Altogether, we recorded about one month's noise data for each type of phone, and then we calculated the noise floor of the smartphones using the method described in *McNamara* (2004). The earthquake data showed in the plot are from *Clinton et al.* (2002).

Figure 2.31.1 shows the noise floor test results. Earthquakes above the noise floor of the phones can be recorded by the smartphones. If the earthquake is below the noise floor, then the earthquake signal will be buried into the noise.

The noise floors of the smartphone are divided into two groups based on the release time, represented by light blue and red color. The blue color noise floors are from phones released before 2012, and the red color noise floors are from phones released between 2012 and 2013. As the technology improves, one starts to see the improvement of the accelerometers across the smartphones. The best quality accelerometers in the tested phones can see earthquakes above magnitude 4 within 10 km of the epicenter.

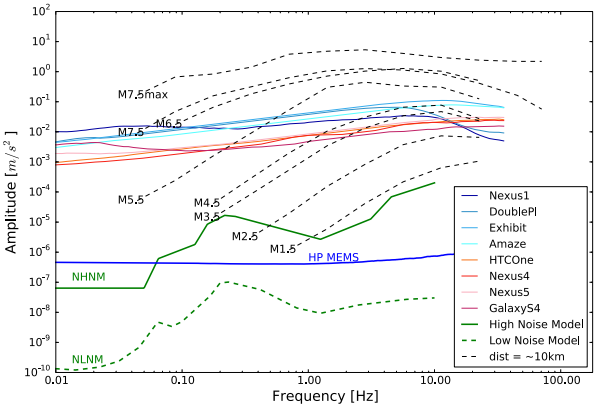

Figure 2.31.1: Noise floor plot of the smartphones. The dotted black lines represent different magnitude earthquakes' signals from within 10 km of the epicenter, as obtained by John Clinton. The green solid and dotted lines are new high noise models (NHNM) and new low noise models (NLNM) of the earth (*Peterson,* 1993). The blue solid line at the bottom is the HP MEMS sensor as a reference line of the potential future sensors. The blue and red lines are the noise floors of the different smartphones whose brands are shown in the legend

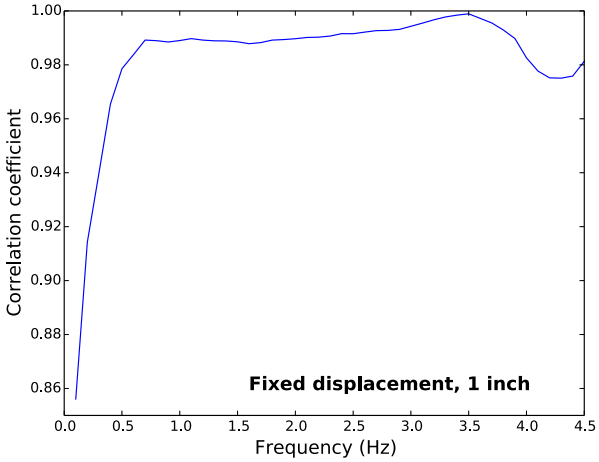

Figure 2.31.2: Correlation coefficient plot of sine wave tests with fixed displacement (1 inch) and different frequencies. The phones are fixed on the shake table, and for each frequency sine wave test, the recording time is 30 seconds. The correlation coefficient is calculated using the Pearson correlation coefficient between the signal recorded by the smartphone and that recorded by a high quality accelerometer attached on the shake table.

The HP MEMS sensor has quite a low noise floor, even comparable to the high quality traditional seismic instrument. Thus, we are hoping the noise floor of the smartphones will continue to drop.

1-Dimensional Shake Table Test

We use a small shake table to test the phone's ability to record and reproduce the shaking generated by the shake table. This shake table is 1 dimensional and can generate both sine waves and converted seismograms. The following are some results from the tests.

The first case we tested was when the smartphones are fixed on the shake table (using a clamp or putty), the smartphones can reproduce the signals quite well. We can see from Figure 2 that most of the correlation coefficients are above 0.98, which shows that the phone-recorded signals reproduce the real motion quite well. The relatively low coefficient below 0.5 Hz is due to the small amplitudes when using a fixed displacement and a small frequency.

The second test was with smartphones placed freely on the shake table. The future network will consist of smartphones

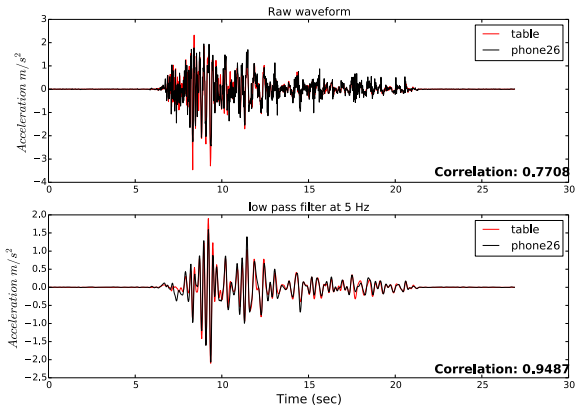

Figure 2.31.3: Waveform recorded by one Samsung Galaxy S4 (phone 26, black color) and high quality accelerometer on the shake table (red color). The top figure is the raw waveform, and the bottom figure is the filtered data (low pass at 5 Hz). This waveform is from one horizontal component of one station during the M_w 6.9 Loma Prieta earthquake, the epicentral distance is 10 km.

put freely on a table or carried by their owners. Therefore, the behavior of the smartphones not rigidly attached to the shake table is also studied.

Figure 2.31.3 shows the raw and filtered waveform from one test. This raw waveform is converted from one component of a station recording the M_w 6.9 Loma Prieta earthquake. The smartphone used in this test was put freely on the shake table, so that the phone can slide when the shaking is large. We can see it can recover the signal very well, and the content below 5 Hz has a correlation coefficient about 0.95.

We also use a one second sliding time window to extract two features from filtered data, as can be seen from Figure 2.31.4. The two features we extracted are zero crossings (when the signal across the zero baseline, we count 1, and then add this count up within the time window, so this parameter is related with frequency) and maximum acceleration (absolute value of the acceleration) from each one second window. Then we compare these features with those extracted from the high quality accelerometer on the shake table. We can see that during the duration of the earthquake, the zero crossings differences between the smartphone recordings and that of the high quality accelerometer are around zero, and the maximum acceleration differences are less than 0.4 m/s^2.

Conclusions

We showed here that smartphones can be used to record earthquake signals and those data can be used to extract useful information about the earthquake, but there are still a couple of issues that need to be addressed. When using the sliding window to extract features from the signal, the amplitude information will under estimate the real amplitude when the phone slides. Characterizing the sliding behavior will help the seismic applications of the smartphone network in the future, such as Earthquake Early Warning.

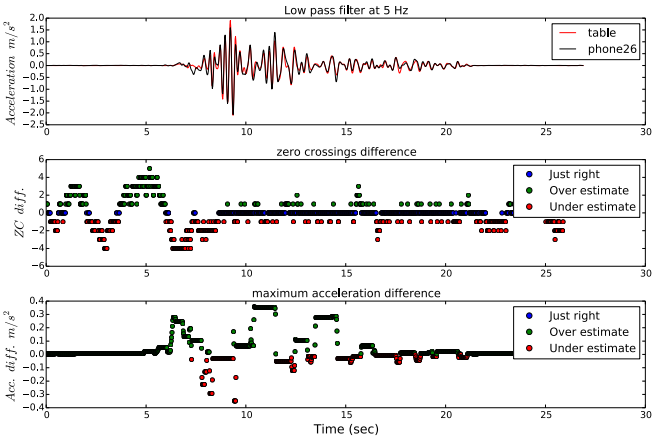

Figure 2.31.4: The top figure is the filtered waveform, the middle figure is the comparison of the zero crossings. The blue dots show when the smartphone and accelerometer have the same value; green dots show where the smartphone value is greater than the raw waveform; red dots show where the smartphone value is less than the raw waveform. The bottom figure shows the difference between the maximum acceleration.

Acknowledgements

This project is funded by Deutsche Telekom. We thank Deutsche Telekom for funding and providing all of the smartphones and developing the applications. Also, we thank Pacific Earthquake Engineering Research Center (PEER) for providing us both the 1-Dimensional and 3-Dimensional shake table.

References

Clinton, J. F., and Heaton, T. H., The potential advantages of a strong-motion velocity meter over a strong-motion accelerometer, *Seismological Research Letters,* 73, 332–342, 2002.

Clinton, J. F., Modern Digital Seismology - Instrumentation, and Small Amplitude Studies for the Engineering World, *Ph.D. Thesis*, California Institute of Technology, 2004.

McNamara, D. E. and Buland, R. P., Ambient Noise Levels in the Continental United States, *Bulletin of the Seismological Society of America*, 94 (4), 1517-1527, 2004.

Peterson, J., Observations and modeling of seismic background noise, *US geological Survey*, open file report 93–322, 1993.

32 High-rate GPS Records Reveal Basin Amplification in the San Joaquin Delta

Ingrid Johanson

Introduction

The M_w 6.9 Ferndale earthquake occurred off the coast of Northern California, near the Mendocino Triple Junction. The large strike-slip earthquake was sufficiently offshore, such that no reported damage or injuries occurred. Nonetheless, it was widely felt throughout coastal Northern California. Aftershocks suggest a northeast striking fault plane, oriented such that the California coast is roughly perpendicular to the rupture plane. Accordingly large amplitude Love waves were observed at California seismic stations. These long-period, large-amplitude surface waves were also detectable at GPS stations in the Bay Area and prompted an examination of GPS data throughout Northern California.

Data Processing

Data were processed from a total of 269 GPS stations from the Bay Area Regional Deformation (BARD) network, the Plate Boundary Observatory (PBO) and USGS, Menlo Park's network. Pairs of stations were processed individually using Track, a high-rate GPS processing algorithm developed at MIT alongside GAMIT/GLOBK (*Herring et al.*, 2010). Track is a network-based processing algorithm, hence it determines relative motion between multiple rovers and a reference site. A processing approach using a single rover and reference (one pair) was used for this study because it allows the motion of each GPS station to be determined relative to only the closest other stations. Common noise sources, in particular atmospheric noise, will then cancel out. As a result, higher precision motions can be detected than in a network solution that includes long baselines.

After processing each pair of stations to determine their relative motion, a network adjustment is performed to transform these into the absolute motion of each station. The inverse problem is underdetermined and so some type of constraint is required to perform the transformation. Potentially a single station could be held stationary and all motions would be transformed to be relative to a single stable site. However, high-rate GPS data do not have insignificant noise, even at the best stations, and a single station constraint would propagate that noise to all the others, essentially doubling their noise levels. A stable network centroid was chosen as a suitable constraint instead. This has the advantage that it averages through the motions at all stations, such that the noise level of the centroid, which is propagated to all stations, is reduced by $1/\sqrt{N}$, where N is the number of pairs in the network adjustment.

The appearance of the Love waves in the resulting GPS timeseries is improved by bandpass filtering. This removes the low frequency portion of the flicker noise spectrum attributable to atmospheric errors and signal multipath. When compared to broadband seismic records at stations where BARD network GPS sites are co-located with Berkeley Digital Seismic Network (BDSN) broadband seismometers, it is apparent that the centroid constraint adequately approximates an absolute reference frame and that the filtered results match many of the same features in the seismic data, even down to the 2–3 mm amplitude level (Figure 2.32.2).

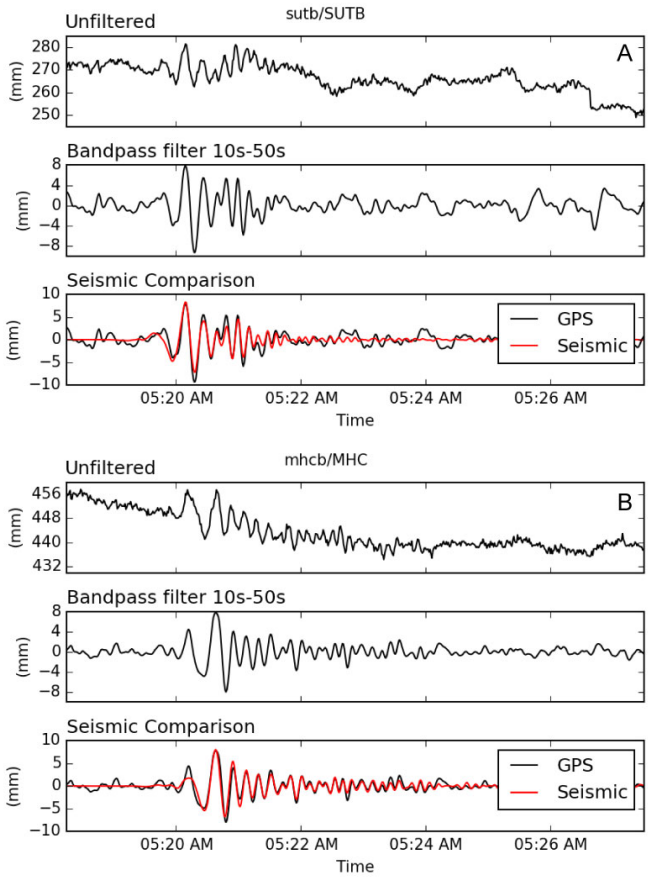

Figure 2.32.1: Comparison of BARD network high-rate GPS timeseries and data from broadband seismometers in the BDSN network. Transverse component of motion is shown (motion perpendicular to azmuthal direction to the earthquake epicenter).

Results and Discussion

The motion at each GPS station is rotated into the transverse and radial components and it is observed that nearly all the motion is in the transverse component. This can be seen quite clearly in Figure 2.32.2, where the peak dynamic displacements in the transverse direction are an order of magnitude larger than in the radial direction. Figure 2.32.2A, in particular, clearly shows the radiation pattern of Love waves propagating in a direction perpendicular to the rupture plane. However, neither Figure 2.32.2C or 2D shows a similar distribution of high radial displacements at 45° to the rupture plane that might be associated with Rayleigh waves.

While the distribution of peak dynamic displacements is dominated in long periods by the radiation pattern, at shorter periods other patterns become visible. In particular, at higher frequencies, stations in the San Joaquin Delta region show higher peak dynamic displacements than those in surrounding areas, as well as longer duration shaking (Figure 2.32.3).

The stations with higher amplitudes on the transverse component also have increased amplitudes on the radial component, suggesting that seismic waves were scattered within this area or reflected off of basin boundaries, transferring energy from the transverse to radial components. The increased duration of shaking at Delta region stations further supports the interpretation that energy is being trapped within a basin.

In general the soft sediments of the Central Valley easily explain the increased amplitudes and longer shaking duration for many of the affected stations. However, sites in the San Joaquin Delta region are more strongly affected than those elsewhere in the Central Valley. Furthermore, two amplified stations are located in the Montezuma Hills; a geologic province that is distinct from the Delta, but nonetheless contains unsorted Pleistocene silt and sand, known as the Montezuma formation (*Strand and Koenig*, 1965). That they also have energy scattered into the radial component, could suggest that the structure responsible underlies both regions.

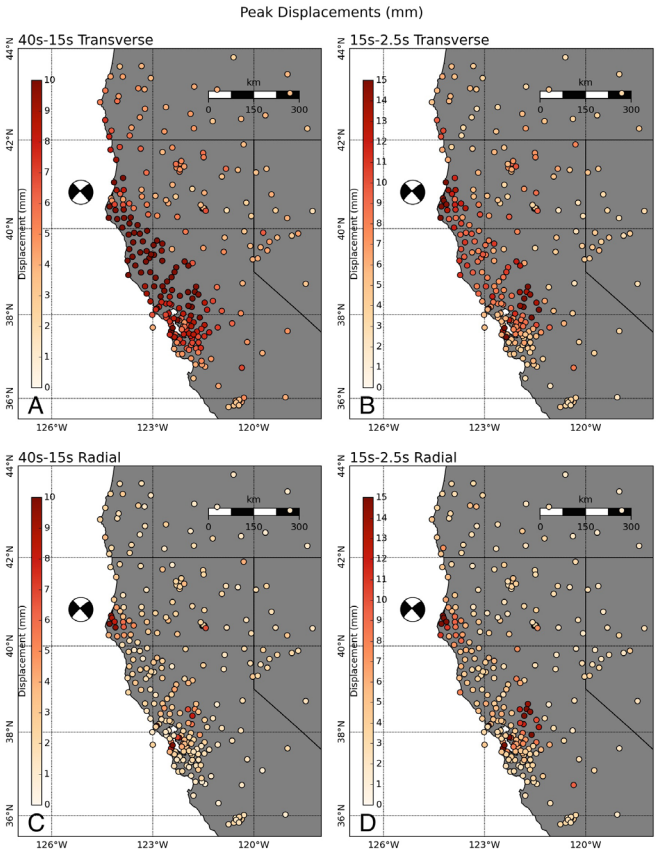

Figure 2.32.2: Peak dynamic displacements (colors) for transverse (A and B) and radial (C and D) components of motion. Left and right sides have been bandpass filtered to the limits shown. The NCSS moment tensor is plotted at earthquake epicenter.

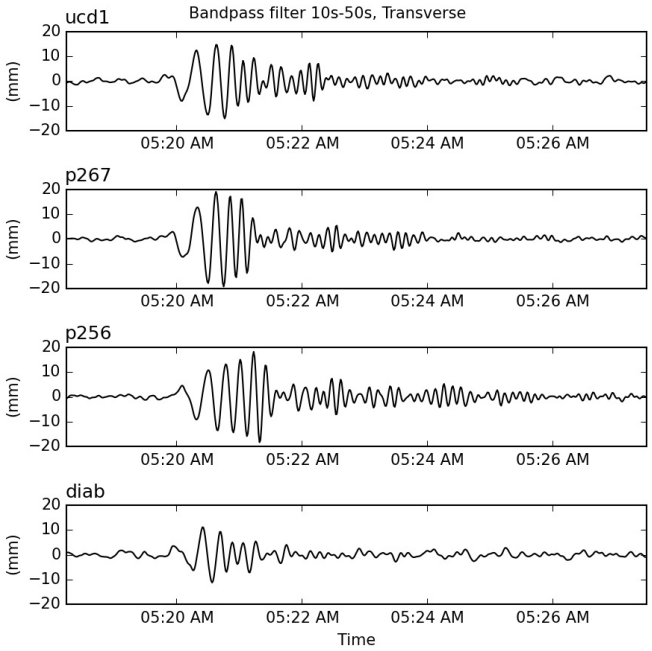

Figure 2.32.3: Comparison of San Joaquin Delta region sites (ucd1, p267, p256) and a nearby hard rock site (diab), showing higher overall amplitudes of shaking in the Delta region and longer duration wave trains.

These data provide an opportunity to probe the structure of Northern California in a way that is not possible with the much more sparsely distributed broadband seismic stations. While GPS is less sensitive than broadband seismometers, when a large earthquake generates high dynamic displacements, the increased resolution due to higher spatial density will be very valuable.

References

Herring, T. A., R. W. King, and S. C. McClusky, GAMIT: GPS Analysis at MIT - Release 10.4, MIT, 2010.

Strand, R. G., and J. B. Koenig, Geologic map of California: Sacramento sheet, California Division of Mines and Geology, (1:250,000), 1965.

33 Predictability of Hydraulic Head Changes and Characterization of Aquifer System Properties from InSAR-Derived Ground Deformation

Estelle Chaussard, Roland Bürgmann

Introduction

Groundwater management relies mostly on ground-based observations, which are expensive and spatially limited. Here, we demonstrate the benefits of space-derived ground deformation measurements for characterization of aquifer properties and groundwater levels. We use Interferometric Synthetic Aperture Radar (InSAR) time-series analysis of ERS, Envisat, and ALOS data to resolve 1992-2011 vertical ground deformation in the Santa Clara Valley, California. T-mode Principal Component Analysis successfully isolates temporally variable deformation patterns embedded in the multi-decadal time series. The data reveal uplift at 4 mm/yr between 1992–2000 and >1 mm/yr in 2000–2011, illustrating the end of the poroelastic rebound following recovery of hydraulic heads after the 1960s low stand. Seasonal elastic deformation with amplitude of 3 cm is observed over the confined aquifer sharply partitioned by the Silver Creek Fault (SCF). Integration of this deformation with hydraulic head data enables characterization of basin-wide aquifer system storativity. Additionally, we show that after a period of calibration, InSAR can be used to accurately characterize water level changes without well measurements.

Approach

We use over 100 SAR acquisitions from the ERS, Envisat, and ALOS satellites to produce ~300 interferograms covering 1992–2011. We then invert a network of small-to-moderate spatial and temporal baselines interferograms, following the Small Baseline (SBAS) technique (*Berardino,* 2002), to retrieve time-dependent ground displacement. We focus here on the vertical deformation that we isolate by combining ascending and descending viewing geometries (*Wright et al.,* 2004).

To separate transient patterns embedded in long-term trends without involving *a priori* models we use T-mode Principal Component Analysis (TPCA), a mathematical transformation of a set of inter-correlated variables into a new set of uncorrelated variables. The Principal Components (PCs) are a transformation of the time-dependent data into a set of representative spatial patterns of deformation, shown by the scores maps, which highlight a signal coherent in space but variable in time (Figure 2.33.1c). The variable gains through time are shown by the eigenvectors (Figure 2.33.1b).

Results

The change of slope of the Scree plot (Figure 2.33.1a) indicates that only the first three PCs need to be kept to represent over 90% of the data variance. The first PC corresponds to the longer-term deformation. Positive scores (red on Figure 2.33.1c) are observed in the Evergreen and Santa Clara basins. The eigenvector time series (Figure 2.33.1b, top) shows an increase (corresponding to uplift in positive-score areas) between 1992–2000 and remains nearly constant during 2000–2011. This pre-2000 uplift at 4 mm/yr can be either correlated with hydraulic head changes (short-period elastic aquifer deformation), or can be associated to delayed poroelastic rebound of aquitards due to their low hydraulic conductivity resulting in a lag of hydraulic heads compared to aquifers (*Terzaghi*, 1925). In the Santa Clara Valley, after the intense groundwater extraction of 1920–1965, artesian levels were reached in the early 1990 (*Galloway et al.,* 1999), which suggest that the post-1992 deformation is due to delayed aquitards poroelastic rebound.

The second and third PCs correspond to seasonal deformation as shown by their eigenvector time-series (Figure 2.33.1b bottom). PC2 consists of spatially extensive deformation encompassing most of the confined aquifer west of the SCF with an average peak-to-peak amplitude of ~2-2.5 cm (Figure 2.33.1c score map PC2). Peaks in PC2 occur immediately after rainfall, also confirmed by cross-correlation analysis, which suggests elastic deformation of a highly permeable aquifer system. PC3 is limited to a ~3 km wide region west of the SCF and has an average peak-to-peak amplitude of ~0.5-1 cm (Figure 2.33.1c score map PC3). Peaks in PC3 occur with a time lag of ~105 days, suggesting that it corresponds to a later phase of deformation, possibly due to delayed aquitards deformation.

Using hydraulic head data from the Santa Clara Valley Water District at 50 wells we normalize the seasonal ground deformation (PC2+PC3) by the head changes to constrain the storativity, *S* (*Burbey*, 2001). The storativity represents the volume of water taken into or released from storage per unit decline in hydraulic head, per unit area, and helps define sustainable pumping rates. *S* is roughly constant across most of the aquifer at ~2×10^{-3} (blue on Figure 2.33.2a), in agreement with values derived from traditional techniques (*Poland and Ireland*, 1988). Higher storativity near the shoreline, over the Holocene Bay mud (red on Figure 2.33.2b, constrained by one well) and around the SCF (constrained by three wells) are highlighted by this basin-wide study, with values representative of clays.

Finally, we evaluate how well seasonal water level changes can be predicted from the observed deformation and calculated storativity. We estimate the storativity using 1995–2001 deformation and water data, the first time period with good InSAR temporal sampling, and examine how well we can predict 2006–2011 hydraulic head changes from InSAR data of that period (second period with good temporal sampling). The mean prediction accuracy for each 2006–2011 season, defined as 100–(100*(observations-predictions)/observations) (*Wu et al.,* 1995) is of 70% for the entire basin (Figure 2.33.2b). The best accuracy is achieved in the confined aquifer west of the SCF, where the deformation and head changes are the largest.

Conclusion

We characterize the 1992–2011 hydrologically induced

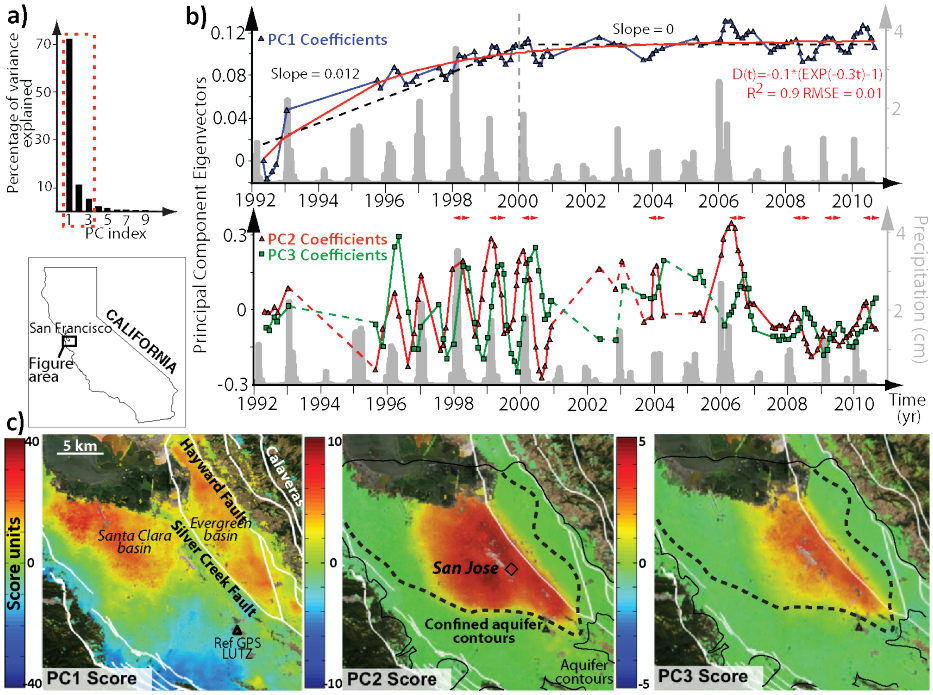

Figure 2.33.1: TPCA results for 1992–2011 InSAR SBAS vertical ground velocity in the Santa Clara Valley. a) Scree plot of the percentage of variance explained by each PC. b) Eigenvectors of PC1 (top) and PC2 and 3 (bottom) showing the temporal variability of the PCs deformation patterns. The red double arrows highlight PC2 and PC3 time lag. Grey bars show monthly precipitations. c) Scores maps showing the spatial patterns of the deformation of PC1, 2 and 3 (left to right). The score maps are converted to deformation by multiplying them by the eigenvector at a given time.

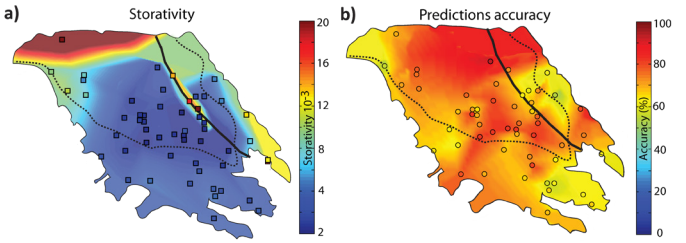

Figure 2.33.2. a) Aquifer storativity, from the ratio of seasonal deformation and head changes at the 50 wells (squares). b) Map of the mean prediction accuracy of the 2006-2011 seasonal InSAR heads compared to the measured 2006-2011 seasonal hydraulic heads.

ground deformation in the Santa Clara Valley, California, using InSAR time-series analysis. Poroelastic rebound of the aquifer system following recovery of hydraulic heads after the 1960s low stand occurs mostly prior to 2000, leading to uplift one order of magnitude smaller than its preceding subsidence.

Using TPCA we isolate temporally variable deformation embedded in the multi-decadal time-series without *a priori* constraints, which show the potential of TPCA for improving characterization of complex deformation. In the Santa Clara Valley two patterns of seasonal deformation exist, both sharply partitioned by the SCF, illustrating that the fault is a barrier to across fluid flow. Combining this seasonal deformation with hydraulic head data, enables characterizing of basin-wide aquifer system properties.

Finally, we show that InSAR-derived ground deformation can be used to evaluate basin-wide water level changes without well measurements with an accuracy of ~70%, which demonstrates its benefits for groundwater management.

Acknowledgements

We thank NASA for support through grant NNX12AQ32G and we thank the Santa Clara Valley Water District for their close collaboration and for sharing the hydraulic head data.

References

Berardino, P., G. Fornaro, R. Lanari, and E. Sansosti, A new algorithm for surface deformation monitoring based on small baseline differential SAR interferograms: *IEEE Transactions on Geoscience and Remote Sensing*, v. 40, no. 11, p. 2375–2383, doi:10.1109/TGRS.2002.803792, 2002.

Wright, T. J., B. E. Parsons, and Z. Lu, Toward mapping surface deformation in three dimensions using InSAR: *Geophysical Research Letters*, v. 31, no. 1, doi:10.1029/2003GL018827, 2004.

Galloway, D., D. R. Jones, and S. E. Ingebritsen, Land subsidence in the United States. US *Geological Survey Circular 1182*, 1999.

Terzaghi, K., Principles of soil mechanics: IV; settlement and consolidation of clay: *Erdbaummechanic*, v. 95, no. 3, p. 874–878, 1925.

Burbey, T. J., Stress-Strain Analyses for Aquifer-System Characterization: *Ground Water*, v. 39, no. 1, p. 128–136, 2001.

Poland, J. F., and R. L. Ireland, Land subsidence in the Santa Clara Valley, California, as of 1982: U.S. *Geological Survey Professional Paper*, 497-F , 1988.

Wu, G., M. Baraldo, and M. Furlanut, Calculating percentage prediction error: a user's note: *Pharmacol Res*., v 32, no. 4, p241-8, 1995.

34 TremorScope: Imaging the Deep Workings of the San Andreas Fault

Roland Bürgmann, Richard Allen, Douglas Dreger, Robert Nadeau, Barbara Romanowicz, Taka'aki Taira, Margaret Hellweg

Introduction

Until recently, active fault zones were thought to deform via seismic slip during earthquakes in the upper, brittle portion of the crust, and by steady, aseismic shear below. However, in the past decade, this view has been shaken by seismological observations of seismic tremor deep in the roots of active fault zones. First recognized on subduction zones in Japan and the Pacific Northwest, tremor has also been found to be very active on a short section of the San Andreas to the southeast of one of the most densely monitored fault segments in the world, near Parkfield (*Nadeau and Dolenc*, 2005). This deep (~20–30 km) zone of activity is located right below the nucleation zone of the great 1857 Fort Tejon earthquake. Thus, learning more about the temporally and spatially complex faulting processes in this zone may help us better understand the conditions that lead to such large ruptures.

The Project Plan and Implementation

The tremor source region is southeast of existing seismic networks around Parkfield, along the San Andreas Fault. We are adding eight seismic stations, the TremorScope (TS) network, in this area to complement existing instrumentation.

In the past year, TS activities have been concentrated on drilling, casing and instrumenting the four boreholes. In the summer of 2013, we hosted walk-throughs for prospective drilling companies in preparation for their bids. Drilling began in November, following the selection of the drilling company.

Since the landowner at seismic station TPPG had leased acreage near our site for oil exploration, we sought an alternative and found a site near the San Andreas Fault near the intersection of Bitterwater Road and Bitterwater Valley Road (Figure 2.34.1). Drilling at all four sites, TRAM, TRAY (Figure 2.34.2), TCAS and TSCS was completed in early April. TSCS

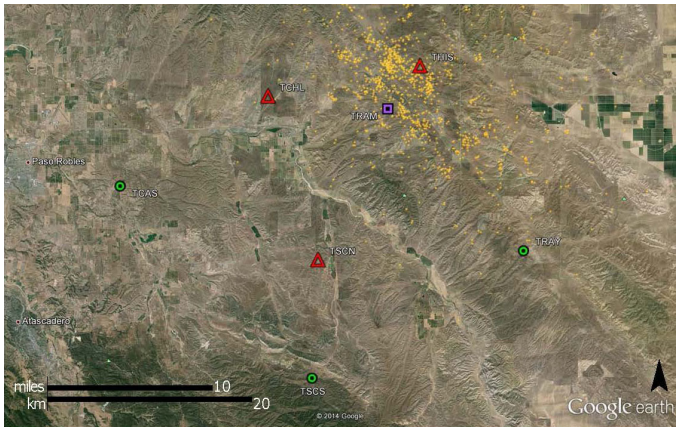

Figure 2.34.1: Google Earth image showing the locations of the TremorScope stations. Circles and triangles indicate borehole and surface sites, respectively. The square marks TRAM, the site with both surface and borehole deployments.

Figure 2.34.2: Drilling commences at TRAY in early March.

is 750 ft deep and from a depth of 350 ft onward is in solid rock. The other three boreholes are 1000 ft deep and mostly in softer material. All exhibit very little drift. The boreholes are cased with Schedule 21 PVC, with an inner diameter of 6 inches. We hope this proves to have less electrical noise than a steel casing would, and also that it provides more protection from lightning strikes and lower resonances.

Huts have been installed over the boreholes to offer a mounting surface for the solar panels which will power the stations, but also to provide protection for the equipment from the sun and cattle (Figure 2.34.3). The borehole sites will have an accelerometer installed at the surface in the hut.

TS data are used in real-time earthquake monitoring (see Operational Section 4.7), as well as for tremor studies. Data from the four surface stations are now being archived and analyzed. In addition to contributing to investigations of tremor, the TS stations also improve our ability to characterize the seismicity in the region. Figure 2.34.4 shows details of the rupture of the December 12, 2013 M_w 4.1 earthquake in nearby Lost Hills, CA, determined from TS data using empirical Greens function deconvolution.

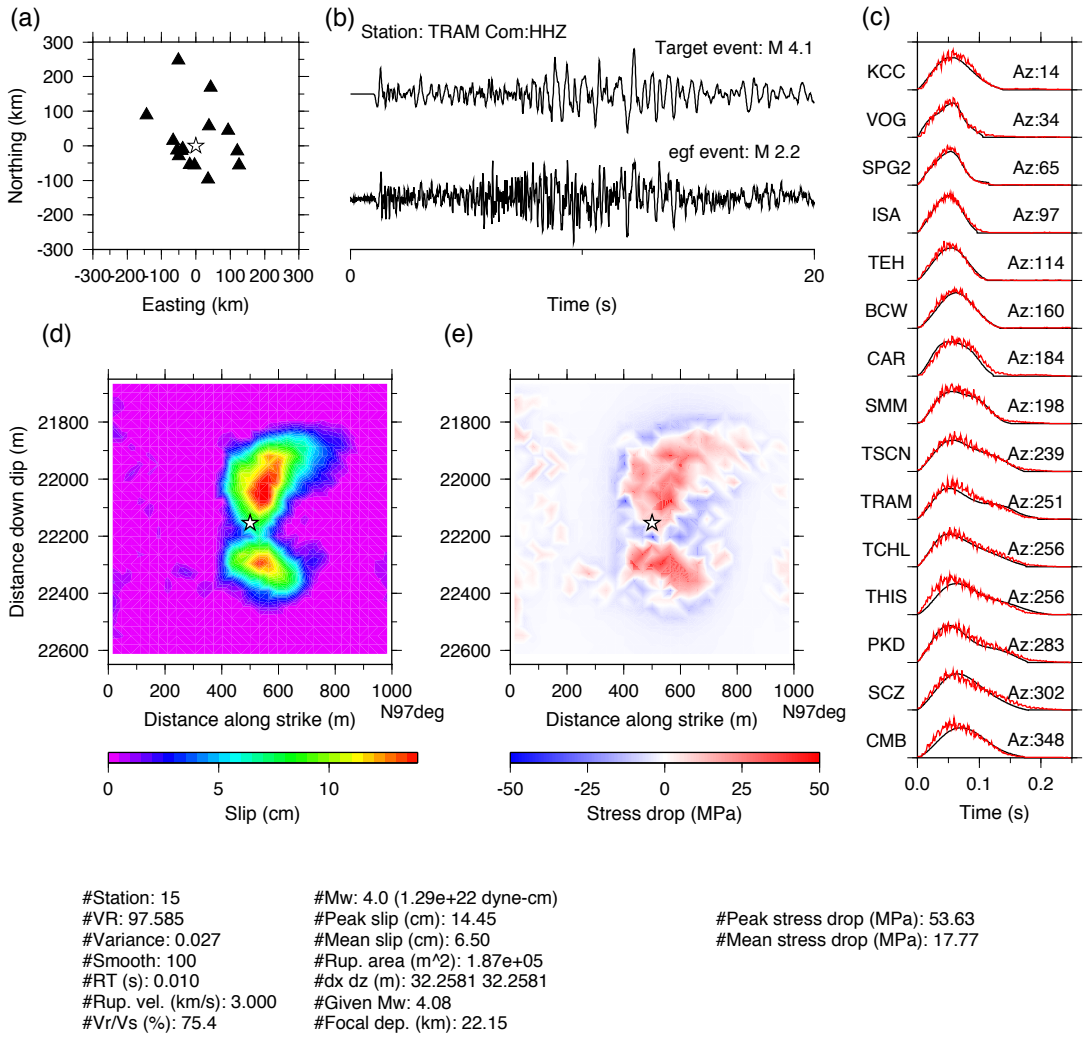

#Station: 15
#VR: 97.585
#Variance: 0.027
#Smooth: 100
#RT (s): 0.010
#Rup. vel. (km/s): 3.000
#Vr/Vs (%): 75.4

#Mw: 4.0 (1.29e+22 dyne-cm)
#Peak slip (cm): 14.45
#Mean slip (cm): 6.50
#Rup. area (m^2): 1.87e+05
#dx dz (m): 32.2581 32.2581
#Given Mw: 4.08
#Focal dep. (km): 22.15

#Peak stress drop (MPa): 53.63
#Mean stress drop (MPa): 17.77

Figure 2.34.4: Triggered tremor in the surface waves of the April 11, 2012, M8.6 earthquake which occurred off the West Coast of Northern Sumatra. Tremor is apparent in the records of HRSN stations CCRB and MMNB as well as at TremorScope station TSCN.

Figure 2.34.3. Installation of the surface hut at TRAM. Solar panels will be mounted on the south-facing roof. The door is 8 ft tall to allow access for installation of borehole equipment.

Perspectives

Data from the TremorScope project are improving earthquake monitoring in the region south of Parkfield. Insights from the project will also contribute to understanding tremor and slip in other regions of the world that are not nearly as accessible. Should a great San Andreas earthquake occur during this experiment, the network will also provide unprecedented and exciting insights into the seismic rupture process. More information about the Tremorscope Project can be found at http://seismo.berkeley.edu/research/tremorscope.html

Acknowledgements

This work is funded by grant 2754 from the Gordon and Betty Moore Foundation.

References

Nadeau, R., and D. Dolenc, Nonvolcanic tremors deep beneath the San Andreas fault, *Science*, 307, 389, doi:10.1126/science.1107142, 2005.

35 Normal Modes: Investigating Signal and Noise Phenomena Across Instrument Types and Deployment

Margaret Hellweg, Taka'aki Taira, Robert A Uhrhammer, Eiichiro Araki (JAMSTEC), Horst Rademacher, Murray McGowan (Guralp)

Introduction

Whether a seismic signal in a certain frequency band can be detected in a recording depends primarily on four factors: the amplitude of the signal at the site, the conditions at the site which affect the ambient noise in that band, the sensitivity and self-noise of the sensor in the band, as well as the sensitivity and self-noise in the digitizer in the band. For the very long period band, between 1.0 and 5.5 mHz, the normal modes provide an excellent signal for exploring the effects of the latter three contributions, since after a large or great earthquake, their amplitudes are similar all over the earth.

The Data

In the past, observatory equipment in an observatory setting were required to observe them. We observed normal modes in the 1.0-5.5 mHz band with good signal-to-noise ratio in the aftermath of the M_w 8.3 Sea of Okhotsk deep earthquake on May 24, 2013 at many stations of the Berkeley Digital Seismic Network and at other stations in other networks. They are equipped with a variety of sensors, including those with a flat passband extending to frequencies lower than the normal modes, and digitizers (Table 2.35.1). They are also deployed in a variety of geologic settings, including cabled ocean bottom stations, like MOBB in California, the Japanese cabled "Dense Ocean-Network for Earthquake and Tsunamis (DONET)" and the IODP seafloor borehole in the south of Japan (Table 2.35.1). The sites have varying physical infrastructure and site preparation.

Observations

Figure 2.35.1 allows one to explore the factors that contribute to the observation of the normal modes on vertical and horizontal components at a suite of amplitudes of excitation. It shows normal mode spectra from a suite of recent earthquakes with magnitudes between 7 and 9.1. Signal-to-noise ratios for the normal modes for a given magnitude of earthquake vary more by deployment type and location than by instrumentation.

Table 1. Stations, equipment and deployment

Station	Seismometer	Data Logger	Deployment
BKS	STS1	Q330	Tunnel
CMB	STS1	Q330	Vault
HOPS	STS1	Q330	Vault
KCC	STS1	Q330	Tunnel
MHC	STS1	Q330	Pier in buliding
SAO	STS1	Q330	Vault
SCZ	STS1	Q330	Old adit (10m)
ORV	STS1	Q330	Pier in building
YBH	STS1	Q330	Old adit (35m)
BDM	STS2	Q330	Old adit (150m)
BRK	STS2	Q330	Pier in building
CVS	STS2	Q330	Wine tunnel
FARB	STS2	Q330	Vault
GASB	STS2	Q330	Vault
HUMO	STS2	Q330	Old adit (100m)
JCC	STS2	Q330	Vault
JRSC	STS2	Q330	Vault
MNRC	STS2	Q330	Vault
MOD	STS2	Q330	Tunnel
PACP	STS2	Q330	Surface vault
PKD	STS2	Q330	Vault
WDC	STS2	Q330	Tunnel (50m)
WENL	STS2	Q330	Wine tunnel
HATC	STS2	Q330	TA vault
HAST	STS2	Q330	TA vault
HELL	STS2	Q330	TA vault
MCCM	STS2	Q330	Vault
RAMR	STS2	Q330	TA vault
SUTB	STS2	Q330	TA vault
BRIB	CMG-3T	Q330	Posthole (10m)
BL67	CMG-3T	Q330	Surface vault
TCHL	CMG-3T	DM-24	TS vault
THIS	CMG-3T	DM-24	TS vault
TRAM	CMG-3T	DM-24	TS vault
TSCN	CMG-3T	DM-24	TS vault
VAK	CMG-3T	Q330	Tunnel
WOL	CMT-3T	DM-24	Borehole (80m)
MOBB	CMG-1T	DM-24	OBS
BHC2	CMG-3T	DM-24	OB borehole (910m)
KMB05	CMG-3T	DM-24	OBS
KMB08	CMG-3T	DM-24	OBS
KMC09	CMG-3T	DM-24	OBS

Figure 2.35.1: Normal modes in the frequency band between 1.5 and 5.5 mHz. The top panel shows normal modes from the vertical channels. For the bottom panel, the normal mode spectra from the two horizontal channels have been summed. All spectra are normalized to 1. Where the traces are missing, no data are available from that station for the earthquake. Station equipment and deployment conditions are listed in Table 2.35.1.

Chapter 3

Broadening Engagement

1 Earthquake Research Affiliates Program

Introduction

The Earthquake Research Affiliates (ERA) program at the Berkeley Seismological Laboratory (BSL) promotes the support of seismological research through industrial and governmental involvement. The affiliates program produces a newsletter, provides a mechanism to link industry and public sector groups with interests in BSL research, and provides an opportunity for resiliency organizations to interface with earthquake science.

Earthquake Research Affiliates Program

The BSL draws on the diversity of the interdisciplinary earthquake and solid earth research community at UC Berkeley. Augmenting these efforts, the ERA program provides a forum for the exchange of ideas and information between industry and public sector organizations with an interest in BSL research and the scientists themselves. The mission of the ERA program is to inspire, nurture, and sustain vibrant public-private and industrial-academic partnerships focused on the development and use of innovative earthquake information products, including alert services, and other novel seismological measurement technologies. The program is designed to promote the application of new research results and technology, and to provide a forum for inviting optimal and essential users to participate in the development and testing of new technologies, with the goal of introducing them into the marketplace. Current ERA members include the Bay Area Rapid Transit District (BART), the University of California, Berkeley Police Department, (UCBPD), the San Francisco Department of Emergency Management (SFDEM), and Google.

Regular interaction with each group is a key aspect of the program. Recently, we have expanded our engagement with the SFDEM to include SF Fire, Police, 311, 911, SFO Airport, the Real Estate division, Public Works, and the MTA. This expansion allows us to begin to work toward uses and automated controls for earthquake early warning messages on a city-wide scale. Monthly meetings with our counterparts at Caltech and the University of Washington are supporting this endeavor.

Senate Bill SB135 Signed into Law

A California bill calling for the creation of a public earthquake early warning (EEW) system for the state was put forward by State Senator Alex Padilla (D-District 20) and unanimously passed both the Senate and the Assembly. In September of 2013, Governor Jerry Brown signed the bill into law, which tasks the California Governor's Office of Emergency Services (CalOES) with defining funding sources to support the build-out and operations costs for the project.

The Berkeley Seismological Laboratory, and in particular Director Richard Allen, have been intimately involved in providing support and scientific expertise for this endeavor. Dr. Allen and Dr. Jennifer Strauss made several trips to the State and Federal Capitol to inform and update legislators on the Shake Alert system, and Dr. Allen has provided testimony at key points during the bill's progress.

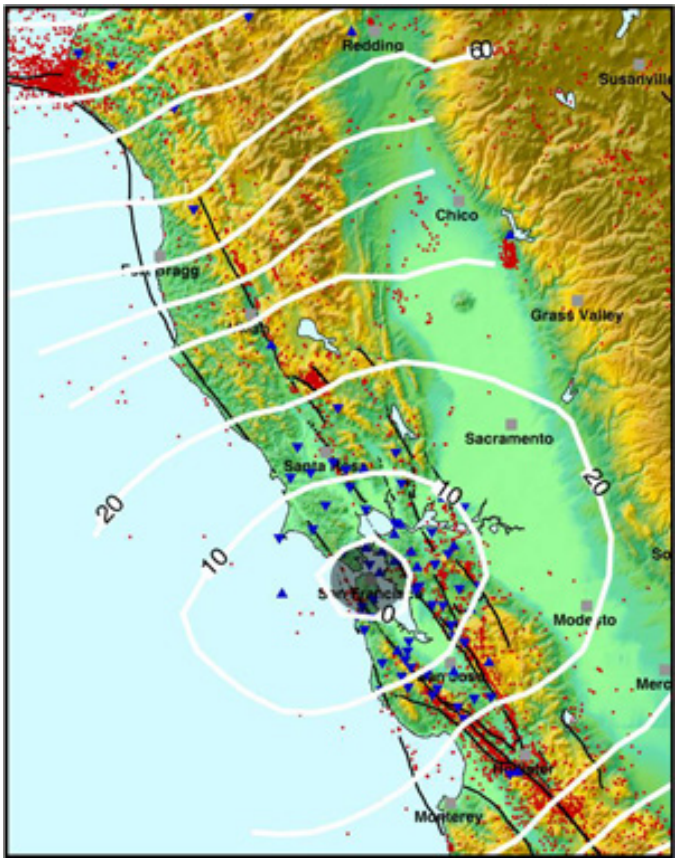

Figure 3.1.1: The lines on this map show warning times for San Francisco for major earthquakes at various locations, which are quickly detected by an early warning system. The gray area marks the "blind zone." There will be no warning for earthquakes in this area.

CalOES Working Groups

Dr. Allen, Dr. Strauss, and Dr. Hellweg were part of CalOES' California Earthquake Early Warning System (CEEWS) working group. This group drafted the charter, discussed stakeholder roles and responsibilities, and crafted a proposal to establish committees and address charter objectives. The CEEWS charter was approved in early 2014, and in May the kickoff meetings to brief interested working group parties were held in Northern and Southern California.

CalOES is now moving forward with an implementation plan to create the system by establishing committees of subject matter experts. The BSL is involved in the Management, Model, Standards, Steering, and Education and Training committees for the CEEWS. Of most interest to the ERA members is the Education and Training committee. Dr. Strauss is interfacing with ShakeAlert beta testers (see 2013 BSL Annual Report section 3.1) and the rest of the committee to ensure that active users have a platform to share their experience with the system. The

experience of beta users such as the SFDEM (see below) will be crucial as it gives a real world outlook and solutions moving forward.

San Francisco EEW Group

This year the San Francisco ERA participants have significantly increased their interaction with the earthquake early warning system beta test. Over a period of six months, various city agencies including those dealing with fire, police, hospitals, and airports have come together for monthly meetings, coordinated by Dr. Strauss, to learn about the ShakeAlert system and start developing their own procedures for earthquake alert response.

The various agencies have installed the UserDisplay and are drafting response action matrices applicable to their particular needs. The agencies are coming together to determine which needs are common amongst all agencies, and which are agency specific. The goal is that the commonalties can all be addressed under one umbrella. Now that the initial meetings have concluded, the agencies are fleshing out what will be required to meet all of their desired automated actions and controls. This is an important step, because some actions and controls might be quick and inexpensive to implement, whereas others might require new funding requests, policy changes, or collaborations that need to be looked into.

100 Resilient Cities

The City of San Francisco, along with Alameda, Berkeley, and Oakland, was selected for the first round of the Rockefeller Foundation Centennial challenge of 100 Resilient Cities. The 100 Resilient Cities offers a unique opportunity to have a regional conversation about shared resilience risks and opportunities. As a 100 Resilient Cities member, the four Bay Area cities have a great opportunity to strengthen their resilience commitment via:

1. Grant funds to hire a Chief Resilience Officer (CRO) who will lead the development and implementation of the City's resilience strategy.
2. Technical support in the development of the City's resilience strategy.
3. Membership in the global 100 Resilient Cities network.
4. Access to a platform of resilience-building tools.

The ERA program interaction with resiliency agencies around the Bay Area prompted Dr. Strauss to receive an invitation from San Francisco's Mayor Lee to participate in the Agenda Setting Workshop March 17–18, 2014. There, she was able to present the ShakeAlert project to other resiliency groups and the ERA members who are helping to drive the effort.

3rd International Conference on EEW

The BSL is organizing the 3rd International Conference on EEW for September, 2014. This three-day meeting will facilitate implementation of earthquake alerts. The event will bring together scientists, policy makers, engineers, social scientists, and business representatives from public and private sector institutions to examine the state of the art in earthquake early warning today and to innovate new ways to push the technology forward. Channeling the experience of these interdisciplinary groups, the meeting will address current challenges, lessons learned from systems currently in operation worldwide, and ultimately forge a path toward fulfillment of public early warning systems in the U.S. and around the world.

ERA members will play a crucial role in this meeting. Unlike the previous two international meetings (held at Caltech and Kyoto University), the aim of this conference is to provide the perspectives of the end user with a more prominent role. ERA members will be able to engage other industry groups from around the world, and get a taste of best practices for automated controls, alert mechanisms, and general hazard mitigation involving early warning.

Continuing Engagement

The ERA program continues to seek out new avenues to foster continuing engagement between seismologists and outside industry and government groups. Dr. Strauss spoke at the Business Recovery Managers Association's July 2013 Membership Meeting in Oakland, CA on July 25, 2013 about shaping response and recovery with Earthquake Early Warning. She gave a similar presentation to the California Emergency Services Association's Annual Training Conference in Santa Rosa, CA on October 16, 2013. She also spoke directly to city resiliency leaders at the San Francisco Planning and Urban Research Association Lunchtime Forum later that same month.

Interactions with other groups, including the San Francisco Office of Earthquake Safety, the Lifelines Council, and the Community Action for Seismic Safety groups, is ongoing.

Acknowledgements

Jennifer Strauss heads the Earthquake Research Affiliates program with oversight by Richard Allen and Peggy Hellweg. Jennifer Strauss and Peggy Hellweg contributed to the preparation of this section.

2 Engaging the Public

Introduction

One of the core missions of the Berkeley Seismological Laboratory is to enable the broad consumption of earthquake information and solid earth science through education and outreach to all sectors of society. While many of our outreach and education activities focus on lectures, tours, and public events, we also engage the public through collaborative initiatives and products. Highlights from this year include contributions to Bloom, MyQuake, and Science on a Sphere.

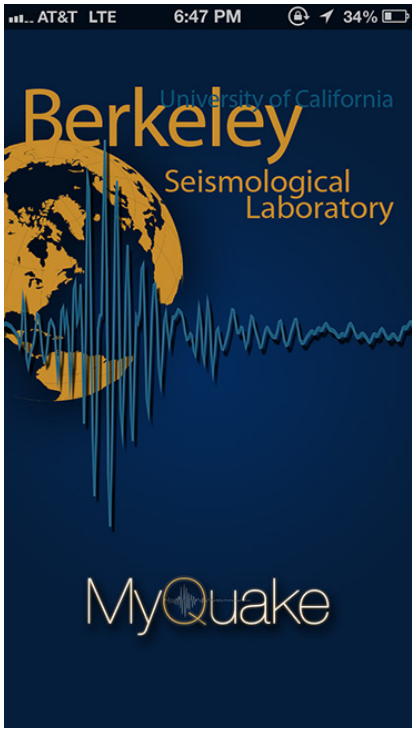

Figure 3.2.2: Opening screen for the BSL's new iPhone app: MyQuake.

MyQuake

The MyQuake app (released in July 2013) is the product of an undergraduate student research project in collaboration with the BSL. Rohan Agarwal (computer science) and Cora Bernard (geophysics) developed the app.

MyQuake maps earthquakes that occurred recently in the California region and across the globe. It also provides information about large damaging historic earthquakes in California, and calculates the shaking intensity at user-defined locations for both the historic and current earthquakes. For example, it calculates that at Berkeley, the shaking for the 1868 Hayward earthquake was Intensity VII, while for the 1906 Great San Francisco earthquake it was Intensity VIII. The app then links to videos that show what it is like to experience shaking of that intensity.

MyQuake is completely ad-free and provides a smooth, intuitive user interface to facilitate learning about earthquakes, keeping the user informed and preparing them for the next big earthquake.

MyQuake is available for free at the iTunes store. Since launching, the app has been downloaded approximately 8000 times and users are accessing the USGS recent earthquake pages around 50 times on a given day. They are also accessing the earthquake history and the tips pages. This means that users are actually using the app and learning more about earthquakes and earthquake preparedness.

Science on a Sphere

In partnership with the Lawrence Hall of Science (LHS), the lab is developing earthquake-related content for joint display on a flat screen, together with NOAA's Science on a Sphere (SOS, http://sos.noaa.gov/What_is_SOS/). The goal of SOS is to amass display products and project them on a six-foot diameter sphere to foster education and discovery in the realm of environmental processes. The final products from boith institutions will be made available to both the Science on a Sphere members and to the IRIS Active Earth Display Kiosk (IAEDK) network (see http://www.iris.edu/hq/programs/education_and_outreach/museum_displays/active_earth). The BSL is tasked with content and scientific accuracy for this project, while the LHS is in charge of technical aspects and evaluation of pedagogical content.

The BSL's contributions consist of two main themes: "Seismic Waves" and "Disasters". This year, Jennifer Taggart, Clay Miller, and William Hawley have assembled content, media, and graphics for inclusion on the IAEDK slides and popups, with a focus on three earthquake-related disasters: Liquefaction, Tsunamis, and Building Collapse. The Tsunami slides explain tsunami generation and discuss the 2011 Tohoku and 2004 Sumatra tsunamis. Building collapse compares and contrasts the 2010 Haiti disaster with the low level of shaking damage in Sendai after the much larger Tohoku earthquake. Finally, the liquefaction slides explain what liquefaction is and give examples of how it can be dangerous (infrastructure damage during the 2011 Christchurch earthquake, landslides in the 2008 Wenchuan earthquake, buildings tilting and then toppling over in a 1964 Japan quake, San Francisco Marina district damage after the 1989 Loma Prieta quake).

We exhibited a scale model of the project at the American Geophysical Union (AGU) fall meeting in San Francisco in December 2013 to gather feedback about the user experience as well as the science presented.

After implementation of the feedback we received, we started drafting content for additional content. Jennifer Taggart and Clay Miller added content about seismic waves and William Hawley added content describing how seismic waves can be used to image the interior of the earth. These topics allow the

Figure 3.2.3: The redesigned homepage of the Berekeley Seismological Lab. Notice the real-time earthquake map that organizes earthquakes by date and magnitude.

BSL to present a little more scientific content than was involved with the previous themes. In addition, the BSL contacted Alan Jones, from Binghamton University in New York, who has written various graphical displays of seismic waves. With feedback from the BSL and the LHS, he modified existing codes to create several beautiful animations that can be displayed on the sphere. The animations made in this process will become part of NOAA's public SOS database, usable by anyone in the world.

BSL Website

This academic year, the BSL's web pages went through several phases of modernization. The most prominent change is the real-time earthquake map on our homepage. Visitors to the homepage are now greeted with a dynamic map showing all earthquakes detected in California. Earthquakes appear in real time as squares, colored by age in days and sized by magnitude in order to give the most emphasis to the earthquakes likely to be felt widely. Each individual square can be clicked on, initiating a popup balloon containing the event's magnitude, date and time, depth, and distance to the nearest town, as well as links to ShakeMaps and other earthquake information products. Users can zoom and pan to explore earthquakes around the world as well as in particular regions like The Geysers, CA. When an earthquake above magnitude 3.5 occurs in the state's reporting area, the default map zooms to that earthquake and stays there for 48 hours (or until a larger earthquake happens). A manual override allows BSL seismologists to hold the map's focus at a particular point, should one or more events of particular interest occur.

In addition to the real-time earthquake map, the homepage is complemented by a slideshow and clickable carousel created from the popular jQuery plugin, bxSlider. Our navigation menu has been improved to funnel visitors toward the pages most relevant to them. Visitors now hover over a menu item describing who they are, such as "For Researchers," which triggers a two-column dropdown menu containing an organized list of pages targeted toward their interests. Last but not least, the BSL webpages are now served up as http://earthquakes.berkeley.edu as well as our old URL, http://seismo.berkeley.edu.

The BSL continues to educate and inform the public through our webpages, providing a seismology blog (http://seismo.berkeley.edu/blog), videos, an earthquake FAQ, and resources for teachers and those who wish to dig deeper. Our "seismic networks" web pages also serve the research community, providing detailed information about each of our seismic stations.

Social Media

The BSL has long been committed to public outreach, and in this digital age, we have expanded the ways in which we can share information with the public by creating a Twitter profile as well as a YouTube page.

The BSL created the twitter account with the handle of @BerkeleySeismo to send interesting and timely tweets out to a broad, global audience. Twitter is a fantastic platform for the BSL to reach a wide audience due to its prevalence and popularity, as well as its functionality as a *de facto* news aggregator. We send tweets on a regular basis that feature exciting new research, public safety, seismic history, the BSL's Seismo Blog, BSL events or other seismic information. The BSL has gained 237 followers in a short amount of time with more following us all the time.

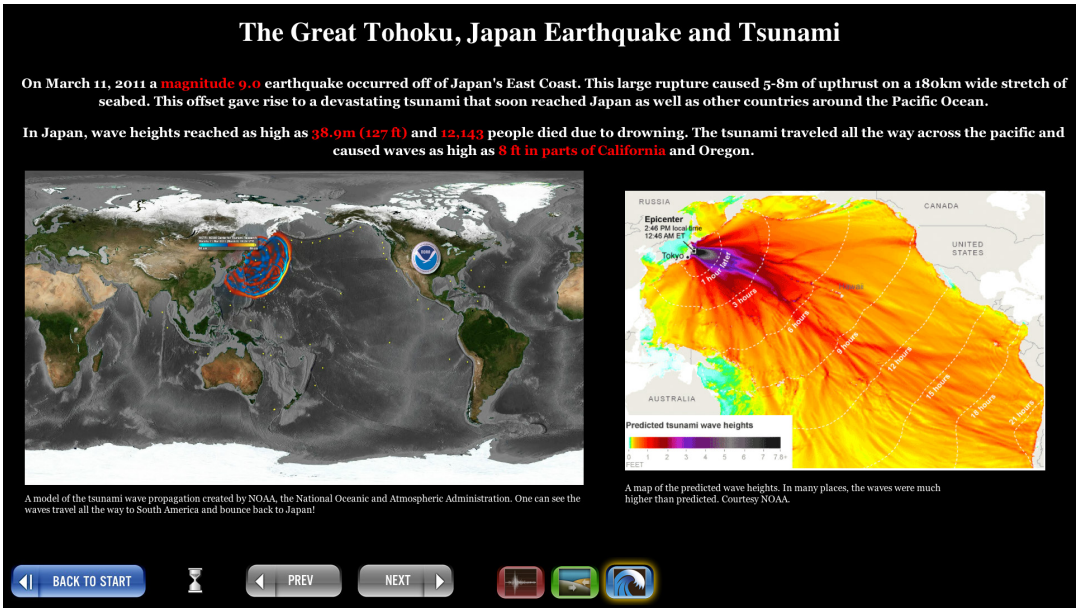

Figure 3.2.4: One of the slides of the IRIS AED the BSL has customized and displayed in McCone Hall. This slide has an animation of wave propagation from the tsunami caused by the *M*9.0 Tohoku earthquake. The image to the right shows predicted wave heights of the tsunami.

Follow us for BSL updates!

Another Social Media outlet the BSL has utilized in the past year to reach a broader, more global audience is YouTube. The BSL has many great videos for the public, and we are constantly creatng more. YouTube was an obvoius outlet to showcase these videos. We have put up several videos of past Lawson Lectures, as well as several other informative and engaging videos, most notably the well made series on a recent scientific cruise that took place in the summer of 2014. Our YouTube page can be found at https://www.youtube.com/user/BerkeleySeismoLab.

The BSL webpages now feature icon links in the top right for Twitter, YouTube, and RSS Feed easy access.

Media

This year, the BSL continued its outreach to the public by providing numerous and varied media sources with interviews and information. The bulk of media requests we get are for newspaper and other print sources; however, we also gave interviews to KQED, a public radio station, as well as to MBC, a Korean broadcasting company. This year was particularly important and busy for media inquiries due to the pronounced status of our Earthquake Early Warning efforts. There were several major events that caused particular interest, including a recent cooperation with Bay Area Rapid Transit (BART) and the announcement of California Senate Bill 135 (see Broadening Engagement Section 1).

DOIs

The BSL has made a much more dedicated effort in the past few years to keep track of metrics about data usage at the lab. It is important for us to know who is using our data and how often it is being used, both in terms of how much data are downloaded from the NCEDC (see Operations Section 4.8) and how often data the BSL collects is used in scholarly journals. The latter part of this goal was especially difficult to discern due to a lack of consistency with how authors cite the BSL/NCEDC. In order to fix this problem, the BSL has created DOIs (digital object identifiers) for various data realms one might use in research. A DOI is a commonly used identifier that refers to a specific and unique data set. We have created four DOIs—one for the NCEDC, BK seismic network, BP network, and BARD network. In addition to the DOI, there are metadata associated with each DOI where we can detail such information as contributing organizations and institutions, the archive date range, and the relationship between the four DOIs. We chose to create custom DOIs for ease of use. The four DOIs are: DOI:10.7932/BDSN, DOI:10.7932/HRSN, DOI:10.7932/NCEDC, DOI:10.7932/BARD for the BK network, the BP network, the NCEDC and the BARD network respectively.

The most important part of the DOI, however, is that it is pithy and we can greatly reduce our citation length. For each of the four DOIs, we have rewritten our citation statement to make it simpler and shorter, as well as made it more visible on the NCEDC website.

Displays

In addition to the more modern look of the BSL's web pages, we have also added several engaging displays throughout our building (McCone Hall) to encourage public education, awareness, and fascination.

In the first floor lobby we have showcased an interactive display that allows visitors to explore current earthquakes and learn about the science of earthquakes. The display was created using an IRIS web-based Active Earth Display (AED) template. The template allows the BSL to create up to 25 unique slides with completely customized content that users can cycle through using a touch pad. The 25 slides are broken into three

categories and users can click on the category they want to view. When the display has been inactive for five minutes, it reloads the home slide, which is a real-time seismogram of the last three days of data from station BKS.BK, located on the UC Berkeley campus. The display is shown on a large monitor, and it has been optimized for our specific setup. However, it is web-based, so it can be accessed anywhere. If one wishes to view the display, he or she can go to http://www.iris.edu/aed2/index.phtml?code=BSL2012.

On the 2nd floor of McCone Hall, with the same setup as in the 1st floor lobby, we have a looping Google Earth tour fly-through. The tour shows viewers faults and historic earthquakes in California and takes them to the sites of a few of our stations, including an underwater site. It does all this by seamlessly "flying" from place to place, taking advantage of Google's visually stunning databases of topography and city data.

In addition to this Google Earth fly-through, this year we have updated the wall on which the monitor is stationed. Thanks to Jennifer Strauss, we have a beautiful display of historic and informative photos and text concerning Bay Area seismicity, including images from the Loma Prieta, 1906, and 1868 earthquakes.

In the BSL conference room, we have three different displays running on four monitors. On one of the monitors is a seismogram from the last four days of data from station BKS.BK, a seismic station located on UC Berkeley's campus. The data is displayed through the SWARM program. We also use the SWARM program to create a vibrant map of California, overlaid with the location of our BK network of seismic stations. We have enabled a few of these stations to show the last 10 minutes of data in real time. With these seismograms displayed throughout the state, one can see seismic activity throughout California in real time.

On our last monitor, we alternate between two programs. The first and most common is *seisnetwatch,* and the other is the California Integrated Seismic Network (CISN) User Display. *Seisnetwatch* is a tool the BSL uses to monitor station quality and health. It allows us to see the stations of the Berkeley Digital Seismic Network (BDSN) and their health for the past month. The CISN User Display is part of an effort at the BSL to create a Earthquake Early Warning System (EEWS) (see Broadening Engagment Section 1). The display will issue an alert of an earthquake before strong shaking is felt at our location (provided the epicenter is not too close).

Acknowledgements

Peggy Hellweg oversees the Public Engagement projects at the BSL. Stephane Zuzlewski created the earthquake map for the BSL homepage. Our seismology blog is written by Horst Rademacher.

Special acknowledgements to our external collaborators: Ken Goldberg, Rohan Agarwal, and Cora Bernard, Toshi Komatsu and Gretchen Walker at LHS. Jennifer Taggart, Clay Miller, Peggy Hellweg, and Jennifer Strauss contributed to the to the preparation of this section.

3 Science and Society

Introduction

BSL faculty, staff, and graduate students are involved in a wide variety of outreach activities, ranging from public lectures to tours of the Hayward Fault geomorphology on campus. This year, we continued our involvement in CalDay and other traditional activities, and also helped a few teams competing for the First Lego League.

Lawson Lecture

The Lawson Lecture is a free, public lecture hosted by the BSL each year around the anniversary of the 1906 San Francisco earthquake. This year, on April 16, 2014, Dr. Lori Dengler gave listeners "A California view of the 1964 Alaska earthquake: lessons learned, forgotten, and relearned about reducing tsunami vulnerability". The lecture was held in the Banatao Auditorium of Sutardja Dai Hall on campus and for the second year, was followed by a light reception.

Prof. Dengler is an expert in earthquake and tsunami hazards and hazard mitigation. She was a member of the team that developed the National Tsunami Hazard Mitigation Program and the author of the first Strategic Implementation Plan for Mitigation Projects for the tsunami program. Prof. Dengler guided those present on a tour of the tsunami program, then versus now.

Her talk described how, at the time of the 1964 Great Alaska Earthquake, U.S. tsunami hazard was considered a Hawaiian problem. On March 27, 1964, it took over three hours for a tsunami alert bulletin to reach California. Crescent City—California's northernmost coastal city—did not begin notifying vulnerable residents until a half hour before surges arrived. In Crescent City, the tsunami killed ten, flooded 29 blocks, damaged or destroyed nearly 100 structures and led to permanently altering the downtown area. The tsunami also caused damage in other California coastal areas, killing a person in Bodega Bay and Los Angeles, destroying boats and docks in San Francisco Bay and wreaking havoc on many areas of the coast. This talk recounted the events of 1964 from a California and Crescent City perspective, traced mitigation measures taken after the tsunami, and examined how California's tsunami hazard and tsunami mitigation efforts have changed in the past five decades.

The Lawson Lectures are viewable as a Flash video at http://earthquakes.berkeley.edu/news/lawson_lecture.html.

First Lego League

Members of the BSL were interviewed by several teams during the First Lego League 2013 Nature's Fury Challenge. The First Lego League is a robotics competition for 9–16 year olds. This year, the theme was Nature's Fury. Teams programmed an autonomous Lego Mindstorms robot to score points on a playing field reflecting various natural disaster scenarios. They also had to identify a natural disaster problem and develop a solution to it.

Figure 3.3.1: From top left clockwise: The Tornado of Ideas and their team captain with their ticket to the state competition, Jennifer Strauss and Michael Faggetter with the Rovers, and Ronni Grapenthin with the Robo Maniacs team.

Beginning in October of 2013, several Lego League groups began contacting the BSL to request interviews from the scientists about earthquake hazards (see Figure 3.3.1). They learned the basics of earthquakes, how shaking can impact buildings and people, and how we measure the earthquake's severity. They also got feedback and asked advice about their team's solution to their chosen natural disaster problem.

A subset of the teams we helped kept in touch and sent us updates on their progress through the competition. The Robo Maniacs team of 5th and 6th graders came in 1st place in the first level qualifier. The Tornado of Ideas group qualified for the state competition in South Carolina and received a Core Values award. We held those interviews over Skype, since they could not take a field trip to California to speak with the BSL in person. The youngest group, the Rovers, were only 8 and 9 years old, but were so hooked on the competition that they are prepared to compete again next year.

CalDay—BSL Open House

The weekend before the Lawson Lecture, the Seismo Lab participated in UC Berkeley's open house for prospective students and general day of fun for community members: CalDay. Many departments have exhibits and demonstrations for everyone and every interest. The Berkeley Seismological Lab is proud to share in this tradition. Visitors learned about earthquakes, plate tectonics, tsunamis and more. Younger guests got to jump up and down to create their own earthquake and received a seismogram of the output. They also explored seismic waves using giant springs and received a stamp in the Science@Cal passport. All guests watched BSL seismic data in real time through the SWARM application running in the conference room.

CalDay ran from 10:00 AM–3:00 PM on Saturday April 12, 2014.

Tours

During 2013–2014, many groups, ranging from middle-school students to international guests, visited the BSL for talks, tours, and hands-on science experiences.

For most of this fiscal year, the tours involved groups from the First Lego League, mentioned above. In October, Jennifer Strauss and Qingkai Kong gave a laboratory tour and discussed Earthquake Early Warning with researchers from Beijing.

On February 6th, Larry Hayne's Richmond-area 2nd grade class visited the Seismo Lab. About 25 children, plus their adult chaperones had a hands-on introduction to seismology. Ronnie Grapenthin, Jennifer Strauss, Clay Miller, and Jennifer Taggart ran "stations" with springs, a stick-slip hand crank, and netquakes activities followed by a question and answer session.

Ongoing Activities

As in previous years, the members of the BSL gave several external lectures.

Jennifer Strauss presented about earthquake early warning at East Bay MUD in Oakland for the BRMA (Business Recovery Managers Association) July meeting. On September 26th, Peggy Hellweg spoke at Point Reyes Bear Valley Visitor Center, about "Earthquakes in your Backyard." Jennifer Strauss spoke at the CESA annual meeting on October 17th in Santa Rosa: "Shaping Response and Recovery with EEW". On October 9th, Peggy Hellweg spoke at Gateway Science Museum in Chico with a reprise of the "Earthquakes in our Backyard" lecture.

The BSL also hosted a delegation from the Beijing Earthquake Administration, who were here to talk with our graduate students and scientists. Richard Allen gave them updates about earthquake early warning and our state-of-the-art seismology network.

Acknowledgements

Peggy Hellweg oversees the outreach activities at the BSL. Richard Allen, Qingkai Kong, Ronni Grapenthin, Jennifer Taggart, Clayton Miller, Jennifer Strauss, and many other faculty, staff, and students at the BSL contribute to the outreach activities. Peggy Hellweg, Clayton Miller, and Jennifer Strauss contributed to the preparation of this section.

Chapter 4

Operations

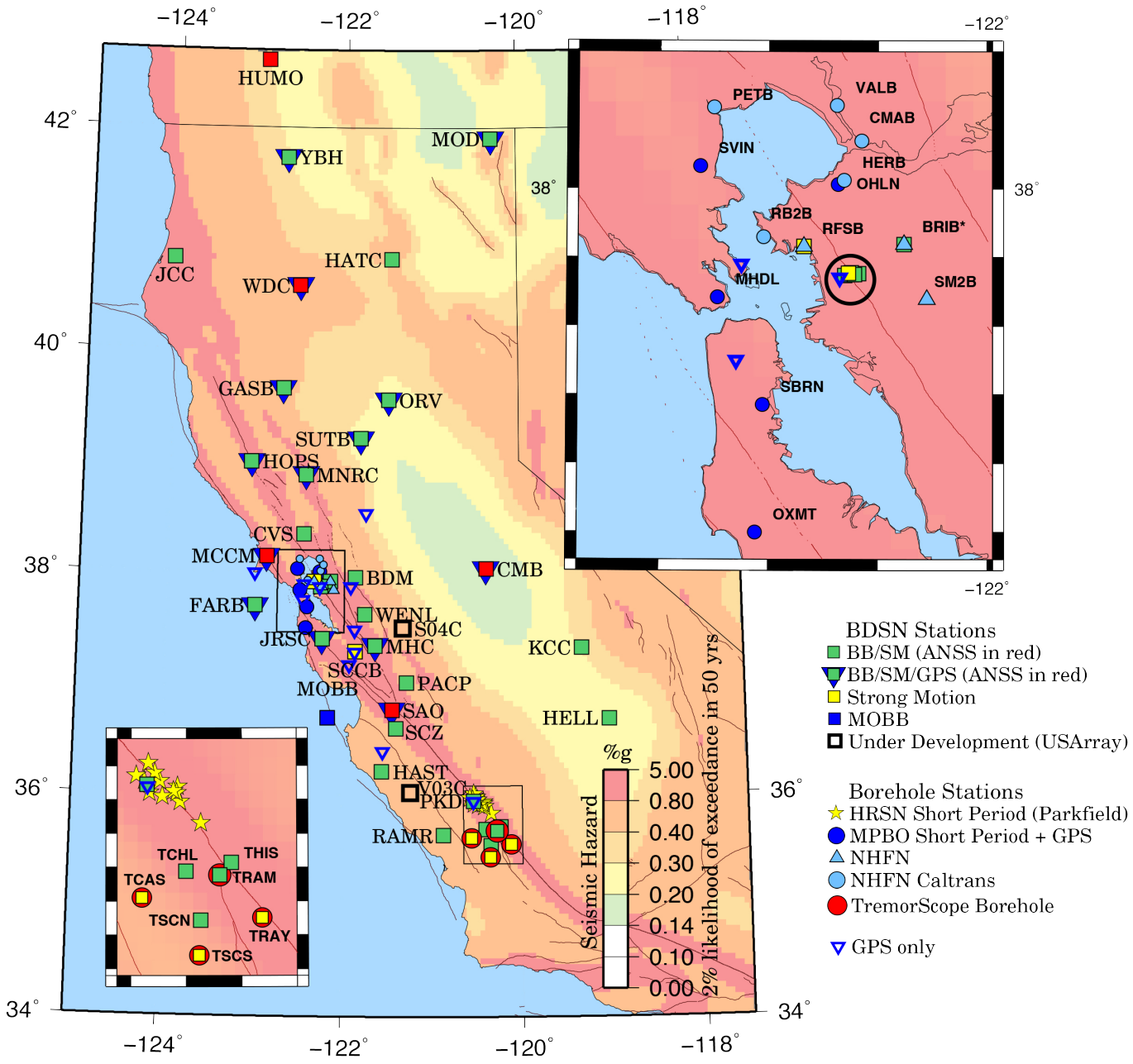

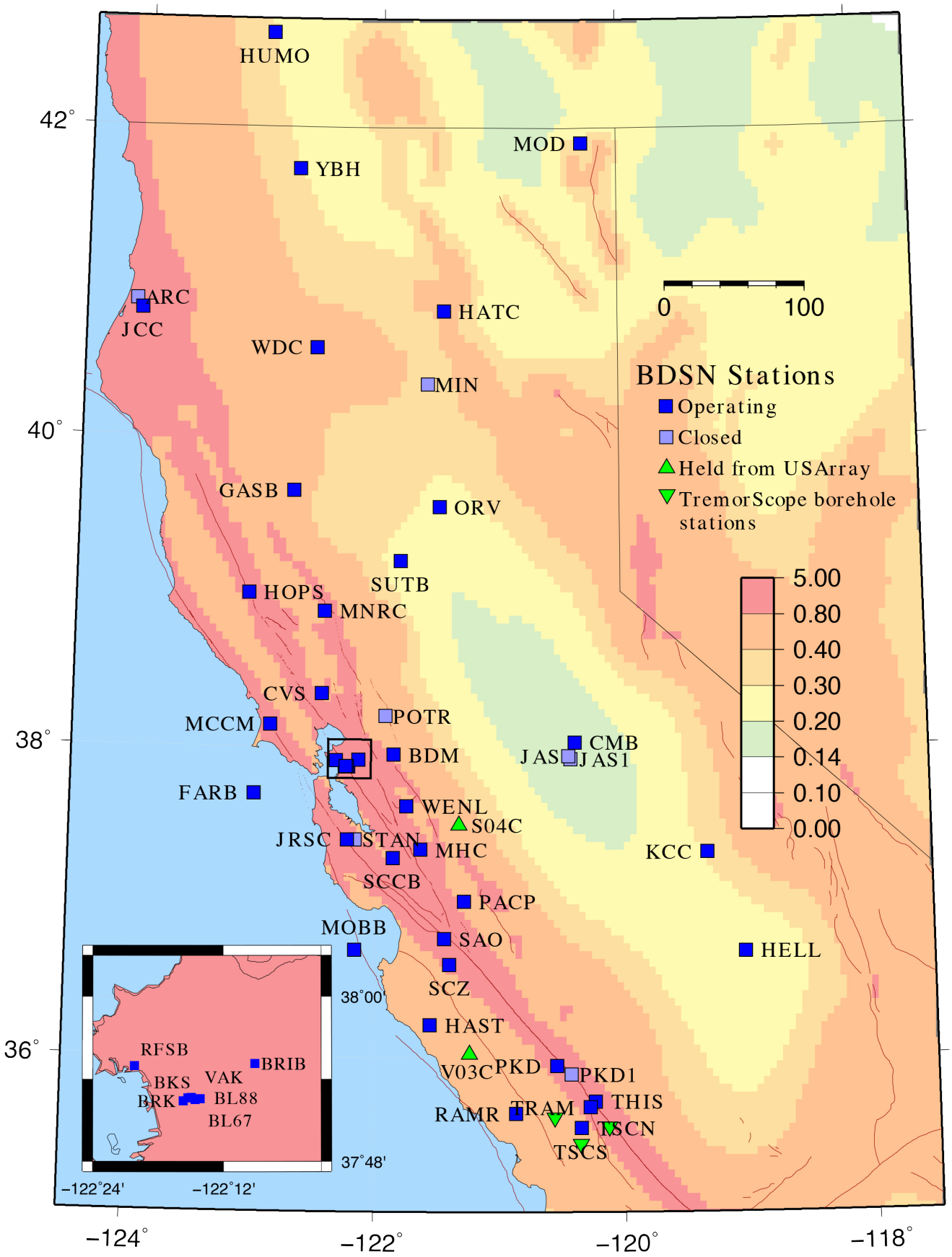

Figure 4.1.1: Map illustrating the distribution of BDSN stations in Northern and Central California. In the inset map, the order of the stations from left to right is: RFSB, BRK, BL88, VAK, BL67, BKS, BRIB.

1 Berkeley Digital Seismic Network (BDSN)

Introduction

The Berkeley Digital Seismic Network (BDSN) is a regional network of very broadband and strong motion seismic stations spanning Northern California and linked to UC Berkeley through continuous telemetry (Figure 4.1.1 and Table 4.1.1). The network is designed to monitor regional seismic activity as well as to provide high quality data for research in regional and global broadband seismology.

Since 1991, the BDSN has grown from the original three broadband stations installed in 1986–87 (BKS, SAO, MHC) to 40 stations, including an ocean-bottom seismometer in Monterey Bay (MOBB). We take particular pride in high quality installations, which often involve lengthy searches for appropriate sites away from sources of low-frequency noise as well as continuous improvements in installation procedures and careful monitoring of noise conditions and problems. Since 2013, our field and operation efforts have been directed toward the installation of stations for the TremorScope project (see Research Section 2.34) and, of course, upgrades, maintenance and repair as necessary. Engineering and research efforts were also devoted to several projects to test instrumentation (see Operational Section 4.5). In the past year, we huddle-tested eight Quanterra environmental add-ons with SETRA pressure sensors, the QEP; recorded data from tilt meters and compared it to signals from broadband horizontal sensors; and compared accelerometers from several manufacturers.

The expansion of our network to increase the density of state-of-the-art strong motion/broadband seismic stations and to improve the joint earthquake notification system in this seismically hazardous region one of BSL's long term goals is coordinated with other institutions and is contingent on the availability of funding. With equipment provided by Lawrence Berkeley National Laboratory (LBNL), we continue to work toward installing a station in the Lawson adit on the UCB campus, very close to the fault. This effort is close to bearing fruit. We also continue our efforts to install all the stations of the TremorScope project funded by the Gordon and Betty Moore Foundation (see Section 2.34). As part of this exciting project for monitoring nonvolcanic tremor sources along the San Andreas Fault south of Parkfield, the BDSN is being augmented by a network of four high-quality borehole stations and four surface stations. All four surface stations are now installed and are collecting data. Finally, in the past year, we were approached by the University of California Santa Cruz (UCSC) and Geoscope (France), which have operated the station SCZ in the Coast Ranges near the city of Salinas, CA. Geoscope can no longer maintain the data logger at the station. The BSL has adopted the station, installed a new data logger, and is providing the data to UCSC.

Data quality and the integrity of the established network are at least as important as network growth, so existing network stations must be preserved. With equipment and funds from the America Recovery and Reinvestment Act (ARRA), the BSL was able to replace almost all of its old data loggers. We continue to operate broadband seismometers from the first generation, however. Some were installed more than 25 years ago. As funds become available, we upgrade their electronics and do our best to keep them operating well. We continue to exercise vigilance and to commit time and resources to repairs and upgrades as necessary.

BDSN Overview

Thirty-five BDSN sites are equipped with three-component broadband seismometers and strong-motion accelerometers, and with 24 or 26-bit digital data acquisition systems or data loggers. Three sites (BL88, RFSB and SCCB) consist of a strong-motion accelerometer and a 24-bit digital data logger. The ocean-bottom station MOBB is equipped with a three component broadband seismometer with integrated digitizer and a differential pressure gauge (DPG). Currently, the station SCZ has two broadband seismometers, a set of STS-1s and an STS-2, installed for comparison purposes. After we confirm the instrument response of the STS-1s, we will install an accelerometer in place of the STS-2, thus, SCZ instrumentation will be consistent with the rest of the BDSN. Data from all BDSN stations are transmitted to UC Berkeley using continuous telemetry, including the ocean-bottom site, MOBB. In order to avoid data loss during utility disruptions, each site has batteries to supply power for three days. The combination of high-dynamic range sensors and digital data loggers ensures that the BDSN has the capability to record the full range of earthquake motion required for source and structure studies. Table 4.1.2 lists the instrumentation at each site.

Most BDSN stations have Streckeisen STS-1 or STS-2 three-component broadband sensors (*Wielandt and Streckeisen*, 1982; *Wielandt and Steim*, 1986).A few exceptions are: BRIB, where a Güralp CMG-3T broadband sensor contributed by LLNL is deployed in a post-hole installation; Güralp CMT-3T broadband seismometers at the new TremorScope sites; and a Güralp CMG-1T at MOBB. All stations, except the TremorScope sites and JRSC, have Kinemetrics FBA-ES-T accelerometers with ±2 g dynamic range. At TremorScope accelerometers are Güralp CMG-5Tc units, also with ±2 g dynamic range, and JRSC has Metrozet TSA-100. Since July, 2011, there are no longer any Q680, Q730, or Q4120 Quanterra data loggers in the BDSN collecting data from seismic sensors. The sites with Quanterras all have Q330, Q330HR or Q330S data loggers. The Quanterra data loggers employ FIR filters to extract data streams at a variety of sampling rates. The same is true for the Güralp DM24 digitizers at the TremorScope sites and at MOBB.

With the ARRA data logger upgrade, several conventions changed: All sites received SEED location codes, with the data logger for the broadband and strong motion sensors having the location code "00," and accelerometer channels are now designated with "HN?" rather than "HL?". Where there is a second broadband seismometer, as at YBH, it is designated with the location code "50". In addition, the BDSN stations now record

Code	Net	Latitude	Longitude	Elev (m)	Over (m)	Date	Location
BDM	BK	37.954	-121.8655	219.8	34.7	1998/11 -	Black Diamond Mines, Antioch
BKS	BK	37.8762	-122.2356	243.9	25.6	1988/01 -	Byerly Vault, Berkeley
BL67	BK	37.8749	-122.2543	736.18	0	2011/04 -	LBNL Building 67, Berkeley
BL88	BK	37.8772	-122.2543	602.21	0	2011/01 -	LBNL Building 88, Berkeley
BRIB	BK	37.9189	-122.1518	219.7	2.5	1995/06 -	Briones Reservation, Orinda
BRK	BK	37.8735	-122.261	49.4	2.7	1994/03 -	Haviland Hall, Berkeley
CMB	BK	38.0346	-120.3865	697	2	1986/10 -	Columbia College, Columbia
CVS	BK	38.3453	-122.4584	295.1	23.2	1997/10 -	Carmenet Vineyard, Sonoma
FARB	BK	37.6978	-123.0011	-18.5	0	1997/03 -	Farallon Island
GASB	BK	39.6547	-122.716	1354.8	2	2005/09 -	Alder Springs
HAST	BK	36.3887	-121.5514	542	3	2006/02 -	Carmel Valley
HATC	BK	40.8161	-121.4612	1009.3	3	2005/05 -	Hat Creek
HELL	BK	36.6801	-119.0228	1140	3	2005/04 -	Miramonte
HOPS	BK	38.9935	-123.0723	299.1	3	1994/10 -	Hopland Field Stat., Hopland
HUMO	BK	42.6071	-122.9567	554.9	50	2002/06 -	Hull Mountain, Oregon
JCC	BK	40.8175	-124.0296	27.2	0	2001/04 -	Jacoby Creek
JRSC	BK	37.4037	-122.2387	70.5	0	1994/07 -	Jasper Ridge, Stanford
KCC	BK	37.3236	-119.3187	888.1	87.3	1995/11 -	Kaiser Creek
MCCM	BK	38.1448	-122.8802	-7.7	2	2006/02 -	Marconi Conference Center, Marshall
MHC	BK	37.3416	-121.6426	1250.4	0	1987/10 -	Lick Obs., Mt. Hamilton
MNRC	BK	38.8787	-122.4428	704.8	3	2003/06 -	McLaughlin Mine, Lower Lake
MOBB	BK	36.6907	-122.166	-1036.5	1	2002/04 -	Monterey Bay
MOD	BK	41.9025	-120.3029	1554.5	5	1999/10 -	Modoc Plateau
ORV	BK	39.5545	-121.5004	334.7	0	1992/07 -	Oroville
PACP	BK	37.008	-121.287	844	0	2003/06 -	Pacheco Peak
PKD	BK	35.9452	-120.5416	583	3	1996/08 -	Bear Valley Ranch, Parkfield
RAMR	BK	37.9161	-122.3361	416.8	3	2004/11 -	Ramage Ranch
RFSB	BK	37.9161	-122.3361	-26.7	0	2001/02 -	RFS, Richmond
SAO	BK	36.764	-121.4472	317.2	3	1988/01 -	San Andreas Obs., Hollister
SCCB	BK	37.2874	-121.8642	98	0	2000/04 -	SCC Comm., Santa Clara
SCZ	BK	36.598	-121.403	261	0	2013/04 -	Chualar Canyon, Santa Cruz
SUTB	BK	39.2291	-121.7861	252	3	2005/10 -	Sutter Buttes
TCHL	BK	35.68812	-120.40092	431	0	2013/06 -	Clark Property, Shandon
THIS	BK	35.714	-120.237	623	0	2012/05 -	South End of Cholame Valley, Shandon
TRAM	BK	35.67691	-120.27093	642	0	2012/12 -	Private Property, Shandon
TSCN	BK	35.544	-121.3481	476.47	0	2012/03 -	Shell Creek North, Shandon
VAK	BK	37.8775	-122.2489	266	10	2010/08 -	LBNL Building 46, Berkeley
WDC	BK	40.5799	-122.5411	268.3	75	1992/07 -	Whiskeytown
WENL	BK	37.6221	-121.757	138.9	30.3	1997/06 -	Wente Vineyards, Livermore
YBH	BK	41.732	-122.7104	1059.7	60.4	1993/07 -	Yreka Blue Horn Mine, Yreka

Table 4.1.1: Stations of the Berkeley Digital Seismic Network currently in operation. Each BDSN station is listed with its station code, network id, location, operational dates, and site description. The latitude and longitude (in degrees) are given in the WGS84 reference frame, and the elevation (in meters) is relative to the WGS84 reference ellipsoid. The elevation is either the elevation of the pier (for stations sited on the surface or in mining drifts) or the elevation of the well head (for stations sited in boreholes). The overburden is given in meters. The date indicates either the upgrade or installation time.

Code	Broadband	Strong-motion	Data logger	GPS	Other	Telemetry	Dial-In
BDM	STS-2	FBA-ES-T	Q330HR			FR	
BKS	STS-1	FBA-ES-T	Q330HR		QEP, E300, Baseplates	FR	X
BL67	CMG-3T	FBA-ES-T	Q330S			LAN	
BL88		FBA-ES-T	Q330S			R	
BRIB	CMG-3T	FBA-ES-T	Q330HR	X	Strainmeter, EM	FR	X
BRK	STS-2	FBA-ES-T	Q330HR			LAN	
CMB	STS-1	FBA-ES-T	Q330HR	X	QEP, E300, Baseplates	FR	X
CVS	STS-2	FBA-ES-T	Q330HR			FR	
FARB	STS-2	FBA-ES-T	Q330HR	X		R-FR/R	
GASB	STS-2	FBA-ES-T	Q330HR	X		R-FR	
HAST	STS-2	FBA-ES-T	Q330HR			R-Sat	
HATC	STS-2	FBA-ES-T	Q330HR			T1	
HELL	STS-2	FBA-ES-T	Q330			R-Sat	
HOPS	STS-1	FBA-ES-T	Q330HR	X	QEP, E300, Baseplates	FR	X
HUMO	STS-2	FBA-ES-T	Q330HR			VSAT	X
JCC	STS-2	FBA-ES-T	Q330HR			FR	X
JRSC	STS-2	TSA-100S	Q330HR	X	EM	Mi-LAN	X
KCC	STS-1	FBA-ES-T	Q330HR		QEP, E300, Baseplates	R-Mi-FR	X
MCCM	STS-2	FBA-ES-T	Q330HR			VSAT	
MHC	STS-1	FBA-ES-T	Q330HR	X		FR	X
MNRC	STS-2	FBA-ES-T	Q330HR	X		Sat	X
MOBB	CMG-1T		DM24		OCM, DPG	LAN	
MOD	STS-1*	FBA-ES-T	Q330HR	X	Baseplates	VSAT	X
ORV	STS-1	FBA-ES-T	Q330HR	X	Baseplates	FR	X
PACP	STS-2	FBA-ES-T	Q330HR			Mi/FR	
PKD	STS-2	FBA-ES-T	Q330HR	X	EM	R-Mi-T1	X
RAMR	STS-2	FBA-ES-T	Q330			R-FR	X
RFSB		FBA-ES-T	Q330HR			FR	
SAO	STS-1	FBA-ES-T	Q330HR	X	QEP, E300, Baseplates, EM	FR	X
SCCB		FBA-ES-T	Q330HR	X		FR	
SCZ	STS-1,STS-2		Q330HR		QEP, E300, Baseplates	?	?
SUTB	STS-2	FBA-ES-T	Q330HR	X		R-FR	
TCHL	CMG-3T	CMG-5TC	DM24			R-Mi	
THIS	CMG-3T	CMG-5TC	DM24			R-Mi	
TRAM	CMG-3T	CMG-5TC	DM24			R-Mi	
TSCN	CMG-3T	CMG-5TC	DM24			R-Mi	
VAK	CMG-3T	FBA-ES-T	Q330S			R	
WDC	STS-2	FBA-ES-T	Q330HR	X		FR	X
WENL	STS-2	FBA-ES-T	Q330HR			FR	
YBH	STS-1,STS-2	FBA-ES-T	Q330HR, Q330**	X	E300, Baseplates	R	X

Table 4.1.2: Instrumentation of the BDSN. Except for BL88, RFSB, SCCB, and MOBB, each BDSN station consists of collocated broadband and strong-motion sensors, with a 24 or 26-bit data logger and GPS timing. The stations BL88, RFSB, and SCCB are strong-motion only, while MOBB only has a broadband sensor. Additional columns indicate collocated GPS receivers as part of the BARD network (GPS) and additional equipment (Other), such as warpless baseplates, new STS-1 electronics (E300) or electromagnetic sensors (EM). The OBS station MOBB also has an ocean current meter (OCM) and differential pressure gauge (DPG). The main and alternative telemetry paths are summarized for each station. Abrreviations: FR - frame relay circuit, LAN - ethernet, Mi - microwave, R - radio, Sat - Commercial Satellite, T1 - T1 line, VSAT - USGS ANSS satellite link. An entry like R-Mi-FR indicates telemetry over several links, in this case, radio to microwave to frame relay. (*) During July 2013–June 2014, the STS-1 at this station was replaced by an STS-2. (**) YBH is CTBT auxiliary seismic station AS-109. It has a high-gain STS-2.

continuous data at 0.1, 1.0, 40, and 100 or 200 samples per second (Table 4.1.3}). In the past, other sample rates may have been available (see past annual reports).

When the broadband network was upgraded during the 1990s, a grant from the CalREN Foundation (California Research and Education Network) in 1994 enabled the BSL to convert data telemetry from analog leased lines to digital frame relay. The frame relay network uses digital phone circuits which support 56 Kbit/s to 1.5 Mbit/s throughput. Today, 21 of the BDSN sites rely on frame-relay telemetry for all or part of their communications system. We are looking for alternatives, as the phone companies will soon deprecate frame relay services. Other stations send their data to the data center via satellite, Internet, microwave, and/or radio (see Table 4.1.2).

As described in Operational Section 4.1, data from the BDSN are acquired centrally at the BSL. These data are used for rapid earthquake reporting as well as for routine earthquake analysis (Operational Sections 4.2 and 4.7). As part of routine quality control (Operational Section 4.5), power spectral density (PSD) analyses are performed continuously and are available on the Internet (http://www.ncedc.org/ncedc/PDF/).

The occurrence of a significant teleseism also provides the opportunity to review station health and calibration. Figure 4.1.3 displays BDSN waveforms for the M_w 8.3 earthquake that occurred off the northern coast of Chile on April 1, 2014.

Special Projects in the BDSN

TremorScope

In 2010, the Gordon and Betty Moore Foundation funded the BSL to complete an exciting project for monitoring non-volcanic tremor sources along the San Andreas Fault south of Parkfield. For this project, the BDSN is being augmented by a network of four high quality borehole stations and four surface stations. Progress on this project is described in Research Section 2.34), and in the 2013–2014 Activities section below. All four surface stations are now installed and are collecting data. Additionally, all four TremorScope boreholes were completed and cased.

The Monterey Bay Ocean Bottom Seismic Observatory (MOBB)

The Monterey Ocean Bottom Broadband observatory (MOBB) is a collaborative project between the Monterey Bay Aquarium Research Institute (MBARI) and the BSL. Supported by funds from the Packard Foundation to MBARI, from NSF/OCE, and from UC Berkeley to the BSL, its goal has been to install and operate a long-term seafloor broadband station as a first step toward extending the onshore broadband seismic network in Northern California to the seaward side of the North America/Pacific plate boundary, providing better azimuthal coverage for regional earthquake and structure studies. It also serves the important goal of evaluating background noise in near-shore buried ocean floor seismic systems, such as may be installed as part of temporary deployments of "leap-frogging" arrays (e.g. Ocean Mantle Dynamics Workshop, September 2002). The project has been described in detail in BSL annual reports since 2002 and in several publications (e.g. *Romanowicz* et al., 2003, 2006, 2009; *Taira et al., 2014).*

Sensor	Channel	Rate (sps)	Mode	FIR
BB	VH?	0.1	C	Ac
BB	LH?	1	C	Ac
BB	BH?	40	C	Ac
BB	HH?	100	C	Ca
SM	LN?	1	C	Ac
SM	BN?	20/40	C	Ac
SM	HN?	100/200	C	Ca/Ac

Table 4.1.3: Typical data streams currently acquired at BDSN stations, with channel name, sampling rate, sampling mode, and the FIR filter type. BB indicates broadband; SM indicates strong-motion; C continuous; Ac acausal; Ca causal. The HH and HN channels are now all recorded and telemetered continuously at 100 sps (200 sps for the accelerometers at the TremorScope sites) and most have causal filtering. In the past, SM channels have beennamed HL? (BL?, LL?). For past sampling rates, see earlier annual reports.

MOBB is now continuously providing data through a cable connected to the Monterey Accelerated Research System observatory (MARS, http://www.mbari.org/mars/), a seafloor node in Monterey Bay connected to a shore facility in Moss Landing by a 52 km electro-optical cable. The cable was deployed in the spring of 2007, and node installation was completed in November of 2008.

MOBB, located ~3 km from the node, was connected on February 28, 2009, through an extension cable installed by the ROV Ventana, with the help of a cable laying toolsled. Technical information about the installation and cabling are provided in past annual reports. After one year of continuous operation, the MOBB real-time telemetry ceased abruptly when the extension cable snapped as a result of repeated trawling, even though the observatory is located in a protected zone. With funds from NSF/OCE to replace the 3.2 km cable, we decided to "go the extra mile" to bury the cable to protect it better. MOBB has been online again since the cable was replaced in June 2012, as described in the 2011–2012 Annual Report. The station has been running well since then, except for "timing" problems due to the way time information is provided through the MARS node. We are working with MBARI to resolve those problems. As of 2012, we have implemented a method for removing infragravity induced noise from data of the vertical seismic channel and are exploring other means to further improve data for use in analysis. As can be seen in Figure 4.1.4, at very long periods (1.5–5 mHz) the data at MOBB are comparable with those from the other stations of the BDSN.

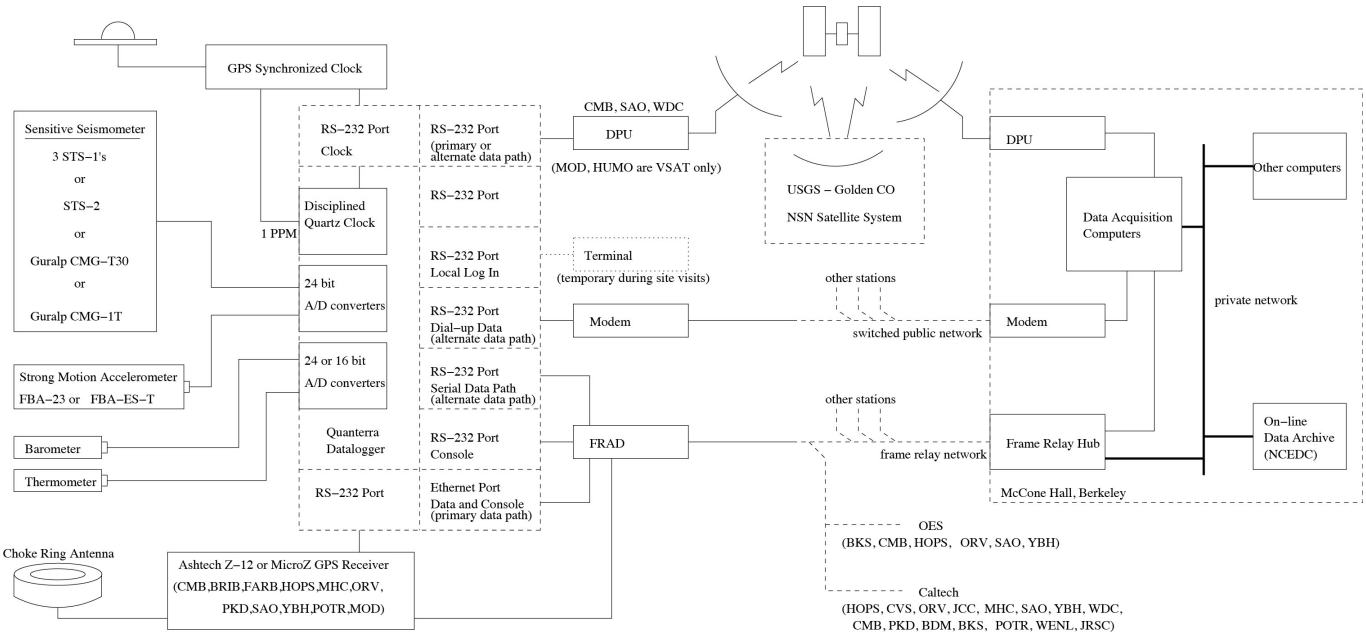

Figure 4.1.2: Schematic diagram showing the flow of data from the sensors through the data loggers to the central acquisition facilities of the BSL.

Electromagnetic Observatories

The BSL's first electromagnetic observatories were deployed in 1995, in collaboration with Dr. Frank Morrison. Well characterized electric and magnetic field measuring systems were installed at two BDSN sites along the San Andreas Fault. These reference sites, now referred to as ultra-low frequency electromagnetic (ULFEM) observatories, are collocated with seismometer sites so that the field data share the same time base, data acquisition, telemetry, and archiving systems as the seismometer outputs. The original UC Berkeley sites were installed at San Andreas Geophysical Observatory (SAO), outside Hollister, halfway between San Francisco and Parkfield; and at the Parkfield earthquake prediction experiment (PKD), 300 km south of the San Francisco Bay Area (Figure 4.1.1). Each of the two sites is equipped with three induction coils and two 100 m electric dipoles. In addition, PKD has two 200 m electric dipoles. The magnetotelluric (MT) data are continuously recorded at 40 Hz, 1 Hz and 0.1 Hz and archived at the NCEDC (Table 4.1.4). For a history of instrumentation siting, see past annual reports.

In 2004 the NSF's EarthScope program funded a Stanford-USGS-Berkeley collaboration, led by Simon Klemperer, Jonathan Glen and Darcy McPhee, to install three additional ULFEM sites within the San Francisco Bay Area. Sites were selected close to the San Andreas fault on Stanford lands at Jasper Ridge (JRSC), on Marin Headlands (MHDL), and in the East Bay near the Hayward fault on UC land near Briones Regional Park. All these three sites are significantly affected by electromagnetic noise from the BART electric train system, but were sited in the populated San Francisco Bay area on the premise that if ULFEM signals were ever detected as precursors to earthquakes, such a discovery would have greater societal benefit in a populated area than in more remote parts of California. The new instrumentation was installed at JRSC in 2004, MHDL in 2006 and BRIB in 2007. JRSC, BRIB and MHDL have three orthogonal EMI-Schlumberger magnetic coils. JRSC and BRIB each also have two independent sets of orthogonal 100 m electric dipoles, each with a shared, common electrode, an arrangement mandated by the limited number of recording channels on the Quanterra digitizing system. MHDL lacks electric sensors due to National Park Service restrictions on land access. Data at the EM/MT sites are currently fed to Quanterra data loggers synchronized in time by GPS, and sent to the BSL via dedicated communication links. The installations use proprietary electric field and magnetic field "signal conditioners" between the electrodes or magnetometers and the Quanterra digitizers.

The availability of new funding from NASA in 2009 led to a joint effort by the USGS, BSL and Stanford towards improving operation and maintenance of the EM/MT sites. BSL engineers met scientists from the USGS and Stanford at SAO in October 2008 to assess the condition of the EM/MT system. The EM coils were not working; they were removed and returned to the manufacturer. EM/MT equipment at PKD was evaluated in August 2008. There, the data logger was removed from the PKD EM/MT system and has not yet been returned. At the same time, the Stanford-USGS sites were suffering from intermittent failures, due to lack of full-time maintenance staff.

In 2008, the BSL began developing a low-cost digitizer intended to be a lower-power, lower-cost replacement for both the signal conditioners and the Quanterra. At the inception of the design process, it was hoped that this new digitizer

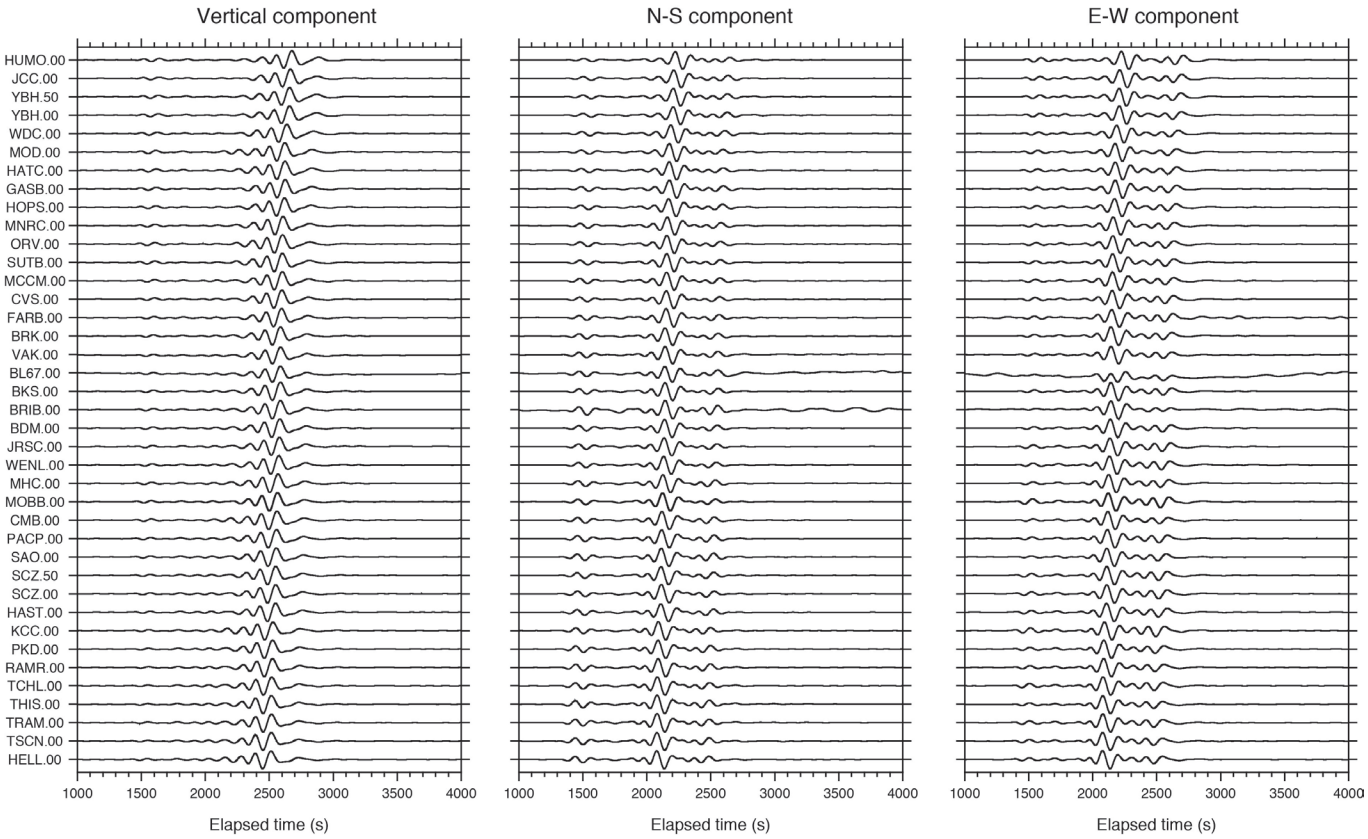

Figure 4.1.3: Long period (100–333 s period) waveforms recorded across BDSN from the M_w 8.2 teleseismic earthquake which occurred on April 1, 2014, off the northern coast of Chile at 19.610 S, 70.760 W. The panels show data from the vertical, north-south and east-west componenets, respectively. The traces are deconvolved to ground velocity, scaled by their maximum values, and ordered from bottom to top by distance from the epicenter. The highly similar waveforms recorded across the BDSN provide evidence that the broadband sensors are operating within their nominal specifications. BDSN data are archived and available at the Northern California Earthquake Data Center. This is described in detail in Operational Section 4.8.

,while not as feature-rich as commercially available data loggers, might serve both seismic and electromagnetic communities. Subsequently, the design process moved to become a Stanford-USGS responsibility. A prototype 24-bit digitizer was developed and field-tested (*Bowden et al*, 2010). A significantly modified version is being retested in the summer of 2013.

The site JRSC is now being used as a test bed for new MT field installations and electronic equipment. There, duplicate recording equipment can be installed alongside the permanent MT station to check the fidelity of new equipment. As of September 2013 the replacement ULFEM digitizer is recording data from magnetometers temporarily installed alongside the permanent magnetometers that are recorded on a Quanterra. Data from identical magnetometers recorded by the old and new systems are being compared to verify that the ULFEM digitizer has acceptable performance before it is installed at any station permanently. In the 2004–2007 original Bay Area deployments, magnetometers were buried directly inside of plastic conduit. At JRSC a new installation system has been implemented for the horizontal magnetic coils. Now, brackets are set in concrete to support plastic conduit that can be accurately leveled, and that can be drained to prevent buildup of condensation. In summer 2013 the horizontal magnetometers at MHDL, BRIB and SAO, are being reinstalled using this new system. In the original installations it was assumed that the magnetometer coils were stable electronically, and no provision was made for regular calibration. A calibration coil system has now been developed and is being tested. In this system a coil is permanently installed around the magnetometers; it will be pulsed at midday every day with a fixed voltage at known frequencies (*Connor et al.*, 2012). The calibration pulse is intended to be automatically initiated from the ULFEM digitizer. Calibration coils will be installed at JRSC, MHDL, BRIB and SAO as soon as the ULFEM digitizer is accepted to replace the existing Quanterras.

Although the Stanford-USGS-Berkeley ULFEM network will be significantly refurbished and improved as a result of summer 2013 field activities, no progress has been made on re-installing the PKD system. Existing grants from federal agencies expire in 2013, and until we succeed in receiving new grants, we anticipate no new progress in maintaining or improving recording systems, but will instead focus on data analysis to justify new grant proposals.

Sensor	Channel	Rate (sps)	Mode	FIR
Magnetic	VT?	0.1	C	Ac
Magnetic	LT?	1	C	Ac
Magnetic	BT?	40	C	Ac
Electric	VQ?	0.1	C	Ac
Electric	LQ?	1	C	Ac
Electric	BQ?	40	C	Ac

Table 4.1.4: Typical MT data streams acquired at SAO, PKD, BRIB, and JRSC with channel name, sampling rate, sampling mode, and FIR filter type. C indicates continuous; Ac acausal. Data loggers for these systems have not been upgraded/replaced, but tests are ongoing with new data loggers.

2013–2014 Activities

Station Upgrades, Maintenance, and Repairs

Given the remoteness of the off campus stations, BDSN data acquisition equipment and systems are designed, configured, and installed so that they are both cost effective and reliable. As a result, there is little need for regular station visits. Nonetheless, repair, maintenance and upgrade visits are occasionally required, especially since many of the broadband seismometers installed by BSL are from the first generation and are about 25 years old.

In the summer of 2009, the USGS received ARRA funds, among other things, to upgrade and improve seismic stations operated as part of the Advanced National Seismic System (ANSS). The BSL continues to benefit from those funds, in the form of a reduction in maintenance and repair visits to our sites. We received the new model of Quanterra data logger, the Q330HR, as government-furnished equipment (GFE). Over the course of the following two years, we installed the Q330HR, replacing the old Quanterras at 25 BDSN seismic stations. In addition, under the ARRA, all remaining Kinemetrics FBA-23 accelerometers were replaced with Kinemetrics' newer, lower noise model, the FBA-ES-T. Some ARRA money was used to purchase Quanterra Environmental Packages (QEP) and SETRA pressure sensors for our quietest sites. Over the years the environmental sensors (pressure, temperature, humidity) installed at many of the sites had died. In addition, the Q330 has only six input channels, which we use for the seismometer and accelerometer components. The QEP offer additional digitizing capacity as well as rudimentary environmental sensors (pressure, temperature, humidity). We purchased the SETRA pressure sensors to ensure high quality pressure measurements for reducing long period noise in the very broadband recordings. During the Spring 2012, we installed all QEP packages and SETRA pressure sensors in a huddle test on the roof of McCone Hall. In 2013, we have installed the QEPs at BKS, CMB, HOPS, KCC, SAO and SCZ.

In addition, over the past four years, we have been able to purchase and install new electronics, the E300 from Metrozet, for our STS-1 sites. Including work in 2013, seven sites have E300s: BKS, CMB, HOPS, KCC, SAO, YBH, and the site we adopted from UCSC and Geoscope, SCZ. Funds for the E300s have come from our IRIS/GSN grant, and from our support from the California Office of Emergency Services (CalOES), and from the Federal Emergency Management Agency, through CalOES.

New Stations

TremorScope: Four TremorScope boreholes were completed and cased. Huts were constructed over boreholes to provide protection and support for solar panels. Each site has four 12 V batteries. We expect to install sensors and data loggers in this summer.

Repair, Maintenance and Upgrades

As always, some of the BSL's technical efforts were directed toward maintaining, repairing existing instrumentation, stations, and infrastructure. We have benefited greatly from the data loggers provided and installed through the ARRA upgrade, and from the installation of the E300s at some of our STS-1 sites. They allow better remote access, troubleshooting and reconfiguration. Now, field visits can be better prepared for as well as more effective. Remotely performed activities will not be reported here. They include seismometer recenters at many sites, remote calibration at sites with STS-1s and E300s and upgrades of the firmware for both Q330s and Balers at all sites.

BKS: The UDS100 was installed for E300 serial port access. The accelerometer was replaced. The TremorScope geophones were tested here (see Operational Section 4.5).

CMB: We installed the UDS100 for the E300 serial port access and the QEP, although the final configuration of this system has not yet been completed.

HOPS: The GPS clock for the Q330HR was replaced.

HELL: We have installed a cube of insulation around the STS-2. One layer of pink, one-inch thick insulating foam was placed around the sides. The STS-2 previously had no insulation other than the removable floor of the vault which sat above it. The vault has the cement floor at its bottom and a removable floor layer above the STS-2. We expect that the new insulation will reduce long period noise at this site. The batteries were also replaced.

KCC: The QEP was moved into the vault so that the temperature measurement more accurately reflects the temperatures seen by the STS-1s. In order to ensure that the pressure measured by the QEP was not filtered by the insulation surrounding the STS-1s, a 1/4" OD vinyl tube was added over the existing vinyl tube exiting the QEP housing and runs to the outside of the insulation along the side facing the tunnel wall.

PKD: The batteries were replaced.

SAO: In the past year, we had to replace the accelerometer, which was GFE and was returned to the ANSS Depot for repair. We accidentally re-oriented the accelerometer.

TSCN: The DM24 digitizer was replaced.

Perspectives for 2014–2015

We have several goals for 2014–2015. One of them is to complete an installation of separate insulation for the STS-2s at the former Transportable Array sites (HAST, HATC, RAMR, SUTB) to explore how this may reduce noise on the horizontal components. At our mini-PBO stations in the Bay Area, we will complete the adoption of their tilt and strain sensors. We already record the strain data on our GFE Basalt data loggers. Together, we developed a plan to replace the Basalt data loggers with Quanterra Q330 data loggers and QEPs. This will allow the collection of nine channels of time series data as well as air pressure data from a SETRA, and pore pressure data from the Paroscientific down-hole instrument. We are also exploring the possibility of recording data from USGS accelerometers in Parkfield that are collocated with some of our borehole stations there. This would also involve an upgrade of our radio telemetry system.

Very Long Period Data from the BDSN

Great earthquakes excite normal modes in frequency bands around 1 mHz, well below those of smaller earthquakes. The April 1, 2014, M_w 8.2 earthquake which occurred off the northern coast of Chile provided an opportunity to look at the noise levels in these bands at our broadband BDSN stations. Figure 4.1.4 shows spectra in the band from 0.15 mHz to 5.5 mHz for all our broadband stations except for HELL and SUTB due to data gaps, which have both a variety of sensors (see Table 4.1.2), and different types of installations. We are pleased to find that in this band, the normal mode signals from the majority of BDSN sites are well above the noise at all stations. We propose to further explore the performance of our stations in this band using a suite of earthquakes of various sizes.

Acknowledgements

Under Richard Allen's general supervision, Peggy Hellweg oversees the BDSN operations. Doug Neuhauser is responsible for organizing BDSN data acquisition operations, and Peggy Hellweg coordinates the engineering team. John Friday, Joshua Miller, Sarah Snyder Taka'aki Taira, and Bob Uhrhammer contribute to the operation of the BDSN. The network equipment upgrades and improvements were funded through the ARRA (American Recovery and Reinvestment Act), under USGS award number G09AC00487. The new STS-1 electronics, E300s, installed at seven of our stations, were purchased with funds from an IRIS/GSN grant and from CalOES and FEMA. The new Q330-E300 cables for KCC and YBH were purchased with funds from the IRIS/GSN grant. The TremorScope deployment is funded by Grant 2754 from the Gordon and Betty Moore Foundation.

MOBB is a collaboration between the BSL and MBARI. From the BSL, Barbara Romanowicz, Taka'aki Taira, and Doug Neuhauser participate in the project. The MBARI team is headed by Paul McGill and has included many others over the years. The MOBB effort at the BSL is supported by UC Berkeley funds. MBARI supports the dives and data recovery. The MOBB seismometer package was funded by NSF/OCE grant 9911392. The development of the interface for connection to the MARS cable is funded by NSF/OCE grant 0648302.

Taka'aki Taira, and Peggy Hellweg contributed to the preparation of this section.

References

Bowden, D.C., Engelland-Gay, H., Enright, A., Gardner, J., Klemperer, S.L., McPhee, D.K., Glen, J.M., Stanford-USGS Ultra-low frequency electromagnetic network: hardware developments in magnetometer calibration and recording. *EOS Trans.* AGU, Abstract NH31A-1338 presented at 2010 Fall Meeting, AGU, San Francisco, CA, 2010.

Connor, D., Klemperer, S.L., Glen, J.M., and McPhee, D.K., Stanford-USGS Ultra-Low Frequency Electromagnetic Network: Magnetometer Calibration Developments, Poster presented at 2012 Annual Biomedical Research Conference for Minority Students (ABRCMS), San Jose, CA, 11/28/2012, 2012.

Romanowicz, B., D. Stakes, R. Uhrhammer, P. McGill, D. Neuhauser, T. Ramirez, and D. Dolenc, The MOBB experiment: a prototype permanent off-shore ocean bottom broadband station, *EOS Trans.* AGU, Aug 28 issue, 2003.

Romanowicz, B., D. Stakes, D. Dolenc, D. Neuhauser, P. McGill, R. Uhrhammer, and T. Ramirez, The Monterey Bay Broadband Ocean bottom seismic observatory, *Ann. Geophys.*, 49, 607-623, 2006.

Romanowicz, B., P. McGill, D. Neuhauser and D. Dolenc, Acquiring real time data from the broadband ocean bottom seismic observatory at Monterey Bay (MOBB), *Seismol. Res. Lett.*, 80, 197-202, 2009.

Taira, T., Z. Zheng, and B. Romanowicz , On the systematic long period noise reduction on ocean floor broadband seismic sensors collocated with differential pressure gauges, *Bull. Seis. Soc. Am.*, 104, 247-259, 2014.

Wielandt, E., and J. Steim, A digital very broadband seismograph, Ann. Geophys., 4, 227-232, 1986.

Wielandt, E., and G. Streckeisen, The leaf spring seismometer: design and performance, *Bull. Seis. Soc. Am.*, 72, 2349-2367, 1982.

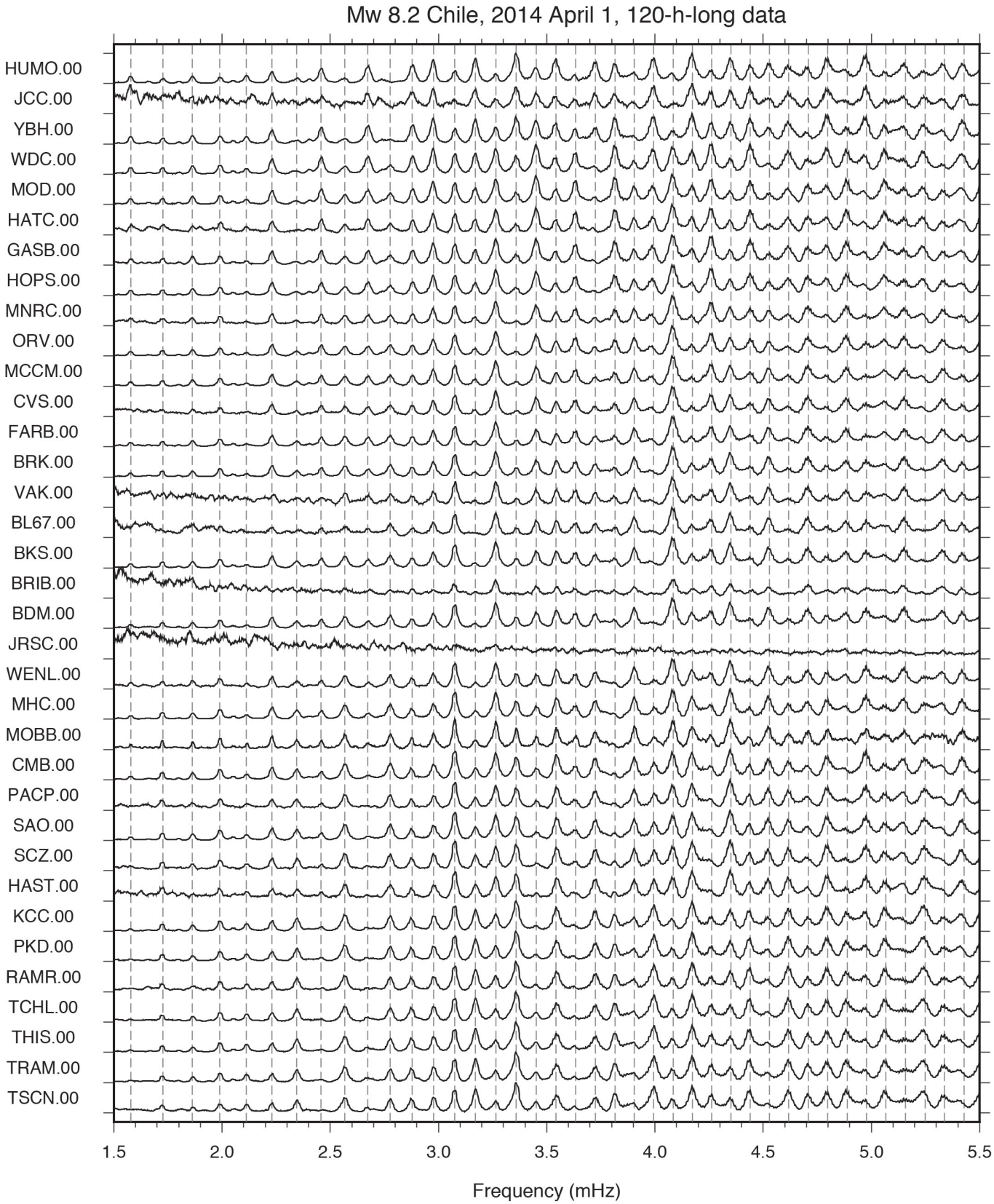

Figure 4.1.4: Amplitude spectra of the vertical component of ground acceleration for the 120-hour-long data recorded at BDSN stations following the April 1, 2014 M_w 8.2 Chile event, off its northern coast. The spectra are normalized by their maximum amplitudes. Dashed lines are expected spheroidal modes with the PREM model.

2 California Integrated Seismic Network (CISN)

Introduction

Advances in technology have made it possible to integrate separate earthquake monitoring networks into a single seismic system, as well as to unify earthquake monitoring instrumentation. In California, this effort began in the south with the TriNet Project where, Caltech, the California Geological Survey (CGS), and the USGS created a unified seismic system for Southern California. With major funding provided by the Federal Emergency Management Agency (FEMA), the California Governor's Office of Emergency Services (CalOES), and the USGS, monitoring infrastructure was upgraded and expanded, combining resources in a federal, state and university partnership. In 2000, the integration effort expanded to the entire state with the formation of the California Integrated Seismic Network (CISN, see 2000–2001 Annual Report). To this end, UC Berkeley and the USGS Menlo Park and Pasadena offices joined forces with Caltech and the CGS. The CISN is now in the thirteenth year of collaboration and its thirteenth year of funding from CalOES.

CISN Background

Organization

The organizational goals, products, management, and responsibilities of the CISN member organizations are described in the founding memorandum of understanding and in the strategic and implementation plans. To facilitate activities among institutions, the CISN has three management centers:

- Southern California Earthquake Management Center: Caltech/USGS Pasadena
- Northern California Earthquake Management Center: UC Berkeley/USGS Menlo Park
- Center for Engineering Strong Motion Data: California Geological Survey/USGS National Strong Motion Program

The Northern and Southern California Earthquake Management Centers operate as twin statewide earthquake processing centers, serving information on current earthquake activities, while the Center for Engineering Strong Motion Data is responsible for producing engineering data products and distributing them to the engineering community.

The Steering Committee, made up of two representatives from each core institution and a representative from CalOES, oversees CISN projects. The position of chair rotates among the institutions; John Parrish from CGS took over as chair of the Steering Committee in January 2013 from Ken Hudnut.

An external Advisory Committee represents the interests of structural engineers, seismologists, emergency managers, industry, government, and utilities, and provides review and oversight. The Advisory Committee is chaired by Loren Turner of Caltrans. It last met in March 2013, and the meeting for 2014

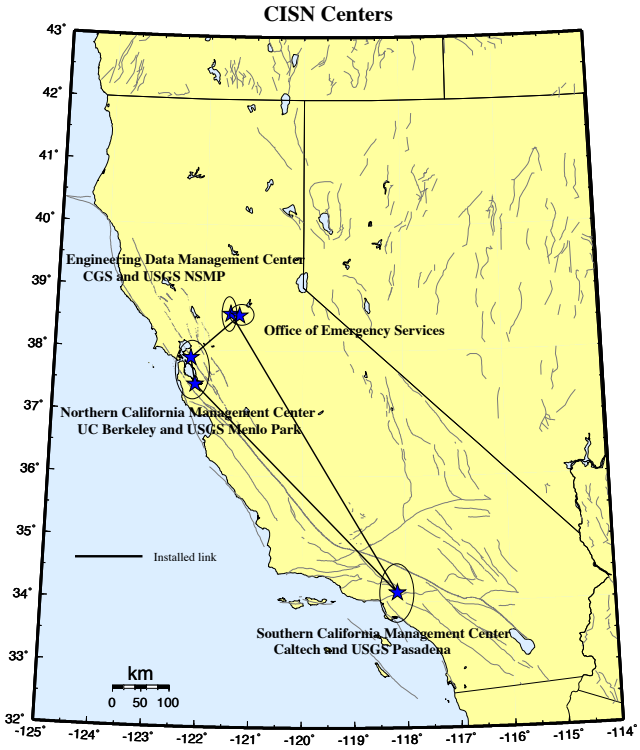

Figure 4.2.1: Map showing the geographical distribution of the CISN partners and centers. The communications "ring" is shown schematically with installed links (solid lines). It was initially a ring of dedicated T1 connections between the partners. The connections are now less robust, as reduced funding has required that the dedicated service was discontinued. Connections are now available as Internet tunnels.

is in the process of being scheduled at the time of publication. Agendas and reports from the meetings are available on the CISN website (http://www.cisn.org/advisory).

The Steering Committee has commissioned other committees, including a Program Management Group to address planning and coordination, and a Standards Committee to resolve technical design and implementation issues.

In addition to the core members, other organizations contribute data that enhance the capabilities of the CISN. Contributing members include: University of California, Santa Barbara; University of California, Santa Cruz; University of California, San Diego; University of Nevada, Reno; University of Washington; California Department of Water Resources; Lawrence Berkeley National Lab; Lawrence Livermore National Lab; and Pacific Gas and Electric Company.

CISN and ANSS

The USGS Advanced National Seismic System (ANSS) has developed along a regionalized model. Eight regions have been organized, with the CISN representing the California region. David Oppenheimer of the USGS represents the CISN on the ANSS National Implementation Committee (NIC).

As the ANSS moves forward, committees and working

groups are established to address issues of interest. BSL faculty and staff have been involved in several working groups of the Technical Integration Committee, including Doug Dreger, Peggy Hellweg, Pete Lombard, Doug Neuhauser, Bob Uhrhammer, and Stephane Zuzlewski.

Since 2010, the software developed and implemented by the CISN for earthquake monitoring has been adopted by the ANSS, as the ANSS Quake Monitoring System (AQMS). It is now operating at many regional seismic networks throughout the United States. Since then, the CISN has expanded the membership of the CISN Standards Committees and its subcommittees by inviting interested members from other regional networks to participate in the regular conference calls, particularly when they have suggestions or need discussion of changes and improvements to the AQMS software.

CISN and CalOES

CalOES has long had an interest in coordinated earthquake monitoring in the State. The historical separation between Northern and Southern California and between strong-motion and weak-motion networks complicated earthquake response. Thus, CalOES has advocated for improving coordination and collaboration in earthquake monitoring, and supported the development of the CISN. In FY 01–02, Governor Gray Davis requested support for the CISN, to be administered through CalOES. Funding for the California Geological Survey (CGS), Caltech and UC Berkeley was made available in spring 2002, officially launching statewide coordination. After the first year, three-year contracts to UC Berkeley, Caltech, and the CGS for CISN activities were established. We have just completed year three of the fourth three-year contract (2011–2014). Unfortunately, state funding to the CISN has been decreasing, putting pressure on our earthquake monitoring and reporting activities.

Past CISN related activities are described in previous annual reports.

2013–2014 Activities

We have just completed the fifth full year of operation in the NCEMC (Northern California Earthquake Management Center) with the new suite of earthquake monitoring software. In the past, this system was called the CISN software. In 2008, it was adopted by the ANSS as the system to be used by US regional networks for their operations and earthquake reporting, and it is now called the ANSS Quake Monitoring System, or *AQMS*. *AQMS* has now been implemented by other regional networks, and BSL staff members continue to provide information and software support to the operators of those networks. The NCEMC transitioned from a hybrid system of software for earthquake monitoring and reporting to the *AQMS* software package in June 2009. The software is now operating at the BSL and in Menlo Park. CISN funding from CalOES contributed to this transition, and has also supported other software development and operational activities at the BSL during the past year as well.

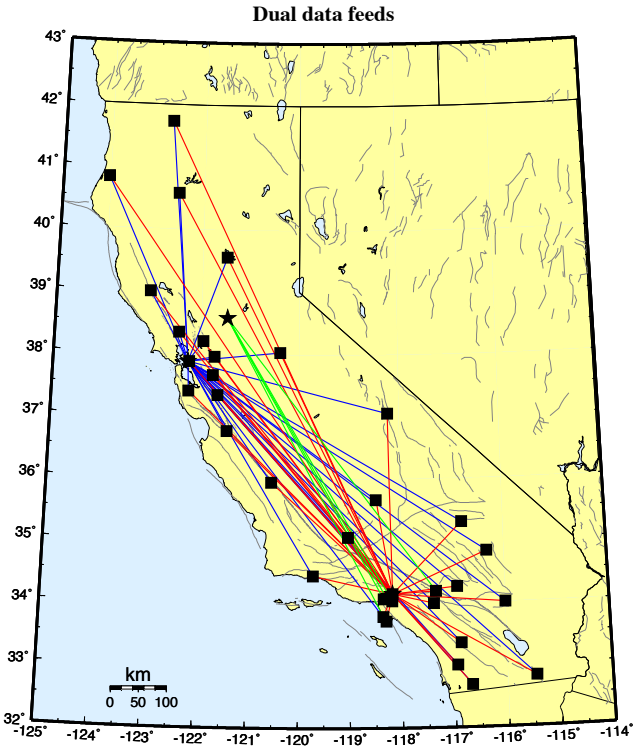

Figure 4.2.2. Map showing the original 30 stations selected to send data directly to the Northern and Southern California processing centers, and the 5 stations that send data directly to the Engineering Data Center and the Southern California processing center. Due to reductions in funding, we have converted this data feed to "data center to data center" exchange, with strong loss in robustness.

Northern California Earthquake Management Center

As part of their effort within the CISN, the BSL and the USGS Menlo Park are operating the AQMS software as the Northern California joint earthquake information system. Operational Section 4.7 describes the operation of this system and reports on progress in implementation and improvements.

For monitoring earthquakes in Northern California, the USGS Menlo Park and the BSL have improved their communications infrastructure. The BSL and the USGS Menlo Park are currently connected by two dedicated T1 circuits. One circuit is supported by CalOES funds, while the second circuit was installed in 2004–2005 (Figure 4.2.3) to support dedicated traffic between Berkeley and Menlo Park above and beyond that associated with the CISN.

Due to the decrease in funding, BSL has eliminated its second T1 for incoming data. BDSN data acquisition is now again limited to a single frame relay circuit, resulting in the reintroduction of a single point of failure.

In the long term, the BSL and USGS Menlo Park hope to be connected by high-bandwidth microwave or satellite service. Unfortunately, we have not yet been able to obtain funding for such an additional communication link, although we are exploring prospects for a very high speed radio link between the two data centers.

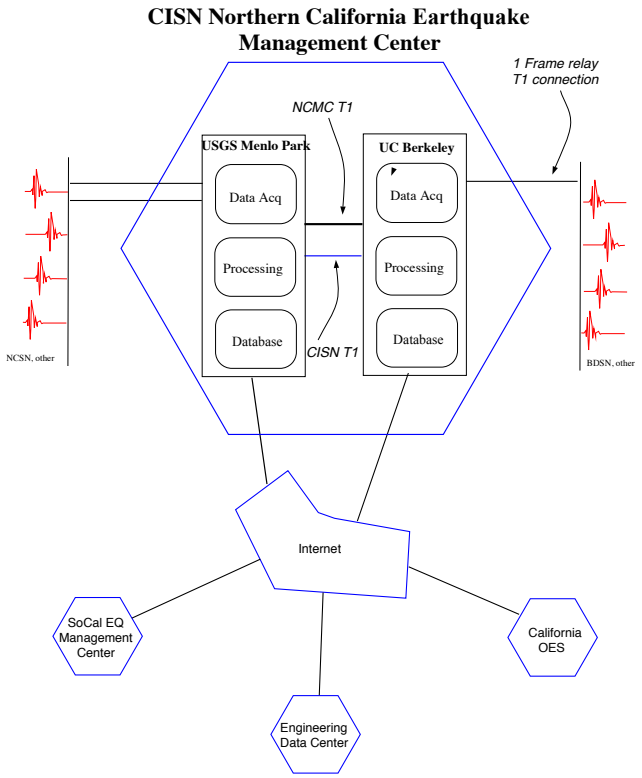

Figure 4.2.3: Schematic diagram illustrating the connectivity between the real-time processing systems at the USGS Menlo Park and UC Berkeley, forming the Northern California Management Center, and with other elements of the CISN.

Statewide Integration

Despite the fact that AQMS software is now operating in both Northern and Southern California, efforts toward statewide integration continue. BSL staff are involved in many elements of these efforts. The Standards Committee, chaired by Doug Neuhauser, continues to define and prioritize projects important to the ongoing development and operation of the statewide earthquake processing system and to establish working groups to address them (see minutes at http://www.cisn.org/standards/meetings.html).

Dual Station Feeds: Early in the existence of the CISN, "dual station feeds" were established for 30 stations to improve robust earthquake reporting (15 in Northern California and 15 in Southern California) (Figure 4.2.2). This year we lost this capability, mainly due to the decrease in funding from the state. We are replacing dual feeds from the stations by "data center to data center" sharing. As we do this, we are also reviewing which stations to share. Since the beginning of the dual feeds, the BSL has added many new stations to its network. The NCEMC uses data from the Southern California stations to estimate magnitudes on a routine basis. In addition, data from some the stations are used in moment tensor inversions, a computation that is sensitive to the background noise level.

Data Exchange: Part of the AQMS software allows reduced amplitude timeseries to be produced and exchanged. Currently, these timeseries are being exchanged in the NCEMC, but not yet statewide. At the end of the year, we agreed within CISN to explore sharing these parameters between Northern and Southern California. Using a common and recently improved format, the CISN partners continue to rapidly exchange observations of peak ground motion with one another following an event or a trigger. This step increases the robustness of generating products such as ShakeMap, since all CISN partners exchange data directly. This also improves the quality of ShakeMaps for events on the boundary between Northern and Southern California by allowing all data to be combined in a single map. Finally, this is a necessary step toward the goal of generating statewide ShakeMaps. In addition, datasets for events of interest to engineers are provided automatically to the Center for Engineering Strong Motion Data (CESMD) in V0 format. We are now improving data exchange with the University of Nevada, Reno, for events near the California-Nevada border, and with the Pacific Northwest Seismic Network for events near the California-Oregon border.

Software Calibration & Standardization: CISN partners have calibrated and standardized much of the software used for automatic earthquake processing and earthquake review, which is now the AQMS software. The AQMS software now serves as the real-time system operating in the NCEMC. The transition was made in June 2009.

Local Magnitudes: Since the transition to the AQMS software in Northern California in June 2009, local magnitudes are calculated throughout the state using the new logA0 function and the associated station-specific corrections for broadband/strong motion stations, and also for strong-motion only stations. We are continuing to focus on adding magnitude corrections for vertical components, whether short period or broadband, and for short period horizontal components to the new local magnitude system. A final component of the magnitude efforts is the determination of a magnitude reporting hierarchy. For the near future, each region will continue to use its own preferences for magnitude reporting.

ShakeMap: At present, ShakeMaps are generated on five systems within the CISN. Two systems in Pasadena generate "SoCal" Shakemaps; two systems in the Bay Area generate "NoCal" Shakemaps; and one system in Sacramento generates ShakeMaps for all of California. In the CISN, we evaluated the new release of the program, ShakeMap 3.5. ShakeMaps have been recalculated for all scenario events, and are about to be published. We will also soon recalculate ShakeMaps for all events in the catalog. This is necessary for two reasons. First, ShakeMap 3.5 adds additional products to the suite, such as ground motion uncertainties. Second, for ShakeMaps produced before November 2006 when the first steps toward AQMS implementation were made, there is a discrepancy between the event ID number on the ShakeMap and that in the database. In the past year, we published new Scenario Shake-

Maps, which are available on the web (http://www.cisn.org/shakemap/nc/shake/archive/scenario.html)

We have achieved the goal of improving the robustness of ShakeMap generation and delivery by CGS providing back-up for all California events. The Sacramento system now uses PDL (Product Distribution Layer) to collect the authoritative event information for Northern and Southern California. The CGS also "listens" for event information from the Alaska Tsunami Warning Center as a backup, should Northern or Southern California fail to produce event information. If no map is generated by the authoritative network within 10 minutes, CGS publishes a ShakeMap. This has been tested by CGS publishing maps for events that are smaller than our usual lower limits. They have appeared on the web, associated with the correct event.

Moment Tensor Analysis: We are continuing to work toward the implementation of the capability of using data from strong motion sensors in the moment tensor interface. This is useful in large events such as the 2010 Cucapa-El Mayor earthquake in Baja California. All broadband stations out to about 600 km were clipped.

Metadata Exchange: Correct metadata are vital to CISN activities, as they are necessary to ensure valid interpretation of data. CISN is working on issues related to their reliable and timely exchange. The CISN Metadata Working Group compiled a list of metadata necessary for data processing and developed a model for their exchange. In this model, each CISN member is responsible for the metadata for its stations and for other stations that enter into CISN processing. For example, Menlo Park is responsible for the NSMP, Crest, and PG&E stations, while Caltech is responsible for data from the Anza network. At the present time, dataless SEED volumes are used to exchange metadata between the NCEMC and the SCEMC. The Metadata Working Group has made progress toward implementing Station XML format in this year. This is a format for metadata exchange. Since this vehicle is expandable, we have worked to define an "extended StationXML" that will allow exchange of a more comprehensive set of metadata than dataless SEED volumes. The extension includes parameters which are necessary for other systems, for example data in V0 format.

Standardization: The CISN's focus on standardization of software continues. The complete AQMS system is now implemented and providing real time earthquake information in the NCEMC (see Operational Section 4.7). The software has been implemented at other regional networks of the ANSS.

Earthquake Early Warning: Caltech, the BSL and the ETH Zürich have been using CISN data in real time to test earthquake early warning algorithms and to develop a demonstration earthquake early warning system (see Research Sections 2.30 and 2.29; see also http://seismo.berkeley.edu/research/early_warning, http://www.shakealert.org/ and http://www.cisn.org/eew). In 2010–2011, we achieved end-to-end processing, with events being published to a user display. The User Display is now running at the CalOES Warning Center in Sacramento, and at the location of many other beta users. They include Bay Area Rapid Transit (BART), the UC Berkeley Police Department, Google and other companies, agencies and organizations throughout California. Since August 2012, BART uses information from our EEW system to alert train operators to slow down and stop trains in the event of an earthquake.

CISN Display

CISN Display is an integrated Web-enabled earthquake notification system designed to provide earthquake information for emergency response at 24/7 operations centers. First and emergency responders, and organizations with critical lifelines and infrastructure with a need for rapid and reliable earthquake information can request an account at http://www.cisn.org/software/cisndisplay.htm.

The application provides users with maps of real time seismicity and automatically provides access to web related earthquake products such as ShakeMaps. CISN Display also offers an open source GIS mapping tool that allows users to plot freely available layers of public highways, roads and bridges, as well as private layers of organizational-specific infrastructure and facilities information. The current version of CISN Display is 1.68 at the time of writing.

Earthquake Information Distribution

The USGS hosted a workshop in October 2004 to develop plans for the installation and use of the EIDS software. Doug Neuhauser and Pete Lombard participated in this workshop, which resulted in a document outlining the steps necessary for the installation and migration of the earthquake notification system from the current Quake Data Distribution Services (QDDS) to the Earthquake Information Distribution System (EIDS). During the time EIDS was operating, shortcomings were noticed, particularly as earthquake information products became larger and more complex. During the past year, the NCEMC has transitioned from using EIDS system for publishing most of its earthquake information to the new tool, developed by the USGS, the Product Distribution Layer (PDL). This tool was initially deployed for transferring so-called add-on information, such as ShakeMaps. The BSL has been using a PDL system to publish ShakeMaps since June, 2011. During the FY 13–14 year, we worked with the USGS in Golden, CO to test and implement PDL for delivery of all real-time products, such as complete event information which includes the picks and amplitudes used for determination of location and magnitude, and other products such as moment tensors and fault plane solutions. Pete Lombard is fundamental to our progress in this effort. We currently publish all products through PDL. The BSL and NCEMC have been a "guinea pig" for implementation and is providing its codes for using PDL with AQMS to the other regional networks.

Outreach

Since FY 05–06, servers for the CISN website (http://www.cisn.org) are located at Berkeley and Caltech. The Web servers were set up so that the load could be distributed between them, providing improved access during times of high demand. With these servers, the CISN provides access to certain earthquake products directly from http://www.cisn.org. For example, ShakeMaps are now served directly from the CISN website, in addition to being available from several USGS Web servers and the CGS. The design and content of cisn.org continues to evolve. The website is an important tool for CISN outreach as well as for communication and documentation among the CISN partners. We are now serving an updated version of this website.

The CISN supports a dedicated website for emergency managers. This website provides personalized access to earthquake information. Known as "myCISN," the website is available at http://eoc.cisn.org. To provide highly reliable access, the website is limited to registered users.

As part of the CISN, the BSL contributes each year to efforts to raise awareness of earthquakes and earthquake preparedness. The BSL is a member of the Earthquake Country Alliance, a statewide organization of people, institutions and agencies associated with earthquake response and research. In the past year, we publicized and participated in the statewide ShakeOut on October 17, 2013. Due in part to our efforts, the entire UC Berkeley campus participated in it as well. We are now working toward the statewide California ShakeOut on October 16, 2014 at 10:16 (see http://www.shakeout.org for more information and to sign up).

Acknowledgements

CISN activities at the BSL are supported by funding from the California Office of Emergency Services (CalOES). Richard Allen and Peggy Hellweg are members of the CISN Steering Committee. Peggy Hellweg and Doug Neuhauser are members of the CISN Program Management Group, and Peggy leads the CISN project at the BSL with support from Doug Neuhauser. Doug Neuhauser is chair of the CISN Standards Committee, which includes Peggy Hellweg, Ivan Henson, Pete Lombard, Taka'aki Taira, and Stephane Zuzlewski as members.

Because of the breadth of the CISN project, many BSL staff members have been involved, including: John Friday, Peggy Hellweg, Ivan Henson, Ingrid Johanson, Pete Lombard, Joshua Miller, Doug Neuhauser, Charley Paffenbarger, Sarah Snyder, Taka'aki Taira, Stephen Thompson, Bob Uhrhammer, and Stephane Zuzlewski.

Peggy Hellweg contributed to this section. Additional information about the CISN is available through reports from the Program Management Group.

3 Northern Hayward Fault Network

Introduction

Complementary to the regional surface broadband and short-period networks, the Hayward Fault Network (HFN) (Figure 4.3.1 and Table 4.3.1) is a deployment of borehole-installed, wide-dynamic range seismographic stations along the Hayward Fault and throughout the San Francisco Bay toll bridge system. Development of the HFN was initiated through a cooperative effort between the BSL (Berkeley Seismological Laboratory) and the USGS, with support from the USGS, Caltrans, EPRI, the University of California Campus/ Laboratory Collaboration (CLC) program, LLNL (Lawrence Livermore National Laboratory), and LBNL (Lawrence Berkeley National Laboratory). The project's objectives included an initial characterization phase followed by a longer term monitoring effort using a backbone of stations from among the initial characterization station set. Funding from Caltrans, has, in the past, allowed for some continued expansion of the backbone station set for additional coverage in critical locations.

The HFN consists of two components. The Northern Hayward Fault Network (NHFN), operated by the BSL, consists of 29 stations in various stages of development and operation. These include stations located on Bay Area bridges, at free-field locations, and now at sites of the Mini-PBO (mPBO) project (installed with support from NSF and the member institutions of the mPBO project). The NHFN is considered part of the Berkeley Digital Seismic Network (BDSN) and uses the network code BK. The Southern Hayward Fault Network (SHFN) is operated by the USGS and currently consists of five stations. This network is considered part of the Northern California Seismic Network (NCSN) and uses the network code NC. The purpose of the HFN is fourfold: 1) to contribute operational data to the Northern California Seismic System (NCSS) for real-time seismic monitoring, for response applications, and for the collection of basic data for long-term hazards mitigation; 2) to substantially increase the sensitivity of seismic data to low amplitude seismic signals; 3) to increase the recorded bandwidth for seismic events along the Hayward Fault; and 4) to obtain deep bedrock ground motion signals at the bridges from more frequent, small to moderate sized earthquakes.

In addition to the NHFN's contribution to real time seismic monitoring in California, the mix of deep NHFN sites at near- and far-field sites and the high sensitivity (high signal to noise) and high frequency broadband velocity and acceleration data recorded by the NHFN also provide unique data for a variety of scientific objectives, including: a) investigating bridge responses to deep strong ground motion signals from real earthquakes; b) obtaining a significantly lower detection threshold for microearthquakes and possible nonvolcanic tremor signals in a noisy urban environment; c) increasing the resolution of the fault zone seismic structure (e.g., in the vicinity of the Rodgers Creek/Hayward Fault step over); d) improving monitoring of spatial and temporal evolution of background and repeating seismicity (to magnitudes below *M*0) to look for behavior indicating the nucleation of large, damaging earthquakes and to infer regions and rates of deep fault slip and slip deficit accumulation; e) investigating earthquake and fault scaling, mechanics, physics, and related fault processes; f) improving working models for the Hayward fault; and g) using these models to make source-specific response calculations for estimating strong ground shaking throughout the Bay Area.

Below, we focus primarily on activities associated with BSL operations of the NHFN component of the HFN.

NHFN Overview

The initial characterization period of HFN development ended in 1997. During that period, the NHFN sensors initially provided signals to on site, stand alone Quanterra Q730 and RefTek 72A-07 data loggers, and manual retrieval and download of data tapes was required. Also during the characterization period, the long term monitoring phase of the project began, involving the gradual transition of backbone monitoring sites to 24-bit data acquisition and communication platforms with data telemetry to the BSL.

Over the years, Caltrans has provided additional support for the upgrade of some non-backbone sites to backbone operational status and for the addition of several entirely new sites into the monitoring backbone. Efforts at continued expansion have been stymied due to propriety issue disputes between Caltrans and U.C. Berkeley at the administrative level. In February of 2007, the stations of the mPBO project were also folded into the NHFN monitoring scheme, increasing the NHFN by five sites.

Of the 29 stations considered part of the NHFN history, nine (E17B, E07B, YBAB, W05B, SAFB, SM1B, DB1B, DB2B, DB3B) are non-backbone stations and were not originally envisioned as long term monitoring stations. Because the borehole sensor packages at these sites could not be retrieved (having been grouted in downhole), the sites were mothballed for possible future reactivation. Support for reactivation of two of these mothballed sites (W05B and E07B) was eventually forthcoming and their reactivation is currently planned, pending completion of the Bay Bridge retrofit and resolution of the propriety issued mentioned above. Efforts at acquiring funds for reactivation/ upgrade of additional mothballed sites are also pending for similar reasons.

Twelve of the remaining 20 stations are currently operational (VALB, PETB, CMAB, HERB, BRIB, RFSB, SM2B, SVIN, MHDL, SBRN, OXMT, RB2B). Operation of an additional site (OHLN) has been temporarily interrupted due to outside parties severing the power cable during local construction. Restoration of normal operations is will happen once repairs are made at the site. Operation of our site outside the Cal Memorial Stadium (CMSB) was also interrupted, due to accidental destruction of the borehole site during retrofit work on the stadium. Respon-

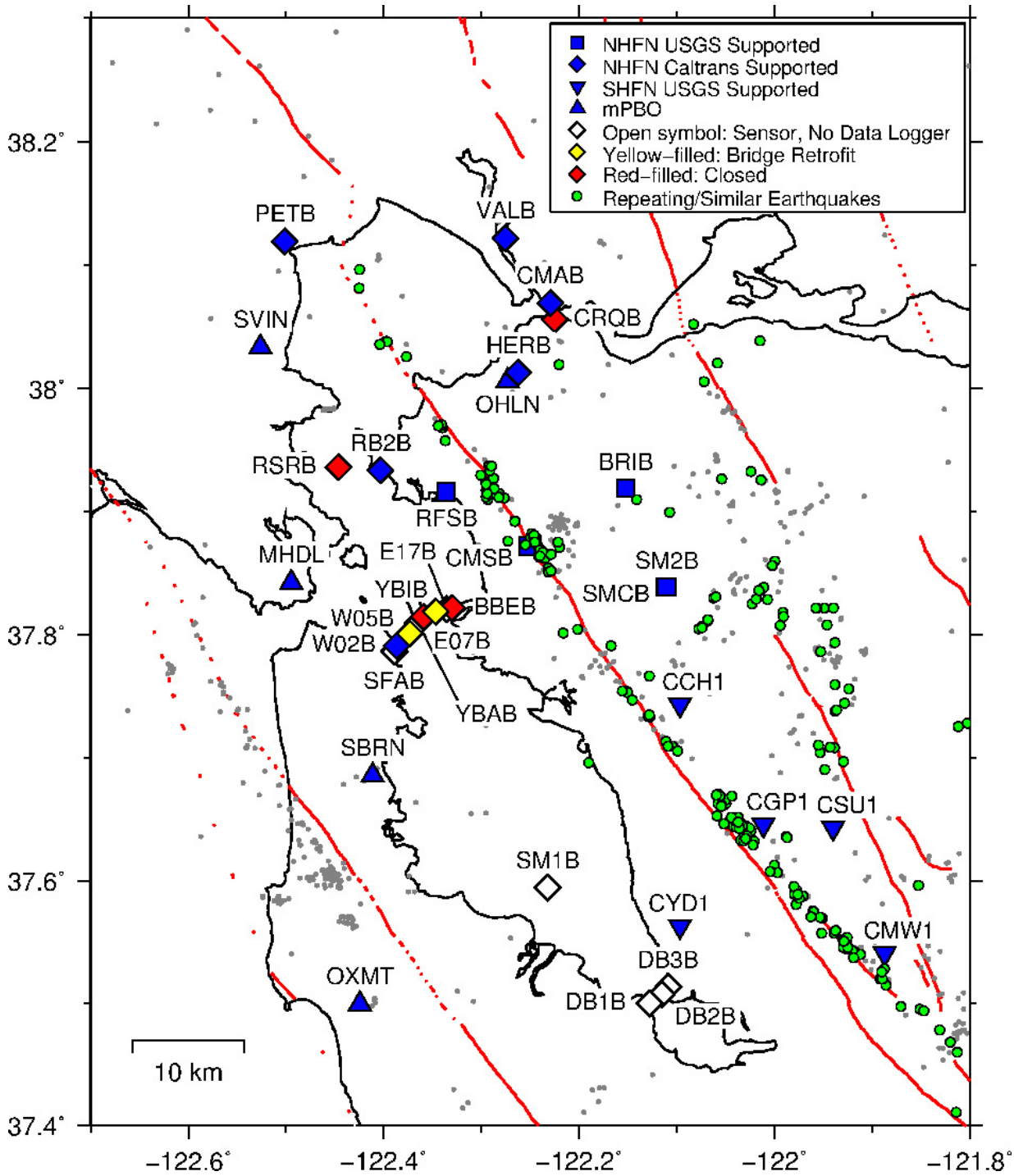

Figure 4.3.1: Map of HFN and mini-PBO stations. Diamonds are NHFN stations operated by the UC Berkeley Seismological Laboratory (BSL). Squares are BSL NHFN operated sites currently funded by the USGS. Inverted triangles are USGS SHFN sites. Triangles are former mini-PBO stations now part of the NHFN, operated by the BSL and funded by the USGS. Blue are currently operational stations. Red are stations that recorded data in the past but are now closed, either due to replacement by higher quality installations (CRQB, SMCB) or due to complications and/or damage from earthquake retrofit activity on Bay Area bridges (RSRB, BBEB, YBIB). The color yellow represents sites whose installation is suspended pending completion of the Bay Bridge retrofit (W05B, E07B) and resolution of Caltrans and U.C. Berkeley proprietary issues. Currently, station BBEB operates only as a telemetry repeater site due to damage from retrofit work. Open symbols represent sites having downhole sensors but are currently non-operational. These could potentially be brought on-line with funding support. Since 2007, the NHFN has been contributing arrival time picks to the Northern California Seismic System (NCSS) for location of Bay Area earthquakes. The small gray dots are double-difference real time relocations (http://ddrt.ldeo.columbia.edu/catalog/NCAeqDDRT.v201001) of events occurring this year that have made use of the NHFN picks. Green circles are locations of similar/repeating events occurring in the area (Taka'aki Taira, personal communication). Data for current and previously active NHFN and SHFN monitoring sites are all available through the NCEDC Web portal.

Code	Net	Latitude	Longitude	Elev (m)	Over (m)	Date	Location
VALB	BK	38.122	-122.275	-24.5	155.8	2005/11 - current	Napa River Bridge
PETB	BK	38.119	-122.501	-30	113	2010/09 - current	Petaluma River Bridge
CMAB	BK	38.069	-122.229	0	142.2	2009/12 - current	Cal Maritime Academy
CRQB	BK	38.056	-122.225	-25	38.4	1996/07 - 2010/05	CB
HERB	BK	38.012	-122.262	-18	217	2001/09 - current	Hercules
BRIB	BK	37.919	-122.152	222.2	108.8	1995/07 - current	BR, Orinda
RFSB	BK	37.916	-122.336	-27.3	91.4	1996/02 - current	RFS, Richmond
CMSB	BK	37.872	-122.252	94.7	167.6	1995/06 - current	CMS, Berkeley
SMCB	BK	37.839	-122.112	180.9	3.4	1998/02 - 2007/06	SMC, Moraga
SM2B	BK	37.839	-122.110	200	150.9	2007/06 - current	SMC, Moraga
SVIN	BK	38.033	-122.526	-27.5	152.4	2003/08 - current	mPBO, St. Vincent's school
OHLN	BK	38.006	-122.273	-0.5	196.7	2001/11 - current	mPBO, Ohlone Park
MHDL	BK	37.842	-122.494	94.5	151.9	2006/05 - current	mPBO, Marin Headlands
SBRN	BK	37.686	-122.411	4	161.5	2002/08 - current	mPBO, San Bruno Mtn.
OXMT	BK	37.499	-122.424	209.1	194.3	2003/12 - current	mPBO, Ox Mtn.
BBEB	BK	37.822	-122.330	-30.8	182.9	2002/09 - 2007/11	BB, Pier E23
E17B	BK	37.821	-122.335	TBD	160	1995/08 - unknown *	BB, Pier E17
E07B	BK	37.818	-122.347	TBD	134	1996/02 - unknown +	BB, Pier E7
YBIB	BK	37.814	-122.359	-27	61	1996/07 - 2000/08	BB, Pier E2
YBAB	BK	37.809	-122.365	TBD	3	1998/06 - unknown *	BB, YB Anchorage
W05B	BK	37.801	-122.374	TBD	36.3	1997/10 - unknown +	BB, Pier W5
W02B	BK	37.791	-122.386	-45	57.6	2003/06 - 2011/02	BB, Pier W2
SFAB	BK	37.786	-122.389	TBD	0	1998/06 - unknown *	BB, SF Anchorage
RSRB	BK	37.936	-122.446	-48	109	1997/06 - 2001/04	RSRB, Pier 34
RB2B	BK	37.933	-122.403	-18	133.5	2009/12 - current	RSRB, Pier 58
SM1B	BK	37.594	-122.232	TBD	298	not recorded *	SMB, Pier 343
DB3B	BK	37.513	-122.109	TBD	1.5	1994/09 - 1994/11 *	DB, Pier 44
					62.5	1994/09 - 1994/09 *	
					157.9	1994/07 - unknown *	
DB2B	BK	37.507	-122.116	TBD		1994/07 - unknown *	DB, Pier 27
					189.2	1992/07 - 1992/11 *	
DB1B	BK	37.499	-122.128	TBD	0	1994/07 - 1994/09 *	DB, Pier 1
					1.5	1994/09 - 1994/09 *	
					71.6	1994/09 - 1994/09 *	
					228	1993/08 - unknown *	
CCH1	NC	37.743	-122.097	345	119	1995/06 - current	Chabot
CGP1	NC	37.645	-122.011	461	121	1995/06 - current	Garin Park
CSU1	NC	37.643	-121.940	623	124	1995/11 - current	Sunol
CYD1	NC	37.563	-122.097	114	137	1996/11 - current	Coyote
CMW1	NC	37.541	-121.887	498	155	1995/06 - current	Mill Creek

Table 4.3.1: Stations of the Hayward Fault Network. For entries with "*" and "+" in the date column, no monitoring data is available. For these sites, dates are periods when data was downloaded manually. These manually retrieved data are not available at the NCEDC, but may be available from Larry Hutchings (at LBNL). Abbreviations: BB - Bay Bridge; BR - Briones Reserve; CMS - Cal Memorial Stadium; CB - Carquinez Bridge; DB - Dumbarton Bridge; mPBO - Mini-Plate Boundary Observatory; RFS - Richmond Field Station; RSRB - Richmond-San Rafael Bridge; SF - San Francisco; SMB - San Mateo Bridge; SMC - St. Mary's College; and YB - Yerba Buena. At the end of the initial characterization phase of the HFN project, the stations labeled with "*" were mothballed with borehole sensors remaining cemented in place. Incorporation of the "+" stations into the monitoring backbone is work in progress. Proposal to Caltrans requesting support to bring more mothballed sites into the NHFN backbone is pending. Due to damage from Bay Bridge retrofit work, station BBEB no longer records seismic data but continues to operate as a telemetry relay station. Data collection at sites CMSB and OHLN have been temporarily suspended to accommodate construction at their respective locations. W02B has been turned off due to equipment failure and lack of access.

Site	Geophone	Accelerometer	Z	H1	H2	Data Logger	Notes	Telem.
VALB	Oyo HS-1	Wilcoxon 731A	-90	336	246	Q330		FR
PETB	Oyo HS-1	Wilcoxon 731A	-90	TBD	TBD	Q330		FR/Rad.
CMAB	Oyo HS-1	Wilcoxon 731A	-90	161	251	BASALT		Rad./VPN
CRQB	Oyo HS-1	Wilcoxon 731A	-90	68	338	None at Present		FR
HERB	Oyo HS-1	Wilcoxon 731A	-90	160	70	Q4120		FR
BRIB	Oyo HS-1	Wilcoxon 731A	-90	79	169	BASALT	Acc. failed, Dilat.	FR
RFSB	Oyo HS-1	Wilcoxon 731A	-90	346	256	BASALT		FR
CMSB	Oyo HS-1	Wilcoxon 731A	-90	19	109	Q4120		FR
SMCB	Oyo HS-1	Wilcoxon 731A	-90	76	166	None at present	Posthole	FR
SM2B	Oyo HS-1	Wilcoxon 731A	-90	TBD	TBD	BASALT		FR
SVIN	Mark L-22		-90	319	49	BASALT	Tensor.	FR/Rad.
OHLN	Mark L-22		-90	300	30	BASALT	Tensor.	FR
MHDL	Mark L-22		-90	64	154	BASALT	Tensor.	FR
SBRN	Mark L-22		-90	6	96	BASALT	Tensor.	FR
OXMT	Mark L-22		-90	120	210	BASALT	Tensor.	FR
BBEB	Oyo HS-1	Wilcoxon 731A	-90	19	109	None at present	Acc. failed	Radio
E17B	Oyo HS-1	Wilcoxon 731A	-90	TBD	TBD	None at present		
E07B	Oyo HS-1	Wilcoxon 731A	-90	TBD	TBD	None at present		
YBIB	Oyo HS-1	Wilcoxon 731A	-90	257	347	None at present	Z geop. failed	FR/Rad.
YBAB	Oyo HS-1	Wilcoxon 731A	-90	TBD	TBD	None at present		
W05B	Oyo HS-1	Wilcoxon 731A	-90	TBD	TBD	None at present		
W02B	Oyo HS-1	Wilcoxon 731A	-90	TBD	TBD	None at present		Radio
SFAB	None	LLNL S-6000	TBD	TBD	TBD	None at present	Posthole	
RSRB	Oyo HS-1	Wilcoxon 731A	-90	50	140	None at present	2 acc. failed	FR
RB2B	Oyo HS-1	Wilcoxon 731A	-90	252	162	Q4120	1 acc. failed	FR
SM1B	Oyo HS-1	Wilcoxon 731A	-90	TBD	TBD	None at present		
DB3B	Oyo HS-1	Wilcoxon 731A	-90	TBD	TBD	None at present	Acc. failed	
DB2B	Oyo HS-1	Wilcoxon 731A	-90	TBD	TBD	None at present		
DB1B	Oyo HS-1	Wilcoxon 731A	-90	TBD	TBD	None at present	Acc. failed	
CCH1	Oyo HS-1	Wilcoxon 731A	-90	TBD	TBD	Nanometrics HRD24	Dilat.	Radio
CGP1	Oyo HS-1	Wilcoxon 731A	-90	TBD	TBD	Nanometrics HRD24	Dilat.	Radio
CSU1	Oyo HS-1	Wilcoxon 731A	-90	TBD	TBD	Nanometrics HRD24	Dilat.	Radio
CYD1	Oyo HS-1	Wilcoxon 731A	-90	TBD	TBD	Nanometrics HRD24	Dilat.	Radio
CMW1	Oyo HS-1	Wilcoxon 731A	-90	TBD	TBD	Nanometrics HRD24	Dilat.	Radio

Table 4.3.2: Instrumentation of the HFN. Every HFN downhole package consists of collocated three-component geophones and accelerometers, with the exception of mPBO sites which have only three-component geophones and are also collecting tensor strainmeter data. ix HFN sites also have dilatometers (Dilat.). The five SHFN sites have Nanometrics data loggers with radio telemetry to the USGS and eventually from there to the NCEDC for archiving. Currently, six NHFN sites have Quanterra data loggers, eight have been upgraded with ARRA funding and one (CMAB) with Caltrans funding to BASALT data loggers with local storage capacity. Of these 15 sites, 12 are currently telemetering continuous data to the BSL for archiving at the NCEDC. The sites CMSB and OHLN have been temporarily shutdown due to construction at their respective locations. Site W02B has been turned off due to equipment failure and lack of access for maintenance. Five additional backbone sites have been decommissioned for reasons ranging from the sites' replacement with nearby higher quality installations (SMCB, CRQB) to irreparable site damage by outside influences such as bridge retrofit activity and construction (BBEB, YBIB, RSRB). Station BBEB, however, continues to operate as a telemetry relay site. The component orientation of the sensors are as follows: vertical (Z) is up; horizontals (H1 and H2): azimuthal direction of positive counts in degrees clockwise from north and are given when known or labeled.

Sensor	Channel	Rate (sps)	Mode	FIR
Accelerometer	CL?	500	T	Ca
Accelerometer	CN?	500	T	Ca
Accelerometer	HL?	200	C	Ca
Accelerometer	HL?	100	C	Ca
Accelerometer	HN?	200	C	Ca
Accelerometer	BL?	20	C	Ac
Accelerometer	BN?	20	C	Ac
Accelerometer	LL?	1	C	Ac
Accelerometer	LN?	1	C	Ac
Geophone	DP?	500	T,C	Ca
Geophone	EP?	200	C	Ca
Geophone	EP?	100	C	Ca
Geophone	BP?	20	C	Ac
Geophone	SP?	20	C	Ac
Geophone	LP?	1	C	Ac

Table 4.3.3: Typical data streams acquired at NHFN sites, with channel name, sampling rate, sampling mode, and FIR filter type. C indicates continuous, T triggered, Ca causal, and Ac acausal. Typically, the DP1 continuous channel is archived and the remaining high sample rate data (i.e., CL?, CN?, DP2 and DP3 channels) are archived as triggered snippets. As telemetry options improve, progress is being made towards archiving higher sample rate and continuous data on more channels. Prior to September 2004, only triggered data was archived for all high sample rate channels. Of the stations that are currently operational, CMAB, HERB, BRIB, RFSB, CMSB, SM2B, W02B, and RB2B record at maximum sample rates of 500 Hz; VALB and PETB at maximum 200 Hz; and mPBO sites (SVIN, OHLN, MHDL, SBRN, OXMT) at maximum 100 Hz.

sibility for the destruction was identified and funds recovered to drill a new borehole in the same area. Drilling was completed in Sept. of 2013. Acquisition of funds for replacement of sensors and cable are currently under negotiation. Operation of station W02B on the western span of the Bay Bridge has been suspended due to the cessation of access to the site previously provided by Caltrans. Access is no longer available due to proprietary issues between Caltrans and U.C. Berkeley.

The operational sites include the five stations folded in from the mPBO project. The operational sites telemeter seismic data continuously into the BSL's BDSN processing stream with subsequent archival in the Northern California Earthquake Data Center (NCEDC).

Six of the 20 stations have been decommissioned for various reasons ranging from the sites' replacement with nearby higher quality installations (SMCB, CRQB) to irreparable site damage by outside influences such as bridge retrofit activity and construction (BBEB, YBIB, RSRB). Station BBEB, however, continues to be operational as a possible telemetry relay site for W02B should access to that site become available.

Installation/Instrumentation

The NHFN Sensor packages are generally installed at depths ranging between 100 and 200 m, the non-backbone, non-operational Dumbarton Bridge sites are exceptions with sensors at multiple depths (Table 4.3.1). The five former mPBO sites that are now part of the NHFN have three-component borehole geophone packages. Velocity measurements for the mPBO sites are provided by Mark Products L-22 2 Hz geophones (Table 4.3.2). All the remaining backbone and non-backbone NHFN sites have six-component borehole sensor packages. The six-component packages were designed and fabricated at LBNL's Geophysical Measurement Facility and have three channels of acceleration, provided by Wilcoxon 731A piezoelectric accelerometers, and three channels of velocity, provided by Oyo HS-1 4.5 Hz geophones.

The 0.1–400 Hz Wilcoxon accelerometers have lower self-noise than the geophones above about 25–30 Hz, and remain on scale and linear to 0.5 g. In tests performed in the Byerly vault at UC Berkeley, the Wilcoxon is considerably quieter than the FBA-23 at all periods, and is almost as quiet as the STS-2 between 1 and 50 Hz.

Currently five of the NHFN backbone sites have Quanterra data loggers, and nine of the sites have been upgraded with BASALT data loggers. When operational, all 14 of these sites telemeter continuously to the BSL. Signals from these stations are digitized at a variety of data rates up to 500 Hz at 24-bit resolution (Table 4.3.3). The data loggers employ causal FIR filters at high data rates and acausal FIR filters at lower data rates (Table 4.3.3).

Data Rates and Channels

Because of limitations in telemetry bandwidth and local disk storage, 6 of the 9 (excluding CMAB, VALB and PETB) six-component NHFN stations transmit maximum 500 Hz data continuously for only one geophone channel (i.e., when functional, on their vertical channel). Triggered 500 Hz data for three additional channels with 180-second snippets are also transmitted. Station VALB also continuously transmits data from only four channels, however, at a maximum of 200 Hz sampling. PETB transmits maximum 200 Hz data continuously on all six channels (three geophone, three accelerometer), and CMAB transmits maximum 500 Hz data continuously on all six channels. Continuous data for the channels of all 9 of these stations are also transmitted to the BSL at reduced sampling rates (20 and 1 sps). A Murdock, Hutt, and Halbert (MHH) event detection algorithm (*Murdock and Hutt*, 1983) is operated independently at each station on 500 sps data for trigger determinations. Because the accelerometer data is generally quieter, the MHH detections are made locally using data from the Wilcoxon accelerometers when possible. However, there is a tendency for these powered sensors to fail, and, in such cases, geophone channels are substituted for the failed accelerometers. The five mPBO-originated sites all transmit their three-cmponent continuous geophone data streams to the BSL at 100, 20, and 1 sps.

Integration with the NCSS, SeisNetWatch, and SeismiQuery

The NHFN is primarily a research network that complements regional surface networks by providing downhole recordings of very low amplitude seismic signals (e.g., from micro earthquakes or nonvolcanic tremor) at high gain with high frequencies and low noise. In addition, data streams from the NHFN are also integrated into the Northern California Seismic System (NCSS) real-time/automated processing stream for response applications and collection of basic data for long term hazards mitigation. The NCSS is a joint USGS (Menlo Park) and Berkeley Seismological Laboratory (BSL) entity with earthquake reporting responsibility for Northern California, and data from networks operated by both institutions are processed jointly to fulfill this responsibility. Through this integration, the NHFN picks, waveforms, and NCSS event locations and magnitudes are automatically entered into a database where they are immediately available to the public through the NCEDC and its DART (Data Available in Real Time) buffer. The capability for monitoring state of health information for all NHFN stations using SeisNetWatch also exists, and up-to-date dataless SEED formatted metadata is made available through the NCEDC with the SeismiQuery software tool.

Station Maintenance

Identifying network maintenance issues involves, in part, automated and semi-automated tracking of power, telemetry and data gaps. In addition, regular inspection of the seismic waveforms and spectra are carried out on samples of background noise and of significant local, regional and teleseismic earthquakes. These efforts are carried out to identify problems that can result from a variety of operational issues including changes in background noise levels from anthropogenic sources, ground loops, failing, damaged or stolen instrumentation, and power and telemetry issues. Troubleshooting and remediation of such problems are carried out through a coordinated effort between data analysts and field engineers.

In addition to routine maintenance and trouble shooting efforts, performance enhancement measures are also carried out. For example, when a new station is added to the NHFN backbone, extensive testing and correction for sources of instrumental noise (e.g., grounding related issues) and telemetry throughput are carried out to optimize the sensitivity of the station. Examples of maintenance and enhancement measures that are typically performed include: 1) testing of radio links to ascertain reasons for unusually large numbers of dropped packets; 2) troubleshooting sporadic problems with excessive telemetry dropouts; 3) manual power recycle and testing of hung data loggers; 4) replacing blown fuses or other problems relating to dead channels identified through remote monitoring at the BSL; 5) repairing telemetry and power supply problems when they arise; and 6) correcting problems that arise due to various causes, such as weather or cultural activity.

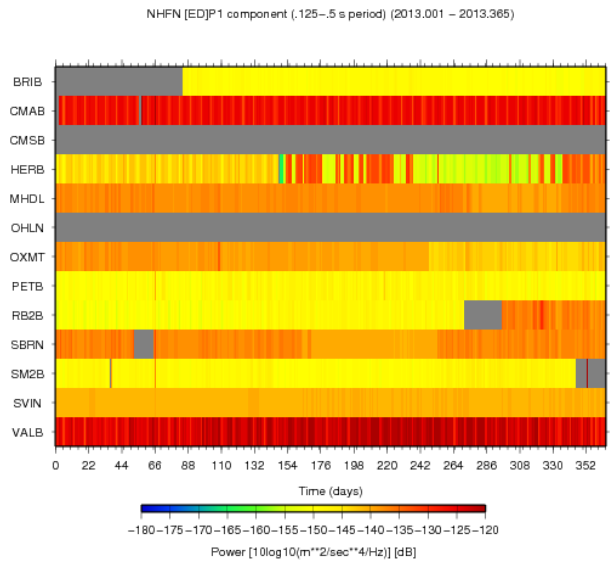

Figure 4.3.2: A summary of plots showing typically observed background noise PSD levels for the vertical DP1/EP1 channels of NHFN borehole stations for 2013. The mean PSD (dB) ranking (lowest to highest) of the non-mPBO stations (top panel) in operation at the time given at 3 Hz obtained from all available 2013 data on these channles are:
BRIB.BK.DP1 -141.885
SM2B.BK.DP1 -139.141
SVIN.BK.EP1 -138.458
PETB.BK.EP1 -136.895
OXMT.BK.EP1 -135.874
MHDL.BK.EP1 -135.736
SBRN.BK.EP1 -133.164
RB2B.BK.DP1 -127.971
HERB.BK.DP1 -126.818
CMAB.BK.DP1 -117.250
VALB.BK.EP1 -111.645
RFSB.BK.DP1 -107.407
PSDs for HFN/mPBO for the following stations are not available: CMSB (closed) and OHLN (power issue) due to construction. Variations in PSD noise among the stations are generally attributable to the stations' proximity to different cultural noise sources such as freeways or train tracks, differences in depth of sensor installation, or to differences in local geologic conditions.

Quality Control

Power Spectral Density Analyses

One commonly used quality check on the performance of the borehole installed network includes assessment of the power spectral density (PSD) distributions of background noise. We have developed and implemented an automated estimation of the power spectral density (PSD) distributions of background noise for all recorded NHFN channels and have developed summary PSD plots of these estimations to promote rapid evaluation of the noise levels through time.

Shown in Figure 4.3.2 are power spectral density (PSD) plots of background noise for 12 vertical NHFN channels in operation during 2013 for the 2–8 Hz frequency band. By

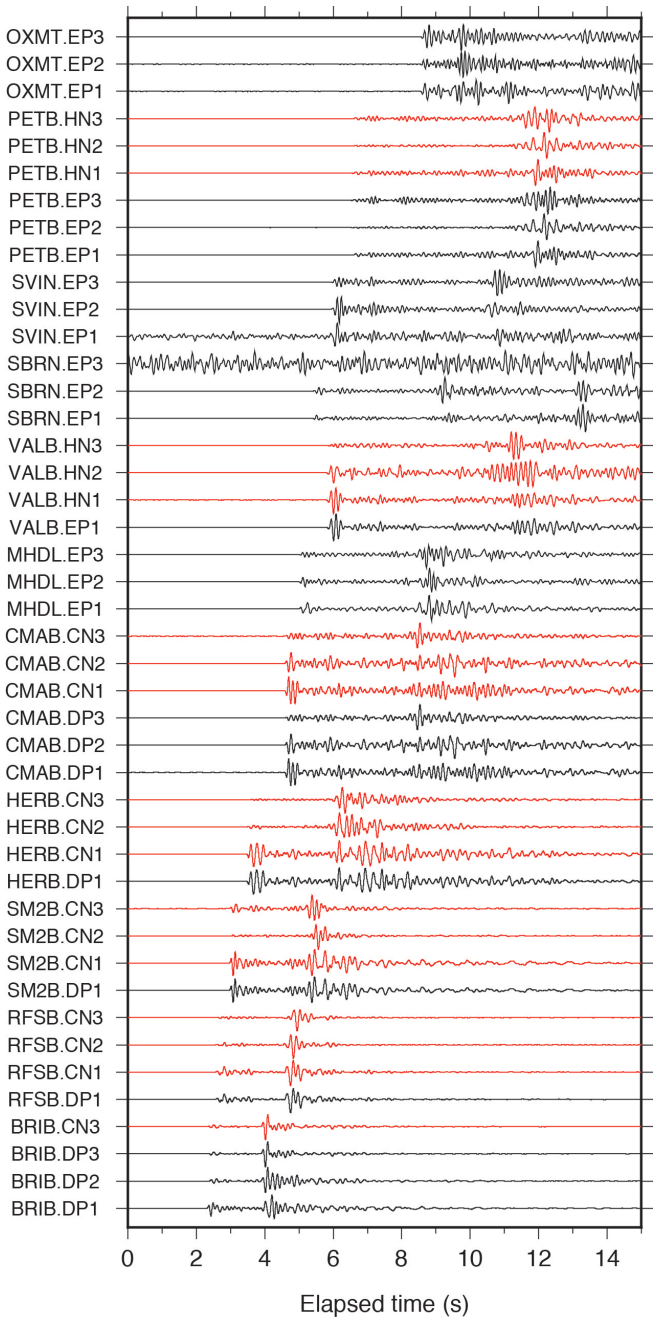

Figure 4.3.3: Plot of ground accelerations recorded on the geophones (black traces) and accelerometers (red traces) of the 11 NHFN borehole stations in operation at the time of a recent Bay Area earthquake (October 7, 2013, *M*3.14 near Orinda, CA). The traces are filtered with a 1–8 Hz bandpass filter, scaled by their maximum values, and ordered from bottom to top by distance from the epicenter.

continuously updating such plots in a variety of bands, we can rapidly evaluate changes in the network's station response to seismic signals across the wide band high-frequency spectrum of the borehole NHFN/mPBO sensors.

Changes in the responses often indicate problems with the power, telemetry, or acquisition systems, or with changing conditions in the vicinity of station installations that are

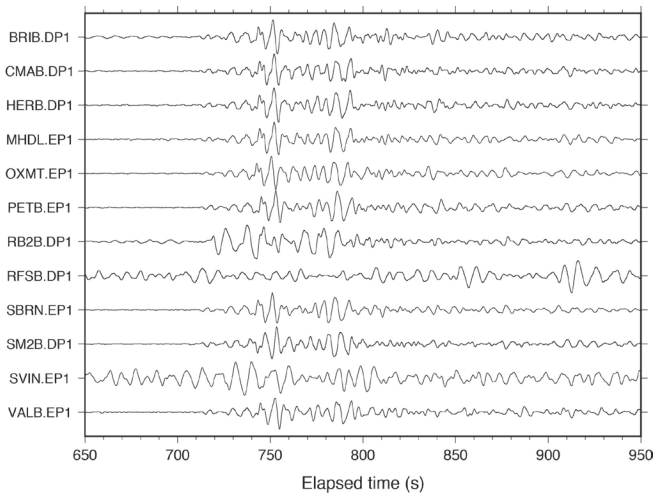

Figure 4.3.4: Plot of surface wave seismograms of the teleseismic M_w 8.2 earthquake off the northern coast of Chile (Lat.: 19.610S; Lon.: 70.760E; depth 25 km) occurring on April 1, 2014 23:46:47 (UTC) recorded on the DP1/EP1 (vertical) channels of the 12 NHFN borehole stations in operation at the time. Here, vertical component geophone (velocity) data have been 0.1–0.5 Hz bandpass filtered and normalized by the maximum amplitude for each trace.

adversely affecting the quality of the recorded seismograms. In general, background noise levels of the borehole NHFN stations are more variable and generally higher than those of the Parkfield HRSN borehole stations (see Parkfield Borehole Network section). This is due in large part to the significantly greater cultural noise in the Bay Area and the siting of several near-field NHFN sites in proximity to Bay Area bridges. On average, the mPBO component of the NHFN sites (MHDL, OXMT, SBRN, and SVIN in Figure 4.3.2) are more consistent with each other and throughout their spectral range. This is due in large part to the greater average depth of the mPBO sensors, the locations of mPBO stations in regions with generally less industrial and other cultural noise sources, and possibly to the absence of powered sensors (i.e. accelerometers) in their borehole sensor packages. The maximum sampling rate of 100 sps at these sites also limits their spectral range to a maximum of 40 Hz, well below the 60 Hz power line noise which often becomes a problem.

One of the most pervasive problems at the other NHFN stations with higher sampling rates is power line noise (60 Hz and its harmonics at 120 and 180 Hz). This noise reduces the sensitivity of the MHH detectors and can corrupt research based on full waveform analyses. When NHFN stations are visited, the engineer at the site and a seismologist at the BSL frequently work together to identify and correct ground loop and inductive-coupling problems, which are often at the root of this contamination.

Real Event Displays

Another method for rapid assessment of network performance is to generate and evaluate the seismograms from moderate local and large teleseismic earthquakes recorded by the NHFN stations. This is an essential component of NHFN

operations because the seismic data from local, regional, and teleseismic events are telemetered directly to the BSL and made available to the Northern California Seismic System (NCSS) real-time/automated processing stream for seismic response applications within a few seconds of being recorded by the NHFN.

Shown in Figure 4.3.3 is an example display of NHFN geophone and accelerometer channels for a recent local Bay Area earthquake (October 7, 2013 February 2013, *M*3.14 near Orinda, CA). It is apparent from this simple display that in general both the velocity and accelerometer channels are operating correctly, however, the channels SVIN.EP1, and SBRN.EP3 show excessive levels of noise that will need to be addressed. Stations CMSB, RB2B and OHLN were offline at the time, due to either landowner or construction related issues at those locations.

Figure 4.3.4 shows seismograms of the recent teleseismic M_w 8.2 earthquake off the northern coast of Chile (Lat.: 19.610S; Lon.: 70.760E; depth 25 km) occurring on April 1, 2014 23:46:47 (UTC). On this date and for this frequency band (0.1–0.5 Hz), network performance appears good for the vertical (DP1 and EP1) channels for nine of the stations in operation at the time. The RB2B.DP1, RFSB.DP1 and SVIN.EP1 channels have unacceptably high levels of noise that need to be addressed.

Signals from teleseismic events also serve as a good source for examining the relative polarities and responses of the BK borehole network station/components to seismic ground motion due to the near similar source-receiver paths after corrections are made for differences in instrument response among the stations. By rapidly generating such plots following large teleseismic events, quick assessment of the NHFN seismometer responses and polarities to real events is easily done and, if needed, corrective measures implemented with relatively little delay.

Both Figures 4.3.3 and 4.3.4 serve to illustrate the value of routine evaluation of both local (higher frequency) and teleseismic (lower frequency) events when monitoring the state of health of NHFN stations.

2013–2014 Activities

As in every year, routine maintenance, operations, quality control, and data collection play an important part in our activities. Other NHFN project activities have included: a) Specific station issues; b) efforts to obtain additional funds for future upgrade and expansion of the network; and c) Efforts to leverage NHFN activities through partnerships with various institutions outside of BSL

Specific Station Issues

BRIB: This year data collection from station BRIB has continued to be problematic. As with most NHFN sites, the BRIB installation is a complex integration of telemetry, power, recording, and sensor instrumentation. The BRIB station is particularly complex in that it collects coincident multi-component surface, borehole, broadband, short-period velocity and accelerometer data. Hence, getting at the root of the problems there has taken considerable effort with multiple site visits and contacts with the property administrators and power/telemetry providers. Considerable progress has been made for problems related to the power system at the site, and efforts to resolve several additional issues are continuing.

OHLN: The dense Bay Area population requires that most NHFN stations be cited on developed land, and permission to use the sites is at the discretion of generous private or public landowners. Consequently, landowner development of their properties sometimes requires temporary cessation and modifications to our station installations to accommodate both the landowners and our needs. This continues to be the case for station OHLN as it remains offline. However, notable progress has been made at modifying the power scheme at the site, and we expect OHLN to be back online soon.

W02B. Over the years, Caltrans has provided field and financial support for the operation and maintenance of this and several additional stations in the NHFN. However, this support has now been stymied by disputes over data propriety between Caltrans and U.C. Berkeley at the administrative level The site is experiencing what appears to be a failure in the data acquisition system. It is also located on the western span of the Bay Bridge and access to the site is limited, requiring travel on Caltrans boats. Due to the absence of maintenance support for this previously Caltrans supported site, operation of the station has had to be suspended. The proprietary issues between Caltrans and U.C. Berkeley were not able to be worked out so it appears that the site will remain inaccessible on a long term basis. Hence, long overdue site maintenance and the installation of a badly needed new BASALT data logger are no longer planned.

CMSB. Operation of our site outside the Cal Memorial Stadium (CMSB) was interrupted in late 2010 due to retrofit work on the stadium. It was later discovered that the borehole was accidentally destroyed during landscaping following the retrofit work. Responsibility for the destruction was identified and funds recovered to drill a new borehole in the same area. Drilling was completed in September of 2013. We are now in the process of working with the U.C. administration to acquire funds for replacement of the sensors and cable that were also destroyed as part of the landscaping. Once these funds become available, we will purchase and install the seismic equipment in the borehole and initiate data collection from the new replacement site.

Additional Funding

Operation of this Bay Area borehole network is supported by the Advanced National Seismic System (ANSS) and in the past through a partnership with the California Department of Transportation (Caltrans). ANSS provides operations and maintenance (O&M) support for a fixed subset of nine operational stations that were initiated as part of previous projects in which the USGS was a participant. Caltrans has in the

past provided field and financial support for development and O&M for the remaining stations that have been added to the network through Caltrans partnership grants. In the past, Caltrans also provided additional support for upgrade and expansion of the network, when possible.

Due to the state budget crisis in the late 2000s, Caltrans began reviewing and modifying its financial commitments and its accounting practices relating to its funding of external projects, such as the NHFN project. This severely complicated effort to receive previously approved NHFN funding from Caltrans, and it imposed many additional administrative roadblocks to acquiring additional Caltrans support. In June of 2010, our team held two meetings at Berkeley with our Caltrans contact and made a presentation at Caltrans in Sacramento to argue against O&M funding reductions and for further upgrade and expansion of the NHFN. These efforts resulted in a request by Caltrans for a proposal to install surface instruments at up to six of our borehole installations and to reactivate three currently mothballed NHFN sites. We submitted our proposal in September of 2010. Subsequently, a reduction in the Caltrans budget for external support resulted in a request from Caltrans for us to reduce the scope of the proposal we submitted. We promptly responded to this request and tentative approval was promised. Funding was held up for over a year, however, by bureaucratic concerns and issues of proprietary rights. Haggling over these issues between the University of California (reaching as high as the UC Office of the President) and Caltrans continued well into 2013 and the resolution was less than beneficial. Both sides have agreed that they cannot come to an agreement, and progress has come to a halt with approval for the proposed project being withdrawn by Caltrans.

This has put an end to any further work on improving and expanding the NHFN with Caltrans help. At this time, maintenance of previously supported Caltrans stations that are accessible without Caltrans assistance continues using some internal BSL funding, though at a greatly reduced effort. This is resulting in significantly longer downtime for failed stations and significantly degraded data. Eventually, if future support is not forthcoming, these sites will need to be closed. Sites such as W02B, where access through Caltrans is required, have had to have operations suspended due to system failure.

Partnerships

The NHFN is heavily leveraged through partnerships with various institutions, and we have continued to nurture and expand these relationships. Over the past year, we have continued our collaborative partnerships with the USGS, St. Mary's College, and the Cal Maritime Academy, as well as striven to renew collaboration with Caltrans. In addition, the BSL has continued to coordinate with Lawrence Berkeley National Laboratory (LBNL) in their project to develop an LBNL array of borehole stations that provide complementary coverage to the HFN.

Acknowledgments

Under Peggy Hellweg's, Robert Nadeau's and Doug Dreger's general supervision, Doug Neuhauser, Taka'aki Taira, and the engineering team (Sarah Snyder, Joshua Miller, and John Friday) all contribute to the operation of the NHFN. Robert Nadeau and Taka'aki Taira prepared this NHFN operations section of the BSL Annual Report.

Support for the NHFN this year was provided by the USGS through the cooperative networks grant program (grant number G10AC00093). In previous years, Pat Hipley of Caltrans has been instrumental in the effort to continue to upgrade and expand the network. Larry Hutchings and William Foxall of LLNL have also been important collaborators on the project in past years.

References

Rodgers, P.W., A.J. Martin, M.C. Robertson, M.M. Hsu, and D.B. Harris, Signal-Coil Calibration of Electromagnetic Seismometers, *Bull. Seism. Soc. Am., 85(3)*, 845-850, 1995.

Murdock, J. and C. Hutt, A new event detector designed for the Seismic Research Observatories, *USGS Open-File-Report 83-0785*, 39 pages, 1983.

Waldhauser, F. and D.P. Schaff, Large-scale relocation of two decades of Northern California seismicity using cross-correlation and double-difference methods, *J. Geophys. Res., 113*, B08311, doi:10.1029/2007JB005479, 2008.

4 Parkfield Borehole Network (HRSN)

Introduction

The operation of the High Resolution Seismic Network (HRSN) at Parkfield, California began in 1987, as part of the United States Geological Survey (USGS) initiative known as the Parkfield Prediction Experiment (PPE) (*Bakun and Lindh*, 1985).

Figure 4.4.1 shows the location of the network stations, their relationship to the San Andreas fault, sites of significance from previous and ongoing experiments using the HRSN, clusters of repeating earthquakes being monitored by the network, nonvolcanic tremors recorded by the network and located using envelope alignment arrival-times and a migrating grid search location method (*Uhrhammer et al.*, 2001), background seismicity occurring this year and the epicenters of the 1966 and 2004 *M*6 earthquakes that motivated much of the research. The HRSN has recorded exceptionally high-quality data, owing to its 13 closely-spaced three-component borehole sensors (generally emplaced in the extremely low attenuation and background noise environment at 200 to 300 m depth (Table 4.4.2, its high-frequency, wide bandwidth recordings (0-100 Hz; 250 sps), and its sensitivity to very low amplitude seismic signals (e.g., recording signals from micro-earthquakes and non-volcanic tremors with equivalent magnitudes below 0.0 M_L).

Several aspects of the Parkfield region make it ideal for the study of small earthquakes and nonvolcanic tremors and their relationship to tectonic processes and large earthquakes. These include the fact that the network spans the SAFOD (San Andreas Fault Observatory at Depth) experimental zone, the nucleation region of earlier repeating magnitude 6 events, a significant portion of the transition from locked to creeping behavior on the San Andreas fault, the availability of three-dimensional P and S velocity models (*Michelini and McEvilly*, 1991; *Thurber et al.*, 2006), a long-term HRSN repeating seismicity catalog (complete to very low magnitudes and that includes over half of the M6 seismic cycle), a well-defined and relatively simple fault segment, the existence of deep nonvolcanic tremor (NVT) activity, and a relatively homogeneous mode of seismic energy release as indicated by the earthquake source mechanisms (over 90% right-lateral strike-slip).

In recent years, these features have also spurred additional investment in seismic instrumentation in the area that greatly enhances the HRSN's utility, including the ongoing installation of the TremorScope array (funded by the Moore foundation) and NFS's EarthScope SAFOD and PBO stations.

In a series of journal articles and Ph.D. theses, the cumulative, often unexpected, results of research by UC Berkeley and others using HRSN data trace the evolution of a new and exciting picture of the San Andreas fault zone, and they are forcing new thinking on the dynamic processes and conditions within both the seismogenic (upper ~15 km depths) and sub-seismogenic layers (~15-35 km depths), where recently discovered nonvolcanic tremors are occurring.

Parkfield has also become the focus of a major component of NSF's EarthScope project known as the San Andreas Fault Observatory at Depth (SAFOD) (http://www.earthscope.org/observatories/safod). The SAFOD project is a comprehensive effort whose objectives include drilling into the hypocentral zone of repeating M ~2 earthquakes on the San Andreas Fault at a depth of about 3 km and establishing a multi-stage geophysical observatory in the immediate proximity of these events. The purpose of such an observatory is to carry out a comprehensive suite of down-hole measurements in order to study the physical and chemical conditions under which earthquakes nucleate and rupture (*Hickman et al.*, 2004). In these efforts, the HRSN plays a vital support role by recording seismic data used to directly constrain seismic signals recorded in the SAFOD main hole and by recording seismic events in the surrounding region to provide information on the larger scale fault zone processes that give rise to any changes observed in the main hole.

HRSN Overview

Installation of the HRSN deep borehole sensors (200-300 m) initiated in late 1986, and recording of triggered 500 sps earthquake data began in 1987. The HRSN sensors are three-component geophones in a mutually orthogonal gimbaled package. This ensures that the sensor corresponding to channel DP1 is aligned vertically and that the others are aligned horizontally. The sensors are also cemented permanently in place, ensuring maximum repeatability of the sensors' responses to identical sources, and allowing for precise relative measurements with minimal need for corrections and assumptions associated with moving the sensors. Originally a 10-station network, fully operational by January 1988, the HRSN was expanded to 13 borehole stations in late July 2001, and the original recording systems (see previous BSL Annual Reports) were upgraded to 24-bit acquisition (Quanterra 730s) and 56K frame relay telemetry to UCB. \ As part of funding from the American Recovery and Reinvestment Act (ARRA), an additional replacement/upgrade of the Quanterra 730 acquisition systems to 24-bit BASALT acquisition systems was accomplished in 2010–2011 and allows for local site storage and later retrieval of data during periods of sporadic telemetry failures. Properties of the sensors are summarized in Table 4.4.3.

The three newest borehole stations (CCRB, LCCB, and SCYB) were added, with NSF support, at the northwest end of the network as part of the SAFOD project to improve resolution of the structure, kinematics, and monitoring capabilities in the SAFOD drill-path and target zones. Figure 4.4.1 illustrates the location of the drill site, as well as locations of repeating earthquakes and nonvolcanic tremors recorded by the HRSN.

The three new stations have a similar configuration to the original upgraded 10 station network and include an additional channel for electrical signals. Station descriptions and instrument properties are summarized in Tables 4.4.2 and 4.4.3. All the HRSN data loggers employ FIR filters and extract data at 250 Hz (causal) and 20 Hz (acausal) (Table 4.4.1).

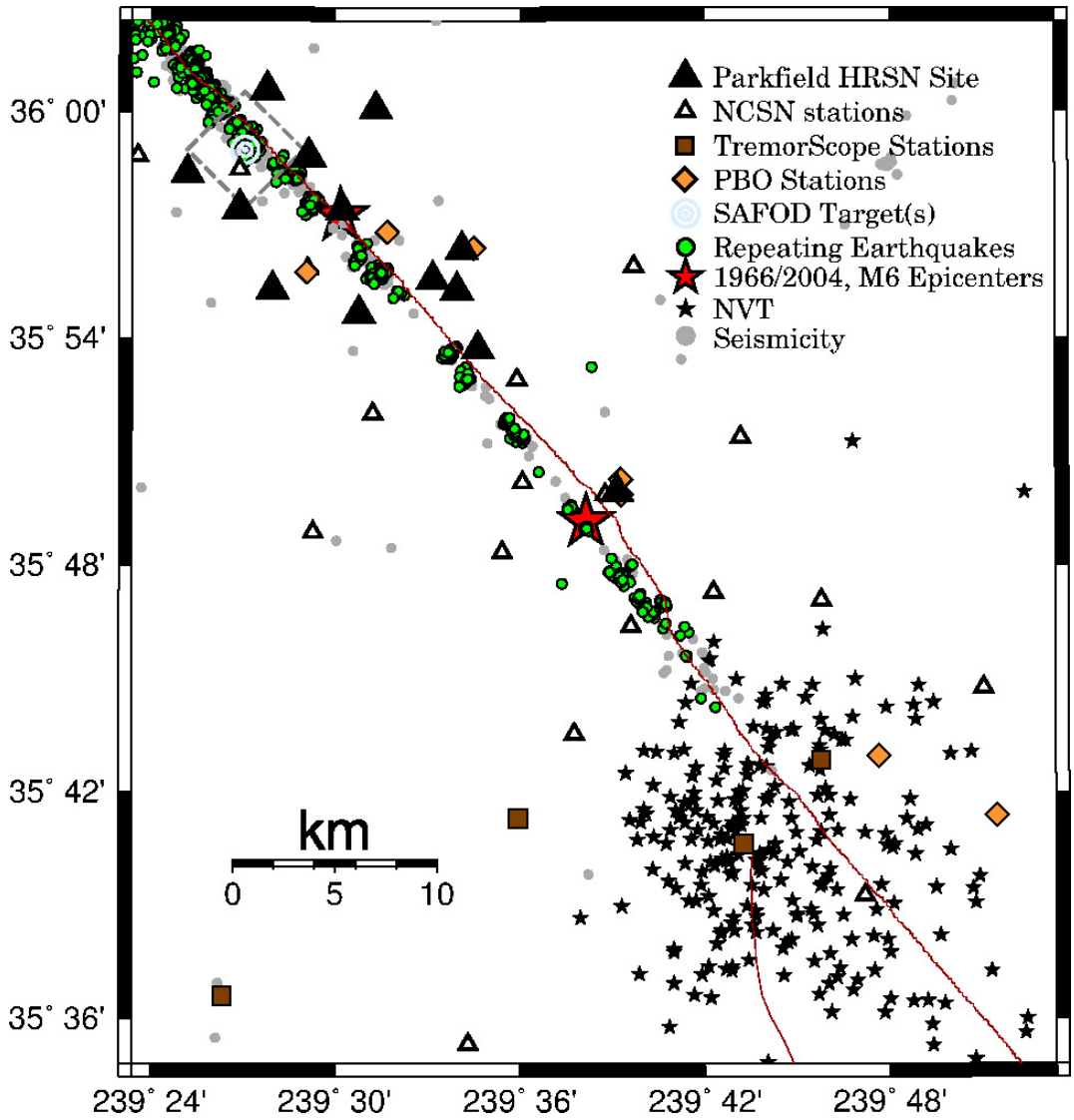

Figure 4.4.1: Map showing the San Andreas Fault trace and locations of the 13 Parkfield HRSN stations. Also shown are the 3 ~M2 SAFOD repeating earthquake targets (a 4 km by 4 km dashed box surrounds the SAFOD target zone), the epicenters of the 1966 and 2004 M6 Parkfield mainshocks, the locations (stars) of nonvolcanic tremors in the Cholame, CA area, and double-difference relocations of background (grey) and repeating (green) earthquakes processed by the integrated HRSN and NCSN networks. Recently installed or planned (Moore Foundation funded) TremorScope and borehole PBO stations (squares and diamonds, respectively) also complement the HRSN borehole coverage and are particularly useful for the study of the tremor. There are an additional five TremorScope and one PBO station outside the map bounds.

The remoteness of the SAFOD drill site and supporting HRSN stations required an installation of an intermediate data collection point at Gastro Peak, with a microwave link to our CDF (California Department of Forestry) facility. There was also one station, RMNB, that was located on Gastro Peak that transmitted directly to the CDF and served as a repeater for station LCCB. Prior to June 2008, eight of the HRSN sites transmitted either directly to or through repeaters directly to the CDF. This included stations RMNB and LCCB. The other five sites transmitted to a router at Gastro Peak, where the data was aggregated and transmitted to the CDF. However, due to disproportionately increasing landowner fees for access to the Gastro Peak site, we reduced our dependence on that site in the summer and fall of 2008 (in cooperation with the USGS) by re-routing telemetry of five of the sites previously telemetered through Gastro Peak to an alternative site at Hogs Canyon (HOGS). This eliminated the Gastro Peak microwave link, but left station RMNB and its repeater for LCCB at the mercy/good-graces of the Gastro Peak landowner. Subsequent negotiations with the landowner stalled and it was decided that RMNB was to be closed. An alternative repeater path for LCCB was also identified and made operational.

Continuous 20 and 250 Hz data from all HRSN channels are recorded and telemetered to the USGS site at Carr Hill for automatic picking and inclusion into Northern California Seismic System (NCSS) processing. The waveform data are also telemetered over a dedicated T1 circuit to the USGS and the Northern California Earthquake Data Center (NCEDC) at UC Berkeley

Sensor	Channel	Rate (sps)	Mode	FIR
Geophone	DP?	250.0	C	CA
Geophone	BP?	20.0	C	Ac

Table 5.4.1: Data streams currently being acquired at operational HRSN sites. Sensor type, channel name, sampling rate, sampling mode, and type of FIR filter are given. C indicates continuous; Ac acausal; Ca causal. "?" indicates orthogonal, vertical, and two horizontal components.

for archiving and for online access by the community. The HRSN system also generates autonomous station triggers and event associations that are also archived at the NCEDC.

The HRSN's telemetry system provides remote access to the local site data acquisition systems for state of health monitoring and control, and the recent upgrade to BASALT acquisition systems allows for local storage and retrieval of the data during telemetry outages.

Another feature of the HRSN system that has been particularly useful both for routine maintenance and for pathology identification has been the Internet connectivity of the central site processing computer and the individual stations' data acquisition systems. Through this connectivity, locally generated warning messages from the central site processor are sent directly to the BSL for evaluation by project personnel. If, upon these evaluations, more detailed information on the HRSN's performance is required, additional information can also be remotely accessed from the central site processing computer and generally from the individual site data loggers as well. Analysis of this remotely acquired information has been useful for trouble shooting by allowing field personnel to schedule and plan the details of maintenance visits to Parkfield. The connectivity also allows for local site acquisition shutdowns and restarts and for remote implementation of data acquisition parameter changes when needed.

The network connectivity and seamless data flow to UC Berkeley also provide near-real-time monitoring capabilities that are useful for rapid evaluation of significant events as well as the network's general state of health.

For example, shown in Figure 5.4.2 are surface wave seismograms of the teleseismic M_w 8.2 earthquake off the northern coast of Chile (Lat.: 19.610S; Lon.: 70.760E; depth 25 km) occurring on April 1, 2014 23:46:47 (UTC) recorded on the SP1 (vertical) channels of the 12 HRSN borehole stations in operation at the time. Station RMNB no longer records data due to landowner issues. The seismic data from the quake was telemetered to Berkeley and available for analysis by the Northern California Seismic System (NCSS) real-time/automated processing stream within a few seconds of being recorded by the HRSN.

This is also a good signal source for examining the relative responses of the BP borehole network station/components to seismic ground motion. In this case, the vertical channels for 10 of the 12 stations in the 0.1-0.5 Hz band appeared to be working well and with the proper polarities at the time of the earthquake. However, the vertical channel for FROB shows an anomaly, and it appears that the vertical channel for VARB did not recorded any signal from the earthquake. By rapidly generating such plots following large teleseismic events, quick assessment of the HRSN seismometer responses to real events is easily done and corrective measures implemented with relatively little delay.

Data Flow

Initial Processing Scheme

Continuous data streams on all HRSN components are recorded at 20 and 250 sps on disk locally on the BASALT data-logger systems and transmitted in near-real-time over the T1 circuit to the USGS at Menlo Park, CA, where they are integrated into the Northern California Seismic System (NCSS) real-time/automated processing stream. The data is also transmitted to the Berkeley Seismological Laboratory (BSL) for archiving at the NCEDC. This integration of HRSN data into the NCSS data flow has significantly increased the sensitivity of the NCSN catalog at lower magnitudes, effectively doubling the number of small earthquake detections in the Parkfield area and SAFOD zone.

Shortly after being collected and recorded to disk on the central site HRSN computer at the USGS Carr Hill facility, event triggers for the individual stations are determined, and a multi-station trigger association routine then processes the station triggers and generates a list of HRSN-specific potential earthquakes.

For each potential earthquake association, a unique event identification number (compatible with the NCEDC classification scheme) is also assigned. Prior to the San Simeon earthquake of December 22, 2003, 30 second waveform segments were then collected for all stations and components and saved to local disk as an event gather, and event gathers were then periodically telemetered to BSL and included directly into the NCEDC earthquake database (DBMS) for analysis and processing.

Because of its mandate to record very low amplitude seismic signals and microearthquakes in the Parkfield area, the HRSN was designed to operate at very high gain levels to enhance signal sensitivity. This comes at the expense of dynamic range for the larger events (above ~*M*3.0). The sensitivity to low amplitude signals is also enhanced by the placement of sensors in the low noise borehole environment (200-300 m depth) and by exhaustive efforts at knocking down extraneous noise sources that arise in each station's electronics, grounding, power, and telemetry systems and from interference from anthropogenic noise sources near the stations. As a consequence of the network's high sensitivity, the HRSN also records numerous outside signals from regional events and relatively distant and small amplitude nonvolcanic tremor events. For example, spot checks of aftershocks following the *M* 6.5 San Simeon earthquake of December 22, 2003 using continuous data and HRSN event detection listings revealed that the overwhelming majority of HRSN generated detec-

Site	Net	Latitude	Longitude	Surf. (m)	Depth (m)	Date	Location
EADB	BP	35.89525	-120.42286	466	245	01/1987 -	Eade Ranch
FROB	BP	35.91078	-120.48722	509	284	01/1987 -	Froelich Ranch
GHIB	BP	35.83236	-120.34774	400	63	01/1987 -	Gold Hill
JCNB	BP	35.93911	-120.43083	527	224	01/1987 - 02/18/2008	Joaquin Canyon North
JCNB*	BP	35.93911	-120.43083	527	4	07/2011 -	Joaquin Canyon North
JCSB	BP	35.9212	-120.43408	455	155	01/1987 -	Joaquin Canyon South
MMNB	BP	35.95654	-120.49586	698	221	01/1987 -	Middle Mountain
RMNB*	BP	36.00086	-120.47772	1165	73	01/1987 - 07/20/2011	Gastro Peak
SMNB	BP	35.97292	-120.58009	699	282	01/1987 -	Stockdale Mountain
VARB	BP	35.92614	-120.44707	478	572	01/1987 - 08/19/2003	Varian Well
VARB*	BP	35.92614	-120.44707	478	298	08/25/2003 -	Varian Well
VCAB	BP	35.92177	-120.53424	758	200	01/1987 -	Vineyard Canyon
CCRB	BP	35.95718	-120.55158	595	251	05/2001 -	Cholame Creek
LCCB	BP	35.98005	-120.51424	640	252	08/2001 -	Little Cholame Creek
SCYB	wBP	36.00938	-120.5366	945	252	08/2001 -	Stone Canyon

Table 5.4.2: Stations of the Parkfield HRSN. Each HRSN station is listed with its station code, network id, location, operation period, and site description. The latitude and longitude (in degrees) are given in the WGS84 reference frame. The surface elevation (in meters) is relative to mean sea level, and the depth to the sensor (in meters) below the surface is also given. Coordinates and station names for the three new SAFOD sites are given at the bottom. Notes, denoted with '*': There are 2 entries for JCNB, which failed in February of 2008 and has been replaced with a post-hole installation with ARRA funds. There are 2 entries for VARB, whose recording from a deep failed sensor (failure in August, 2003) was changed to a shallower sensor. Recording of data from station RMNB ended in July of 2011, due to landowner issues.

tions following San Simeon resulted from seismic signals generated by San Simeon's aftershocks, despite the HRSN's ~50 km distance from the events. Data from the California Integrated Seismic Network (CISN) show that there were ~1,150 San Simeon aftershocks with magnitudes >1.8 in the week following San Simeon, and during this same period, the number of HRSN event detections was ~10,500 (compared to an average weekly rate before San Simeon of 115 HRSN detections). This suggests that the HRSN was detecting San Simeon aftershocks well below magnitude 1 at distance of ~50 km or more.

Current Processing

Since the beginning of the network's data collection in 1987, and up until 2002, local and regional events were discriminated based on analyst assessment of S-P times, and only local events with S-P times less than ~2.5 s at the first arriving station were picked and located as part of the HRSN routine catalog. However, because of the network's extreme sensitivity to the large swarm of aftershocks from the 2003 San Simeon and 2004 Parkfield *M*6 earthquakes (e.g., in the first five months following the San Simeon mainshock, over 70,000 event detections were made by the HRSN system, compared to an average five month detection rate of 2500 prior to San Simeon) and because of ever declining funding levels, analyst review of individual microearthquakes was abandoned.

In addition, the dramatic increase in event detections following the San Simeon and Parkfield earthquakes vastly exceeded the HRSN's capacity to process and telemeter both continuous and triggered event waveform data. To prevent the loss of seismic waveform coverage, processing of the triggered waveform data was discontinued to allow the telemetry and archival of the 20 and 250 sps continuous data to continue uninterrupted. Subsequent funding limitations have since precluded reactivation of the triggered event processing. Cataloging of associated event triggers from the modified REDI real-time system algorithm continues, however, and both the continuous waveform data and trigger times are telemetered to and archived at the NCEDC, for access by the research community.

Because funding to generate catalogs of local micro-events from the tens of thousands of San Simeon and Parkfield aftershocks was not forthcoming, major changes in our approach to cataloging events had to be implemented. For example, HRSN data flow has now been integrated into the NCSS automated event detection, picking, and catalog processing. In addition, we have implemented a high resolution cross-correlation (pattern matching) based procedure to automatically detect, pick, locate, double-difference relocate, and determine magnitudes for select similar and repeating earthquake families down to very low magnitudes (i.e., below -0.0M_L). These new schemes are discussed in more detail in the activities section below under subsection "SOH using Similar and Repeating Events".

Site	Sensor	Z	H1	H2	RefTek 24	Quanterra 730	BASALT
EADB	Mark Products L22	-90	170	260	01/1987 - 06/1998	03/2001 - 07/2011	07/2011 -
FROB	Mark Products L22	-90	338	248	01/1987 - 06/1998	03/2001 - 11/2010	11/2010 -
GHIB	Mark Products L22	90	failed	unk	01/1987 - 06/1998	03/2001 - 07/2011	07/2011 -
JCNB	Mark Products L22	-90	0	270	01/1987 - 06/1998	03/2001 - 02/2008	-
JCNB*	Oyo GeoSpace GS-20DX	90	0	90	-	-	09/2011 -
JCSB	Geospace HS1	90	300	210	01/1987 - 06/1998	03/2001 - 04/2011	04/2011 -
MMNB	Mark Products L22	-90	175	265	01/1987 - 06/1998	03/2001 - 12/2010	12/2010 -
RMNB*	Mark Products L22	-90	310	40	01/1987 - 06/1998	03/2001 - 07/2011	-
SMNB	Mark Products L22	-90	120	210	01/1987 - 06/1998	03/2001 - 04/2011	04/2011 -
VARB	Litton 1023	90	15	285	01/1987 - 06/1998	03/2001 - 04/2011	-
VARB*	Litton 1023	90	358	88	01/1987 - 06/1998	03/2001 - 04/2011	04/2011 -
VCAB	Mark Products L22	-90	200	290	01/1987 - 06/1998	03/2001 - 04/2011	04/2011 -
CCRB	Mark Products L22	-90	258	348	-	05/2001 - 08/2011	08/2011 -
LCCB	Mark Products L22	-90	50	140	-	08/2001 - 09/2011	09/2011 -
SCYB	Mark Products L22	-90	342	72	-	08/2001 - 08/2011	08/2011 -

Table 5.4.3: Instrumentation of the Parkfield HRSN. Most HRSN sites have L22 sensors and were originally digitized with a RefTek 24 system. The WESCOMP recording system failed in mid-1998, and after an approximate three year hiatus the network was upgraded and recording was replaced with a new 4-channel system. The new system, recording since July 27, 2001, uses a Quanterra 730 4-channel acquisition. Three new stations were also added during the network upgrade period (bottom) In 2010-2011, with ARRA funding, additional replacement/upgrade to 24-bit BASALT acquisition with station-local data storage took place. Notes, denoted with '*': There are 2 entries for JCNB, which failed in February of 2008 and has replaced with a post-hole installation with ARRA funds. There are 2 entries for VARB, whose recording from a deep failed sensor (failure in August, 2003) was changed to a shallower sensor. Recording of data from station RMNB ended in July of 2011, due to landowner issues.

2013–2014 Activities

In addition to routine operations and maintenance, project activities this year include: a) Presentation to the National Earthquake Prediction Evaluation Council (NEPEC) on the state of research and monitoring at Parkfield using the HRSN, b) Further development and implementation of HRSN state of health (SOH) monitoring using repeating events, c) Routine monitoring of non-volcanic tremor activity in the Parkfield-Cholame area and routine updates of the web-page on tremor activity in support of the TremorScope project, and d) Continued support of SAFOD activities with updates of the repeating and similar event seismicity catalog.

Routine Operations and Maintenance

Routine maintenance tasks required this year to keep the HRSN in operation include replacement of aging with new preamplifier units and testing/confirmation of the new design's performance, cleaning and replacing corroded electrical connections, grounding adjustments, cleaning solar panels, testing and replacing failing batteries, ventilating battery and data logger housings to address problems with low power during hot weather, and repairing and realigning repeater sites and antennas.

Remote monitoring of the network's health using the Berkeley Seismological Laboratory's internally developed tools and SeisNetWatch software is also performed to identify both problems that can be resolved over the Internet (e.g., rebooting of data acquisition systems due to clock lockups) and more serious problems requiring field visits. Over the years, such efforts have paid off handsomely by providing exceptionally low noise recordings of low amplitude seismic signals produced by microearthquakes (below 0.0M_L) and nonvolcanic tremors.

The network connectivity over the T1 circuit also allows remote monitoring of various measures of the state of health (SOH) of the network in near-real-time using waveforms directly. For example, background noise levels can be rapidly evaluated. We have developed and implemented an automated estimation of the power spectral density (PSD) distributions of background noise for all recorded HRSN channels and have developed summary PSD plots of these estimations to promote rapid evaluation of the noise levels through time.

Shown in Figure 5.4.3 are power spectral density (PSD) plots of background noise for the 12 vertical HRSN channels in operation during 2013 for the 2-8 Hz frequency band where strong tremor signals are typically recorded. Continuous automated updating of such data plots in a variety of bands allow BSL personnel to rapidly evaluate changes in the network's station response to seismic signals across the wide band high frequency spectrum of the borehole HRSN sensors. Changes in the responses often indicate problems with

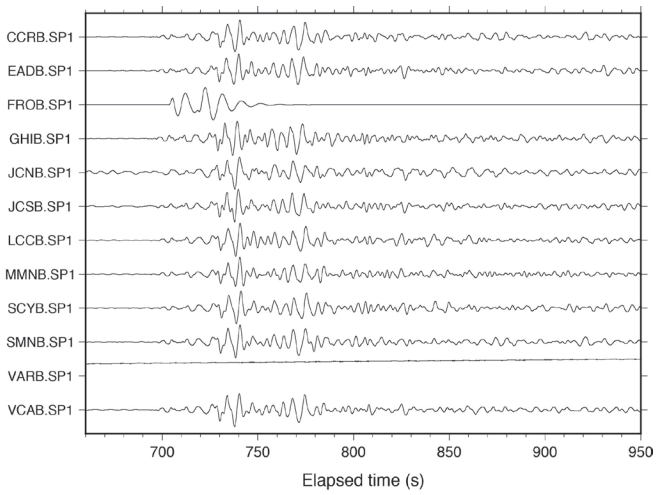

Figure 5.4.2: Plot of surface wave seismograms of the teleseismic Mw 8.2 earthquake off the northern coast of Chile (Lat.: 19.610S; Lon.: 70.760E; depth 25 km) occurring on April 1, 2014 23:46:47 (UTC) recorded on the SP1 (vertical) channels of the 12 HRSN borehole stations in operation at the time. Here, vertical component geophone (velocity) data have been 0.1-0.5 Hz bandpass filtered and normalized by the maximum amplitude for each trace.

the power, telemetry, or acquisition systems, or with changing conditions in the vicinity of station installations that are adversely affecting the quality of the recorded seismograms. Once state of health issues are identified, further remote tests can be made to more specifically determine probable causes, and corrective measures are then planned in advance of field deployment within a relatively short period of time.

Presentation to NEPEC

In a cost cutting effort, the USGS asked the National Earthquake Prediction Evaluation Council (NEPEC) this year to review the state of research and monitoring work around Parkfield, and to provide recommendations for future priorities. Roland Bürgmann and Robert Nadeau of the BSL were asked to attend the meeting, to provide a briefing on research and monitoring efforts in the area using HRSN data, to listen to other presentations on Parkfield area research and monitoring efforts, and to share in discussions on the relative importance and future possibilities of the various data collection and analysis efforts taking place in the area. While it was worrisome that this discussion, prompted by squeezed budgets within the USGS EHP program was even needed, the case for continued support for HRSN operations was relatively easy to make and a number of positive comments were made about the HRSN by the NEPEC members (e.g., "The HRSN has come out very high on the priority list" and "If anything ought to stay, it is the HRSN".). It seems likely, therefore, that funding for continued HRSN operations will survive this round of USGS budget prioritization.

SOH using Similar and Repeating Events

The increased microseismicity (thousands of events) resulting from the San Simeon *M*6.5 (SS) and Parkfield *M*6 (PF) events, the lack of funds available to process and catalog the increased number of microearthquakes, and the increased interest in using the microquakes in repeating earthquake and SAFOD research have required new thinking on how to detect and catalog microearthquakes recorded by the HRSN.

One action taken to help address this problem has been to integrate HRSN data streams into the NCSN event detection and automated cataloging process. This approach has been successful at detecting and locating a significantly greater number of microearthquakes over the previous NCSN detection and location rate, essentially doubling the number of events processed by the NCSN. However, the HRSN-sensitized NCSN catalog is still only catching about half the number of local events previously cataloged by the HRSN using the old, HRSN-centric processing approach. Furthermore, triggered waveforms for the additional small NCSN-processed events are often not reviewed by an analyst, nor do these smaller events often have NCSN magnitude determinations associated with them.

These limitations can severely hamper research efforts relying on the more numerous similar and characteristically repeating microevents (*e.g.*, earthquake scaling studies, SAFOD related research, deep fault slip rate estimation, and the compilation of recurrence interval statistics for time-dependent earthquake forecast models). They also reduce the efficacy of using frequently recurring microevents as a tool for monitoring the network state-of-health (SOH).

To help overcome these limitations, we continued this year to implement our semi-automated similar-event cataloging scheme based on pattern matching (match filter) scans using cross-correlation of the continuous HRSN data. The method uses a library of reference event (pattern) waveforms, picks, locations, and magnitudes that have been accurately determined, to automatically detect, pick, locate, and determine magnitudes for events similar to the reference event with a level of accuracy and precision that only relative event analysis can bring.

The similar event detection is also remarkably insensitive to the magnitude of the reference event used, allowing similar microevents ranging over about three magnitude units to be fully cataloged using a single reference event, and it does a remarkably good job at discriminating and fully processing multiple superposed events.

Once a cluster of similar events has been processed, an additional level of resolution can then be achieved through the identification and classification of the subset of characteristically repeating microearthquakes (*i.e.*, near identical earthquakes) occurring within the similar event family (Figure 5.4.4). The pattern scanning approach also ensures optimal completeness of repeating sequences owing to scans of the matching pattern through "all" available continuous data, which is critical for applications relying on recurrence interval information. For example, only about half of the magnitude 0.26 events shown in Figure 5.4.4 were picked up by the NCSN-HRSN integrated network.

Figure 5.4.4 also shows how stable the performance of channel DP1 on the borehole VCAB.BP has remained over the ~five year period shown. Due to station malfunctions or

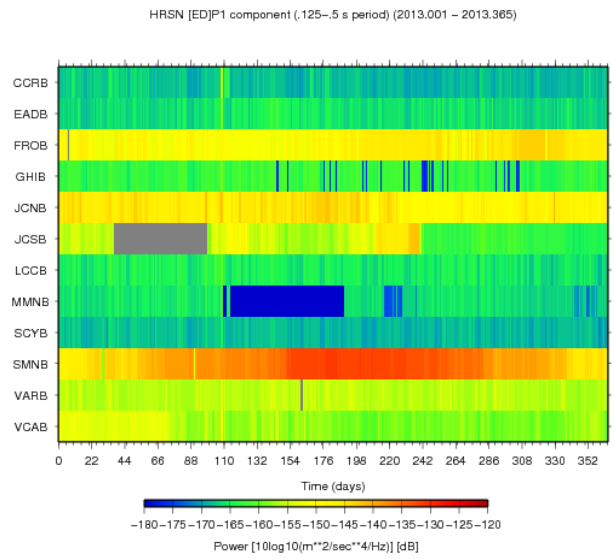

Figure 5.4.3: 2013 summary plots of 250 sps vertical component (i.e., DP1 channel) background noise Power Spectral Density (PSD) levels for the 12 operating HRSN borehole stations in the strong tremor frequency band (2-8 Hz or period 0.125–.5 s). The mean PSD (dB) ranking (lowest to highest) at 3 Hz obtained from all available 2013 data on these channles are:
MMNB.BP.DP1 -166.636
SCYB.BP.DP1 -163.456
CCRB.BP.DP1 -161.935
LCCB.BP.DP1 -159.035
EADB.BP.DP1 -156.827
GHIB.BP.DP1 -154.757
JCSB.BP.DP1 -151.567
VCAB.BP.DP1 -150.041
VARB.BP.DP1 -149.134
FROB.BP.DP1 -141.947
JCNB.BP.DP1 -139.245
SMNB.BP.DP1 -136.973
Note that failed station JCNB (failure in late 2007) has been reopened as a post-hole installation. The blue period for station MMNB between ~days 110 and 180 reflects a malfunction eventually found to be occuring in the aging pre-amplifier unit. The new pre-amplifier replacement was tested at MMNB first and eventually fixed the problem.

human error during field maintenance, this would not necessarily have been the case. Because repeating events can generally be reliably identified using any combination of 4 of the HRSN's 35 channels, assessment of the channel responses for channels not in the 4 channel combination can be carried out. This can be carried out repeatedly through time as additional repeats are identified with time resolutions depending on the number of repeating sequences used and the frequency of their repeats. Repeating sequences of this magnitude typically repeat every one to two years, and we are in the process of expanding our similar event monitoring capability to 61 of these sequences. Hence, on average, evaluations of this type can be possible approximately every 10 days on an automated basis. However, there are on the order of 200 such sequences known in the Parkfield area, and if one is willing to include even more frequently occurring similar but non-identical events into the equation, near-daily automated SOH analyses are a possibility.

Armed with this type of information, technicians and field engineers can quickly identify and address major problems. In addition to a visual assessment, the high similarity of the events lends itself to the application of differencing techniques in the time and frequency domains to automatically identify even subtle SOH issues. For other networks recording continuously in the Parkfield area (e.g., NCSN, BDSN/TremorScope) it is also a relatively simple process to extend the SOH analysis using characteristic repeating event signals recorded at their stations (See BDSN station RAMR example in Figure 5.4.5 of the BSL's 2011–2012) annual report. Furthermore, numerous repeating and similar event sequences are also known to exist in the San Francisco Bay, San Juan Bautista and Mendocino Triple Junction areas, where continuous recording takes place. Hence, application of the repeating event SOH technique to these zones should also be feasible.

This year we have finished adapting our cataloging codes to take advantage of faster computing now available on LINUX based machines. We have expanded the library of reference event patterns and retroactively scanned these patterns through previously recorded and ongoing data to capture and catalog an ever growing body of similar and repeating earthquakes for research purposes, in support of SAFOD, and for SOH monitoring (including the use of repeaters to identify and correct problems associated with the recently activated TremorScope stations). We have also continued to revise and automate our SOH waveform displays for rapid evaluation of HRSN performance based on repeater waveforms and have begun development of additional automated processing and display schemes to include visualization of spectral characteristics to the repeating event SOH analyses.

Tremor Monitoring and TremorScope

The HRSN played an essential role in the initial discovery of nonvolcanic tremors (NVT) and associated Low Frequency Events (LFE) along the San Andreas Fault (SAF) below Cholame, CA (*Nadeau and Dolenc*, 2005; *Shelly et al.*, 2009), and continues to play a vital role in ongoing NVT and LFE research. The Cholame tremors occupy a critical location between the smaller Parkfield (~*M*6) rupture zone and the adjacent and much larger Ft. Tejon (~*M*8) rupture zone along the SAF to the southeast (Figure 5.4.1). Because the time-varying nature of tremor activity is believed to reflect time-varying deep deformation and presumably episodes of accelerated stressing of faults (*Guilhem and Nadeau*, 2012), and because anomalous changes in Cholame area NVT activity preceded the 2004 Parkfield *M*6 earthquake (*Nadeau and Guilhem*, 2009; *Shelly*, 2009), and because tremor activity appears to be an ongoing process in the area (*Guilhem and Nadeau*, 2012) we are continuing to monitor the tremor activity observable by the HRSN to look for additional anomalous behavior that may signal an increased likelihood of another large SAF event in the region.

To date, over 3200 NVT bursts have been identified and

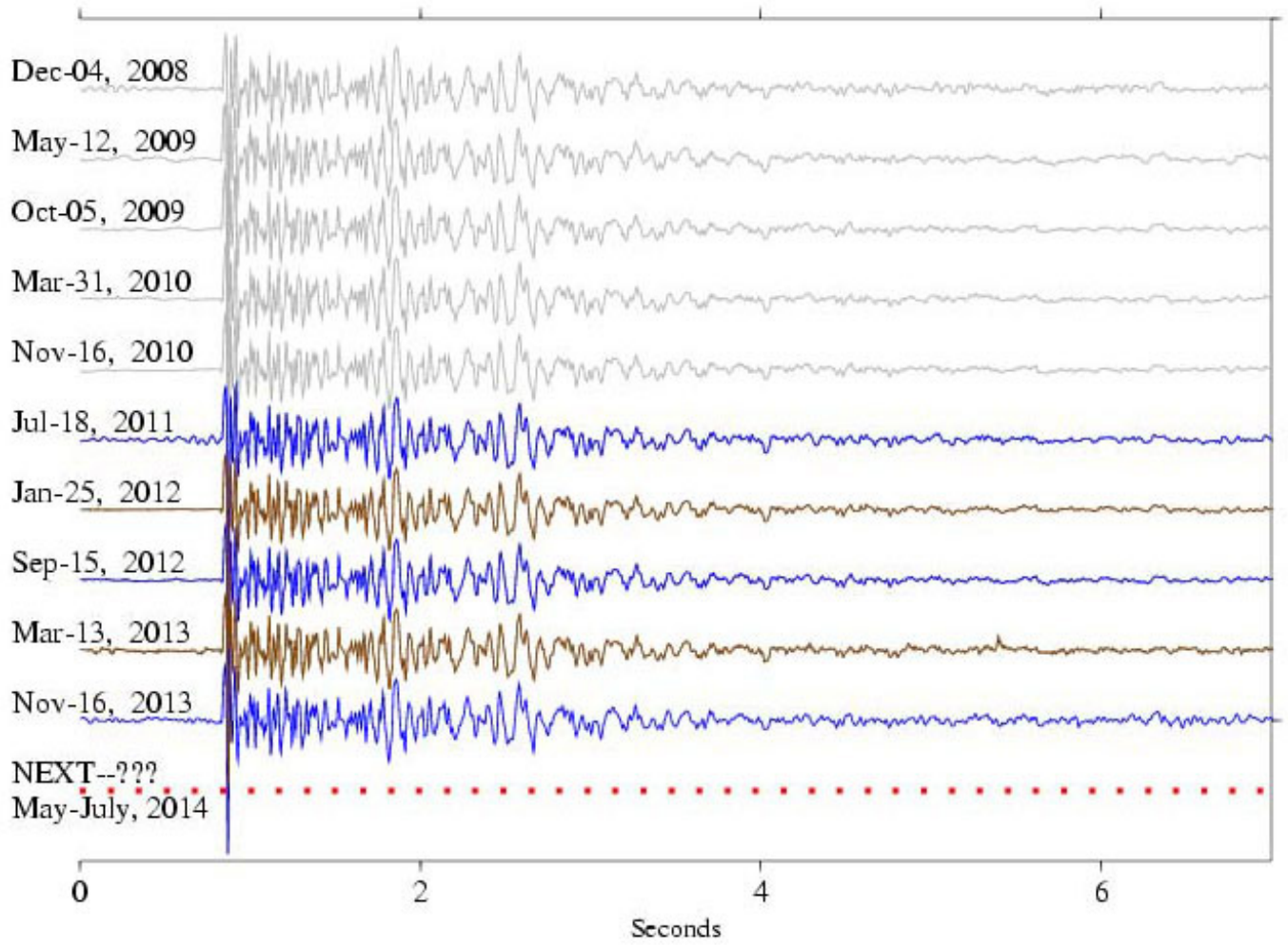

Figure 5.4.4: The ten most recent repeats of a characteristic sequence of repeating magnitude 0.26 (M_p, USGS preferred magnitude) microearthquakes recorded by vertical (DP1) channel of HRSN station VCAB. This sequence has repeated 50 times since the initiation of HRSN recording in 1987. Characteristically repeating microevents are extremely similar in waveform (typically 0.95 cross-correlation or better). High-precision relative location and magnitude estimates of these events show they are also nearly collocated (to within 5-10 m) and have essentially the same magnitude (+/- 0.13 M_p units, among all sequences studied). Immediately following the Parkfield *M*6 mainshock on Sept. 28, 2004, the frequency of repetition was greatly accelerated due to post-seismic loading from the main-shock (e.g., seven repeats in the three months following the mainshock). As time passes, however, the post-seismic effects from the mainshock have gradually diminished, repeating about two times a year.

In the BSL annual reports for 2010–2011, 2011–2012 and 2012–2013 we noted that the recurrence intervals (i.e., times between events in the repeating sequence) for events in this sequence were on the order of six to eight months. Based on this we predicted in the 2010–2011 report that the next repeat of the sequence would take place sometime in May through July of 2011. The occurrence of the July 18, 2011 event (blue/black) proved our prediction to be correct, and a subsequent repeat on January 25, 2012 (brown/dark-gray) also followed the six to eight month recurrence pattern. Another prediction was made in the following 2011–2012 annual report where we predicted at least one and possibly two additional repeats within the next year, with the next repeat expected in July through September of 2012. These preditictions were also fulfilled with the occurrence of the September 15, 2012 (blue/black) and March 13, 2013 (brown/dark-gray) events. Again in the 2012–2013 annual report we predicted once again that at least one and possibly two more additional repeats would occur within the next year, with the next repeat expected in September through November of 2013. This prediditiction was also fulfilled with the occurrence of the November 16, 2013 (blue/black) event. The dashed line labeled "NEXT" serves to illustrate our expectation that events in this sequences will continue the repeat pattern. Because the recent recurrence intervals continue to range between about six to eight months, we again predict at least one and possibly two additional repeats within the next year, with the next repeat expected to occur sometime in May through July of 2014. The most recent search period for repeats at at the time of this writing went through April 7 of 2014, with no subsequent repeat yet expected nor observed.

For network operational purposes, the repeating behavior of this and other sequences in the Parkfield area allows us to use repeating sequences to monitor changes in channel response relative to past performance and to rapidly identify and correct state-of-health (SOH) issues with real, naturally occurring signals. Making future predictions for such frequently repeating events and testing the prediction using real earthquakes could also be a useful motivating tool for teaching about earthquakes in an educational setting.

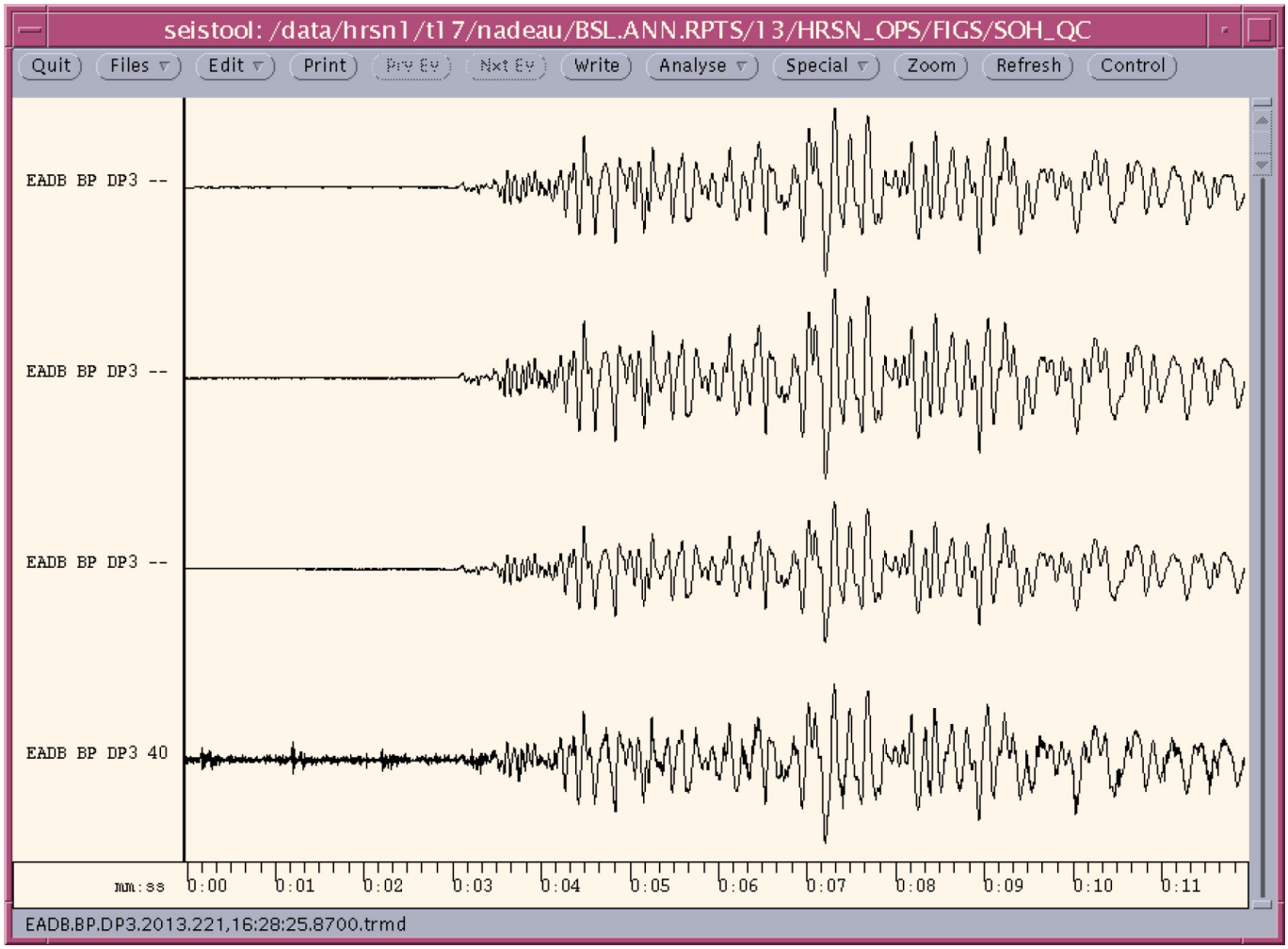

Figure 5.4.5: Repeating earthquake data illustrating their utility for identifying problematic channel responses. Here a repeat of EarthScope's SAFOD SF sequence (~*M*2.1) occurring on August 09, 2013 was identified using HRSN stations. The event and its previous repeats were used to evaluate the performance of stations from the HRSN and other networks out to distances greater than 50 km from the HRSN. Shown are the last four SF sequence events recorded on the DP3 horizontal channel of Berkeley's HRSN station EADB with no filtering. EADB is 16 km from the repeating events. From top to bottom, the events occurred on 11/02/2006, 12/20/2008, 11/23/2010, 05/30/2007, and 08/09/2013, respectively. Waveforms for the first three events are well recorded and consistent, indicating healthy station response. However, for the most recent event a significant degradation in response is seen. Signal from the 2013 event is contaminated with spiking about every second (indicative of soloar charger issues) and a background noise buzz with an ~ white spectrum is superposed on the earthquake signal. Corrective action taken was to ensure proper grounding of the electronic components at the installation and to replace the datalogger.

cataloged, and regular updates of the NVT catalog continue on an ~biweekly basis. Over the last year we have also developed a website displaying a map and section of recent 90-day tremor activity as well as a complete list of detected Parkfield-Cholame area tremor from July of 2001. This can be downloaded by researchers and the public at http://seismo.berkeley.edu/research/recent_tremor.html.

Efforts in Support of SAFOD

An intensive and ongoing effort by the EarthScope component called SAFOD (San Andreas Fault Observatory at Depth) was undertaken to drill through, sample, and monitor the active San Andreas Fault at seismogenic depths and in very close proximity (within a few tens of meters or less) to a repeating magnitude 2 earthquake site. The HRSN data play a key role in these efforts by providing azimuthal coverage of low noise and high sensitivity seismic waveforms from active and passive sources in the SAFOD region, by providing a backbone catalog of very small similar and repeating earthquakes detections, and by recording and archiving continuous waveform data.

As of early September 2007, SAFOD drilling had penetrated the fault near the HI repeating target sequence and collected core samples in the fault region that presumably creeps and surrounds the repeatedly rupturing HI patch. Unfortunately, due to complications during drilling, penetration and sampling of the fault patch involved in repeating rupture was not possible, though core sampling and installation of seismic instrumentation in the region adjacent to the repeating patch was achieved. Current efforts are focused on analysis of col-

lected core samples and long-term monitoring of the ongoing chemical, physical, seismological, and deformational properties in the zone (in particular any signals associated with subsequent repeats of the SAFOD target sequences).

HRSN activities this year have contributed in three principal ways to these and longer-term SAFOD monitoring efforts:

1) Processing of integrated HRSN and USGS data streams in the Parkfield area continues, effectively doubling the number of small events available for monitoring seismicity in the SAFOD target zone and for constraining relative locations of the ongoing seismic activity.

2) Telemetry of all HRSN channels (both 20 and 250 sps data streams) continues to flow directly from Parkfield, through the USGS Parkfield T1 and the Northern California Earthquake Management Center (NCEMC) T1, to the USGS and the BSL for near real-time processing, catalog processing, and data archiving at the Web-accessible NCEDC portal. This also provides near-real-time access to the HRSN data for the SAFOD community, without the week- or month-long delay associated with the previous procedure of having to transport DLT tapes to Berkeley to upload and quality check the data.

3) Continued monitoring and expansion of our repeating (characteristic and similar event sequences) earthquake catalog, with particular focus on expansion and refinement of repeating event data within the 1.5 cubic km volume centered on the SAFOD target zone. In 2012–2013, we expanded the number of repeating sequence reference patterns in this zone from 3 to 18 and cataloged (detected, double-difference relocated, and determined magnitudes for) repeating and similar events associated with these sequences. This year we have continued to update the sequences with ongoing similar and repeated events, resulting in an expansion of the number of earthquakes within this small SAFOD focused volume to over 1,300 unique microquakes. The pattern matching approach to detection is prone to identifying the same event from more than one reference earthquake, so a procedure was also developed to remove redundant events from the overall catalog. A procedure was also developed to integrate arrival time information from the redundant pattern matches to improve connectivity of events from different similar event sequences in the double-difference relocations.

Continued monitoring of the 18 sequences in the immediate SAFOD zone this year has also led to the identification of the next repeats of the SAFOD SF and LA sequences which both occurred on August 09, 2013. The apparent triggering within less than a day of the repeat of the LA sequence by the repeat of the SF sequence reflects the first evidence of a return of this triggering relationship since its disruption at the time of the 2004 Parkfield *M*6 mainshock.

Figure 5.4.5 shows recordings of the horizontal (DP3) channel from HRSN station EADB for the most recent (bottom) and three previous repeats of the SAFOD SF sequence. While the repeated nature of these events is clearly apparent in the waveforms, it is also clear that the quality of the recording of the most recent event is below standard. Waveforms recorded on most other HRSN channels do not show the high frequency lower amplitude buzz and spiking apparent on the EADB DP3 channel. Replacement of the old preamp with the new preamp design in the spring of 2014 has rectified the problem. While degradation of the signal is apparent visually, such degradation is not generally apparent from automated quality control checks of station performance. This illustrates, then, the additional benefit of visual inspection and comparison of repeating events in SOH evaluations.

Acknowledgments

Under Peggy Hellweg's and Robert Nadeau's general supervision, Doug Neuhauser, Taka'aki Taira, and the engineering team (Joshua Miller, Sarah Snyder and John Friday) all contribute to the operation of the HRSN. Robert Nadeau prepared this section with help from Taka'aki Taira. During this reporting period, operation, maintenance, and data processing for the HRSN project was supported by the USGS, through grant G10AC00093.

References

Bakun, W. H., and A. G. Lindh, The Parkfield, California, prediction experiment, *Earthq. Predict. Res., 3*, 285-304, 1985.

Guilhem, A. and R.M. Nadeau, Episodic tremors and deep slow-slip events in Central California, *Earth Planet. Sci. Lett., 357-358,* 1-10, doi:10.1016/j.epsl.2012.09.028 2012.

Hickman, S., M.D. Zoback and W. Ellsworth, Introduction to special section: Preparing for the San Andreas Fault Observatory at Depth, *Geophys. Res. Lett., 31*, L12S01, doi:10.1029/2004GL020688, 2004.

Michelini, A. and T.V. McEvilly, Seismological studies at Parkfield: I. Simultaneous inversion for velocity structure and hypocenters using B-splines parameterization, *Bull. Seismol. Soc. Am., 81*, 524-552, 1991.

Nadeau, R.M. and A. Guilhem, Nonvolcanic tremor evolution and the San Simeon and Parkfield, California earthquakes, *Science, 325*, 191-193, doi:10.1126/science.1174155, 2009.

Nadeau, R.M. and D. Dolenc, Nonvolcanic Tremors Deep Beneath the San Andreas Fault, *Science, 307*, 389, 2005.

Shelly, D.R., Possible deep fault slip preceding the 2004 Parkfield earthquake, inferred from detailed observations of tectonic tremor, *Geophys. Res. Lett., 36*, L17318, doi:10.1029/2009GL039589, 2009.

Shelly, D.R., W.L. Ellsworth, T. Ryberg, C. Haberland, G.S. Fuis, J. Murphy, R.M. Nadeau and R. Burgmann, Precise location of San Andreas Fault Tremors near Cholame, California using seismometer clusters: Slip on the deep extension of the fault?, *Geophys. Res. Lett., 36*, L01303, doi:10.1029/2008GL036367, 2009.

Thurber, C., H. Zhang, F. Waldhauser, J. Hardebeck and A. Michael, Three-dimensional compressional wavespeed model, earthquake relocations, and focal mechanisms for the Parkfield, California region, *Bull. Seismol. Soc. Am., 96*, S38-S49, doi:10.1785/0120050825, 2006.

Uhrhammer, R.A., D. Dreger, and B. Romanowicz, Best Practice in Earthquake Location Using Broadband Three-component Seismic Waveform Data, *Pure and Applied Geophys, 158*, 259-276, 2001.

Zhang, H., R.M. Nadeau, R.N. Toksoz, C.H. Thurber and M. Fehler, Nonvolcanic Tremors in Localized Low Shear Wave Velocity Zones Beneath the San Andreas Fault, *J. Geophys. Res.*, (*in revision*), 2012.

5 Data Acquisition and Quality Control

Introduction

Stations from the networks operated by the BSL transmit data continuously to the BSL facilities on the UC Berkeley campus for analysis and archiving. In this section, we describe activities and facilities which pertain to the individual networks described in Operational Sections 4.1, 4.3, and 4.4, including procedures for data acquisition and quality control, and sensor testing capabilities and procedures. Some of these activities are continuous from year to year and have been described in prior BSL annual reports. In this section, we describe changes and activities which are specific to 2013–2014.

Data Acquisition Facilities

The data acquisition computers and associated telemetry equipment are located in the campus computer facility in Warren Hall at 2195 Hearst Avenue. This building was constructed according to current "emergency grade" seismic codes and is expected to be operational even after a *M*7 earthquake on the nearby Hayward Fault. The hardened campus computer facility within was designed with special attention for post-earthquake operations. The computer center contains state-of-the art seismic bracing, UPS power and air conditioning with generator backup, and extensive security and equipment monitoring.

Data Acquisition

Central-site data acquisition for data from the BDSN/HRSN/NHFN/mPBO networks is performed by two computer systems in the Warren Hall data center (Figure 4.5.1). These acquisition systems also collect data from the Parkfield-Hollister electromagnetic array and the BARD network. A third system is used primarily for data exchange. It transmits data to the U.S. National Seismograph Network (USNSN) from HOPS, CMB, SAO, WDC, HUMO, JCC, MOD, MCCM, ORV and YBH. Data from various subsets of stations also go to the Pacific and Alaska Tsunami Warning Centers, to the University of Washington and to the University of Reno, Nevada. In addition, the Southern California Earthquake Management Center has access to our wavepools for retrieving waveform data to include in its event gathers. Data for all channels of the HRSN are now telemetered continuously from Parkfield to the BSL over the USGS T1 from Parkfield to Menlo Park, and over the NCEMC T1 from Menlo Park to Warren Hall.

The BSL uses the programs *qmaserv, seedlink,* and *scream* to collect data from data loggers. These programs receive data from remote Quanterra, Basalt and Guralp data loggers and redistribute it to one or more client programs. The clients include: *datalog*, which writes the data to disk files for archival purposes; *wdafill*, which writes the data to the shared memory region for processing with the network services routines that provide parameters to AQMS, the earthquake monitoring software system; and to other programs such as the DAC480 system feeding our helicorder and the feed for the Memento Mori Web page.

The two computers performing data acquisition are also "network services" computers that reduce waveforms for processing with the AQMS software (Figure 4.5.2). To facilitate processing, each system maintains a shared memory region containing the current 30 minutes of data for each channel.

Currently, BDSN data loggers from sites which use frame relay telemetry are configured to enable data transmission over a single frame relay T1 circuit to UCB, a possible point of failure. We formerly had a second T1 circuit, which was discontinued due to the decrease in funding from the State. For Quanterra data loggers, the *qmaserv* client program *cs2m* receives data and multicasts it over a private ethernet. The program *mcast* receives the multicast data from *cs2m*, and provides a *comserv*-like interface to local *comserv* clients. Thus, each network services computer has a *qmaserv* server for all stations, and each of the two systems has a complete copy of all waveform data.

The multicasting approach now handles data received from other types of data loggers and from other networks like the NCSN and UNR (University of Nevada, Reno). Data from partner networks are received by Earthworm data exchange programs, are converted to MiniSEED and are also multicast. On both network services computers, *mserv* receives multicast data and handles it just as it does BSL MiniSEED data.

In 2006, the BSL established a real-time data feed of all BSL waveforms between the BSL acquisition systems and the NCEDC computers using the open source Freeorb software. This allows the NCEDC to provide near-real-time access to all BSL waveform data through the NCEDC DART (Data Availabile in Real Time) system.

We monitor seismic stations and telemetry using the program *seisnetwatch*. This program extracts and displays current information such as time quality, mass positions, and battery voltage. If the parameter departs from the nominal range, the station is marked with yellow or red to indicate a possible problem.

Seismic Noise Analysis

BSL seismic data are routinely monitored for state of health. An automated analysis is computed regularly to characterize the seismic noise level recorded by each broadband seismometer. In addition, this year we took advantage of the April 1, 2014, M_w8.2earthquake off the northern coast of Chile to check noise levels at our STS-1 stations in the frequency band from 0.2 mHz to 2 mHz, by looking at the normal mode spectra (see Operational Section 4.1).

In 2000–2001, the BSL began to routinely monitor the Power Spectral Density (PSD) of ground motion recorded at its seismic stations (see past Annual Reports, http://earthquakes.berkeley.edu/annual_report/). The PSD provides an objective measure of background seismic noise characteristics over a wide range of frequencies. Observing it throughout the year also provides an objective measure of seasonal variation in noise characteristics and supports early diagnoses of instrumental problems.

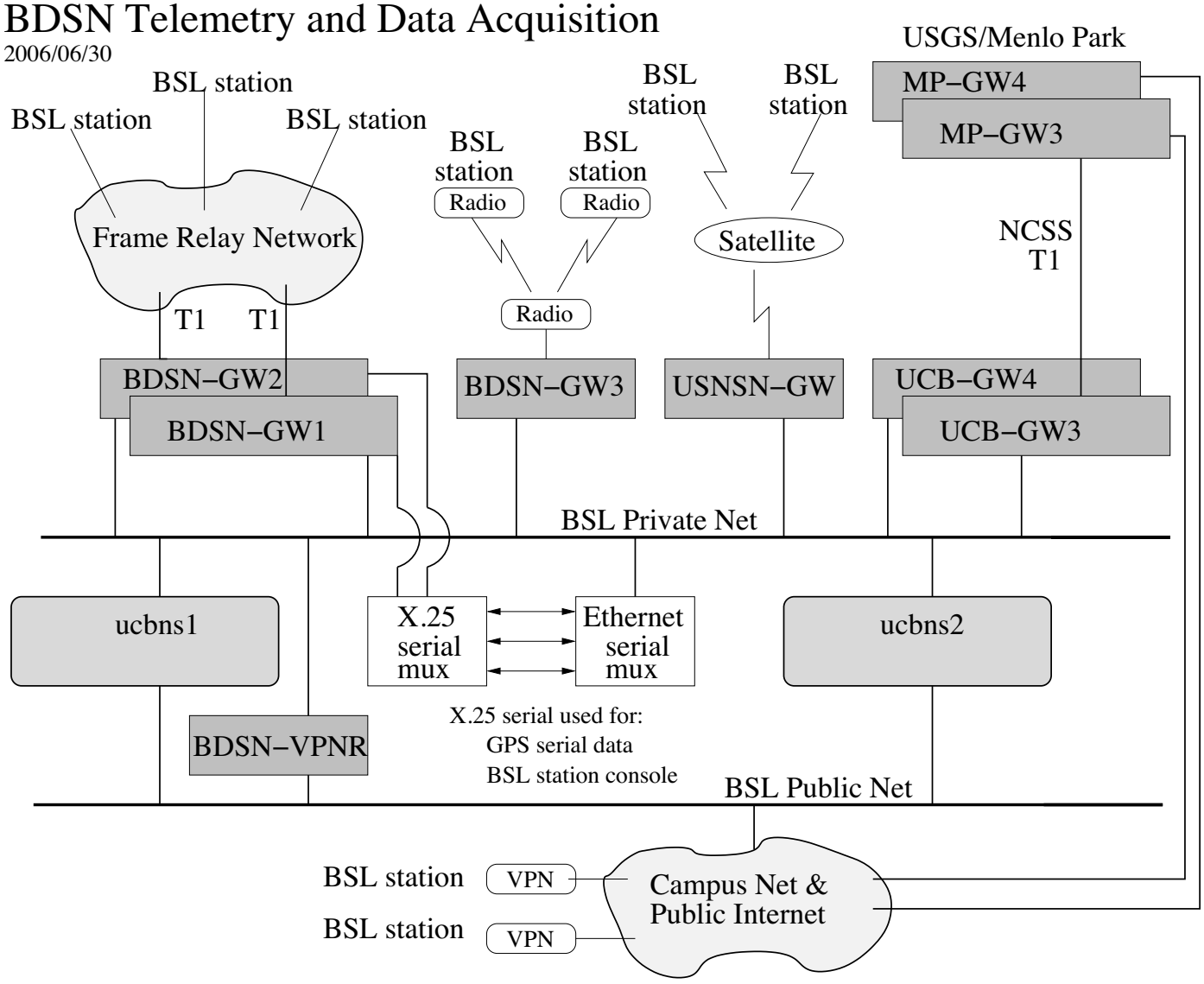

Figure 4.5.1: Data flow from the BDSN, NHFN, mPBO, HRSN, nad BARD networks into the BSL central processing facility.

The PSD estimation algorithm was developed at the BSL by Bob Uhrhammer in the early 1990s for characterizing the background seismic noise, and as a tool for quality control. That algorithm generates a bar graph output in which all the BDSN broadband stations can be compared by component. Cumulative PSD plots were generated for each station which showed the noise level in five frequency bands for the broadband channels. In addition to the station based plots, a summary plot was produced for each channel. Although we have moved to new noise monitoring procedures, these figures remain available on the web at http://earthquakes.berkeley.edu/seismo/bdsn/psd/, as they provide a record of equipment performance for the years 2000–2005.

Our main tool for monitoring seismic noise is now the Ambient Noise Probability Density Function (PDF) analysis system developed by *McNamara and Buland* (2004). This system performs its noise analysis over all the data of a given time period (week or year). The data processed include earthquakes, calibration pulses, and cultural noise. This is in contrast to Bob Uhrhammer's PSD analysis which looked at only the quietest portion of data within a day or week. Pete Lombard of the BSL extended the McNamara code to cover a larger frequency range and to support the many different types of sensors employed by the BSL. Besides the originally supported broadband sensors, our PDF analysis now includes surface and borehole geophones and accelerometers, strainmeters, and electric and magnetic field sensors. The enhancements to the PDF code, plus a number of bug fixes, were provided back to the McNamara team for incorporation in their work. The results of the PDF analysis are presented on our webpage at http://www.ncedc.org/ncedc/PDF/. The entry page now provides summary figures of the noise at each station for the BDSN and for other networks and stations we archive at the NCEDC. To provide an overview, figures are available for all components in two spectral bands, 32-128 s and 0.125-0.25 s for broadband sensors, and in the short period band for other sensors. This web page also provides access to the PDF plots for all stations, by network and component. In addition, each station's web page now provides

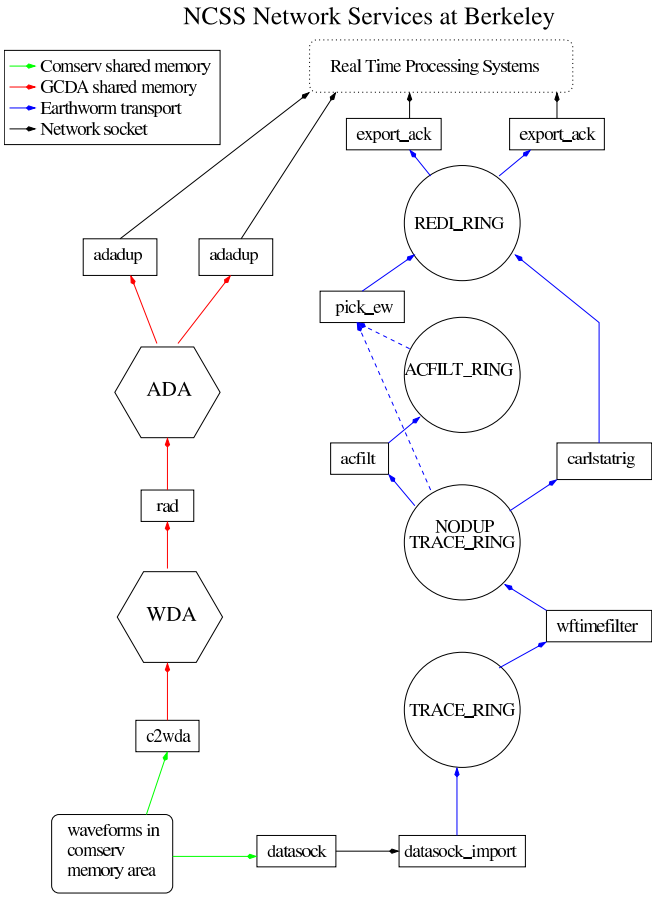

Figure 4.5.2: Flow of data from *qmaserv* areas through network services processing. One stream of the network services provides picks and an additional service provides associated codas determined using the programs shown in the right flow path. Every five seconds, ground motion parameters are also determined, including PGA, PGV, PGD, and ML100 (left flow column). Parameters from the network services are available to the AQMS software for event detection and characterization. Data are also logged to disk (via *datalog*), distributed to other computers (*mserv*), and spooled into a trace ring for export.

a summary of the noise performance of each channel (for an example, see the Data Quality tab at http://seismo.berkeley.edu/station_book/ybh.html).

Sensor Testing and Calibration

The BSL has an Instrumentation Test Facility in the Byerly Seismographic Vault where the characteristics of sensors can be systematically determined and compared. The test equipment consists of one or more six-channel Quanterra Q330 high-resolution data loggers and a custom interconnect panel. The panel provides isolated power and preamplification, when required, to facilitate the connection and routing of signals from the sensors to the data logger with shielded signal lines. The vault also has a GPS rebroadcaster, so that all data loggers in the Byerly vault operate on the same time base. Upon acquisition of data at up to 200 sps from the instruments under test, PSD analysis, coherence analysis, and other analysis algorithms are used to characterize and compare the sensor performance. Tilt tests and seismic signals with a sufficient signal level above the background seismic noise are also used to verify the absolute calibration of the sensors. A simple vertical shake table is used to assess the linearity of a seismic sensor. The BSL's sensor testing facility is described in detail in the 2001–2002 Annual Report (http://earthquakes.berkeley.edu/annual_report).

Testing STS-1 and STS-2 Sensors

In the past year, we have been testing several STS-1 sensors with hopes of replacing the slowly changing E-sensor at YBH. Three STS-1 seismometers (1 vertical, 2 horizontals) were set up in the Byerly Vault, along with an E300 electronics box and a STS-2 seismometer for testing purposes. Unfortunately, at the time of publication we have not yet been able to complete the testing as the individual sensors have not yet been responding properly.

TremorScope Geophone Cluster Test

Four three-component geophone packages with gimballed sensors will be installed in the TremorScope boreholes (see Research Section 2.34). During the spring, the geophone packages were temporarily connected to their respective cables. During two sessions the cables were connected by pigtails to the TremorScope data loggers and data were recorded on the Guralp EAM/DM24-6 units that will be used in the TremorScope deployments. During the first session, the geophones were strapped to a support in the Byerly Vault and recorded at 200 sps with a gain of 1 programmed in the data loggers (Figure 4.5.3). Because of problems with the data loggers and a dearth of interesting input signals, a second round of measurements were taken, with the geophone packages "emplaced" in sand and using a digitizer gain of 32. In neither case were the geophone packages placed so that the horizontal components had coherent orientations.

However, all sensors responded to ground movement. Initial results from both tests indicate that it will be important to know the exact response of each sensor for calculating the overall instrument response information, and for the correct rotation to compare sensor performance.

Monitoring Temporal Stability of Instrument Response in the BDSN

Monitoring the temporal stability of instrument response remains and important task at the BSL. We continue to evaluate sensor response as a function of time using the tools we have developed in the past years (see previous Annual Reports). For example, recent "sensor orientation" problems at KCC were discovered using these tools (see Operations Section 4.1).

We continue to monitor the response of the STS-1 seismometers operating in the BDSN. In the past year, fewer calibrations have been performed at the STS-1/E300 sites, since we have encountered challenges in communicating with the E300s following transitions away from frame relay telemetry.

Figure 4.5.3: The first geophone test in Byerly Vault, January 2014. The geophone borehole packages were strapped to the support between two instrument bays during the test.

A calibration of the sensors at KCC after telemetry was reinstated brought to light inconsistencies in our understanding of the orientation of the horizontal sensors. Following some remote sleuthing, we have corrected the instrument orientations in the database to reflect our understanding of the current status. On an upcoming site visit, we will investigate further and correct any inconsistencies in the hardware. It appears that there have been changes in the response of the E component at KCC, which we will also track down. We did perform a manual, on-site calibration at MHC, where we have original STS-1 factory electronics boxes. There the instrument response of the three sensors appears to be steady.

Acknowledgements

Doug Neuhauser, Bob Uhrhammer, Taka'aki Taira, Peggy Hellweg, Pete Lombard, Jennifer Taggart and Clay Miller are involved in the data acquisition and quality control of BDSN/HRSN/NHFN/mBPO data.

Bob Uhrhammer, Taka'aki Taira, Peggy Hellweg, Pete Lombard and Doug Neuhauser contributed to the preparation of this section.

References

McNamara, D. and R. Buland, Ambient Noise Levels in the Continental United States *Bull. Seism. Soc. Am., 94,* 4, 2004.

6 Bay Area Regional Deformation Network (BARD)

Introduction

The Bay Area Regional Deformation (BARD) network is a collection of permanent, continuously operating GPS receivers that monitor crustal deformation in the San Francisco Bay Area (SFBA) and Northern California. Started in 1991 with two stations spanning the Hayward Fault, BARD has been a collaborative effort of the Berkeley Seismological Laboratory (BSL), the USGS at Menlo Park (USGS/MP), and several other academic, commercial, and governmental institutions. The BARD network is designed to study the distribution of deformation in Northern California across the Pacific-North America plate boundary and interseismic strain accumulation along the San Andreas fault system in the Bay Area for seismic hazard assessment, and to monitor hazardous faults and volcanoes for emergency response management. It also provides data in real time for use in earthquake early warning (EEW) and rapid response applications. The BSL maintains and/or has direct continuous telemetry from 33 stations comprising the BARD Backbone, while additional stations operated by the USGS, US Coast Guard and others fill out the extended BARD network.

Since the completion of some major construction on the Plate Boundary Observatory (PBO) portion of EarthScope in 2004, the number of GPS stations in Northern California has expanded to over 250 (Figure 4.6.1). Together, PBO and BARD stations provide valuable information on the spatial complexity of deformation in the SFBA and Northern California, while the BARD network has the infrastructure and flexibility to additionally provide information on its temporal complexity over a wide range of time scales and in real time. All BARD Backbone stations collect data at 1 Hz sampling frequency and stream their data in real time to the BSL, where it is also provided to the public in real time. Furthermore, 18 BARD Backbone sites are collocated with broadband seismic stations of the BDSN, where they share continuous telemetry to UC Berkeley. As geodetic

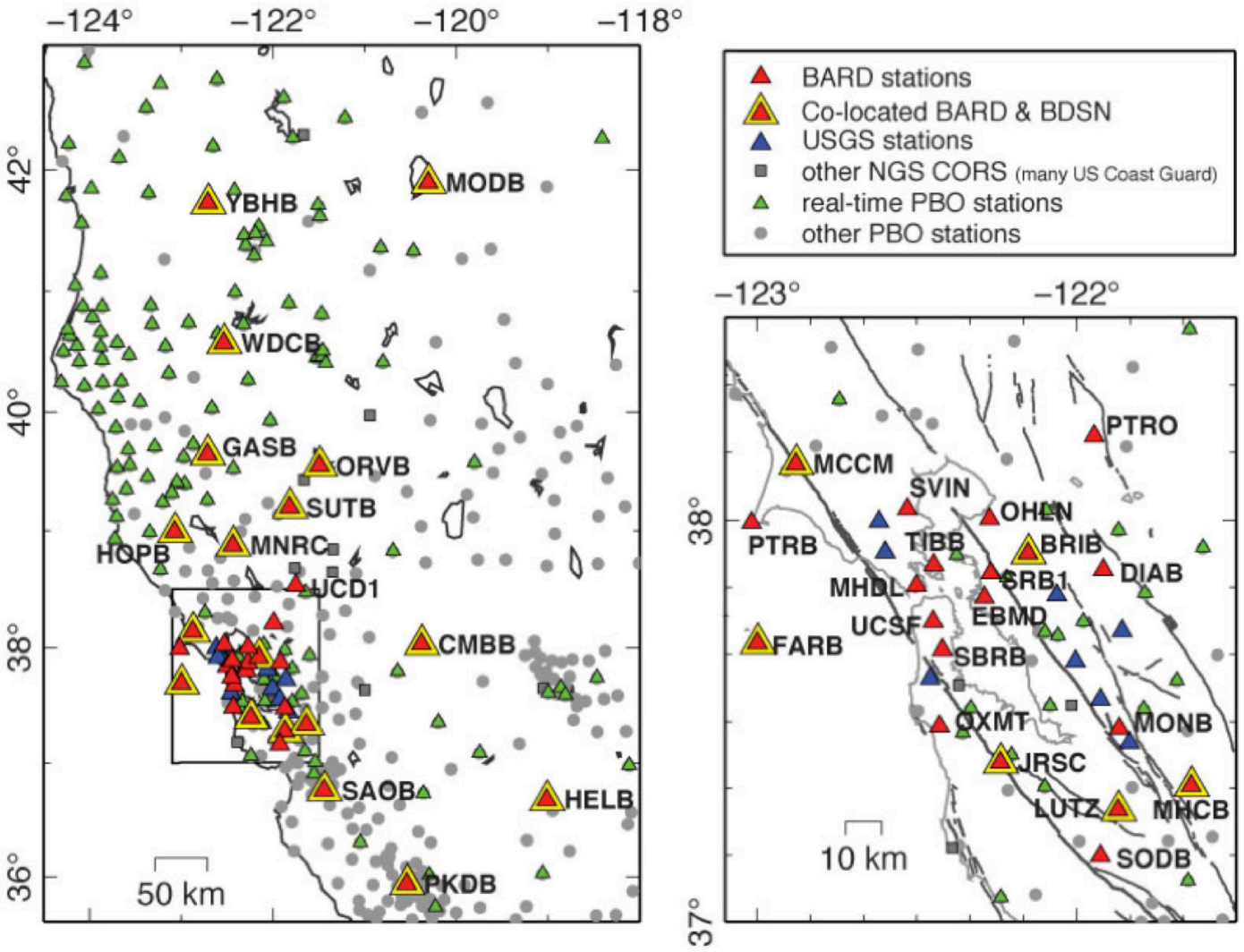

Figure 4.6.1: Map of the BARD Backbone network and surrounding PBO sites in Northern California. The box in the left figure indicates the extent of the figure on right.

and seismic data become more closely integrated, these collocated stations are already available to provide combined data products.

Station configuration

The BARD network includes two models of receiver: Trimble NetRS and Topcon Net-G3A. All BARD stations use a radome equipped, low multipath choke-ring antenna, designed to provide security and protection from weather and other natural phenomena, and to minimize differential radio propagation delays. A low-loss antenna cable is used to minimize signal degradation on the longer cable setups that normally would require signal amplification. Low-voltage cutoff devices are installed to improve receiver performance following power outages.

All BARD stations are continuously telemetered to the BSL. Many use frame relay technology, either alone or in combination with radio telemetry. However, with frame relay being phased out by telecommunication companies, we have been seeking alternatives. This year, stations BRIB and CMBB were moved off of frame relay to internet based methods. BRIB is now received over a T1 line shared through an agreement with UC Berkeley's Department of Astronomy. Station CMBB, which is on the grounds of Columbia College, is now connected through the college's campus internet. Both of these have been reliable for regular daily use.

Other telemetry methods in the BARD network include direct radio link to Berkeley and satellite telemetry. At MODB, MCCM, and MNRC we are able to telemeter 1 Hz data using the USGS VSAT system that collects seismic broadband data as part of the National Seismic Network (NSN).

BARD station monumentations broadly fall into three types. Most are anchored into bedrock, either directly or via a steel-reinforced concrete cylinder. The five "mini-PBO" stations that are still operated by the BSL are collocated with USGS strainmeters and the GPS antennas are bolted onto the borehole casing using an experimental mount developed at the BSL, which has since been adopted by PBO for their strainmeter sites. Four sites (UCD1, SRB1, UCSF, SBRB) are located on the roofs of buildings. Most of the last type have been installed in the past four years, and their stability over long periods of time is yet to be evaluated. Six stations installed under the American Recovery and Reinvestment Act (ARRA) have PBO style short-brace monuments cemented into bedrock.

New Station—HELB

In December 2013 we finished installation of a new station, HELB, located in the Sierra Foothills (Figure 4.6.1), which had been postponed several times due to weather. It is a short-brace monument, cemented into hard rock and has a clean sky view (Figure 4.3). The overall RMS for daily processing has been low (6.9-7.3 mm), however there is not yet enough data to fully analyze the position stability. HELB is situated on a private residence, and data is telemetered by radio from the field site to the house and then is sent on to the BSL over satellite connection. Data collection, archival and streaming have all been fully implemented for HELB; daily RINEX files are available from the NCEDC and real-time streams are available through our NTRIP caster.

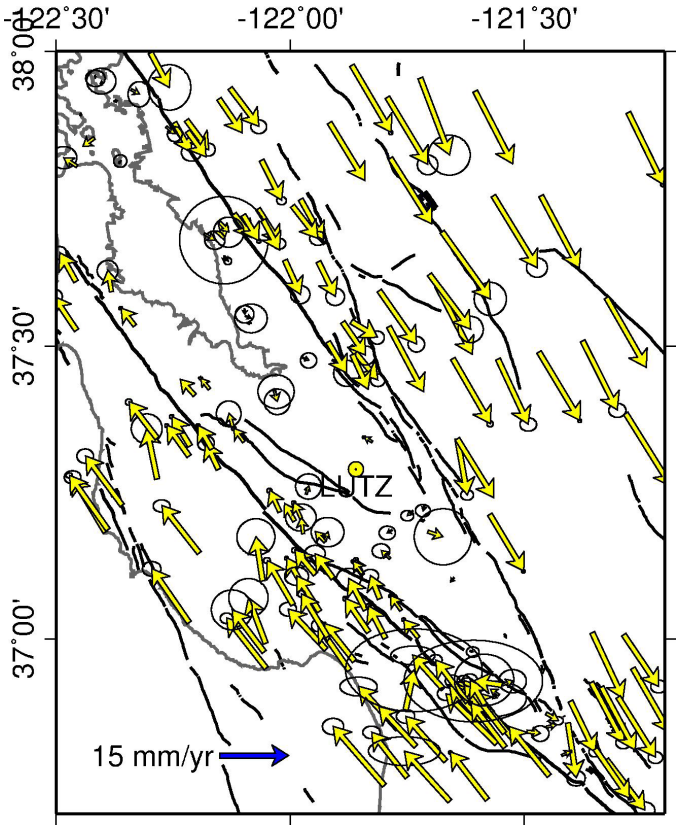

Figure 4.6.2: Velocities from BAVU3β, including BARD stations, as well as campaign, and PBO stations. Yearly velocities are relative to station LUTZ, marked by a yellow circle.

Data Handling

Archival

Raw and RINEX data files from the 33 BARD Backbone stations and several other stations run by BARD collaborators, such as the USGS and LBNL, are archived at the Northern California Earthquake Data Center (NCEDC). The data are checked to verify their integrity, quality, completeness, and conformance to the RINEX standard, and are then made accessible, usually within 1 hour of the end of the UTC day, to all participants and other members of the GPS community through the internet, both by anonymous FTP and through the internet (http://ncedc.org/). BARD data are also available to the community through the GPS Seamless Archive Centers (GSAC), such as that hosted by the Scripps Orbit and Permanent Array Center (SOPAC, http://gsac.ucsd.edu). High-rate raw data are also decimated to create 15 s RINEX data files. 1 Hz RINEX files are available for all BARD Backbone sites after May 2010.

As part of the activities funded by the USGS through the BARD network, the NCEDC has established an archive of the 10,000+ survey mode occupations collected by the USGS since 1992 and the NCEDC is the principal archive for this dataset. These and other survey mode data are used together with data from BARD and PBO stations to produce BAVU (Bay Area

Site	Lat. (deg)	Lon. (deg)	Receiver	Telem.	Samp. Rate	Colloc. Net.	Location
BRIB	37.92	-122.15	NETRS	T1	1 Hz	BDSN	Briones Reservation, Contra Costa County
CMBB	38.03	-120.39	NET-G3A	Int	1 Hz	BDSN	Columbia College, Tuolumne County
DIAB	37.88	-121.92	NETRS	FR	1 Hz		Mt. Diablo , Contra Costa County
EBMD	37.82	-122.28	LEICA	R	1 Hz		East Bay MUD Headquarters, Alameda County
FARB	37.70	-123.00	NETRS	R-FR	1 Hz	BDSN	Farallon Island , San Francisco County
GASB	39.65	-122.72	NET-G3A	R-FR	1 Hz	BDSN	Alder Springs, Glenn County
HELB	36.68	-119.02	NET-G3A	R/VSAT	1 Hz	BDSN	Miramonte
HOPB	39.00	-123.07	NET-G3A	R/FR	1 Hz	BDSN	Hopland Field Station, Mendocino County
JRSC	37.41	-122.23	NET-G3A	Int	1 Hz	BDSN	Jasper Ridge Biological Preserve, San Mateo County
LUTZ	37.29	-121.87	NET-G3A	FR	1 Hz	BDSN	SCC Communications , Santa Clara County
MCCM	38.14	-122.88	NET-G3A	VSAT	1 Hz	BDSN	Marconi Conference Center, Marin County
MHCB	37.34	-121.64	NETRS	FR	1 Hz	BDSN	Lick Observatory, Santa Clara County
MHDL	37.84	-122.49	NETRS	R/FR	1 Hz	mini-PBO	Marin Headlands, Marin County
MNRC	38.88	-122.44	NET-G3A	VSAT	1 Hz	BDSN	McLaughlin Mine, Lake County
MODB	41.90	-120.30	NETRS	VSAT	1 Hz	BDSN	Modoc Plateau , Modoc County
MONB	37.50	-121.87	NET-G3A	FR	1 Hz		Monument Peak, Santa Clara County
OHLN	38.01	-122.27	NET-G3A	FR	1 Hz	mini-PBO	Ohlone Park, Contra Costa County
ORVB	39.55	-121.50	NET-G3A	FR	1 Hz	BDSN	Oroville , Butte County
OXMT	37.50	-122.42	NET-G3A	FR	1 Hz	Mini-PBO	Ox Mountain , San Mateo County
PKDB	35.95	-120.54	NETRS	R/T1	1 Hz	BDSN	Bear Valley Ranch, Monterey County
PTRB	38.00	-123.01	NETRS	R/FR	1 Hz		Point Reyes Lighthouse , Marin County
PTRO	38.21	-121.94	NET-G3A	FR	1 Hz		Potrero Hills, Solano County
SAOB	36.77	-121.45	NETRS	FR	1 Hz	BDSN	San Andreas Observatory, San Benito County
SBRB	37.69	-122.41	NET-G3A	FR	1 Hz	mini-PBO	San Bruno Replacement, San Mateo County
SODB	37.17	-121.93	NET-G3A	R/FR	1 Hz		Soda Springs, Santa Clara County
SRB1	37.87	-122.27	NET-G3A	Fiber	1 Hz		Seismic Replacement Building, Alameda County
SUTB	39.21	-121.82	NETRS	R/FR	1 Hz	BDSN	Sutter Buttes , Sutter County
SVIN	38.03	-122.53	NET-G3A	R/FR	1 Hz	mini-PBO	St Vincents , Marin County
TIBB	37.89	-122.45	NET-G3A	R/Int	1 Hz		Tiburon , Marin County
UCD1	38.54	-121.75	NETRS	Int	1 Hz		UC Davis , Yolo County (operated by UC Davis)
UCSF	37.76	-122.46	NET-G3A	FR	1 Hz		UC San Francisco , San Francisco County
WDCB	40.58	-122.54	NET-G3A	FR	1 Hz	BDSN	Whiskeytown Dam, Shasta County
YBHB	41.73	-122.71	NETRS	FR	1 Hz	BDSN	Yreka Blue Horn Mine, Siskiyou County

Table 4.6.1: List of BARD stations maintained by the BSL. The receivers operating now are: Trimble NETRS, (NETRS) and Topcon Net-G3A (Net-G3A). Site EBMD, operated by the East Bay Municipal Utility District, has a Leica GX1230 receiver and Leica AR10 antenna. The telemetry types listed are FR = Frame Relay, R = Radio, Int = Internet, VSAT = Satellite, T1 = Private T1 line. Telemetry often includes a radio hop from the GPS site to the seismic vault, indicated by an initial R. All (except EBMD) are equipped with Ashtech or Topcon choke ring antennas.

Velocity Unification), a united set of continuous and survey data from the wider San Francisco Bay Area, processed under identical conditions using GAMIT (*d'Alessio et al., 2005).*

Data from five of our sites (HOPB, MHCB, CMBB, OHLN, and YBHB) are sent to the National Geodetic Survey (NGS) in the framework of the CORS (Continuous Operating Reference Stations) project (http://www.ngs.noaa.gov/CORS/). The data from these five sites are also distributed to the public through the CORS FTP site.

Real-time Streaming

All BARD stations are available in real time with 1 Hz data sampling; a step toward our goal of integrating GPS with the Northern California Seismic System (NCSS) for use in hazard assessment and emergency response and for Earthquake Early Warning applications. Data streams are received from the stations in BINEX format and converted into RTCM using Sharc software package (maintained by USGS, Pasadena). Both the original BINEX and RTCM streams are then made available to the public from an Ntrip-caster operated by the BSL (http://seismo.berkeley.edu/bard/realtime). The BSL also acts as a conduit for real-time streams for seven continuous GPS stations operated by the USGS, Menlo Park and five stations installed by the Lawrence Berkeley National Lab (LBNL), in order to make those data easily accessible to the GPS community.

Interseismic Velocities and Daily Time Series

Average station coordinates are estimated from 24 hours of observations for BARD stations and other nearby continuous GPS sites using the GAMIT/GLOBK software developed at MIT and SIO (*Herring et al.*, 2010a & b). GAMIT uses double-difference phase observations to determine baseline distances and orientations between ground-based GPS receivers. Ambiguities are fixed using the widelane combination followed by the narrowlane, with the final position based on the ionospheric free linear combination (LC). Baseline solutions are loosely constrained until they are combined togeth-

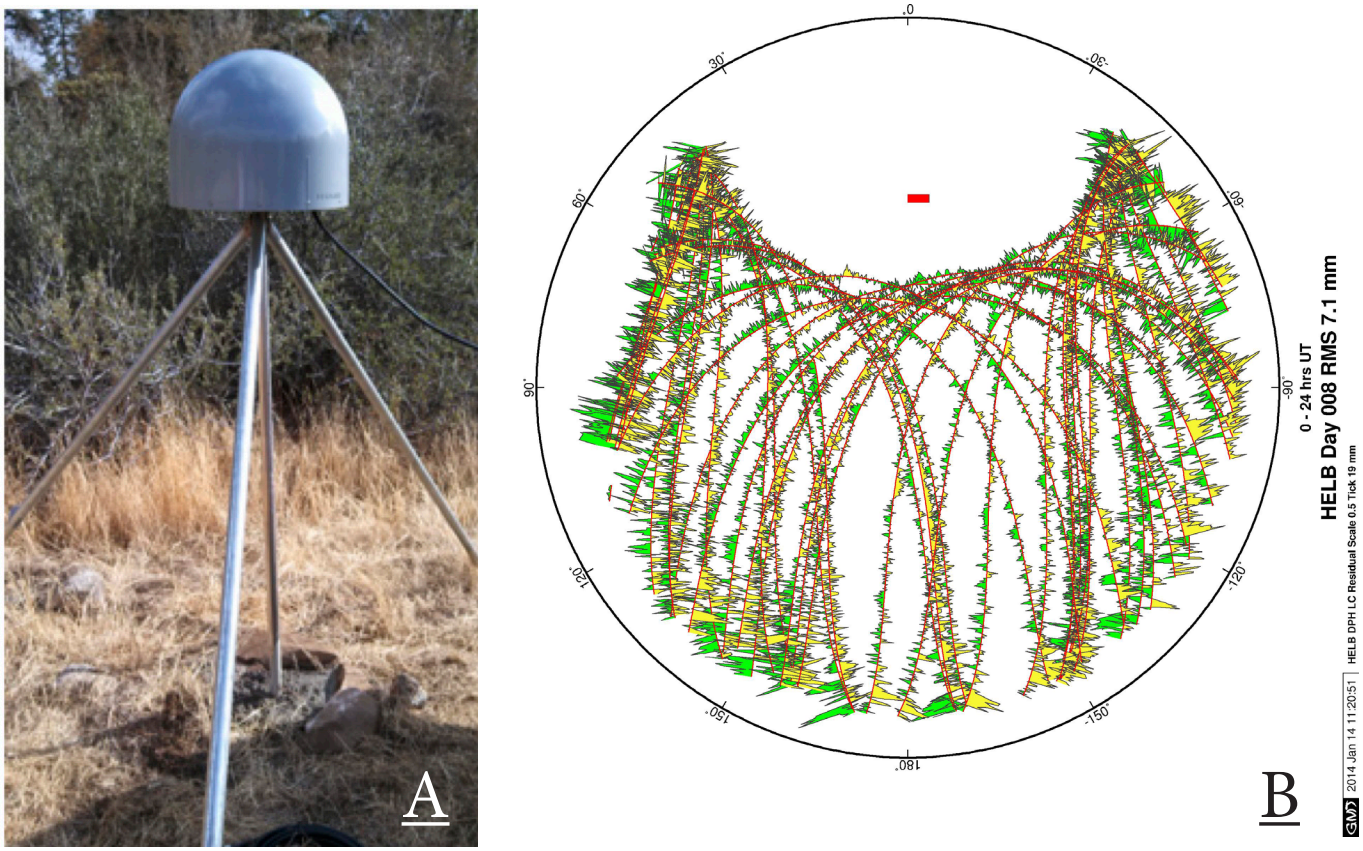

Figure 4.6.3: A) Photo of station HELB showing completed monumentation. B) Phase residual plot from daily processing for HELB on 1/8/2014. This shows the goodness of fit for observations throughout the day. Small excursions from the red lines (orbit tracks) indicate phase measurements that are well fit by a stable position. The plot is oriented such that the north direction is at the top.

er. GAMIT produces solutions as "H-files", which include the covariance parameters describing the geometry of the network for a given day and summarize information about the sites. We combine daily, ambiguity-fixed, loosely constrained H-files using the Kalman filter approach implemented by GLOBK (*Herring*, 2010b). They are combined with solutions from the IGS global network and PBO and stabilized in an ITRF2005 reference frame. The estimated relative baseline determinations typically have 2-4 mm long term scatter in the horizontal components and 10-20 mm scatter in the vertical.

BARD data are an important component of the Bay Area Velocity Unification (BAVU) project (*d'Alessio et al.*, 2005). BAVU contains all available campaign data in Northern California and processes them in a consistent manner to produce a comprehensive and high-density velocity map. It relies on a network of CGPS stations to provide a framework on which these data can be combined. With data going back to 1992, BARD stations can provide such a framework (Figure 4.6.2). Average linear velocities for each station are estimated from monthly combinations of the campaign, BARD, PBO and IGS solutions and are shown in Figure 4.6.2.

Time series of station positions are produced with daily, automated updates. BARD data are processed within 24 hours using IGS rapid orbit information and the time series are updated immediately. When rapid PBO and IGS global station solutions become available (usually within 2-3 days), they are combined with the rapid BARD solutions using GLOBK and the time series is again updated. Final processing with both GAMIT and GLOBK occurs when IGS final orbits and final PBO solutions become available (1-2 weeks); the time series is then updated for the last time with the final positions.

After each update, the time series are cleaned by removing outliers and common mode noise. Common mode noise is estimated by stacking the difference between observations and modeled motion for all stations. The model is derived from *a priori* values for station velocity, coseismic offsets and postseismic decay. The cleaned data is then used to re-estimate the *a priori* model parameters in an iterative process. Outliers are identified as points whose misfit to a linear trend is greater than 4 s on any single component of motion (North, East, or Up). Overall time series scatter is low; with average RMS values across the BARD network of 1.8 mm, 2.9 mm, and 5.8 mm for the north, east and up directions respectively. Plots of station time series are posted daily on the BARD website (http://seismo.berkeley.edu/bard/timeseries).

Earthquake Early Warning and Rapid Response

With support from the Gordon and Betty Moore Foundation, we have been working on integrating information from GPS into earthquake early warning (EEW) algorithms in a module we call G-larms. Our goals for this project include establishing a robust system for processing GPS data streams

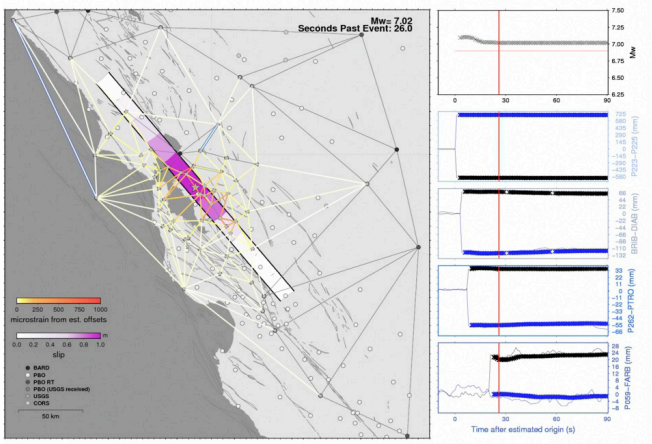

Figure 4.6.4: Snapshot during a real-time test of G-larms; the red line on the right side shows the timing of the snapshot. Top right figure shows the estimated earthquake magnitude for the slip model in magenta on the left. The test is based on a simulated *M*6.9 earthquake. G-larms begin estimating position after the S-wave arrival (blue and black symbols). Offsets are updated and input into an inversion for fault slip every second. Testing was run in true real time; synthetic offsets were added to GPS position time series on-the-fly in order to capture true real time noise and data availability.

into displacement time series and designing and implementing methods to use these results to supplement seismic earthquake early warning systems during large earthquakes.

The BSL is currently using data from 62 GPS stations in the greater San Francisco Bay Area to generate real time position estimates on a routine basis. This includes 26 stations that are operated as part of the BARD network and 8 that are operated by the USGS, Menlo Park. We also process 29 stations operated by the Plate Boundary Observatory (PBO), who collect real time data for a subset of their stations and make these publicly available over the internet.

We use trackRT, together with predicted orbits from the International GPS service (IGS) to produce high sample rate displacement time series with 2-4 second latency. TrackRT was developed at MIT and is based on GAMIT/GLOBK, which we use for daily processing (*Herring et al.*, 2010a). TrackRT follows a network processing approach, with displacements generated with respect to a reference station. The benefits of this approach are that common noise sources, such as local atmosphere, are canceled out, leading to more precise relative displacements.

We employ a fully triangulated network scheme in which neighboring station pairs are processed individually, such that no station serves as the universal reference site (Figure 4.6.4). This makes our network resilient against an outage or telemetry loss at any individual station. The low processing overhead of trackRT makes it possible for us to run separate instances of the program to produce displacement time series for all ~160 baselines in our network. The scatter in the displacement time series for each baseline depends on distance and increases during days with changeable weather conditions. However, it is often within 2 cm over the course of 24 hours, which is considered a stable result.

This past year we reached a major milestone in our progress toward integrating GPS information into earthquake early warning, with our GPS module, G-larms, which now provides the final link between GPS stations in the field and a deliverable earthquake warning. G-larms actively monitors the incoming GPS position estimates and calculates mean position and variance in a five-minute rolling buffer. When it receives an earthquake alert from the seismic system it records the current mean position as the pre-event value and then begins to measure the post-event position as it evolves. Static offsets "arrive" at a location concurrently with the S-wave, therefore G-larms waits until the estimated S-wave arrival time to begin calculations (see right side of Figure 4.6.4).

Once the offsets are estimated, they are input into a model inversion for slip on a fault. The fault location is determined from the epicenter estimated by the seismic alert system and its orientation is determined based on the tectonic regime of the epicenter. Assuming these values allows the underlying calculations to remain linear and helps the inversion to run quickly (within one second). As shown in Figure 4.6.4, in a test that occurred in true real time and included true real time data noise, G-larms determined the magnitude of a synthetic earthquake within 0.1 magnitude units within 20 seconds following the event origin. Similar tests using real data from the 2010 *M*7.2 El Mayor-Cucapah earthquake show that even in the presence of shaking (and with the difficult station distribution at the US-Mexico border) the earthquake magnitude can be well estimated within 40 seconds.

While real time processing of GPS data is capable of providing measurements of displacement within seconds of its occurrence, post-processing provides results with lower noise levels, leading to better precision. This leads to better estimates of the finite fault plane, which when used with ShakeMap provides more accurate shaking estimates than a point source model. Rapid post-processing (RPP) techniques can be used to estimate static offsets from moderate to large earthquakes, which will constrain a non-linear search for fault plane parameters. Rapid post-processing requires waiting 1-2 minutes after the earthquake for data to accumulate, but displacement time series can then be generated within 5 minutes using the software Track, developed at MIT. From these, full fault plane determination can be performed within another 5 minutes. While real-time processing techniques are critical for using GPS data for Earthquake Early Warning, rapid post-processing provides higher precision in the static offset measurement. This allows GPS data to be used for smaller earthquakes and still finishes within a time frame appropriate for ShakeMap.

GPS-Seismograms for Large Earthquakes

An M_w6.9 earthquake offshore of Northern California on March 10, 2014 provided an opportunity to investigate the ability of GPS stations in Northern California to resolve dynamic shaking from a large event. Although most stations

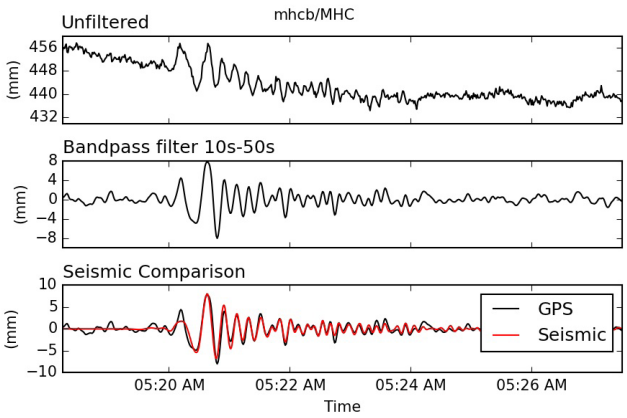

Figure 4.6.5: Comparison of BARD network high-rate GPS timeseries and data from a broadband seismometer at site MHCB in the Marin Headlands. The transverse component of motion is shown (motion perpendicular to azmuthal direction to the earthquake's epicenter).

were too far away to resolve a measurable static offset, dynamic motions with amplitudes of 1-2 cm were felt within the network. 1 Hz data is routinely collected and archived for BARD and USGS stations, however high-rate data is only downloaded from PBO stations for special events. In response to the earthquake, UNAVCO triggered a download for all stations in California and archived these data in their public FTP site.

I. Johanson, in Research Section 2.32, shows the results of this analysis in more detail. Nonetheless, where GPS and seismic equipment are collocated, the two match very well, providing confidence in the accuracy at non-collocated sites (Figure 4.6.5). The results represent a marked increase in spatial density of long-period motions (2 Hz and lower), which otherwise are measured only by broadband seismometers. As shown in the report by Johanson, the dense data set reveals detail in the subsurface structure that is otherwise missed by the sparsely distributed broadband seismic instruments.

Acknowledgements

Ingrid Johanson and Richard Allen oversee the BARD program. Joshua Miller, Sarah Snyder, John Friday, Doug Neuhauser, Mario Aranha, Jennifer Taggart and Clay Miller contributed to the operation of the BARD network in 2013–14. Operation of the BARD network is partially supported by funding from the USGS/NEHRP program grant #G10AC00141. Real-time data processing is supported by a grant from the Moore Foundation.

References

d'Alessio, M. A., I. A. Johanson, R. Bürgmann, D. A. Schmidt, and M. H. Murray, Slicing up the San Francisco Bay Area: block kinematics and fault slip rates from GPS-derived surface velocities, *J. Geophys. Res.*, 110(B06403), doi:10.1029/2004JB003496, 2005.

Herring, T. A., R. W. King, and S. C. McClusky, GAMIT: GPS Analysis at MIT - Release 10.4, *MIT*, 2010a. [online] Available from: http://www-gpsg.mit.edu/~simon/gtgk/GAMIT_Ref.pdf.

Herring, T. A., R. W. King, and S. C. McClusky (2010b), GLOBK: Global Kalman filter VLBI and GPS analysis program - Version 10.4, *MIT*, 2010b. [online] Available from: http://www-gpsg.mit.edu/~simon/gtgk/GLOBK_Ref.pdf.

7 Northern California Earthquake Monitoring

Introduction

Earthquake information production and routine analysis in Northern California have been improving over the past two decades. Since June 2009, the BSL and the USGS in Menlo Park have been operating mirrored software systems (see 2010 Annual Report). For this system, processing begins as the waveforms arrive at the computers operating the real time, or AQMS, software, and ranges from automatic preparation of earthquake information for response to analyst review of earthquakes for catalogs and quality control.

This is the most recent step in a development at the BSL that began in the mid-1990s with the automated earthquake notification system called Rapid Earthquake Data Integration (REDI, *Gee et al.*, 1996; 2003a). That system determined earthquake parameters rapidly, producing near real time locations and magnitudes for earthquakes in Northern and Central California, estimated rupture characteristics and the distribution of ground shaking following significant earthquakes, and provided tools for the rapid assessment of damage and estimation of loss.

A short time later, in 1996, the BSL and the USGS began collaborating to produce information for Northern and Central California earthquakes. Software operating in Menlo Park and Berkeley were merged to form a single, improved earthquake notification system using data from both the NCSN and the BDSN (see past annual reports). Since 2000, the USGS and the BSL operate as the Northern California Earthquake Management Center (NCEMC) of the California Integrated Seismic Network (Operational Section 4.2).

With support from the USGS and the Gordon and Betty Moore Foundation, the BSL is now also participating in the development and assessment of a statewide prototype Earthquake Early Warning system. A fully fledged system will provide warning of imminent ground shaking in the seconds after an earthquake has initiated but before strong motion begins at sites that may be damaged. This Annual Report has several Research Studies describing the project (???put in references here.)

Northern California Earthquake Management Center

In this section, we describe how the Northern California Earthquake Management Center fits within the CISN system. Figure 4.2.3 in Operational Section 5.2 illustrates the NCEMC as part of the CISN communications ring. The NCEMC is a distributed center, with elements in Berkeley and in Menlo Park. The 35 mile separation between these two centers is in sharp contrast to the Southern California Earthquake Management Center, where the USGS Pasadena is located across the street from the Caltech Seismological Laboratory.

As described in Operational Section 5.2, the CISN partners are now connected by an internet based communications link. The BSL has maintained two T1 communication links with the USGS Menlo Park as robust and reliable links for shipping waveform data and other information between the two processing systems.

Figure 5.7.1 provides more detail on the system operating at the NCEMC since mid-June, 2009. Currently, complete earthquake information processing systems operate in parallel in Menlo Park and Berkeley. Incoming data from each network are processed locally at each of the two data centers in network services computers. The continuously reduced data, which include picks, codas, ground motion amplitudes, and ML100, are exchanged between the data centers and fed into both processing streams. Real time analysis is coordinated using up-to-date information from the local real time database, which is replicated to the local data center database. Event review and automatic downstream processes, such as computation of fault plane solutions, access the internal data center databases. To maintain redundancy, robustness, and completeness, these two databases replicate with each other across the San Francisco Bay. They also replicate with the public database from which information is made available to the public. The system includes the production of location and origin time as well as estimates of M_d, M_L, and M_w. For events with $M \geq 3.5$, ShakeMaps are also calculated on two systems, one in Menlo Park and one in Berkeley. Finite fault calculation is not yet integrated into the new processing system. It is only calculated at the BSL at this time.

This system combines the advantages of the NCSN with those of the BDSN. The dense network of the NCSN contributes to rapid and accurate earthquake locations, low magnitude detection thresholds, and first-motion mechanisms. The high dynamic range data loggers, digital telemetry, and broadband and strong-motion sensors of the BDSN provide reliable magnitude determination, moment tensor estimation, calculation of peak ground motions, and estimation of source rupture characteristics. Robust preliminary hypocenters, or "Quick Looks" are published within a few tens of seconds of the origin time. Event information is updated when preliminary coda magnitudes are available, within 2-4 minutes of the origin time. Estimates of local magnitude are generally available a few seconds later, and other parameters, such as the peak ground acceleration and moment magnitude, follow within 1-4 minutes (Figure 5.7.2).

During the past year, we made the transition from distributing earthquake information through the Earthquake Information Distribution System (EIDS) to using the Product Distribution Layer (PDL). The earthquake information is available on the web and, as a push service through the Earthquake Notification Service (http://sslearthquake.usgs.gov/ens). Now all information products for ongoing earthquake activity are transferred to the USGS in Golden, CO. We are working on the tools and standards for the transfer of historical earthquake information, event and associated products from past earthquakes to complete the "Comprehensive Catalog" (ComCat) that will be hosted by the USGS. We are also developing readers and writers for QuakeML. For organizations which need very rapid access to earthquake information, the CISN Display is a useful tool

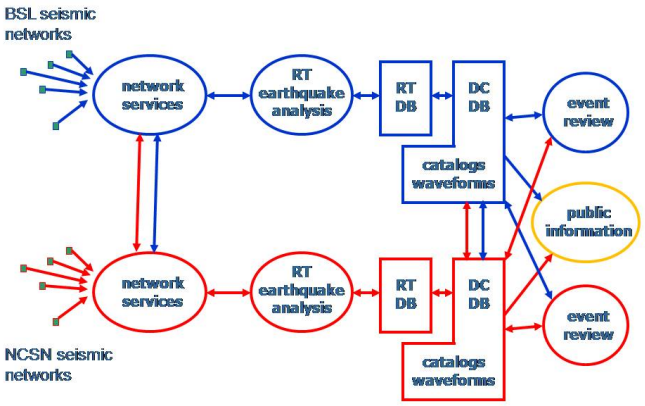

Figure 5.7.1: Details of the Northern California earthquake information processing system. Network services processing, that is, production of picks, ground motion amplitudes, and other reduced information, occurs at both datacenters, and the information is exchanged. Complete earthquake information processing systems exist on both sides of the San Francisco Bay, and up-to-date information is exchanged by database replication.

(http://www.cisn.org/software/cisndisplay.htm). The USGS has upgraded its earthquake information site with a new url as has the BSL (http://earthquakes.berkeley.edu). The public will have an easier time navigating to the word "earthquakes" than the old "seismo". These web sites provide valuable resources for information which are useful not only in the seconds immediately after an earthquake, but in the following hours and days as well.

Earthquake Information Processing

In June 2009, we began operating the ANSS Quake Monitoring System (AQMS) software, formerly CISN Software, as the production system in the Northern California Seismic System (NCSS) for monitoring and reporting on Northern California earthquakes. This came as the result of a long effort to adapt and test software developed for the TriNet system operating in Southern California.

Data flow in the Northern California system (Figure 5.7.3) allows for our diverse forms of data acquisition as well as variability in network distribution. In addition, the BSL and the USGS have minimized the use of proprietary software in the system.

One exception is the database program, Oracle. The NCEDC Oracle database hosts all earthquake information and parameters associated with the real time monitoring system. It is the centerpoint of the system, providing up-to-date information to all processing modules. Reliability and robustness are achieved by continuously replicating the databases. The public, read-only, database provides event and parametric information to catalog users and to the public.

During the last few years, BSL staff members, particularly Pete Lombard, have become extremely familiar with elements of the TriNet software. The software is now adapted for Northern California, with many adjustments and modifications completed along the way. For example, Pete Lombard adapted the TriNet magnitude module to Northern California. Pete has made a number of suggestions on how to improve the performance of various modules of AQMS and has worked closely with Caltech and the USGS in Pasadena on modifications.

The BSL and the USGS Menlo Park are exchanging "reduced amplitude time series". One of the important innovations of the TriNet software development is the concept of continuous processing (*Kanamori et al.*, 1999). Waveform data are constantly processed to produce Wood Anderson synthetic amplitudes and peak ground motions. A program called *rad* produces a reduced time series, sampled every 5 seconds, and stores it in a memory area called an "Amplitude Data Area" or ADA. Other modules can access the ADA to retrieve amplitudes to calculate magnitude and ShakeMaps as needed. The BSL and the USGS Menlo Park have collaborated to establish tools for ADA-based exchange. The first step toward improving reliability and robustness, by implementing ADA exchange with Southern California, was taken in June 2014, with a draft proposal on implementation.

2013–2014 Activities

Moment Tensor Solutions with *tmts* and Finite Fault Analysis

The BSL continues to produce moment tensor solutions and to perform finite fault analysis for quakes with M_w>6.0. We use the package, *tmts,* which is a Java and web based moment tensor processing system and review interface based on the complete waveform modeling technique of *Dreger and Romanowicz* (1994). The web based review interface has been operating in Northern California since July 2007, and the automatically running version for real time analysis since June 2009. The version of *tmts* currently operating in Northern California allows full inversions that include an isotropic element of the source, i.e. explosions or collapses. From July 2013 through June 2014, BSL analysts reviewed many earthquakes in Northern California and adjoining areas of magnitude 2.9 and higher. Reviewed moment tensor solutions were obtained for 70 of these events (through 6/30/2014). Figure 5.7.4 and Table 5.7.2 display the locations of earthquakes in the BSL moment tensor catalog and their mechanisms. During this year, no finite fault inversions were produced for Northern California earthquakes.

We are currently developing a new version of the moment tensor system which will permit the use of records from strong motion sensors.

StationXML development

Just as the exchange of earthquake information is now based on the transfer of QuakeML, a XML schema describing earthquake-related parameters, information and metadata describing a station can be more completely encompassed using a XML schema called StationXML. The schema being used is based on one developed by the Federation of Digital Seismograph Networks (FDSN), however, we have extended it to encompass pa-

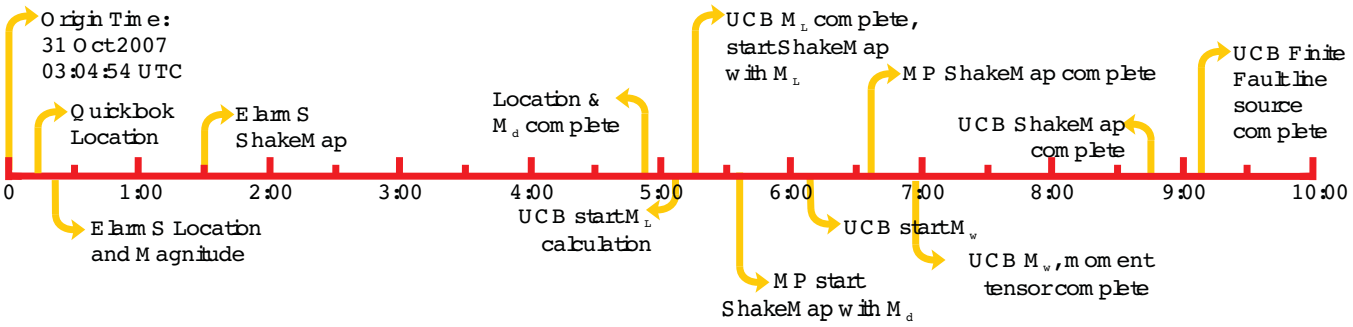

Figure 5.7.2: Illustration of the earthquake products timeline for the M_w 5.4 Alum Rock earthquake of October 30, 2007. Note that all processing was complete within 10 minutes of the origin time.

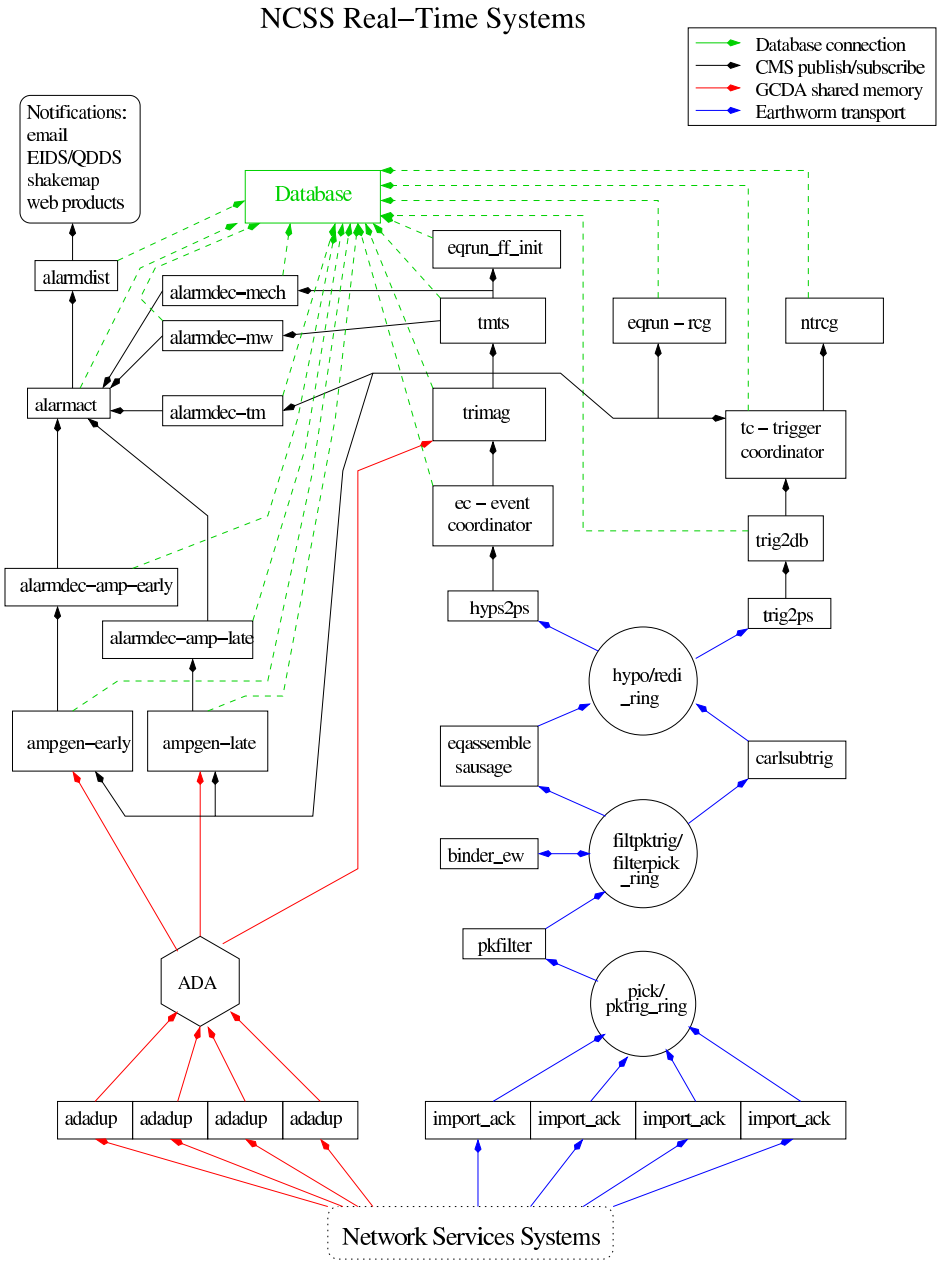

Figure 5.7.3: Schematic diagram of processing in the NCSS system. The design combines elements of the Earthworm, TriNet, and REDI systems.

rameters needed to describe parameters used in engineering seismology as well. The BSL has written both readers for importing parameters from StationXML into the AQMS database system, as well as writers for taking station information from the AQMS system and putting it into StationXML and its extensions. Progress on the development and use of the Station Information System (SIS) proposed by Southern California would not be as rapid without these contributions from the BSL.

Implementation of GridMT

GridMT, a grid-search based system for searching for earthquakes, particularly large earthquakes, offshore of Northern California and Oregon, has now been operating in "production mode" for several years. We regularly review the events it produces and compare the GridMT locations and moment tensor solutions with those from the AQMS system. We hope to implement GridMT into the production system soon.

EEW in the Production System

In production mode the Earthquake Early Warning System (EEW) will be running in parallel and in conjunction with the AQMS earthquake information system. In Northern California, we have been slowly moving elements of the EEW system into the production AQMS environment. In particular, in the past year we have moved the EEW waveform processing onto production machines in Menlo Park and at UCB, to improve reliability and robustness. We are very pleased to note that improvements to the ElarmS processing, and the use of one second packets from the Q330 data loggers has allowed us to produce earthquake alerts for several earthquakes in the Los Angeles area within five seconds of the earthquakes' onset (see Research Sections 3.30 and 3.29).

M_L project

Local magnitude, or M_L, remains an important parameter to describe earthquake size and continuity between new and old earthquake catalogs. In Northern California, we have only been using data from the horizontal components of broadband and strong motion sensors, since the implementation of the new CISN magnitude system. For the past several years, we have been making progress toward the calibration of local magnitude parameters for both the horizontals of geophones and short-period sensors, where they are available, and for the use of vertical sensors. When these parameters are available, we expect to be able to provide M_L values for many of the small earthquakes in The Geysers, for example, that are currently too small for duration magnitudes (M_d).

Moving AQMS to the Linux Environment

AQMS was developed under the Solaris environment. This environment has become more challenging during the past few years for a variety of reasons. In the previous year, Pete Lombard reviewed all the AQMS software in use in Northern California in the Linux environment, and produced a package that compiled and ran for more than a year. This year, we made the decision to begin to transition our production system to Linux. Just at the end of the year, the first production computers were configured and brought into service. We expect to complete the process for UCB and Menlo Park real time production computers during the next few months.

Routine Earthquake Analysis

In fiscal year 2013-2014, almost 35,000 earthquakes were detected and located by the automatic systems in Northern California. This compares with more than 32,000 in 2012–2013, 27,000 in 2011–2012 and over 25,000 in 2010–2011. Of these events, 172 had preliminary magnitudes of three or greater. 29 events had M_L or M_w greater than four. The largest event, on March 10, 2014, offshore of Ferndale, had a magnitude of 6.8. Many of the events with magnitude greater than 4 were aftershocks of this earthquake (see Table 5.7.1 for more details). 47 ShakeMaps were also produced for earthquakes in our region of responsibility during this fiscal year.

Although BSL staff no longer read BDSN records for local and regional earthquakes (see Annual Report of 2003-2004), they now participate in timing and reviewing earthquakes with *Jiggle*, mainly working on events from past sequences that have not yet been timed. This work contributes to improving the earthquake catalog for Northern California, but also ensures robust response capabilities, should the Menlo Park campus be disabled for some reason.

Acknowledgements

Peggy Hellweg oversees our earthquake monitoring system and directs the routine analysis. Peter Lombard and Doug Neuhauser contribute to the development of software, and Stephane Zuzlewski manages the databases. Peggy Hellweg, Taka'aki Taira, Ingrid Johanson, Doug Dreger, Sierra Boyd, Cheng Cheng, Andrea Chiang, Brent Delbridge, Scott French, Mong-Han Huang, Chris Johnson, Qingkai Kong, Clay Miller, Avinash Nayak, Jennifer Strauss, Jennifer Taggart, and Zhou (Allen) Zheng contribute to the routine analysis of moment tensors. Peggy Hellweg and Doug Neuhauser contributed to the writing of this section. Partial support for the development, implementation and maintenance of the AQMS software, as well as for the production of earthquake information, is provided by the USGS under Cooperative Agreement G10AC00093, and from the California Office of Emergency Services.

References

Dreger, D., and B. Romanowicz, Source characteristics of events in the San Francisco Bay region, *USGS Open File Report 94-176*,301-309, 1994.

Gee, L., D. Neuhauser, D. Dreger, M. Pasyanos, R. Uhrhammer, and B. Romanowicz, The Rapid Earthquake Data Integration Project, *Handbook of Earthquake and Engineering Seismology*, IASPEI,1261-1273, 2003a.

Gee, L., D. Neuhauser, D. Dreger, M. Pasyanos, B. Romanowicz,

and R. Uhrhammer, The Rapid Earthquake Data Integration System, *Bull. Seis. Soc. Am., 86*, 936-945, 1996.

Pasyanos, M., D. Dreger, and B. Romanowicz, Toward real-time estimation of regional moment tensors, *Bull. Seis. Soc. Am., 86*, 1255-1269, 1996.

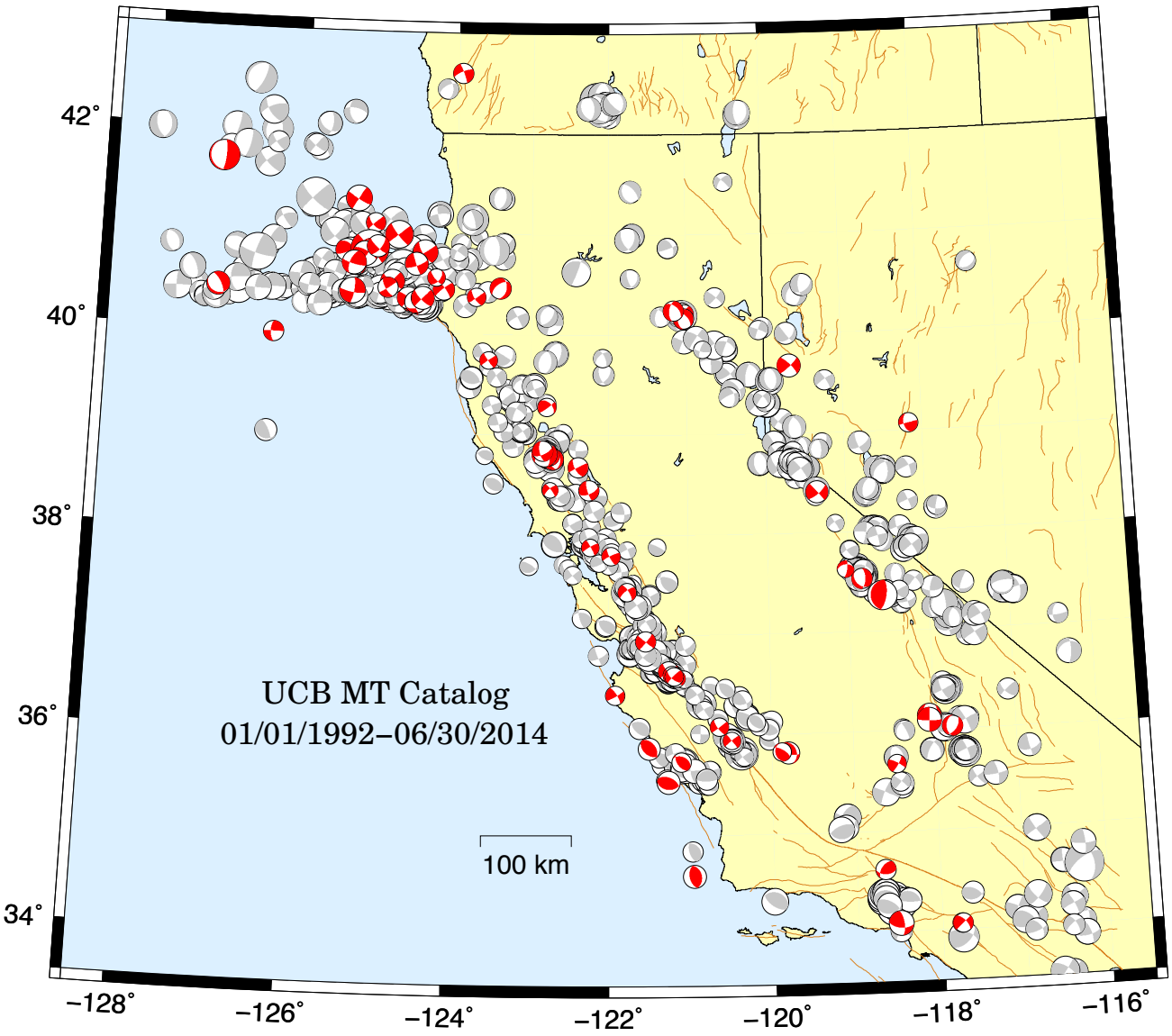

Figure 4.7.4: Map comparing reviewed moment tensor solutions determined by the BSL from past years (gray) with those from the fiscal year 2012-2013 (red/dark).

Location	Date	UTC Time	Lat.	Lon.	MT Depth	M_L	M_w	M_o	Str.	Dip	Rake
Ridgemark, CA CA	7/3/2013	09:05:00 PM	36.64	-121.26	14	3.35	3.7	4.44E+21	234	89	7
Greenville, CA	7/7/2013	6:31:32 AM	40.21	-121.02	3.5	3.13	3.35	1.30E+21	305	78	-167
The Geysers, CA	7/14/2013	010:40:38 PM	38.81	-122.79	3.5	3.35	3.7	4.35E+21	256	86	17
East Foothills, CA	7/15/2013	07:02:44 PM	37.43	-121.77	8	3.36	3.28	1.04E+21	328	72	-161
The Geysers, CA	7/18/2013	1:16:10 AM	38.81	-122.82	3.5	3.1	3.5	2.19E+21	40	56	-56
Westhaven-Moonstone, CA	7/18/2013	10:02:30 AM	41.09	-125.06	18	3.09	3.5	2.20E+21	229	85	30
Soledad, CA	7/19/2013	4:07:02 AM	36.57	-121.16	5	3.02	3.19	7.52E+20	233	78	27
Santa Rosa, CA	7/24/2013	12:13:00 AM	38.45	-122.74	8	0	2.87	2.49E+20	323	79	-161
The Geysers, CA	7/25/2013	010:36:38 PM	38.81	-122.81	1.5	2.85	3.25	9.44E+20	176	51	-119
Bayview, CA	8/3/2013	2:25:50 AM	40.81	-124.4	18	3.92	4.47	6.39E+22	56	89	-20
Coalinga, CA	8/6/2013	03:02:33 PM	36.08	-120.64	5	3.3	3.35	1.33E+21	54	90	-16
Greenville, CA	8/19/2013	11:08:19 AM	40.15	-121.03	1.5	3.27	3.43	1.76E+21	295	67	-125
Greenville, CA	8/19/2013	11:09:55 AM	40.16	-121.03	3.5	3.5	3.63	3.43E+21	316	57	-120
Vandenberg AFB	8/24/2013	1:16:31 AM	34.59	-120.96	5	4.21	4.1	1.75E+22	167	51	88
Spanish Springs, NV	8/27/2013	12:51:44 AM	39.68	-119.68	11	4.43	4.23	2.73E+22	47	81	12
The Geysers, CA	8/28/2013	4:43:05 AM	38.76	-122.71	1.5	3.59	3.76	5.42E+21	162	58	-91
West Bishop, CA	9/6/2013	09:08:54 PM	37.36	-118.58	8	3.26	3.34	1.55E+24	10	68	93
Ferndale, CA	9/9/2013	010:37:18 PM	40.81	-125.43	18	3.64	4.02	1.34E+22	66	75	51
Hayfork, CA	9/24/2013	09:36:34 PM	40.46	-123.41	36	3.46	3.84	7.23E+21	232	55	-66
Cobb, CA	10/2/2013	08:38:32 PM	38.83	-122.8	1.5	3.11	3.12	5.98E+20	40	62	-62
Rio Dell, CA	10/4/2013	02:42:07 PM	40.44	-124.15	27	3.71	3.9	8.75E+21	231	81	-13
Berkeley, CA	10/7/2013	4:26:08 AM	37.88	-122.23	8	2.97	2.99	3.82E+20	327	89	175
Wofford Heights, CA	10/10/2013	1:34:23 AM	35.67	-118.48	8	3.52	3.34	1.29E+21	299	79	168
Bayview, CA	10/11/2013	011:05:37 PM	40.98	-124.75	24	4.91	4.94	3.24E+23	231	89	7
Berkeley, CA	10/15/2013	8:07:27 AM	37.88	-122.23	5	3.05	3.15	6.66E+20	331	85	-171
Soledad, CA	10/19/2013	4:02:24 AM	36.6	-121.21	11	3.27	3.38	1.46E+21	133	89	178
Mammoth Lakes, CA	10/21/2013	05:04:11 PM	37.53	-118.83	8	4.23	3.75	5.25E+21	2	62	-66
Laytonville, CA	10/26/2013	1:29:26 AM	39.74	-123.55	8	0	3.23	8.61E+20	145	87	175
Crescent City, CA	11/8/2013	10:46:56 AM	41.33	-125.29	3.5	4.45	4.65	1.17E+23	211	89	7
San Ramon, CA	11/13/2013	05:30:31 PM	37.79	-121.97	11	3.29	3.32	1.20E+21	244	81	14
The Geysers, CA	11/14/2013	8:47:18 AM	38.79	-122.76	1.5	3.19	3.43	1.72E+21	317	70	-153
Ferndale, CA	11/17/2013	010:45:010 PM	40.31	-124.56	14	3.29	3.65	3.71E+21	19	88	24
Redway, CA	11/21/2013	12:48:55 AM	40.37	-123.72	33	3.1	3.41	1.62E+21	55	86	-20
Gilroy, CA	12/2/2013	10:05:22 AM	36.94	-121.54	8	3.91	3.65	3.66E+21	129	88	-175
Angwin, CA	12/6/2013	6:44:55 AM	38.68	-122.39	8	3.67	3.65	3.71E+21	242	88	26
Lost Hills, CA	12/13/2013	7:49:57 AM	35.81	-119.8	21	4.16	4.08	1.65E+22	97	78	64
Ferndale, CA	12/17/2013	01:28:02 PM	40.69	-124.51	21	3.94	4.11	1.85E+22	161	85	-166
Ferndale, CA	12/24/2013	10:28:50 AM	40.51	-124.82	11	3.82	4.3	3.54E+22	220	85	9
Ferndale, CA	1/2/2014	6:23:010 AM	40.29	-124.45	24	3.64	4.02	1.32E+22	100	87	172
The Geysers, CA	1/2/2014	9:32:28 AM	38.79	-122.74	1.5	3.08	3.25	9.40E+20	209	54	-65
The Geysers, CA	1/12/2014	08:24:47 PM	38.81	-122.82	3.5	4.01	4.53	7.76E+22	345	57	-136
The Geysers, CA	1/21/2014	11:11:12 AM	38.84	-122.84	1.5	3.54	3.74	5.15E+21	65	65	-29
Ferndale, CA	1/23/2014	4:10:41 AM	40.41	-125.34	8	4.24	4.63	1.09E+23	8	78	-13
Mammoth Lakes, CA	2/5/2014	9:08:06 AM	37.63	-119.03	8	3.01	3.06	4.82E+20	10	74	-132
Ferndale, CA	2/6/2014	2:55:42 AM	40.29	-124.51	18	3.16	3.56	2.73E+21	90	55	-100

Cambria, CA	2/6/2014	07:42:21 PM	35.53	-121.27	5	4.27	4.13	1.98E+22	293	52	100
Coalinga, CA	2/14/2014	03:07:23 PM	35.94	-120.49	11	3.15	3.2	7.86E+20	321	89	-175
Cambria, CA	2/27/2014	06:52:30 PM	35.87	-121.5	8	4.32	4.06	1.55E+22	131	45	82
Carmel-by-the-Sea, CA	3/8/2014	12:53:20 PM	36.4	-121.92	3.5	3.72	3.43	1.75E+21	60	82	16
Ferndale, CA	3/10/2014	5:18:13 AM	40.83	-125.13	18	5.82	6.8	2.00E+26	318	88	-169
Ferndale, CA	3/10/2014	9:42:43 AM	40.76	-125.21	8	3.31	3.64	3.59E+21	105	75	148
Ferndale, CA	3/10/2014	9:54:26 AM	40.83	-125.12	3.5	3.34	3.71	4.53E+21	47	78	-99
Ferndale, CA	3/10/2014	10:28:19 AM	40.78	-125.19	14	4.22	4.47	6.21E+22	33	76	22
Ferndale, CA	3/10/2014	10:46:23 AM	40.66	-125.3	5	3.49	3.46	1.96E+21	62	77	22
Ferndale, CA	3/10/2014	03:16:29 PM	40.45	-124.88	18	3.24	3.65	3.70E+21	57	85	160
Kernville, CA	3/13/2014	2:11:05 AM	36.1	-118.06	5	4.62	4.41	5.04E+22	182	90	-172
Ferndale, CA	3/14/2014	04:32:35 PM	40.35	-124.61	21	3.58	4	1.24E+22	33	86	5
Bayview, CA	3/16/2014	3:46:010 AM	40.86	-125.02	5	3.72	4.01	1.30E+22	133	77	-155
Westwood, CA	3/17/2014	01:25:35 PM	34.08	-118.5	8	4.63	4.42	5.40E+22	353	69	147
Ferndale, CA	3/18/2014	10:33:59 AM	40.69	-125.33	21	3.96	4.41	5.09E+22	105	78	151
Ferndale, CA	3/19/2014	9:57:08 AM	40.31	-124.51	5	3.53	3.95	1.04E+22	166	76	47
Soledad, CA	4/1/2014	6:41:35 AM	36.59	-121.19	8	3	3.27	9.98E+20	225	82	26
Upper Lake, CA	4/2/2014	04:27:05 PM	39.28	-122.79	5	2.88	3.34	1.26E+21	53	83	45
Yountville, CA	4/4/2014	4:04:55 AM	38.45	-122.25	8	3.56	3.63	3.50E+21	163	77	-151
Chester, CA	5/12/2014	1:14:44 AM	40.24	-121.16	8	3.57	3.67	3.95E+21	187	56	-53
Smith Valley, NV	5/30/2014	7:48:33 AM	38.41	-119.36	11	4.3	4.02	1.34E+22	319	90	164
Ferndale, CA	6/2/2014	011:54:20 PM	40.35	-124.42	18	3.87	4.14	2.04E+22	224	88	15
Cambria, CA	6/3/2014	8:53:43 AM	35.73	-121.11	5	3.48	3.5	2.18E+21	144	56	108
Ferndale, CA	6/25/2014	05:00:26 PM	40.56	-124.25	24	0	3.2	7.86E+20	140	73	-141
Kettleman City, CA	6/25/2014	010:01:36 PM	35.82	-119.88	11	3.21	3.37	1.43E+21	301	68	69

Table 5.7.1: Moment tensor solutions for significant events from July 1, 2012 through June 30, 2013 using a complete waveform fitting inversion. Epicentral information is from the UC Berkeley/USGS Norhtern California Earthquake Management Center. Moment is in dyne-com and depth is in km.

8 Northern California Earthquake Data Center

Introduction

The Northern California Earthquake Data Center (NCEDC) is a permanent archive and distribution center primarily for multiple types of digital data relating to earthquakes in central and northern California. The NCEDC is located at the Berkeley Seismological Laboratory, and has been accessible to users via the internet since mid-1992. The NCEDC was formed as a joint project of the Berkeley Seismological Laboratory (BSL) and the U.S. Geological Survey (USGS) at Menlo Park in 1991, and current USGS funding is provided under a cooperative agreement for seismic network operations.

Time series data come from broadband, short period, and strong motion seismic sensors, and geophysical sensors such as electromagnetic sensors, strain meters, creep meters, atmospheric pressure, pore pressure, water level, and wind speed sensors. Earthquake catalogs can include event time, hypocenters, magnitudes, moment tensors, mechanisms, phase arrivals, codas, and amplitude data. GPS data are available in both raw observables and RINEX formatted data.

The NCEDC also provides support for earthquake processing and archiving activities of the Northern California Seismic System (NCSS), which includes the seismic networks of UC Berkeley, USGS Menlo Park, and other partners contributing seismic data from northern and central California. The NCSS earthquake processing system and the NCEDC are part of the Northern California Earthquake Management Center (NCEMC), which is one of three earthquake management centers in the California Integrated Seismic Network (CISN). The CISN is the California regional organization of the USGS Advanced National Seismic System (ANSS).

2013–2014 Activities

By its nature, data archiving is an ongoing activity. In 2013–2014, the NCEDC continued to expand its data holdings and enhance access to the data. Projects and activities of particular note:

- Continued to develop and install production Web services for the distribution of station metadata using Station XML, waveform inventory, and miniSEED data at http://service.ncedc.org. The latest webservice, ncedc-eventdata, delivers pre-assembled waveforms for events listed in the NCSS and EGS catalogs.
- Continued receiving, archiving, and distributing event information (hypocenter, magnitude, phase, and amplitude data) and waveforms for the DOE Enhanced Geothermal Systems (EGS) monitoring project.
- Continued to support the NCEMC earthquake analysis by providing real-time access to earthquake parameters and waveforms from the NCEDC for the CISN
- Continued work with the NCSN and USGS National Strong Motion Program (NSMP) to import the metadata and build dataless SEED volumes for all NSMP dialup and triggered stations.
- Developed an extended stations XML writer to facilitate exporting existing station metadata maintained by the NCEDC to the newly developed ANSS Station Information System (SIS).
- Finished the development of programs to convert EarthScope SAFOD vertical strain time series data to miniSEED format, processed three TBytes of SAFOD vertical strain data collected from May 2007 through December 2013, and delivered the resulting miniSEED data to the IRIS DMC.
- Database schema enhancements to accommodate double-difference origins and the addition of double-difference locations to the NCSS catalog.

Data Types and Contributors

Table 4.8.1 and Figure 4.8.1 provide a breakdown of the NCEDC data by data type.

BDSN/NHFN/mPBO Seismic Data

The BDSN (Operational Section 5.1), NHFN (Operational Section 5.3), and Mini-PBO (Operational Section 5.6) stations (all network code BK) send real-time data from 65 seismic data loggers to the BSL. These data are written to disk files, used by the CISN AQMS software for real-time earthquake processing and by the prototype CISN ShakeAlert earthquake early warning (EEW) system, and delivered to the DART (Data Available in Real Time) system at the NCEDC, where they are immediately available to anyone on the internet. Continuous high-rate data (200-500 samples/second) are now available for all of the NHFN borehole seismic data channels. All time series data from the Berkeley networks continue to be processed and archived by an NCEDC analyst using *calqc* quality control procedures in order to provide the highest quality and most complete data stream for the NCEDC archive. The recent upgrade to the BDSN stations increased the onsite storage at each site, which allows us to recover data from the station after telemetry outages and improve the completeness of the BDSN data archive.

NCSN Seismic Data

The USGS Northern California Seismic Network (NCSN) continuous waveform data from USGS Menlo Park are converted to MiniSEED, transferred in real time to the NCEDC via the internet, and made available to users immediately through the NCEDC DART and NCEDC web services. NCSN event waveform data, as well as data from all other real time BSL and collaborating networks, are automatically collected by the NCSS waveform archiver and stored at the NCEDC for event review

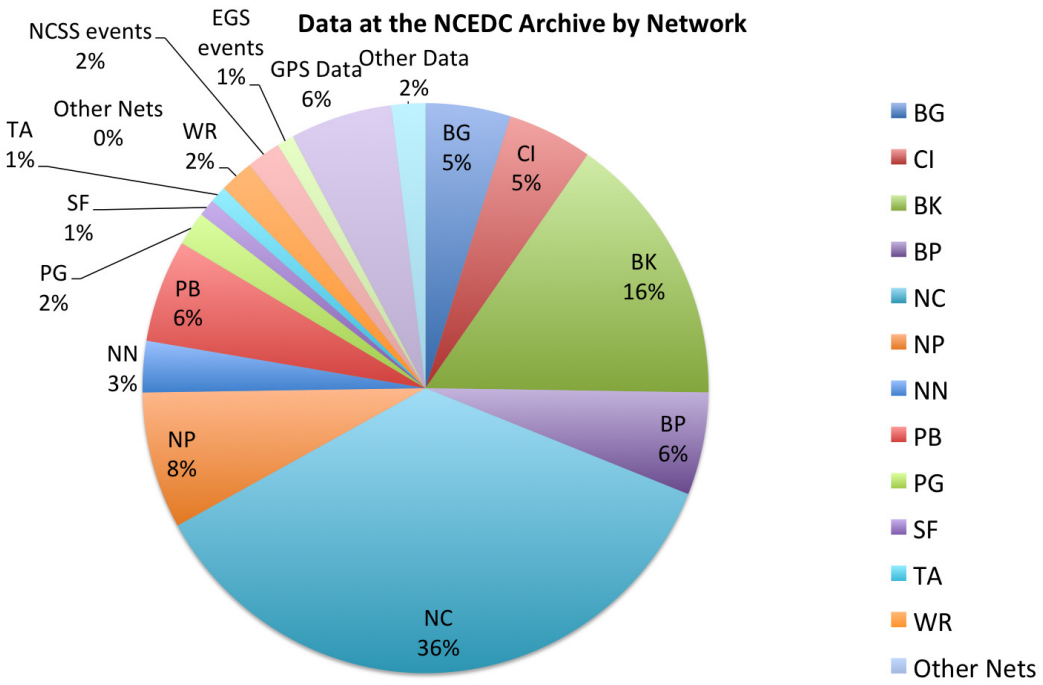

Figure 4.8.1: Chart showing the relative proportion of each data set at the NCEDC. BK - Berkeley Digital Seismic Network; BP - Berkeley High-resolution Seismic Network in Parkfield; NCSN - Northern California Seismic Network and collaborators; CI - Southern California Seismic Network; NN - University of Nevada, Reno Seismic Network; GPS - various GPS datasets, including BARD; EarthScope - data from various EarthScope activities; Other - various small data sets.

Data Set (Net or Collection)	Total Data Archive Size(GB)	Percent of Archive
BG	3,837.55	4.68%
BK	13,018.89	15.87%
BP	5,004.54	6.1%
CI	3,762.78	4.59%
NC	30,330.59	36.96%
NN	2,795.98	3.41%
NP	6,394.37	7.79%
PB	4,945.03	6.03%
PG	1,433.39	1.75%
SF	527.49	0.64%
TA	656.34	0.8%
WR	1,396.79	1.7%
Other Nets	105.79	0.13%
NCSS events	1,306.81	1.59%
EGS events	497.24	0.61%
GPS Data	4,559.71	5.56%
Other Data	1,484.23	1.81%
Total	82,057.53	100%

Table 4.8.1: Volume of data archived at the NCEDC by network code.

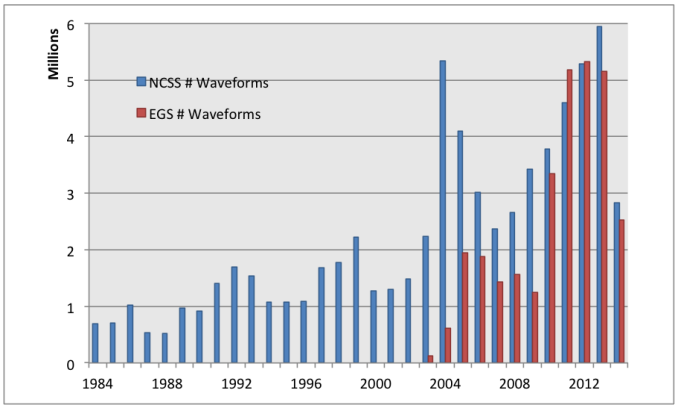

Figure 4.8.2: Number of events in the NCSS and EGS event catalogs by year.

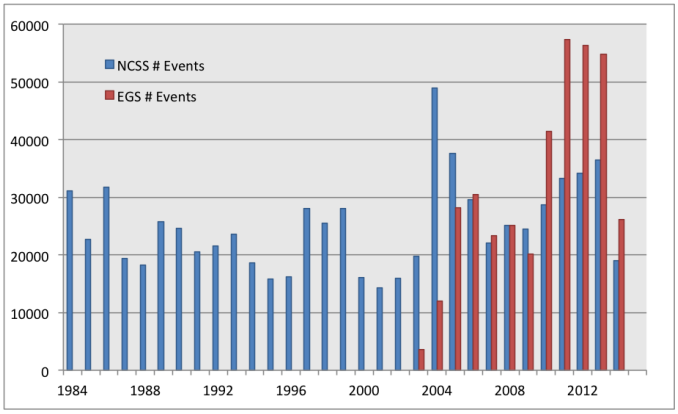

Figure 4.8.3: Number of waveforms for events in the NCSS and EGS event catalogs by year.

and analysis and for distribution to users. All NCSS time series data are archived in miniSEED format.

Improvements in the acquisition of NCSN data, described in the 2005–2006 BSL Annual Report, enabled the NCEDC to start archiving continuous NCSN waveforms in early 2006. We then started the process of reading and archiving continuous NCSN waveforms from previous years that had been saved on tapes. We completed the continuous waveform archiving of NCSN tape data from 1993 through 2005 in 2013.

Parkfield High Resolution Seismic Network (HRSN) Data

The history of upgrades to the acquisition and archival of HRSN data can be found in the 2010–2011 BSL Annual Report. We continue to archive continuous 250 and 20 sample-per-second data from the HRSN stations. The most recent HRSN station upgrade added 16 GB of local storage at each site, which allows us to recover data from the station after telemetry outages, and greatly improves the completeness of the HRSN data archive.

EarthScope Plate Boundary Observatory (PBO) and SAFOD Time Series Data

The NCEDC was one of two funded archives for PBO EarthScope borehole and laser strain data. Strain data are collected from all of the PBO strain sites and are processed by UNAVCO. miniSEED data are delivered to the NCEDC using SEEDLink, whereas raw and XML processed data are delivered to the NCEDC using Unidata's Local Data Manager (LDM). The miniSEED data are inserted into the NCEDC DART and are subsequently archived from the DART. UNAVCO provides EarthScope funding to the NCEDC to help cover the processing, archiving, and distribution costs for these data. In early 2010, the NCEDC began receiving and archiving all of the continuous seismic waveform data from the PBO network to complement the PBO strain data. The seismic data are received from an Antelope ORB server at UNAVCO and converted from their native format to miniSEED on a data import computer. The data are then transferred via the SEEDLink protocol to the NCEDC, inserted into the NCEDC DART for immediate internet access, and subsequently archived from the DART.

The NCEDC was an archive center for the SAFOD event data and has also processed the continuous SAFOD data. Starting with the initial data in July 2002 from the SAFOD Pilot Hole, and later, data from the SAFOD Main Hole, the NCEDC converted data from the original SEG-2 format data files to miniSEED, and developed the SEED instrument responses for this data set. Continuous four kHz data from SAFOD written to tape at SAFOD were periodically sent to the BSL to be converted, archived, and forwarded to the IRIS DMC (IRIS Data Management Center). SAFOD EarthScope funding to the NCEDC is to cover the processing, archiving, and distribution costs for these data. A small subset of the continuous SAFOD data channels are also incorporated into the NCSN, and are available in real time from the NCEDC DART, and are archived at the NCEDC, and are forwarded to the IRIS DMC. After the failure of the SAFOD permanent instrument in September 2008, the USGS deployed a temporary network in the Main Hole, and the NCEDC continued to process and archive these data. Both the permanent and temporary seismic instruments were removed in mid-2010 in order to analyze the failure of the permanent SAFOD instrument packet, but the temporary seismic instruments were reinstalled in late 2010 and continue to send data for distribution and archiving to the NCEDC.

Through a UNAVCO EarthScope contract, the NCEDC developed software to convert raw data from the SAFOD vertical laser strainmeter operated by UCSD to miniSEED format for long term archiving and distribution. By the end of 2013, the NCEDC finished the process of converting ~three TBytes of SAFOD vertical strain data collected from May 2007 through December 2013 to miniSEED format. The miniSEED data and metadata for all channels were delivered to the IRIS DMC for permanent archiving and distribution.

Due to a significant cut in UNAVCO's EarthScope funding, UNAVCO discontinued all funding for NCEDC EarthScope data processing and archiving activities at the end of 2013. As of January 2014, the NCEDC is only archiving PBO seismic data channels that are used by the NCSS earthquake processing system.

UNR Broadband Data

The University of Reno in Nevada (UNR) operates several

broadband stations in western Nevada and eastern California that are important for Northern California earthquake processing and analysis. Starting in August 2000, the NCEDC has been receiving and archiving continuous broadband data from selected UNR stations. The data are transmitted in real time from UNR to UC Berkeley, where they are made available for CISN real time earthquake processing and for archiving. Initially, some of the stations were sampled at 20 Hz, but all stations are now sampled and archived continuously at 100 Hz.

The NCEDC installed Simple Wave Server (SWS) software at UNR, which provides an interface to UNR's recent collection of waveforms. The SWS is used by the NCEDC to retrieve waveforms from UNR that were missing at the NCEDC due to real time telemetry outages between UNR and UC Berkeley.

In early 2006, the NCEDC started to archive continuous data from the UNR short-period stations that are contributed to the NCSN. Both the broadband and short-period UNR stations contributed to the CISN are available in real time through the NCEDC DART.

Electro-Magnetic Data

The NCEDC continues to archive and process electric and magnetic field data acquired at several UC Berkeley sites. The BSL operates both magnetic and electric field sensors at SAO. However, most of these channels have been down for repair during the 2010–2011 year. In collaboration with Professor Simon Klemperer at Stanford, we acquire magnetic and electric field channels at BSL sites JRSC and BRIB, and magnetic field channels at site MHDL. The three magnetic field channels and either two or four electric field channels are digitized at 40 Hz, 1 Hz, and 0.1 Hz, and are telemetered in real-time along with seismic data to the Berkeley Seismological Laboratory, where they are processed and archived at the NCEDC in a similar fashion to the seismic data.

GPS Data

The NCEDC continues to archive GPS data through the BARD (Bay Area Regional Deformation) network of continuously monitored GPS receivers in Northern California (Operational Section 5.6). The NCEDC GPS daily archive now includes 80 continuous sites in Northern California. Of these, there are ~32 core BARD sites owned and operated by UC Berkeley, USGS (Menlo Park and Cascade Volcano Observatory), LLNL, UC Davis, UC Santa Cruz, Trimble Navigation, and Stanford. Data are also archived from sites operated by other agencies, including the East Bay Municipal Utilities District, the City of Modesto, the National Geodetic Survey, and the Jet Propulsion Laboratory (JPL).

In addition to the standard 15 second continuous GPS data files, the NCEDC is now archiving and distributing high-rate 1 Hz continuous GPS data from all of the BSL-operated BARD stations. In collaboration with UC San Diego Scripps Institution of Oceanography (UCSD/SIO), USGS Pasadena and USGS Menlo Park, the BSL is now streaming real time 1 Hz continuous data from over 40 sites, including all BSL sites and the 13 PBO stations in Parkfield, to the BSL, where it makes the data available to researchers in real time through an Ntripcaster.

The NCEDC also archives non-continuous survey GPS data. The initial dataset archived is the survey GPS data collected by the USGS Menlo Park for Northern California and other locations. The NCEDC is the principal archive for this dataset. Significant quality control efforts were implemented by the NCEDC to ensure that the raw data, scanned site log sheets, and RINEX data are archived for each survey.

Geysers Seismic Data

The monitoring network for micro-seismicity in the Geysers region in Northern California was initially installed and operated by Unocal Geothermal Division, and later operated by Calpine Corporation. Through various agreements, both Unocal and Calpine have released triggered event waveform data from 1989 through 2000 along with preliminary event catalogs for the same time period for archiving and distribution through the NCEDC. This dataset represents over 296,000 events recorded by the Calpine/Unocal Geysers network, and is available as an assembled dataset at the NCEDC.

In late 2002, the Lawrence Berkeley National Laboratory (LBNL), with funding from the California Energy Commission, began installing a digital seismic network in the Geysers, and currently operates 33 stations in the Geysers region with an emphasis on monitoring seismicity related to well water injection. Initially, earthquake locations and event waveforms from this network were sent to the NCEDC, and the locations were forwarded to the NCSN so that they could be merged into the NCSN earthquake catalog. In August 2007, the NCSN installed an Earthworm system at The Geysers that received continuous waveform data from the LBNL Geysers network. The Earthworm system supplies the appropriate waveforms for events detected by the NCEMC real time earthquake monitoring and processing system and these waveforms are included in the pre-assembled event data archive at the NCEDC. In March 2012, the NCEDC started to receive and archive continuous data from the stations in near real-time for time-dependent velocity studies.

DOE Enhanced Geothermal Monitoring (EGS) Data

Starting in 2010–2011, LBNL funded the BSL to archive and disseminate seismic event parameters and corresponding waveform time series from monitoring networks operated under the auspices of the US Department of Energy Geothermal Monitoring Program. This includes the LBNL network installed at The Geysers. We have collected and verified the station metadata for these networks, and populated the data into the database. In 2012–2013 we began to receive and archive the event data and waveforms from these networks. The time series data are available via our suite of data delivery methods, and the event and parametric information are available via a new web catalog search page.

In 2013–2014 we started receiving the backlog of Geysers

event waveforms starting in April 2003. As of June 2014, we have over 378,000 events, corresponding phase data, and time series data for the the EGS catalog. Although many of the events in the Geysers region are also included in the NCSS event catalog, the EGS catalog is maintained as a separate catalog for uniformity in event detection and location procedures.

The NCEDC also plans to include any appropriate EGS Geysers waveform data with the pre-assembled waveform set for any corresponding NCSS event from April 2003 to August 2007.

USGS Low Frequency Data

Starting in 1974, the USGS at Menlo Park, in collaboration with other principal investigators, collected an extensive low-frequency geophysical data set that contains over 1300 channels of tilt, tensor strain, dilatational strain, creep, magnetic field, and water level as well as auxiliary channels such as temperature, pore pressure, rain and snow accumulation, and wind speed. In collaboration with the USGS Menlo Park, we assembled the requisite information for the hardware representation of the stations and the instrument responses for many channels of this diverse dataset, and developed the required programs to populate and update the hardware database and generate the instrument responses. We developed the programs and procedures to automate the process of importing the raw waveform data and converting it to mini-SEED format. Since these data are delivered to the NCEDC on a daily basis and immediately archived, these data are not inserted into the NCEDC DART.

We have currently archived time series data from 887 data channels from 167 sites, and have instrument response information for 542 channels at 139 sites. The waveform archive is updated on a daily basis with data from 350 currently operating data channels.

In 2011–2012 the USGS significantly reduced support for these stations, and most stations have been shut down. The last data delivered to the NCEDC for this network was in Feb 2013.

SCSN/Statewide Seismic Data

In 2004, the NCEDC started to archive broadband and strong motion data from 15 Southern California Seismic Network (SCSN) stations that were telemetered to the NCEMC. These data were used in the prototype real-time state-wide earthquake processing system and also provide increased coverage for Northern California events. Since the data are telemetered directly from the stations in real time to both the SCSN and to the NCEMC, the NCEDC archives the NCEMC's copy of the data to ensure that at least one copy of the data will be preserved. Due to reduced state funding, the SCSN has gradually reduced the number of telemetered stations to seven.

In early 2006, the NCEDC started to continuously archive all of the selected SCSN short period stations that are contributed to the NCSN. All of these data are also available in real time from the NCEDC DART. In 2009, the NCEMC started incorporating data from ~25 additional SCSN stations near the southern border of the NCEMC monitoring area in its event waveform collection to provide better azimuthal coverage of events in that area. In 2009–2010, the NCEMC also started retrieving event waveform data from the SCSN for other SCSN stations that are expected to receive signals from Northern California earthquakes. All of these event waveforms are also archived at the NCEDC.

Earthquake Catalogs

The NCEDC hosts multiple earthquake catalogs.

Northern California catalog: The NCEDC provides searchable access to both the USGS and BSL earthquake catalogs for Northern and Central California. The "official" UC Berkeley earthquake catalog begins in 1910 and runs through 2003, and the "official" USGS catalog begins in 1966. Both of these catalogs are archived and available through the NCEDC, but the existence of two catalogs has caused confusion among both researchers and the public.

In late 2006, the NCEMC began archiving and distributing a single unified Northern California earthquake catalog in real time to the NCEDC through database replication from the NCEMC's real-time systems. The NCEDC developed and tested the required programs used to enter all previous NCSN catalog data into the NCEDC database. In 2008, we migrated all of the historic NCSN catalog, phase, and amplitude data from 1967 through 2006 into the NCEMC catalog. In addition, we spent a considerable effort addressing the mapping of phase data in the BSL catalog to SEED channel names. We plan to merge the BSL catalog with the NCEMC catalog to form a single unified Northern California catalog from 1910 to the present. The BSL and the USGS have also spent a considerable effort over the past years to define procedures for merging the data from the two catalogs into a single northern and central California earthquake catalog in order to present a unified view of Northern California seismicity. The differences in time period, variations in data availability, and mismatches in regions of coverage all complicate the task.

Enhanced Geothermal Systems (EGS) catalog: The US Department of Energy Geothermal Monitoring Program is operating a number of seismic networks that monitor earthquakes in the regions of enhanced geothermal systems. The event catalogs and parametric information are available via a new EGS catalog search page.

Worldwide catalog: The NCEDC, in conjunction with the Council of the National Seismic System (CNSS) in the 1990s, produced and distributed a world-wide composite catalog of earthquakes based on the catalogs of the national and various U.S. regional networks. Each network updates their earthquake catalog on a daily basis at the NCEDC, and the NCEDC constructs a composite world-wide earthquake catalog by combining the data, removing duplicate entries that may occur from multiple networks recording an event, and giving priority to the data from each network's *authoritative*

region. The catalog, which includes data from 14 regional and national networks, is searchable using a web interface at the NCEDC. The catalog is also freely available for bulk download by anyone on the internet.

With the disbanding of the CNSS and the development of the Advanced National Seismic System (ANSS), the NCEDC was asked to update its web pages to present the composite catalog as a product of the ANSS. This conversion was completed in the fall of 2002. The NCEDC continues to create, house, distribute, and provide a searchable Web interface to this ANSS composite catalog, and to aid the regional networks in submitting data to the catalog. The ANSS is currently developing a new ANSS Combined Catalog (ComCat) which, when fully populated with historical events, may replace the current NCEDC's ANSS composite catalog.

The BSL made significant progress on data submission to the new ANSS ComCat using the new Product Distribution Layer (PDL), and provided timely feedback to the USGS Earthquake Hazards (EHZ) development team on both PDL and QuakeML issues. In 2012–2013, the BSL developed a flexible XML writer for AQMS systems that can generate QuakeML for any or all of the following PDL products:

1. Origin products (hypocenter and magnitudes)
2. Phase products (hypocenter, magnitudes, phase, and amplitudes readings)
3. Mechanism products (mechanism information with related gif images)
4. Moment tensor products (moment tensor information with related gif images).

The BSL has provided the AQMS QuakeML writer to all ANSS AQMS operators, and the NCSS is using it to generate real-time and reviewed Origin, Phase, Mechanism and Moment Tensor that are submitted to ComCat.

NCEDC Operations

The current NCEDC facilities consist of a mass storage environment hosted by an eight-core Sun X4150 computer, a 150 slot LTO5 tape library with three tape drives, and 180+ TBytes of RAID storage, all managed with the SAMFS hierarchical storage management (HSM) software. Four additional eight-core Sun computers host the DART data import, data archiving, computing Probability Density Function (PDF) plots for the bulk of the NCEMC waveforms, data quality control procedures, and internet distribution. Two 64-bit Linux systems host redundant Oracle databases used by the NCSS and NCEDC.

In 2005, the NCEDC relocated its archive and distribution system from McCone Hall to a new state-of-the-art campus data center in a new seismically braced building on the Berkeley campus. The facility provides seismically braced equipment racks, gigabit Ethernet network, air conditioning, and power conditioning. The data center is powered by UPS with generator backup.

The SAMFS HSM software used by the NCEDC is configured to automatically create multiple copies of each data file in the archive. The NCEDC creates one copy of each file on an online RAID, a second copy on LTO tape which remains online in the tape library, and a third copy on LTO tape which is stored offline and offsite. In addition, all NCEDC SAMFS data are cached in an online disk cache that provides instant access to these data. In 2011-2012, we renewed our SAMFS license, which now allows us to manage an unlimited amount of storage.

The NCEDC operates two instances of its Oracle database, one for internal operations and one for external use for user data queries and data distribution programs, and communicates with a third identical database operated offsite by the USGS in Menlo Park. These three databases are synchronized using multi-master replication.

DART (Data Available in Real Time)

The DART (Data Available in Real Time) provides a network-accessible structured file system to support real-time access to current and recent time series data from all networks, stations, and channels. All real-time time series data streams delivered to the NCEDC are placed in miniSEED files in a web accessible directory structure. The DART currently contains the most recent 40 days of data. Data from the DART is available to users through NCEDC web services and other data services described in the data distribution section of this chapter, and directly through web browsers and command-line programs such as *wget*.

We use the IRIS ringserver software as the primary method for delivering real time data to the DART. The ringserver packages implement an object ring buffer (ORB) and server, which provides a reliable storage ring buffer and an interface for client programs to read, write, and query the server. Clients running at the NCEDC computer connect to remote servers at the BSL, USGS Menlo Park, and other sites, retrieve the miniSEED time series data records, and write them to daily channel files in the NCEDC DART.

The NCEDC developed an automated data archiving system to archive data from the DART on a daily basis. It allows us to specify which stations should be automatically archived, and which stations should be handled by the NCEDC's Quality Control program, *calqc*. The majority of non-BSL data channels are currently archived automatically from the DART.

Data Quality Control

The NCEDC developed the GUI-based state-driven system *calqc* to facilitate the quality control processing that is applied to the BSL stations continuously archived data sets at the NCEDC.

The quality control procedures for these datasets include the following tasks:

- data extraction of a full day of data,
- a quickcheck program to summarize the quality and stability of the stations' clocks,
- determination if there is missing data for any data

channel,

- provided procedures to retrieve missing data from the stations and incorporate it into the day's data,
- optional creation of multi-day time series plots for state-of-health data channels,
- optional timing corrections for data,
- optional extraction of event-based waveforms from continuous data channels,
- optional repacking of miniSEED data,
- creating waveform inventory entries in the NCEDC database,
- publishing the data for remote access on the NCEDC.

calqc is used to process all data from the BDSN and HRSN network, and all continuous broadband data from the NCSN, UNR, and SCSN networks that are archived by the NCEDC. The remainder of the continuously archived data are automatically archived without any analyst interaction.

Database Activity

The NCEDC continues to support the Northern California Earthquake Management Center (NCEMC) by providing information and resources vital to the NCEMC's role of rapid earthquake analysis and data dissemination. The NCEDC receives earthquake parametric data in real time from the NCEMC real-time systems and provides real-time access to the NCEDC database for *jiggle*, the CISN event analysis tool. The NCEMC continues to support the maintenance and distribution of the hardware configurations and instrument responses of the UCB, USGS Menlo Park NCSN, and other seismic stations used by the NCEMC. BSL staff currently chair the CISN Schema Change working group, which coordinates all database schema changes and enhancements within the CISN.

The NCEDC instrument response schema represents full multi-stage instrument responses (including filter coefficients) for the broadband data loggers. The hardware tracking schema represents the interconnection of instruments, amplifiers, filters, and data loggers over time, and is used to describe all of the UC Berkeley and USGS stations and channels archived at the NCEDC.

Database developments in the 2013–2014 year include support for preferred origin information for multiple types of location algorithms. This allowed us to add double-difference locations for events in addition to the current single event travel-time locations computed by hypoinverse. We are now effectively store multiple earthquake catalogs in the same database based on the location method. We allows users to select and search the desired catalog based on a consistent earthquake location methodology.

Full details on the database schema used at the NCEDC may be found at http://www.ncedc.org/db.

Data Distribution

The NCEDC continues to use the internet as the interface for users to request, search for, and receive data from the NCEDC. In fall 2005, the NCEDC acquired and began using the domain name ncedc.org. Information about the NCEDC, it's data sets and networks, and catalog search forms are located at http://www.ncedc.org. The NCEDC Web Services are available at the new web site http:/service.ncedc.org.

Earthquake Catalogs

The NCEDC provides users with searchable access to Northern California earthquake catalogs, the DOE EGS catalogs, and the ANSS world-wide catalog via the Web. Users can search the catalogs by time, magnitude, and geographic region, and can retrieve either hypocenter and magnitude information or a full set of earthquake parameters including phase readings, amplitudes, and codas. Moment tensor, first motion mechanisms, and the option of double different locations have been added to the NCEMC California earthquake catalog and are searchable from the NCEDC Web catalog search page.

Station Metadata

In addition to the metadata returned through the various data request methods, the NCEDC provides dataless SEED volumes and SEED RESP files for all data channels archived at the NCEDC. The NCEDC currently has full SEED instrument responses for 27,343 data channels from 3,185 stations in 24 networks. This includes stations from the California Geological Survey (CGS) strong motion network that will contribute seismic waveform data for significant earthquakes to the NCEDC and SCEDC, stations in the EGS networks, and strong motions stations in the USGS National Strong Motion Program (NSMP). In collaboration with the USGS, NCSN, and the NSMP (National Strong Motion Program), the NCEDC constructed the metadata and dataless SEED volumes for over 700 stations and 4700 data channels of the NSMP dialup stations. Station metadata can be acquired from fdsnws station or by downloading pre-assembled dataless SEED files, using *ncedc-dataless* web service or NetDC to request metadata by station, channel and time.

NCEDC Website Upgrade

This year, the front end of the NCEDC web site was upgraded. While BSL programmers have steadily pushed out new tools for researchers to use in acquiring data as well as maintaining existing tools, the web page itself had been suffering from a lack of attention. The existing site was previously updated circa 2003 by seismologist Lind Gee, and the structure and content were poorly maintained upon her departure, resulting in a difficult to navigate maze of pages with repeated and in some cases out of date content.

We performed a content inventory of the pages, drafted a new menu structure, and iterated with the data center manager Doug Neuhauser and a team of BSL seismologists until

a sensible menu scheme emerged. We also worked with partner agencies to create updated content about our networks for the network description pages. The new look and feel was adapted from the upgraded BSL site to reflect the close association between the NCEDC and BSL while acknowledging our partner agencies. We also implemented an NCEDC email list signup form. Future work on the NCEDC page's front end will include creation of an NCEDC blog and removal of no-longer-needed pages.

Web Services

The NCEDC has developed and deployed web services for distributing time series data, related channel metadata, and event catalog data. Web services use standard web HTTP protocol for sending requests and receiving data. Web services can be used interactively from a web browser, from scripts, and directly from user-written programs and libraries such as python or matlab. Whenever possible the *ncedcws* web services are compatible with the corresponding IRIS DMC *irisws* web services of the same name. The currently supported data services are:

- *ncedc-sacpz*—provide poles and zeros for the specified channels and time interval in SAC ASCII format.
- *ncedc-resp*—provide response information for the specified channels and time intervael in RESP format.
- *ncedc-dataless*—provide station information and channel response in FDSN dataless SEED format.
- *ncedc-eventdata*—provides time series data from pre-assembled collection of waveforms identified by the specified earthquake catalog and eventid.

In order to encourage standards for data delivery from data centers, in 2012 the International Federation of Digital Seismograph Networks (FDSN) defined specifications for three web services that could provide earthquake catalog information, station and channel metadata, and time series data. In 2013, the NCEDC developed and deployed production web services for each of the FDSN-defined web services, and retired older web services that FDSN services replaced.

- *fdsn-dataselect*—returns one or more channel of time series data in miniSEED format for specified time ranges.
- *fdsnws-station*—provides station and channel metadata and optional time series availability in StationXML format.
- *fdsnws-event*—provides earthquake catalog information in QuakeML format.

The *fdsnws-dataselect* service now delivers time series data seamlessly merged from the NCEDC archive and NCEDC DART. This provides users a single request method that can deliver both current and historic time series.

FDSN StationXML is an XML (Extensible Markup Language) schema for representing station and channel metadata. StationXML was originally designed at the SCEDC and later adopted by the FDSN. RESP format is the ASCII channel response format created by the IRIS *rdseed* program, and supported by programs such as *evalresp*. Documentation on FDSN Station XML is available at http://www.fdsn.org/xml/station/.

SeismiQuery

The NCEDC ported and installed the IRIS *SeismiQuery* program at the NCEDC, which provides a web interface to query network, station, and channel attributes and query the availability of archived time series data.

NetDC

In a collaborative project with the IRIS DMC and other worldwide datacenters, the NCEDC helped develop and implement *NetDC*, a protocol which will provide a seamless user interface to multiple datacenters for geophysical network and station inventory, instrument responses, and data retrieval requests. *NetDC* builds upon the foundation and concepts of the IRIS *BREQ_FAST* data request system. The *NetDC* system was put into production in January 2000 and operated at several datacenters worldwide, including NCEDC, IRIS DMC, ORFEUS, Geoscope, and SCEDC. The *NetDC* system receives user requests via email, automatically routes the appropriate portion of the requests to the appropriate datacenter, optionally aggregates the responses from the various datacenters, and delivers the data (or FTP pointers to the data) to the users via email.

The IRIS DMC deprecated NetDC in 2012, but the NCEDC continues to support NetDC data, inventory, and metadata requests.

STP

In 2002, the NCEDC wrote a collaborative proposal with the SCEDC to the Southern California Earthquake Center, with the goal of unifying data access between the two data centers. As part of this project, the NCEDC and SCEDC are working to support a common set of 3 tools for accessing waveform and parametric data: *SeismiQuery*, *NetDC*, and *STP*.

The *Seismogram Transfer Program* or *STP* is a simple client-server program, developed at the SCEDC. Access to *STP* is either through a simple direct interface that is available for Sun or Linux platforms, or through a GUI Web interface. With the direct interface, the data are placed directly on a user's computer in several possible formats, with the byte-swap conversion performed automatically. With the web interface, the selected and converted data are retrieved with a single FTP command. The *STP* interface also allows rapid access to parametric data such as hypocenters and phases.

The NCEDC continued work on *STP*, working with the SCEDC on extensions and needed additions. We added support for the full SEED channel name (Station, Network, Channel, and Location), and are now able to return event as-

sociated waveforms from the NCSN waveform archive.

EVT_FAST

In order to provide Web access to the NCSN waveforms before the SEED conversion and instrument response for the NCSN has been completed, the NCEDC implemented *EVT_FAST*, an interim email-based waveform request system similar to the *BREQ_FAST* email request system. Users email *EVT_FAST* requests to the NCEDC and request NCSN waveform data based on the NCSN event ID. *EVT_FAST* event waveforms can be delivered in either miniSEED or SAC format, and are now named with their SEED channel names.

FISSURES

The *FISSURES* project developed from an initiative by IRIS to improve earth scientists' efficiency by developing a unified environment that can provide interactive or programmatic access to waveform data and the corresponding metadata for instrument response, as well as station and channel inventory information. *FISSURES* was developed using CORBA (Common Object Request Broker Architecture) as the architecture to implement a system-independent method for the exchange of this binary data. The IRIS DMC developed a series of services, referred to as the *Data Handling Interface (DHI)*, using the *FISSURES* architecture to provide waveform and metadata from the IRIS DMC.

The NCEDC has implemented the *FISSURES Data Handling Interface (DHI)* services at the NCEDC, which involves interfacing the DHI servers with the NCEDC database schema. These services interact with the NCEDC database and data storage system and can deliver NCEDC channel metadata as well as waveforms using the *FISSURES* interfaces. We have separate *FISSURES DHI* waveform servers to serve archived and DART data streams. Our *FISSURES* servers are registered with the IRIS *FISSURES naming services*, which ensures that all *FISSURES* users have transparent access to data from the NCEDC.

The IRIS DMC deprecated its support for FISSURES in 2012–2013, but the NCEDC continues to support all of its FISSURES servers and assumed responsibility for the FISSURES name service.

SWC and SWS

UC Berkeley developed the Simple Wave Server, *sws,* and Simple Wave Client, *swc,* programs to provide access to its miniSEED data from the DART and the NCEDC archive. It currently operates a separate server for each of the above services. The *swc* program is a command-line client program written in perl that runs under Linux, Unix, and MacOS and allows users to easily retrieve waveform data in miniSEED format by channel and time window or by NCEMC event gathers. The program is packaged for easy user installation and can be downloaded from the NCEDC web site.

The NCEDC operates two distinct SWS services. The *ncedc_archive* service provides access to data that has been formally archived at the NCEDC, and the *dart* service provides access to real time data from the DART.

GPS

GPS data (raw data, RINEX data at 15 second interval, and high-rate 1 Hz RINEX data) are all available via HTTP or FTP over the internet in a well-defined directory structure organized by data type, year, and day-of-year.

Metrics for 2013–2014

- NCEDC uptime for data delivery was over 99.9% for the year.
- Tables 4.8.2 and 4.8.3 provide a breakdown by network or type of data of the total NCEDC archive size, statistics about this fiscal year's waveform archive after QC work, statistics for month of data without QC, and data distribution information for the fiscal year.

Acknowledgements

The NCEDC is a joint project of the BSL and the USGS Menlo Park and is funded primarily by BSL and USGS Cooperative Agreements G10AC00141 and G10AC00093. Additional funding for the processing and archiving of the EarthScope PBO and SAFOD data were provided by EarthScope subawards EAR0732947-07 through UNAVCO. Archival of geothermal monitoring data are provided through LBNL project number 6948613.

Douglas Neuhauser is the manager of the NCEDC. Stephane Zuzlewski, Mario Aranha, Ingrid Johanson, Taka'aki Taira, Jennifer Taggart, Clay Miller, and Peggy Hellweg of the BSL contribute to the operation of the NCEDC. Doug Neuhauser, Peggy Hellweg, and Clay Miller contributed to the preparation of this section.

Network	Total Archive Size (GB)	2013-14 % of Waveform Data Archived	Avg # of Waveform Segments	Avg Segment Length (days)	% of Stations with <= 12 Segments
BG	3,837.55	98.67%	714	15.16	0%
BK	13,018.89	99.23%	26	246.85	75%
BP	5,004.54	98.28%	95	149.48	50%
CE	102.42	99.20%	146	17.99	0%
CI	3,762.78	85.93%	1030	22.69	13%
NC	30,330.59	95.83%	728	27.22	2%
NN	2,795.98	98.89%	520	28.43	8%
NP	6,394.37	n/a	n/a	n/a	n/a
PB	4,945.03	n/a	n/a	n/a	n/a
PG	1,433.39	90.84%	280	13.56	0%
SF	527.49	99.22%	181	8.89	0%
TA	656.34	96.56%	175	64.20	0%
UL	0.45	n/a	n/a	n/a	n/a
US	2.91	n/a	n/a	n/a	n/a
WR	1,396.79	79.25%	2229	6.20	0%
Other Net	n/a	n/a	n/a	n/a	n/a
NCSS events	1,306.81	n/a	n/a	n/a	n/a
EGS events	497.24	n/a	n/a	n/a	n/a
Subtotal	76,013.59				
GPS Data	4,559.71	n/a	n/a	n/a	n/a
Other Data	1,484.23	n/a	n/a	n/a	n/a
Catalog Data	n/a	n/a	n/a	n/a	n/a
Total	82,057.53				

Table 4.8.2: Total NCEDC archive broken down by continuous waveforms from seismic networks, event waveforms for different catalogs, GPS data, and other data sets for the year 2013–2014. Each network is broken down into the percentage of possible waveforms actually archived, the average number of distinct continuous waveform segments, the average lengthof waveform segments in days, and the percentage of stations that have fewer than12 continuous segments per year. A perfect complete waveform archive would be represented by 100% data return, average segment length of 365 days, and 100% of stations with ≤12 segments.

Network	June 2014 % of Waveform Data Archived	Avg # of Waveform Segments	Avg Segment Length (days)	% of Stations with 1 Segment	Data Distributed (GB) this year	Unique Users this year
BG	99.98%	127	7.53	0%	1,846.77	129
BK	96.54%	11	27.10	67%	1,023.16	510
BP	97.07%	6	26.50	67%	781.02	92
CE	100.00%	12	7.20	0%	0.47	31
CI	87.69%	92	7.12	23%	8.19	81
NC	95.49%	1169	5.51	0%	669.80	176
NN	99.19%	83	8.62	0%	16.60	52
NP	91.73%	143	8.36	0%	3.65	46
PB	99.53%	3	21.70	42%	23.49	96
PG	81.25%	41	4.26	0%	24.44	47
SF	76.31%	19	5.86	0%	5.88	54
TA	n/a	n/a	n/a	n/a	1.68	33
UL	n/a	n/a	n/a	n/a	0.01	1
US	n/a	n/a	n/a	n/a	0.09	25
WR	83.18%	4365	3.09	0%	2.25	18
Other Net	n/a	n/a	n/a	n/a	0.33	37
NCSS events	n/a	n/a	n/a	n/a		
EGS events	n/a	n/a	n/a	n/a		
Subtotal					4,407.83	745
GPS Data	n/a	n/a	n/a	n/a	303.06	269
Other Data	n/a	n/a	n/a	n/a	36.58	264
Catalog Data	n/a	n/a	n/a	n/a	22,846.76	8468
Total					27,594.22	9626

Table 4.8.3: This table shows the same statistics as Table 4.8.2. The first column shows the percent of June 2014 data real-time waveform stored in the NCEDC DART. This represents data transmitted in real-time or near-real time to the NCEDC, and includes no data backfilling from QC (quality control) processes. In addition, the table shows the total data distributed by network and other data sets during the reporting year, and the number of distinct users of each network or data set.

Glossary of Common Acronyms

Acronym	Definition
ADA	Amplitude Data Area
ANSS	Advanced National Seismic System
ANSS NIC	ANSS National Implementation Committee
AQMS	ANSS Quake Monitoring System
ARRA	American Recovery and Reinvestment Act
BARD	Bay Area Regional Deformation
BAVU	Bay Area Velocity Unification
BDSN	Berkeley Digital Seismic Network
BSL	Berkeley Seismological Laboratory
CalEMA	California Emergency Management Agency
Caltrans	California Department of Transportation
CDF	California Department of Forestry
CGS	California Geological Survey
CISN	California Integrated Seismic Network
DART	Data Available in Real Time
EEW	Earthquake Early Warning
ElarmS	Earthquake Alarm Systems
EM	Electromagnetic
FACES	FlexArray along Cascadia Experiment for Segmentation
FEMA	Federal Emergency Management Agency
HFN	Hayward Fault Network
HRSN	High Resolution Seismic Network
InSAR	Interferometric Synthetic Aperture Radar
IRIS	Incorporated Research Institutions in Seismology
IRIS DMC	IRIS Data Management Center
LBNL	Lawrence Berkeley National Laboratory
LFE	Low Frequency Event
LLNL	Lawrence Livermore National Laboratory
MARS	Monterey Accelerated Research System
MBARI	Monterey Bay Aquarium Research Institute
MOBB	Monterey Ocean Bottom Broadband Observatory
mPBO	Mini-Plate Boundary Observatory
MT	Magnetotelluric
MT	Moment Tensor
MTJ	Mendocino Triple Junction
NCEDC	Northern California Earthquake Data Center
NCEMC	Northern California Earthquake Management Center
NCSN	Northern California Seismic Network
NCSS	Northern California Seismic System
NHFN	Northern Hayward Fault Network

Continued on next page

NVT	Non-volcanic Tremor
PBO	Plate Boundary Observatory
PDF	Probability Density Function
PGV	Peak Ground Velocity
PSD	Power Spectral Density
QDDS/EIDS	Quake Data Distribution System/Earthquake Information Distribution System
REDI	Rapid Earthquake Data Integration
RES	Repeating Earthquake Sequence
SAF	San Andreas Fault
SAFOD	San Andreas Fault Observatory at Depth
SCSN	Southern California Seismic Network
SEED	Standard for Exchange of Earthquake Data
SEM	Spectral Element Method
SHFN	Southern Hayward Fault Network
SOH	State of Health
SSE	Slow Slip Event
UNACO	University NAVSTAR Consortium
USGS/MP	United States Geological Survey/ Menlo Park
USNSN	United States National Seismic Network

Appendix I: Publications, Presentations, Awards and Panels

Publications

Amos, C. B., S. J. Brownlee, D. H. Rood, G. B. Fisher, R. Bürgmann, P. R. Renne, and A. S. Jayko, Chronology of tectonic, geomorphic, and volcanic interactions and the tempo of fault slip near Little Lake, California, *Geological Society of America Bulletin*, 125(7-8), doi: 10.1130/B30803.30801, 2013.

Amos, C. B., P. Audet, W. C. Hammond, R. Bürgmann, I. A. Johanson, and G. Blewitt, Contemporary uplift and seismicity in central California driven by groundwater depletion, *Nature*, 509, 483-486, doi:doi:10.1038/nature13275, 2014.

Ballmer, M.D., G. Ito, and C. Cheng, Thermochemical convection of bilaterally asymmetric plumes and implications for Hawaiian lava composition, in: Hawaiian Volcanism: From Source to Surface, *AGU Monograph*, Eds.: R. Carey, M. Poland and D. Weis, *in press*.

Beeler, N. M., A. Thomas, R. Bürgmann, and D. Shelly, Inferring fault rheology from low-frequency earthquakes on the San Andreas, *Journal of Geophysical Research*, 118(11), doi:10.1002/2013JB010118, 2013.

Bie, L., I. Ryder, S. E. J. Nippress, and R. Bürgmann, Coseismic and postseismic activity associated with the 2008 Mw 6.3 Damxung earthquake, Tibet, constrained by InSAR, *Geophysical Journal International*, 196(2), doi: 10.1093/gji/ggt1444, 2014.

Bodin, T., Y Capdeville, B Romanowicz, JP Montagner, Interpreting Radial Anisotropy in Global and Regional Tomographic Models, Book Chapter, The Earth's heterogeneous mantle, A Khan, F Deschamps & K Kawai (eds), Springer, in press.

Bodin, T., H Yuan, B Romanowicz, Inversion of receiver functions without deconvolution, *Geophysical Journal International*, 196 (2), 1025–1033.

Bürgmann, R., and W. Thatcher, Space geodesy: a revolution in crustal deformation measurements of tectonic processes, in The Web of Geological Sciences: Advances, Impacts, and Interactions, edited by M. E. Bickford, *Geological Society of America Special Paper 500*, doi:10.1130/2013.2500(12), 2013.

Calò, M., Dorbath, C., Frogneux, M., Injection tests at the EGS reservoir of Soultz-sous-Forêt. Seismic response of the GPK4 stimulations, *Geothermics*, http//dx.doi.org/10.1016/j.geothermics.2013.10.007, 2013.

Carlson, R. W., E. Garnero, T. M. Harrison, J. Li, M. Manga, W. F. McDonough, S. Mukhopadhyay, B. Romanowicz, D. Rubie, Q. Williams, and S. Zhong, How did Early Earth become our modern World?, *Ann. Rev. Earth Planet. Sci.*, doi: 10.1146/annurev-earth-060313-055016, 2014.

Chaussard, E., and Amelung, F., Regional controls on magma ascent and storage in volcanic arcs, *Geochem. Geophys. Geosyst.*, 15, no. 4, pp. 1407–1418, 2014.

Chaussard, E., Amelung, F., and Aoki, Y., Characterization of open and closed volcanic systems in Indonesia and Mexico using InSAR time series, *Journal of Geophysical Research-Solid Earth*, 118, 1–13, doi:10.1002/jgrb.50288, 2013.

Chen, K.-H., R. Bürgmann, R.M. Nadeau, Do earthquakes talk to each other?: Triggering and interaction of repeating sequences at Parkfield, *J. Geophys. Res.*, 118, 1–18, doi:10.1029/2012JB009486, 2013.

Cheng, C, Allen, R. M., Porritt, R. W., and Ballmer, M. D., Seismic constraints on a double-layered asymmetric whole-mantle plume beneath Hawaii, in: Hawaiian Volcanism: From Source to Surface, *AGU Monograph*, Eds.: R. Carey, M. Poland and D. Weis, *in press*.

Chiang, A., Dreger, D. S., Ford, S. R., Walter, W. R., Source characterization of underground explosions from combined regional moment tensor and first motion analysis, *Bull. Seismol. Soc. Am.*, 104, doi:10.1785/0120130228, *in press*.

Cottaar, S. and B. Romanowicz (2013) Observations of changing anisotropy across the southern margin of the African LLSVP, *Geophys. J. Int.*, doi: 10.1093/gji/ggt285, 2013.

Cottaar, S., M. Li, A. McNamara, R. Wenk and B. Romanowicz, Synthetic anisotropy models within a slab impinging on the core-mantle boundary, *Geophys. J. Int.*, *in press*.

Dou, S. and Ajo-Franklin, J. B., Full-wavefield inversion of surface waves for mapping embedded low-velocity zones in perma-

frost, *Geophysics, in press*.

Durand, S., J. Matas, S. Ford, Y. Ricard, J.P. Montagner and B. Romanowicz, Insights from ScS-S measurements on deep mantle attenuation, *Earth Planet. Sci. Lett.*, 374, 101-110, 2013.

Dziewonski, A. M. and B. Romanowicz, Overview, *Treatise of Geophysics, Vol. 1*, Ed. G. Schubert, 2014 re-edition, published by Elsevier, *in press*.

French, S., Lekic, V., Romanowicz, B., Waveform Tomography Reveals Channeled Flow at the Base of the Oceanic Asthenosphere, *Science*, 342, 227-230, 2013.

Grapenthin, R., CrusDe: A plug-in based simulation framework for composable CRUStal DEformation simulations. *Computers & Geosciences, Vol. 62*, pp. 168-177 doi: 10.1016/j.cageo.2013.07.005, 2014.

Grapenthin, R., I.A. Johanson, R.M. Allen, Operational Real-time GPS-enhanced Earthquake Early Warning, *J. Geophys. Res.*, *submitted*.

Guang-Yin, W., Liu Yu-Zhu, Yang Ji-Zhong, Dong Liang-Guo. Joint inversion of VTI parameters using nonlinear traveltime tomography, *Chinese Journal of Geophysics* (in Chinese), 2014.

Guilhem, A., R. Bürgmann, A. M. Freed, and S. A. Tabrez, Testing the accelerating moment release (AMR) hypothesis in areas of high stress, *Geophysical Journal International*, *195(2)*, doi: 10.1093/gji/ggt1298, 2013.

Guilhem, A., L. Hutchings, D. S. Dreger and L. R. Johnson, Moment tensor inversion of ~M3 earthquakes in the Geysers Geothermal Field, California, *Journ. Geophys. Res.,* 10.1002/2013JB010271, 2014.

Hreinsdóttir, S., F. Sigmundsson, M.J. Roberts, H. Björnsson, R. Grapenthin, P. Arason, Th. Árnadóttir, J. Hólmjárn, H. Geirsson, R.A. Bennett, M.T. Gudmundsson, B. Oddsson, B.G. Ófeigsson, T. Villemin, T. Jónsson, E. Sturkell, Á Höskuldsson, G. Larsen, T. Thordarson, and B.A. Óladóttir, Volcanic plume height correlated with magma-pressure change at Grímsvötn Volcano, Iceland, *Nature Geoscience*, doi:10.1038/ngeo2044, 2014.

Huang, M.-H., R. Bürgmann, and A. M. Freed, Probing the lithospheric rheology across the eastern margin of the Tibetan Plateau, *Earth and Planetary Science Letters, 396*, 88-96, doi:doi:10.1016/j.epsl.2014.04.003, 2014.

Huang, M.-H., D. Dreger, R. Bürgmann, S.-H. Yoo, and M. Hashimoto, Joint inversion of seismic and geodetic data for the source of the 4th March 2010 Mw 6.3 Jia-Shian, SW Taiwan, earthquake, *Geophysical Journal International, 193(3)*, doi:10.1093/gji/ggt1058, 2013.

Iaffaldano, G., R Hawkins, T Bodin, M Sambridge, REDBACK: open-source software for efficient noise-reduction in plate kinematic reconstructions, *G-cubed*, DOI: 10.1002/2014GC005309,

Jiang, Z., M. Wang, Y. Wang, Y. Wu, S. Che, Z.-K. Shen, R. Bürgmann, J. Sun, Y. Yang, and H. L. Li, GPS constrained coseismic source and slip distribution of the 2013 Mw6.6 Lushan, China, earthquake and its tectonic implications, *Geophysical Research Letters, 41(2)*, doi:10.1002/2013GL058812, 2014.

Kelly, C.M., A. Rietbrock, D.R. Faulkner and R.M. Nadeau, Temporal Changes in Attenuation associated with the 2004 M6.0 Parkfield Earthquake, *J. Geophys. Res.*, *118*, 630–645, doi:10.1002/jgrb.50088, 2013.

Langbein, J., J. R. Evans, F. Blume, and I. A. Johanson, Response of Global Navigation Satellite System receivers to known shaking between 0.2 and 20 Hertz, *U. S. Geological Survey Open-File Rep. 2013-1308*, doi:10.3133/ofr20131308, 2014.

Lifton, Z.M., A. V. Newman, K. L. Frankel, C.W. Johnson, and T. H. Dixon, Insights into distributed plate rates across the Walker Lane from GPS geodesy, *Geophys. Res. Lett., 40*, doi:10.1002/grl.50804.

Masson, Y., P. Cupillard, Y. Capdeville and B. Romanowicz, On the numerical implementation of time reversal mirrors for tomographic imaging, *Geophys. J. Int.*, doi: 10.1093/gji/ggt459, 2013.

Meng, L., J.-P. Ampuero, and R. Bürgmann, The 2013 Okhotsk Deep-Focus Earthquake: Rupture Beyond the Metastable Olivine Wedge and Thermally-Controlled Rise Time near the Edge of a Slab, *Geophys. Res. Lett.*, 14, doi: 10.1002/2014GL059968, 2014.

Nayak, A., and D. S. Dreger, Moment tensor inversion of seismic events associated with the sinkhole at Napoleonville Salt Dome, Louisiana, *Bull. Seism. Soc. Am.*, *in press*.

Pollitz, F., R. Bürgmann, R. S. Stein, and V. Sevilgen, The profound reach of the 11 April 2012 M8.6 Indian Ocean earthquake: short-term global triggering followed by a long-term global shadow, *Bull. Seismol. Soc. Am., 104(2)*, doi: 10.1785/0120130078, 2014.

Romanowicz, B. and B. J. Mitchell, Deep Earth structure: Q of the Earth from crust to core, *Treatise of Geophysics, Vol. 1*, Ed. G.

Schubert, 2014 re-edition, published by Elsevier, *in press*.

Rueda, J., D. S. Dreger, R. M. G. Blanco, and J. Mezcua, Directivity detection and source properties of the 11th May 2011, Lorca (Spain) Mw5.2 earthquake, *Bull. Seism. Soc. Am., in press*.

Shelly, D., D. Hill, F. Massin, J. Farrell, R.B. Smith, and T. Taira, A fluid-driven earthquake swarm on the margin of the Yellowstone caldera, *J. Geophys. Res*., 118, 4872-4886, doi:10.1002/jgrb.50362, 2013.

Shirzaei, M., R. Bürgmann, J. Foster, T. R. Walter, and B. A. Brooks, Aseismic deformation across the Hilina fault system, Hawaii, revealed by wavelet analysis of InSAR and GPS time series, *Earth and Planetary Science Letters, 376(0)*, doi: 10.1016/j.epsl.2013.1006.1011, 2013.

Shirzaei, M., T. R. Walter, and R. Bürgmann, Coupling of Hawaiian volcanoes during mantle-driven surge, *Geophys. Res. Lett., 40*, doi:10.1002/grl.50470, 2013.

Sun, J., Z.-K. Shen, R. Bürgmann, M. Wang, L. Chen, and X. Xu, A three-step maximum a posteriori probability method for InSAR data inversion of coseismic rupture with application to the 14 April 2010 Mw 6.9 Yushu, China, earthquake, *Journal of Geophysical Research, 118(8)*, 4599-4627, doi:10.1002/jgrb.50244, 2013.

Sun, J., Z. K. Shen, R. Bürgmann, and X. Xu, Coseismic slip distribution of the March 24, 2011 Tarlay (Myanmar) Mw 6.8 earthquake from ALOS PALSAR interferometry, *Bull. Seismol. Soc. Am.*, *103(5)*, doi: 10.1785/0120120365, 2013.

Taira, T., Z. Zheng, and B. Romanowicz, On the systematic long period noise reduction on ocean floor broadband seismic sensors collocated with differential pressure gauges, *Bull. Seis. Soc. Am.*, 104, 247-259, 2014.

Tkalcic, H., T Bodin, M Young, M Sambridge, On the nature of the P-wave velocity gradient in the inner core beneath central America, *J. Earth Sci. - Special Volume on Core Dynamics, Vol. 24*, No. 5, p. 699-705

Thomas, A. M., R. Bürgmann, and D. Dreger, Incipient faulting near Lake Pillsbury, CA and the role of accessory faults in plate boundary evolution, *Geology*, 41, doi:10.1130/G34588.34581, 2013.

Turner, R.C., R.M. Nadeau and R. Bürgmann, Aseismic Slip and Fault Interaction from Repeating Earthquakes in the Loma Prieta Aftershock Zone, *Geophys. Res. Lett., 40*, 1079–1083, doi:10.1002/grl.50212, 2013.

Yang J. Z., Y. Z. Liu, L. G. Dong, A multi-parameter full waveform inversion strategy in acoustic media, *Chinese Journal of Geophysics* (in Chinese), 57(2): 628-643, 2014.

Young, M., H Tkalcic, T Bodin, M Sambridge, Global P-wave Tomography of Earth's Lowermost Mantle from Partition Modeling, *Journal of Geophysical Research – Solid Earth*, 118, 1-20.

Yuan, H., French, S., Cupillard, P., Romanowicz, B., Lithospheric expression of geological units in central and eastern North America from full waveform tomography, *Earth Planet. Sci. Lett.*, *in press*.

Yuzhu, L., Xie Chun, Yang Jizhong, Gaussian beam first-arrival waveform inversion based on Born wavepath, *Chinese Journal of Geophysics* (in Chinese), 2014.

Zulfakriza, E., E Saygin, PR Cummins, S Widiyantoro, AD Nugraha, BG Luhr, T Bodin, Upper Crustal Structure of Central Java, Indonesia, from Transdimensional Seismic Ambient Noise Tomography, *Geophysical Journal International*, doi: 10.1093/gji/ggu016.

Presentations

CIG-QUEST Joint Workshop on Seismic Imaging of Structure and Source, Fairbanks, AK, July 14–17, 2013

French, S., Lekic, V., and Romanowicz, B., Oceanic low-velocity structure in SEMum2: Interpretations and synthetic validation.

Business Recovery Managers Association, July 2013 Membership Meeting, Oakland, CA, July 25, 2013

Strauss, J. A., Shaping Response and Recovery with Earthquake Early Warning.

SCEC Annual Meeting, Palm Springs, CA, September 9–11, 2013

Dreger, D., Broadband Platform Validation Exercise for Pseudo-Spectral Acceleration: Review Panel Summary.

Johnson, C. W., Bürgmann, R., Seismicity in the central Gulf of California region following the Mw 8.6 2012 Indian Ocean earthquake.

Taira, T., Variability of Fault Slip Behaviors along the San Jacinto Fault, Inferred from Characteristically Repeating Earthquake Activity.

Living Planet Symposium 2013, Edinburgh, United Kingdom, September 9–13, 2013

Chaussard, E., Amelung, F., and Aoki, Y., Detection of Cyclic Behaviors and Characterization of Magma Storage at Andesitic Volcanoes using Regional Time Series.

Chaussard, E., Wdowinski, S., Amelung, F., Cabral-Cano, E., Abidin, H., Hong, S-H., Land subsidence in central Mexico and Indonesia: Differences and Similitudes from Regional ALOS Time-series Surveys.

Seismological Society of Japan (SSJ) 2013 Fall Meeting, Yokohama, Japan, October 7–9, 2013

Uchida, N., T. Linuma, R.M. Nadeau, R. Bürgmann, R. Hino, Periodic slow slip in the northeastern Japan subduction zone.

NERSC Large Scale Production Computing and Storage Requirements for Basic Energy Sciences: Target 2017, Gaithersburg, MD, October 8-9, 2013

French, S., and Romanowicz, B., Present and Future Computing Requirements: Imaging and Calibration of Mantle Structure at Global and Regional Scales Using Full-Waveform Seismic Tomography.

8th ILP-Task Force workshop on Sedimentary Basin, Marseille, France, October 14–18, 2013

Di Stefano P., Favara R., Luzio D., Renda P., Cacciatore M. S., Calò M., Caracausi A., Napoli G., Parisi L., Todaro S., Zarcone G., A Mesozoic paleomargin in Western Sicily, its Tertiary evolution and its present-day seismogenetic potential.

International Continental Scientific Drilling Program Conference, Potsdam, Germany, November 11–14, 2013

Taira T., D.S. Dreger, R.M. Nadeau, Borehole Seismic Monitoring of Deep Fault Deformation along the Hayward Fault, CA.

COSMOS Annual Meeting, Emeryville, CA, November 22, 2013

Dreger, D., Review of Methods Currently Available on the SCEC Broadband Platform.

GeoPrisms Aleutians Mini-Workshop, San Francisco, CA, December 8, 2013

Grapenthin, R., J.T. Freymueller, A.M. Kaufman, The 2009 Redoubt Eruption Observed with GPS: Aseismic Inflation, Mid-crustal Remobilization and Net-Deflation

American Geophysical Union, 2013 Fall Meeting, San Francisco, CA, December 9–13, 2013

Adam, J., B. Romanowicz, Seismic models of the F-layer from a global dataset: observations of scattered energy from the core, Abstract DI23A-2290.

Alexandrakis, C., M. Calò, F. Bouchaala, V. Vavrycuk. Imaging the West Bohemia Seismic Zone, abstract S23A-2466.

Allen, R., R. Grapenthin, L. Meng, et al., Designing a network-based earthquake early warning system for California, Abstract S43C-05.

Bodin, T., Capdeville, Y. Romanowicz, B., The Inverse Homogenization or "Downscaling" of Smooth Tomographic Models: Separating Intrinsic and Apparent Anisotropy, Abstract S22B-08.

Boyd, O.S., D.S. Dreger, A. Kim, and R. Gritto, Characterization and modeling of earthquake source processes at The Geysers geothermal field, Abstract S33D-2458.

Cabral-Cano, E., Arciniega-Ceballos, A., Vergara-Huerta, F., Chaussard, E., Wdowinski, W., DeMets, C., Salazar-Tlaczani, L., Shallow Faulting in Morelia, Mexico, Based on Seismic Tomography and Geodetically Detected Land Subsidence, Abstract NH23C-1542.

Cai, M., Cottaar, S., Romanowicz, B., Further constraints on the Ultra-Low Velocity Zone beneath the north-central Pacific, Abstract DI51A-2263.

Calò M., Bodin T., Yuan H., Romanowicz B.A., Larmat C.S., Maceira M., Constructing a starting 3D shear velocity model with sharp interfaces for SEM-based upper mantle tomography in North America, abstract S33A-2400.

Chaussard, E., Bürgmann, R., Shirzaei, M., and Baker B., Long-term and seasonal ground deformation in the Santa Clara Valley, California, revealed by multi decadal InSAR time series, Abstract G31A-0949.

Cheng, C., Allen, R., Bodin, T., Porritt, R., Ballmer, M., Comparing different mantle plumes using seismic imaging methods, Abstract DI21A-2258.

Chiang, A., Dreger, D.S., Ford, S.R., Walter, W.R., and Yoo, S.-H., Moment tensor analysis of shallow sources. Abstract S24B-08.

Delbridge, B., R. Burgmann, E. Fielding, S. Hensley, W. Schulz, 3D surface flow kinematics derived from airborne UAVSAR interferometric synthetic aperture radar to constrain the physical mechanisms controlling landslide motion, Abstract G33D-08.

Dominguez L. A., and T. Taira, Investigating Fault Slip Budget in the Cocos Subducting Plate from Characteristically Repeating Earthquake Activity, Abstract S41B-2430.

Dou, S. and Ajo-Franklin, J. B., Ultrasonic measurements of unconsolidated saline sediments during freeze/thaw cycles: the seismic properties of cryopeg, Abstract C53C-05.

Frank, W., N. Shapiro, V. Kostoglodov, A.L. Husker, E.G. Daub, M. Radiguet, R.A. Guyer, R.M. Nadeau, M. Campillo, J.S. Payero, G.A. Prieto, D.R. Shelly, and P.A. Johnson, Investigating the Low-Frequency Earthquake and Non-Volcanic Tremor System, Abstract S41B-2455.

Grapenthin, R., I. Johanson, R. Allen, G-larmS: Integrating Real-Time GPS into Earthquake Early Warning, Abstract G53B-092.

French, S. and Romanowicz, B., Global waveform tomography with the SEM: Toward a whole-mantle radially anisotropic shear-velocity model, Abstract S21E-07.

Hawley, William B., and Allen, Richard M., Ridge to Trench Body Wave Tomography of the Juan de Fuca Plate System., Abstract S21C-2438.

Hawley, William B., Mitrovica, Jerry X. and Hay, Carling, The effects of artificially impounded water on tide gauge measurements of sea level over the last century. Abstract G33C-01.

Hellweg, M., E. Araki, H. Rademacher, T. Taira, R.A. Uhrhammer, and M. McGowan, Normal Modes: Investigating Signal and Noise Phenomena Across Instrument Types and Deployment, Abstract S11A-2287.

Hellweg, M., M. Vinci, R.M. Allen, M. Boese, I.H. Henson and C. Felizardo, CISN ShakeAlert: Beta Test Users Receive Earthquake Early Warning Alerts and Provide Feedback for Improving Alert Delivery, Abstract S52B-03.

Kong, Q., R.M. Allen, Building a Smartphone Seismic Network, Abstract S51A-2291.

Kuyuk, H.S., H. Brown, R.M. Allen, D.S. Neuhauser, I.H. Henson and M. Hellweg, CISN ShakeAlert: Next Generation ElarmS, Abstract S52B-02.

Lai, V. H., T. Taira, and D.S. Dreger, Ambient Seismic Noise Monitoring for Stress-Induced Changes in Geysers Geothermal Field, California, Abstract S33D-2459.

Leiva, J., P. Clouzet, S. French, H. Yuan and B. Romanowicz, Isotropic and anisotropic shear velocity model of the North American upper mantle using Earthscope data, Abstract S21A-2380.

Johanson, I.A., R.C. Turner, T. Taira, R.M. Nadeau, and R. Bürgmann, Creep Variability and Seismicity at the Junction of the Calaveras and San Andreas Faults, Abstract G32B-04.

Johnson, C.W. and R. Burgmann, Spatial and temporal global seismicity patterns following large magnitude earthquakes, Abstract S51B-2359.

Malagnini, L., I. Munafo, S.-H. Yoo, K.E. Wooddell, D.S. Dreger, K.M. Mayeda, and R.M. Nadeau, Source Parameters of ~ 750 Repeating Micro-Earthquakes in the Parkfield Area, Abstract S21D-05.

Masson Y., and B. Romanowicz, Towards regional-scale adjoint tomography in the deep earth, Abstract S31D-06.

Meschede, M., B. Romanowicz, A Study of Long-Period Mantle Wave Scattering, Abstract DI41A-2320.

Munkhsaikhan A., Schlupp A., Dorbath C., Calò M., Ulziibat M., Seismic swarm investigated using double-difference tomography: 3D velocity structure in and around Emeelt fault, Abstract S11B-2370.

Nayak, A., Dreger, D.S., Investigation of Seismic Events associated with the Sinkhole at Napoleonville Salt Dome, Louisiana, Abstract S33D-2451.

Neuhauser, D., S. Zuzlewski, P. Lombard, R. Allen, Web Services and Data Enhancements at the Northern California Earthquake Data Center, Abstract S51A-2326.

Parisi L., Calò M., Evidences of a Lithospheric Fault Zone in the Sicily Channel Continental Rift (Southern Italy) from Instrumental Seismicity Data, Abstract T53D-2616.

Perry-Houts, Calò M., Eddy C. L., Guerri M., Holt A., Hopper E., Tesoniero A., Romanowicz B. A., Becker J. T. W., Wagner L. S., Deep vs. shallow expressions of continental cratons: Can cratonic roots be destroyed by subduction? Abstract T22A-06.

Randolph-Flagg, N.G., Day, J., Bürgmann, R., Manga M., Seasonal variability in Tibetan seismicity 1991-2013, Abstract S33D-2485.

Ray, A., Key, K., Bodin, T., Almost but not quite 2D, Non-linear Bayesian Inversion of CSEM Data, Abstract NS34A-06.

Rickers, F., B. Romanowicz, Full-waveform tomography of the Pacific region using the adjoint method, Abstract S33A-2401.

Romanowicz, B., S. French, F. Rickers and H. Yuan, Source stacking for numerical wavefield computations: application to continental and global scale seismic mantle tomography, Abstract S21E-05.

Shapiro, N., W. Frank, V. Kostoglodov, A.L. Husker, E.G. Daub, M. Radiguet, C. Wu, R.A. Guyer, R.M. Nadeau, M. Campillo, J.S. Payero, G.A. Prieto, D.R. Shelly, and P.A. Johnson, Burst, Background, and Triggered Low-Frequency Earthquakes and Non-Volcanic Tremors, Abstract S51B-2347.

Strauss, J. A., Vinci, M., Steele, W. P., Allen, R. M., and Hellweg, M., From Demonstration System to Prototype: Shake Alert Beta Users Provide Feedback to Improve Alert Delivery, Abstract S44A-08.

Taira T., and A. Kato, Automated Measurement of P- and S-Wave Differential Times for Imaging Spatial Distributions of Vp/Vs Ratio, with Moving-Window Cross-Correlation Technique, Abstract S42A-08.

Uhrhammer, R.A., T. Taira, and M. Hellweg, Remote Calibration Procedure and Results for the CTBTO AS109 STS-2 HG at YBH, Abstract S33B-2414.

Ventosa, S., B. Romanowicz, Regional Core-Mantle-Boundary modeling with PcP-P using high-density seismic networks, Abstract DI51A-2269.

Vidale, J.E., P.EBodin, R.M.EAllen, M. Hellweg, T. Thomas, I.H. Henson, and D.S. Neuhauser, Early Warning of Cascadian Megaquakes for Pacific Northwestern cities, Abstract S52B-01.

Werner, C., M.P. Poland, J.A. Power, A.J. Sutton, T. Elias, Grapenthin, R., W.A. Thelen, Detecting deep crustal magma movement: Exploring linkages between increased gas emission, deep seismicity, and deformation, Abstract V43D-08.

Wooddell, K.E., S.-H. Yoo, D.S. Dreger, K.M. Mayeda, and R.M. Nadeau, Source Scaling of Micro-Repeating Earthquakes in Parkfield, CA, Abstract S11B-2348.

Zheng, Z., Ventosa, S., and Romanowicz, B., Application of the Local Slant-Stack Filters (LSSF) for High Resolution Upper Mantle Discontinuity Imaging, Abstract DI21B-2275.

Data Science Faire, Berkeley, CA, December 12, 2013

Kong, Q., Richard Allen, myShake: Sensing earthquakes with smartphones.

CIG-EarthScope Institute for Lithospheric Modeling Workshop, Tempe, AZ, February 3–4, 2014

Grapenthin, R. ,CrusDe: A Plug-in Based Simulation Framework for Composable Crustal Deformation Simulations.

11th Annual Northern California Earthquake Hazards Workshop, USGS Menlo Park, Menlo Park, CA, February 11–12, 2014

Allen, R. M., Hellweg, M., Neuhauser, D., Henson, I., Kuyuk, H. S., Strauss, J. A., CISN Earthquake Early Warning 2013.

Johanson, I., R. Grapenthin, R. Bürgmann, R. Allen, The BARD Continuous GPS Network: Monitoring Earthquake Hazards in Northern California and the San Francisco Bay Area.

Taira, T., D.S. Dreger and R.M. Nadeau, High-resolution Imaging of Earthquake Rupture Process for Hayward Microearthquakes.

UNAVCO Science Workshop, Broomfield, CO, March 4–6, 2014

Grapenthin, R., I.A. Johanson, R.M. Allen, Real-time GPS enhanced Earthquake Early Warning: The Northern California Setup.

2nd KACST-KAUST-JCCP International workshop on surface and subsurface 4D monitoring, KAUST, Thuwal, Saudi Arabia, March 4–6, 2014

Chaussard, E. and Bürgmann, R., Characterizing aquifer and fault hydro-mechanical properties at basin-scale using InSAR-derived ground deformation.

SEG/DGS Workshop, Near Surface Modeling & Imaging, Manama, Bahrain, March 7-10

Wang, G.Y., Y.Z.Liu, L.G.Dong, J.Z.Yang. Strategy for joint inversion of VTI parameters in near surface.

Liu, Yuzhu, Chun Xie, Liangguo Dong, Jizhong Yang, First-arrival Gaussian beam waveform inversion based on Born wavepath.

Xie, CHun, Yuzhu Liu, Liangguo Dong, Jizhong Yang, First-arrival traveltime tomography with adjoint-state method based on finite frequency.

European Geosciences Union General Assembly 2014, Vienna, Austria, April 27–May 2, 2014

Graveleau, F., Suppe, J., Chang, K.-J., Dominquez, S., Ustazewski, M., and Huang, M.-H., Incremental vs. geological growth of folds: Examples of Tungshih anticline and Neiwan syncline during Taiwan Mw 7.6 ChiChi earthquake.

Kato, A. and T. Taira, Automated measurement of differential P and S times for imaging near-source Vp/Vs ratio with moving-window cross-correlation analysis.

Masson, Y., Z. Zheng and B. Romanowicz, Local full-waveform inversion using distant data.

Piana Agostinetti N., Calò M., Close-up to the stimulation phase of an EGS geothermal site: mapping the time-evolution of the subsurface elastic parameters using a trans-dimensional Monte Carlo approach, Abstract EGU2014-10769.

Prudencio, J., T. Taira, L.D. Siena, S. Onizawa, J. Ibañez, M. Hellweg, E. Del Pezzo, H. Aoyama, A. García-Yeguas, H.Oshima, A. Díaz-Morenoa, First attenuation study at Usu volcano (Hokkaido, Japan).

Taira, T., R.M. Nadeau, and D.S. Dreger, High-resolution imaging of earthquake rupture process for Hayward microearthquake.

Ventosa, S., and B. Romanowicz, Regional modeling of lateral heterogeneity near the CMB from central America to the eastern part of the Pacific LLSVP.

Annual Meeting of the Seismological Society of America, Anchorage, AK, April 30–May 2

Delbridge, B., B. Buffett, S. Kita, T. Matsuzawa, Bürgmann, R., Temporal Variations of Intraplate Earthquake Activity Following the 2011 Tohoku-Oki Earthquake.

Evans, J.R., R.M. Allen, A.I. Chung, E.S. Cochran, R. Guy, M. Hellweg and J.F. Lawrence, Performance of Several Low-Cost Accelerometers, *Seismol. Res. Lett.*, 85, 527.

Grapenthin, R., I. Johanson, R. Allen, Real-time GPS enhanced Earthquake Early Warning: The Northern California Setup, *Seism. Res. Lett., 85(2)*, 2014.

Hellweg, M., Allen, R. H., Grapenthin, R., Johanson, I., Henson, I., Neuhauser, D., Strauss, J. A., CISN ShakeAlert: An Update on Earthquake Early Warnings from ElarmS, *Seismol. Res. Lett.*

Hellweg, M., E. Araki, H. Rademacher, T. Taira, R.A. Uhrhammer and M.G. McGowan, Normal Modes: Investigating Signal and Noise Phenomena across Instrument Types and Deployment, Seismol. Res. Lett., 85, 433.

Hellweg, M., R.A. Uhrhammer and T. Taira, Remote Calibration Procedures for STS-2s: Example from the STS-2HG for CTBTO at YBH, *Seismol. Res. Lett.*, 85, 494.

Lai, V. H., T. Taira, and D.S. Dreger, M-H. Huang, Ambient Noise Monitoring of Temporal Changes in Seismic Velocity at the Geysers Geothermal Field, California, *Seism. Res. Lett., 85(2)*, 492, 2014.

2014 IRIS Workshop, Sunriver, OR, June 9–11, 2014

Hawley, William B., and Allen, Richard M. Body Wave Tomography of the Juan de Fuca Plate, Abstract 0081.

76th EAGE International Conference and Exhibition, Amsterdam, Netherlands, 2014

Jizhong, Y., Liu Yuzhu, Dong Liangguo, A multi-parameter full waveform inversion strategy in acoustic media.

Speaking Engagements

Allen, R.M., Scientific briefings for Advisors to California Senator Padilla and Assembly Members Cooley, Nestande and Holden, Sacramento, California, July 17, 2013.

Allen, R.M., Scientific Briefing for Suzette Kimball, Acting Director, U.S. Geological Survey, Berkeley, California, July 18, 2013.

Allen, R.M., Earthquake early warning: Now, or after the next big quake?, Palm Springs, California, September 11, 2013.

Allen, R.M., Warning California: Extracting earthquake signals from noise before the shaking starts, UC Berkeley Data Science Lecture Series, Berkeley, California, September 27, 2013.

Allen, R.M., Earthquake early warning for the US West Coast: Status and new opportunities, Zürich, Switzerland, October 23, 2013.

Allen, R.M., Earthquake early warning: New science and technology to mitigate earthquakes, Rio de Janeiro, Brazil, November 16, 2013.

Allen, R.M., MyShake: Smartphone seismic networks, Hoover Institution, Stanford University, California, December 4-5, 2013.

Allen, R.M., Scientific briefing for Advisors for U.S. Senator Feinstein and Representatives Schiff and Calvert,Washington DC, January 8, 2014.

Allen, R.M., Warning California: Science and technology to reduce the growing earthquake threat, American Society of Home Inspectors, Golden Gate Chapter, Berkeley, California, February 13, 2014.

Allen, R.M., Earthquake Alert: Harnessing BIG data to satisfy societal needs and facilitate new science, Earth Science Colloquium, Lamont-Doherty Earth Observatory, Columbia University, New York, February 21, 2014.

Allen, R.M., Earthquake Alert: Harnessing BIG data to satisfy societal needs and facilitate new science, Institute for Nuclear and Particle Astrophysics, Lawrence Berkeley National Laboratory, February 28, 2014.

Allen, R.M., Earthquake Alert: Harnessing BIG data to satisfy societal needs and facilitate new science, Yuval Ne'eman Distinguished Lectures in Geophysics, Atmosphere and Space Sciences, Tel Aviv University, Israel, March 31, 2014.

Allen, R.M., Imaging the origin of hotspots and the fate of slabs, Yuval Ne'eman Distinguished Lectures in Geophysics, Atmosphere and Space Sciences, Tel Aviv University, Israel, April 2, 2014.

Allen, R.M., Earthquake Alert: Blending seismic and GPS data to reduce risk and facilitate new science, Royal Astronomical Society, London, UK, May 9, 2014.

Allen, R.M., MyShake: Smartphone seismic networks. Intelligence Challenges Workshop, Hoover Institution, Stanford University, California. May 15, 2014.

Allen, R.M., CISN ShakeAlert, Cal Maritime, Vallejo, California. May 19, 2014.

Allen, R.M., Warning California: The day the earthquake comes, SwissNex Hackathon on earthquake resilience, San Francisco, California, May 31, 2014.

Allen, R.M., Earthquake Alert: Harnessing BIG data to satisfy societal needs, FutureCT meeting, Berkeley, California. June 3, 2014.

Allen, R.M., Testimony to the United States House of Representatives, Committee on Natural Resources, Subcommittee on Energy and Mineral Resources. Oversight hearing on "Whole Lotta Shakin: An Examination of America's Earthquake Early Warning System Development and Implementation." Washington, DC, June 10, 2014.

Allen, R.M., Scientific briefing for Advisors for U.S. Representatives Schiff, Lee, Honda, Chu and Swalwell, Washington DC, June 10 and 17, 2014.

Bodin, Thomas, Trandimensional Inference in Geosciences ,Lawrence Berkeley National Laboratory (LBNL), May 16, 2014.

Bodin, Thomas, Trandimensional Inference in Geosciences ,University of Strasbourg, France, March 28, 2014.

Bodin, Thomas, Trandimensional Inference in Geosciences ,Earth and Planetary Science, UC Berkeley, September 26, 2013.

Bürgmann, R., Megathrust Earthquake Cycles, 2013 Birch Lecture, Tectonophysics Section of American Geophysical Union,

2013 Fall Meeting, December 10, 2013.

Bürgmann, R., Periodic Deformation and Seismicity: From Tides to Seasonal Water Loads, Department of Earth Sciences, University of Southern California, May 5, 2014.

Bürgmann, R., Periodic Deformation and Seismicity: From Tides to Seasonal Water Loads, USGS Western Region Colloquium, June 9, 2014.

Bürgmann, R. and R.M. Nadeau (Invited), Briefing on the Borehole High-Resolution Seismic Network (HRSN) at Parkfield, CA and its Associated Research and Monitoring, Meeting of the National Earthquake Prediction Evaluation Council (NEPEC) for Review of the State of Research and Monitoring Work Around Parkfield, California, USGS Menlo Park, Menlo Park, CA, November 4-5, 2013.

Calò M., Fluid-related induced seismicity and Enhanced Geothermal fields. Insights from the 4D seismic tomography, UC Berkeley, Berkeley Seismological Laboratory Seminar, February 4, 2014.

Calò M., Induced Seismicity and Geothermal Fields. Constraints from 4D seismic tomography on the fault-fluid interaction, University of Santa Cruz, IGPP, California, February 7, 2014.

Calò M., Use of the induced seismicity and seismic noise correlation tomography for improving exploration and optimization of geothermal fields, Universidad Nacional Autónoma de México (UNAM), Mexico City, Mexico, May 14, 2014.

Chaussard, E., Characterization of geohazards at regional scales using space geodesy: examples of land subsidence and volcanic eruptions, Berkeley Seismological Laboratory Seminar, Berkeley, CA, October 1, 2013.

Chaussard, E., Remote sensing of ground deformation: an indispensable tool for groundwater resources and hazards management, Massachusetts Institute of Technology, Department of Earth, Atmospheric, and Planetary Sciences Special Seminar, May 22, 2014.

Delbridge, B., B. Buffett, S. Kita, T. Matsuzawa, Application of thin sheet dynamics to subduction zones: Implications for lithospheric rheology, seismogenesis and estimates of bending dissipation, International Summer School on Earthquake Science.

Delbridge, B., R. Burgmann, E. Fielding, S. Hensley, W. Schulz, Landslide-wide kinematics revealed by combining interferometric synthetic aperture radar and continuous GPS observations, European Space Agency.

Dreger, D., Exotic Event Moment Tensor Analysis Including the Latest Results for Bayou Corne, USGS Menlo Park, Menlo Park, CA, March 19, 2014.

Grapenthin, R., Plumbing, Plumes, and Early Warning: Using GPS near Volcanoes, Department Seminar, DTM ,Carnegie Institution for Science, Stanford, CA, March 11, 2014.

Grapenthin, R., Plumbing, Plumes, and Early Warning: Using GPS near Volcanoes, Department Seminar, South Dakota School of Mines and Technology, Rapid City, SD, February 18, 2014.

Grapenthin, R., Plumbing, Plumes, and Early Warning: Using GPS near Volcanoes, Department Seminar, New Mexico Tech, Socorro, NM, January 30, 2014.

Grapenthin, R., Kinematic GPS and Earthquakes: From a Single Time Series to Early Warning, Active Tectonics guest lecture, Cornell University, Ithaca, NY, October 16, 2013.

Grapenthin, R., Plumbing, Plumes, and Early Warning: Using GPS near Volcanoes, Department Seminar, Cornell University, October 16, Ithaca, NY, 2013.

French, S., Toward a full-waveform radially anisotropic shear-velocity model of the earth's whole mantle, Lawrence Berkeley National Laboratory, Earth Sciences Division, Geophysics Seminar Series, January 30, 2014.

Hellweg, M., Earthquakes in our Backyard, Pt. Reyes National Monument, CA, September 26, 2013.

Hellweg, M., Earthquakes in our Backyard, Gateway Science Museum, Chico, CA, October 9, 2013.

Huang, M.-H., Probing the deep rheology across the eastern margin of the Tibetan Plateau: Constraints from the 2008 Mw 7.9 Wenchuan, China earthquake, Department of Earth, Atmospheric and Planetary Sciences, Massachusetts Institute of Technology, January 28, 2014.

Johanson, I., The BARD network: Two Decades of Multi-scale Deformation Measurements in Northern California, California Spatial Reference Center Coordinating Council Semi-Annual Meeting, May 1, 2014.

Johanson, I., R. Grapenthin, P. Lombard, D. Dreger and R. Allen, High-rate GPS for Earthquake Early Warning and Rapid Response, Caltech Seismological Lab Seminar, March 14, 2014.

Romanowicz, B., Low velocities in the oceanic upper mantle and their relations to plumes: insights from SEM-based waveform tomography, CIG/QUEST joint workshop, Fairbanks, Alaska, July 17, 2013.

Romanowicz, B., Global Earth structure in the 21st century, Ettore Majorana Center, Erice, Sicily, August 31, 2013.

Romanowicz, B., Channeled flow at the base of the oceanic asthenosphere: evidence from full waveform tomography, Univ. of Uppsala, Sweden, September 12, 2013.

Romanowicz, B., Low velocity fingers in the oceanic upper mantle and their relations to plumes, IPG Paris, October 1, 2013.

Romanowicz, B., Subduction zones, mantle plumes and recent results from global waveform tomography, IPG Paris, Symposium in the honor of Renata Dmowska, October 14, 2013.

Romanowicz, B., Channeled flow at the base of the oceanic asthenosphere: evidence from full waveform seismic tomography, University of Cambridge, UK, October 23, 2013.

Romanowicz, B., Voyage à l'Intérieur de la Terre, Bibliothèque Polonaise à Paris, France, November 27, 2013.

Romanowicz, B., Voyage à l'Intérieur de la Terre, Collège de France, CLAS, November 29, 2013.

Romanowicz, B., Channeled flow at the base of the oceanic asthenosphere: evidence from full waveform seismic tomography, University of Leeds, UK, November 30, 2013.

Romanowicz, B., Imagi(ni)ng the Earth's Interior, Geological Society of Northern California, Orinda, CA, January 30, 2014.

Romanowicz, B., Imagi(ni)ng the Earth's Interior", Cal Day, UC Berkeley, April 20, 2014.

Romanowicz, B., Imagerie Sismique Globale du Manteau Terrestre par Inversion de Forme d'Onde: panaches mantelliques et convection à petite échelle?, University of Lyon, France, June 1, 2014.

Romanowicz, B., Science au féminin: réflexion sur le parcours d'une géophysicienne", Nuit des Science, ENS Ulm, June 6, 2014.

Strauss, J. A., Shaping Response and Recovery with Earthquake Early Warning, Business Recovery Managers Association, July 2013 Membership Meeting, Oakland, CA, July 25, 2013.

Strauss, J. A., Shaping Response and Recovery with Earthquake Early Warning, California Emergency Services Association, Annual Training Conference 2013, Santa Rosa, CA, October 16, 2013.

Strauss, J. A., and R. M. Allen, Warning California: Science and technology to reduce the growing earthquake threat, San Francisco Planning and Urban Research Association, Lunchtime Forum, San Francisco, CA, October 31, 2013.

Taira, T., Seismic Constraints on Fault-Zone Rheology at Depth from Characteristically Repeating Earthquakes at Parkfield, California, Solid Earth group seminar, University of Tokyo, Japan, July 4, 2013.

Taira, T., Investigating transient slip behavior and fault frictional properties from repeating microearthquake activity along the San Andreas fault in the San Juan Bautista region, the National Institute of Advanced Industrial Science and Technology, Japan, July 16, 2013.

Taira, T., On the Systematic Long Period Noise Reduction on Ocean Floor Broadband Seismic Sensors Collocated with Differential Pressure Gauges, Ocean Hemisphere Project group seminar, Earthquake Research Institute, Japan, July 19, 2013.

Taira, T., Investigating transient slip behavior and fault frictional properties from repeating microearthquake activity along the San Andreas fault in the San Juan Bautista region, Earthquake Research Institute Friday Seminar, Japan, July 25, 2013.

Taira, T., Seismic Constraints on Fault-Zone Strength and Rheology at Seismogenic Depth on the San Andreas Fault, Parkfield, Yokohama City University, Japan, July 29, 2013.

Taira, T., Seismic Constraints on Fault-Zone Strength and Rheology at Seismogenic Depth on the San Andreas Fault, Parkfield, Hot Springs Research Institute of Kanagawa Prefecture, Japan, July 31, 2013.

Taira, T., Investigating transient slip behavior and fault frictional properties from repeating microearthquake activity along the San Andreas fault in the San Juan Bautista region, Hokkaido University, Japan, August 7, 2013.

Taira, T., Borehole Seismic Monitoring of Deep Fault Deformation along the Hayward Fault, CA, Seismology Group Seminar, Ludwig-Maximilians-Universität München, Germany, November 19, 2013.

Awards

Taka'aki Taira

Best Young Scientist Poster Award, International Continental Scientific Drilling Program

Visiting Fellowship, Earthquake Research Institute, University of Tokyo, Japan

Barbara Romanowicz

Elected Member of the French Academy of Sciences

Panels and Professional Service

Richard M. Allen

Lead Organizer, 3rd International Conference on Earthquake Early Warning: Implementing Earthquake Alerts
Chair, U.S. Earthquake Early Warning Coordination Committee, February 2013–present
Chair, International Earthquake Early Warning Advisory Committee, Geological Institute of Israel, 2012-present
Member, Scientific Advisory Board, European Union Framework 6 Project: Strategies and Tools for Real Time Earthquake Risk Reduction (REAKT), 2011–present
Member, Cascadia Initiative Expedition Team, Responsible for deploying ocean-bottom instrumentation for the community-designed Cascadia Initiative funded by NSF, 2011–present
Chair, U.S. Earthquake Early Warning Scientific Coordination Committee, July 2006–present
Co-Organizer, 6th CIDER Summer Program: From mantle to crust: Continental formation and destruction

Roland Bürgmann

Associate Editor, Bulletin of the Seismological Society of America
Editorial Board, Earth and Planetary Science Letters
Member, Facilities Committee of DEFORM
Member, Membership Committee of UNAVCO
Member, National Earthquake Prediction Evaluation Council (NEPEC)
Member, Board of Directors of Southern California Earthquake Center (SCEC)
Member, Earth Science Subcommittee of NASA Advisory Council
Member, AGU Tectonophysics Union Fellows Committee
Co-Chair, IRIS Grand Challenge Science Advisory Committee

Douglas S. Dreger

Cosmos Board of Directors

Margaret Hellweg

Commissioner, Alfred E. Alquist Seismic Safety Commission
Member, CISN Program Management Committee
Member, CISN Standards Committee
Member, CISN Steering Committee
Member, CISN Outreach Committee
Member, ANSS Performance Standards Committee
Member, ANSS Depth Datum Working Group
Chair, CISN ShakeMap Working Group
Chair, ANSS Class C Instrumentation Evaluation Committee
Member, Bay Area Earthquake Alliance Committee
Member, Bay Area Earthquake Alliance Executive Committee
Member, Editorial Board of Journal of Volcanology and Geothermal Research
Member, New Media Committee, Seismological Society of America
Member, California Earthquake Early Warning System Standards Committee
Member, California Earthquake Early Warning System Charter Committee

Bob Nadeau

Member, Berkeley Institute for Data Sciences (BIDS)

Douglas S. Neuhauser

Chair, Standards Group, California Integrated Seismic Network (CISN)
Acting Member, CISN Program Management Committee

Barbara Romanowicz

Member, Conseil d'établissement, Collège de France
Member, advisory committee, COMPRES program
Chair, section 16, National Academy of Sciences (USA)
Chair, doctoral thesis committee, Scott French, UC Berkeley, May 2014
Chair, doctoral thesis committee,, Zhao Zheng, UC Berkeley, May 2014
Participation in the preparation of a "white paper" in the framework of the european program EPOS
Member, Science advisory committee, GEOSCOPE program
Selection committee member, Arthur Holmes Medal, European Geophysical Union.
Organization of post-AGU CIDER workshop, December 8, 2013, Berkeley
PI, Cooperative Institute for Dynamic Earth Research

Jennifer Strauss

Member, California Earthquake Early Warning Planning Committee
Member, California Earthquake Early Warning System Education and Training Committee
Chair, CISN Earthquake Early Warning Communications Committee
Participant, Lifelines Council, San Francisco
Participant, Rockefeller Foundation 100 Resilient Cities Agenda-Setting Workshop

Taka'aki Taira

Member, Editorial board for Solid Earth
Member, California Integrated Seismic Network, Standards Committee
Member, California Integrated Seismic Network, ShakeMap Working Group
Member, Plate Boundary Observatory, Data Working Group

Appendix II: Seminar Speakers

Norm Abrahamson
UC Berkeley
"Seismological Research that will have the largest effects on seismic hazard evaluations in California in the next 5-10 years."
September 3, 2013

Yan Hu
UC Berkeley
"Upper Mantle Rheology Constrained From Subduction Zone Earthquake Cycle Deformation and Post-Glacial Rebound."
September 10, 2013

Abhijit Ghosh
University of California, Riverside
"Slow earthquakes and tremor -- where are we headed?"
September 17, 2013

Charlie Sammis
University of Southern California
"The Role of Deep Creep in the Timing of Large Earthquakes."
September 24, 2013

Estelle Chaussard
UC Berkeley
"Characterization of geohazards at regional scales using space geodesy: examples of land subsidence and volcanic eruptions."
October 1, 2013

Lingseng Meng
UC Berkeley
"Application of Back Projection Imaging to Earthquake Early Warning and Deep-Focus Earthquakes."
October 8, 2013

Dave Stegman
UC San Diego
"The amazing story of Yellowstone-related volcanism."
October 15, 2013

Ken Hudnut
USGS
"UAVSAR Reveals Surface Faulting and GPS PPP(AR) Assists in Earthquake Early Warning."
October 22, 2013

Peter Shearer
University of California, San Diego
"Has the probability of big earthquakes recently increased?"
October 29, 2013

Fukashi Maeno
ERI, University of Tokyo
November 05, 2013

Tom Parsons
USGS
"The global aftershock zone."
November 12, 2013

Julian Lozos
UC Berkeley, PEER
"Rupture and Ground Motion Models on the Claremont - Casa Loma Stepover of the San Jacinto Fault, Incorporating Complex Fault Geometry, Stresses, and Velocity Structure."
November 19, 2013

Donna Eberhart-Phillips
University of California, Davis
"Imaging P and S Attenuation in the Termination Region of the Hikurangi Subduction Zone, New Zealand."
November 26, 2013

Jennifer Frederick
UC Berkeley
"Relict Arctic permafrost-associated gas hydrate deposits: Methane gas escape in response to warming due to natural climate variability."
December 3, 2013

Emily Brodsky
University of California, Santa Cruz
"Stress on Faults.."
January 21, 2014

David Schmidt
University of Washington
"The interseismic accumulation and transient release of strain on the Cascadia Subduction Zone"
January 28, 2014

Marco Calo
UC Berkeley
"Fluid-related induced seismicity and Enhanced Geothermal fields. Insights from the 4D seismic tomography. ."
February 04, 2014

Thorsen Becker
University of Southern California
"Seismic anisotropy as a tool for understanding regional tectonics."
February 18, 2014

James Badro
Institut de Physique du Globe Paris
"Accreting the Earth and Forming its Core: Experimental and Theoretical Constraints"
February 25, 2014

Eric Geist
USGS
"Tsunami Edge Waves: An Oceanic Analog to Love Waves."
March 3, 2014

Michael Thorne
University of Utah
"Ultra-low velocity zones and deep mantle flow."
March 11, 2014

Maxim Ballmer
University of Hawai'i, Manoa
"Long-term survival of compositional layering across the Transition Zone in the presence of whole-mantle convection ."
March 18, 2014

Heidi Houston
University of Washington
"Slow slip,tremor, and tidal stressing: Fault weakening during ETS."
April 1, 2014

Yuning Fu
California Institute of Technology/JPL-NASA
"TGPS as a high resolution technique for estimating water storage variations in Washington, Oregon, and California."
April 8, 2014

Anna Kelbert
Oregon State University
"High resolution global electrical conductivity variations in the Earth's mantle."
April 15, 2014

Scott French
UC Berkeley
"New Constraints on Whole-mantle Structure using Full-Waveform Tomography."
April 22, 2014

Romain Jolivet
California Institute of Technology
"Bayesian exploration of the sources parameters of the 2013, Mw 7.7, Balouchistan earthquake."
April 29, 2014

Zhao Zheng
UC Berkeley
"High resolution upper mantle discontinuity images across the Pacific from SS precursors "
May 6, 2014

Berkeley Seismological Laboratory
Organizational Chart
2013 -2014

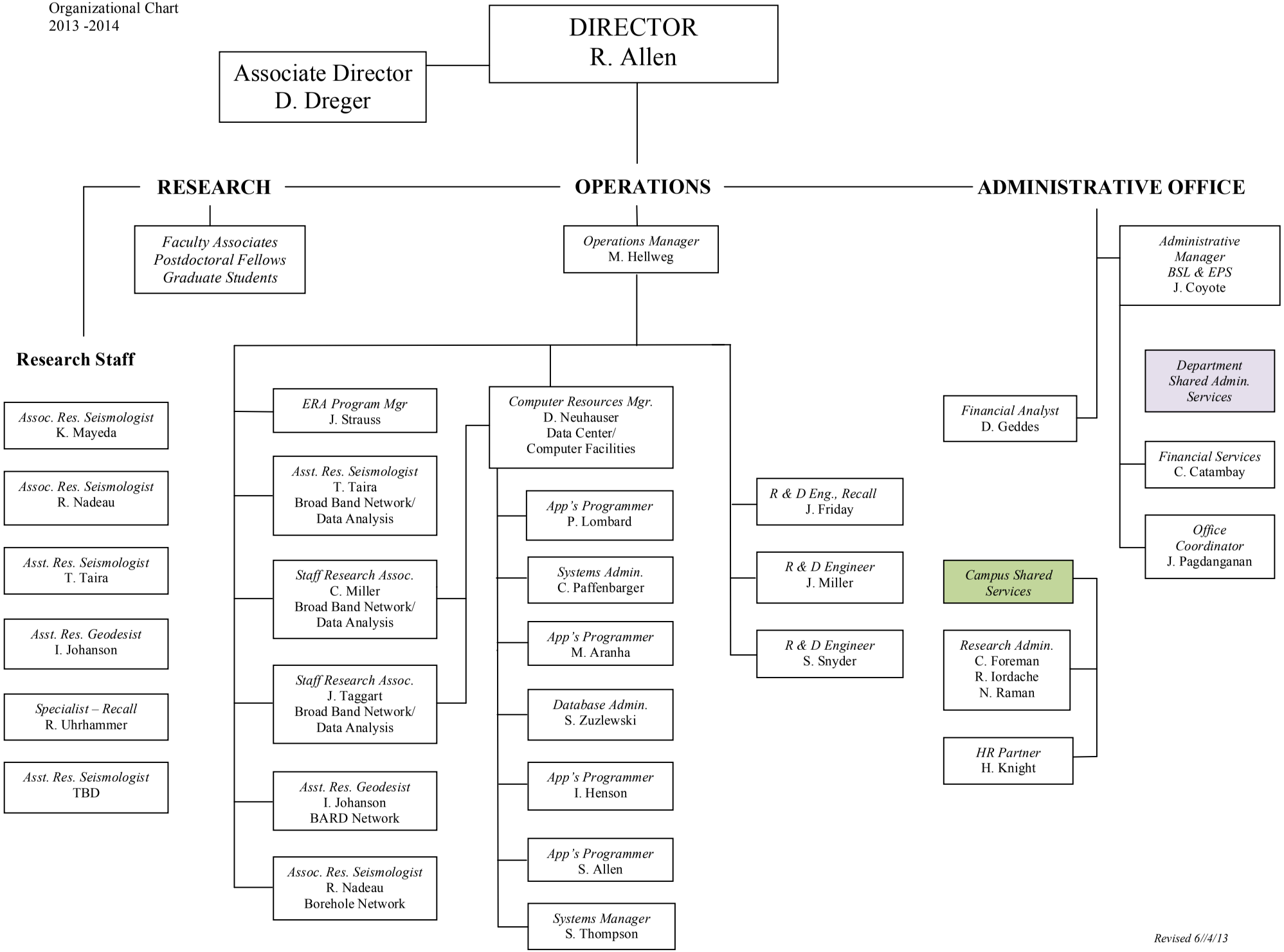

Revised 6//4/13